Fabrication of multi-component nanomaterials in colloidal solution

Wang, Yong

2012

https://hdl.handle.net/10356/49495

https://doi.org/10.32657/10356/49495

Fabrication of Multi-component Nanomaterials in Colloidal Solution

WANG Yong

School of Physical and Mathematical Sciences

A thesis submitted to the Nanyang Technological University in partial

fulfillment of the requirement for the degree of Doctor of Philosophy

Singapore

May 2012

Advisor: Associate Professor, Dr. Chen Hongyu

Acknowledgement

I would like to thank many people in the past several years during my graduate study. Their kindly helps, suggestion, support help me to finish this study stage successfully. First, I want to give my sincerest appreciation to you, my advisor, Prof. Chen Hongyu. Thanks for your patient guidance on the research and circumspective care in my life. You guided me into the wonderful world of nanoscience, trained me the abilities of thinking and solving problems. I could not forget how I started the primary study in this research filed with the help of your direction, patient discussion. You also taught me how to improve my presentation skill, encourage me to collaborate with many other researchers. All these experience will help me in the future work, not only for the research, but also for the daily life.

I also appreciate Prof. Li Shuzhou from Division of Materials Science, School of Materials Science and Engineering for your efforts in helping me simulate the extinct spectra of different kind of nanostructures.

I would like to thank Prof. Han Yu and Wang Qingxiao in King Abdullah University of Science and Technology, Saudi Arabia, for your help on the HRTEM characterization as well as the significance discussions.

Thank Prof. Lu Xianmao, Prof. Chan Yin Thai, as well as Zhang Weiqing in

Contents

Abstract

This thesis focused on the fabrication of multi-component nanomaterials in colloidal solution. The optical properties of these novel structures also have been studied. Multi-component nanostructures usually have abundant structural variety. They can provide not only the properties of each individual, but also the new feature originated from the interaction of them. Therefore, insight into the multi-component system may offer new synthetic strategies and novel architectures, satisfying the requirement of future nanodevices. Two strategies have been adopted for the fabrication of multi-component nanomaterials in this dissertation: rational assembly of nano-objects; direct synthesis based on wet chemistry.

We demonstrate a complete nanoreaction system whereby colloidal nanoparticles are rationally assembled and purified (**Chapter 2**). Two types of functionalized gold nanoparticles (A and B) are bonded to give specific products AB, AB_2, AB_3 and AB_4. The stoichiometry control is realized by fine-tuning the charge repulsion among the B's. The products are protected by polymer, which allowed their isolation in high purity. With the concrete integration of hetero-assembly, stoichiometry control, protection scheme, and separation method, we attempt to create a scalable means to fabricate sophisticated nanostructures. By using this strategy, many nanostructures,

which cannot be obtained through the routine method, also have been fabricated.

Recently, the creation of nanostructures with environment-responsive shape transformation behavior is one hot topic. With the shape conversion of nanostructures, mechanical energies will represent, ensuring the application in smart nanodevices. In **Chapter 3**, one new type of ultrathin Au-Ag alloy nanowires has been synthesized in colloidal solution. This nanowire can exhibit shape transformation behavior: by growing a thin metal (Pd, Pt, or Au) layer, the NW can wind around itself to form double helix. We conclude that the winding action originates from the chirality within the synthesized Au-Ag alloy nanowires, which likely have the Boerdijk-Coxeter-Bernal type twisted lattice.

The exploration of nano-chiral science is still very limited due to the challenge of the manufacture of helical nanostructures. The synthesis of metallic helical nanostructure is especially rare. In **Chapter 4**, helical gold nanowires have been synthesized in colloidal solution without any hard template. This is the first case of metallic nanosprings synthesized in colloidal solution. By analyzing the reaction conditions, we find that the growth solution consists of several small organic molecules derived from 4-mercaptobenzonic acid. However, the yield is still very low, which prevents insight into the formation mechanism. The continuous study will be carried out in the future work.

It has been witnessed that wet chemistry synthesis strategy is one powerful weapon to create multi-component nanostructures, especially since the seed-mediated growth process was used. Two kinds of polycrystalline NPs are used as seeds to synthesize heterodimers (**Chapter 5**). Pt-M, (M = Au, or Ag) heterodimers have been obtained owing to the large lattice mismatching of Pt-Au and Pt-Ag, in which Volmer-Weber growth mode is adopted. Au-M (M = Au, or Ag) heterodimers are obtained by tuning the surface molecules coating of the Au seeds. When the molecules coat on the Au seeds surface, the interface energy will increase, thus the Stranski-Krastanov growth mode, even the Volmer-Weber growth mode will be adopted.

In **Chapter 6**, one kind of Ag cluster superlattices has been synthesized in colloidal solution. These superlattices structures can be encapsulated into the copolymer cavity and docked onto other nanostructures by the polymer coating procedure. We propose that the superlattices are formed by the close packing of Ag domains, which are fully coated by thiol-ended hydrophobic molecules. This assembly mode can decrease the surface energy of each Ag domain as much as possible.

Finally, in **Chapter 7**, I summarize the whole work and propose the future work.

Chapter 1   Introduction

1.1   Nanotechnology and Nanomaterials

Nanoscience and nanotechnology is a new technology that was born in the 1980s and rapidly growing up in last dozens of years. The basic concept of this technology is to understand and change the nature, to create new materials thorough direct manipulating and arranging atoms and molecules on atom scale. It has been imaginatively predicted by Nobel laureate Richard Feynman in his famous talk "There's Plenty of Room at the Bottom" in 1959.[1] The invention of scanning tunneling microscopy in 1981 is another milestone of nanoscience,[2] which ideally verified the assertion of Richard Feynman and initiated the manipulating of individual atoms.

Nanomaterials are defined for the solid materials composed of nanoscale building blocks, in which the size of these building blocks is not more than 100 nm in at least one dimension. The nanoscale building blocks can be classified by shapes: zero dimension nanoclusters[3, 4] (the aggregates of several dozens of atoms), semiconductor quantum dots[5] (QDs) and nanoparticles (NPs);[6-8] one dimension nanofibres, nanowires (NWs), nanotubes, nanorods (NRs);[9] two dimension nanofilms, nanodisks, nanoprisms, *etc*.[10] Since the materials drop to nanometer scale, the properties can be remarkably changed from the bulks, the development of nanoscience and technology offers the new opportunity to the

multidisciplinary of mechanics, material science, physics, chemistry, medicine, biology, *etc*. In the past several decades, a numerous of nanomaterials have been manufactured by the direct syntheses strategy or the controlled assembly of nano building blocks with designed properties, which have exhibited satisfactory applications in many fields, such as photonics, electrics, magnetic, sensing, detection, diagnostics, catalysis, electronic devices, fuel cell, solar cell, and so on.[11-26]

1.2 Properties and Applications of Metallic Nanomaterials

In last several decades, noble metallic NPs played an important role in the nanoscience and nanotechnology field. When the sizes of materials decrease to nanoscale, novel properties can be achieved in consequence of: size-dependent properties, surface effect, *etc*. One significant property of metallic NPs is the optical property.[12] Gold colloid was first used in the middle of 17th century for the ruby color glass preparation owing to the bright color. With the development of nanotechnology, the noble metallic NPs have been widely used in lots of other fields, such as catalysis,[24] diagnostics,[14] electrics,[27] Surface Enhanced Raman Spectrum (SERS).[13] Metallic NPs will inevitably be the critical building blocks for the next generation electronic, photonic, and chemical devices. In this thesis, I will discuss the fabrication of multi-component nanostructures of noble metal, such as gold (Au), silver (Ag), palladium (Pd), and platinum (Pt). Therefore, the noble metallic nanostructures will be focused

on in the following introduction. A brief introduction about the optical, catalytic properties of noble metallic nanomaterials will be presented.

1.2.1 Optical Property

Noble metallic NPs (mostly for Au and Ag) always have fancy optical properties (Figure 1-1).[28-30] Macroscopically, these metallic colloid solutions are of vivid color. This special property is derived from the interaction between irradiation light and free electrons in the metallic NPs: the electromagnetic wave can travel along the interface between the metallic NPs and a dielectric media,[31, 32] when the electromagnetic field of the light couple to the oscillation frequency of the free electrons, the Surface Plasmon Resonance (SPR) will generate. In practical, this oscillation frequency of electrons will decrease due to the damping, lattice defect, and inelastic collisions, *etc*. So in order to maintain this movement, these electrons will absorb energy from the light. Only the light with the frequency close to these electrons will be absorbed, consequently this selectivity results in the different optical absorption of different NPs in UV-Vis range. The wavelength and breadth of the absorption relate closely with the size, distribution, morphology, surface charge, and the environment,[30, 33-39] thus can be controlled by tailoring the sizes, shapes, and assemblies of the metallic NPs.

One typical example of the shape-dependent SPR is the nanospheres (NSs) and NRs.[28] Au NSs only show one characteristic peak at about 520-530 nm; Au NRs exhibit two peaks. Because the oscillation of electrons in NSs is

isotropy, just one identical oscillation frequency is represented. For the NRs, the oscillation frequencies at long and short axes are obviously different, thus two distinct oscillation frequencies are exhibited, *i.e.* longitudinal and transverse SPR.
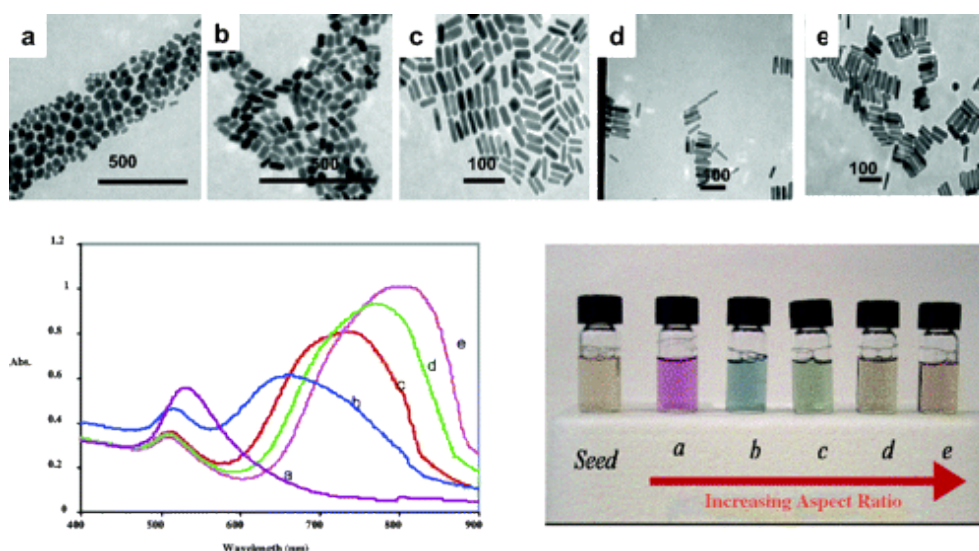
Figure 1-1 Transmission electron micrographs (top), optical spectra (left), and photographs of (right) aqueous solutions of gold nanorods of various aspect ratios. Seed sample: aspect ratio 1; sample a, aspect ratio 1.35 ±0.32; sample b, aspect ratio 1.95 ± 0.34; sample c, aspect ratio 3.06 ±0.28; sample d, aspect ratio 3.50 ± 0.29; sample e, aspect ratio 4.42 ± 0.23. Scale bars: 500 nm for a and b, 100 nm for c, d, e. Reprinted with permission from ref. [30]. Copyright (2005) American Chemical Society.

When metallic NPs are assembled together with very small gaps, the inter-particle plasmon coupling will appear. Our group has devoted many efforts on the small size aggregates of NPs (dimers and trimers), in which clear longitudinal SPR appeared in the UV-Vis spectra, indicating strong coupling within the nanoclusters (Figure 1-2).[40, 41] Recently, the plasmon coupling is widely used in SERS labeling and sensing application, because of the highly enhancement and sensitivity.[42-46]

The SPR and the derived applications have been widely studied via the experimental and theoretic methods.[47-56] Discrete dipole approximation (DDA) is one popular simulation approach towards to reproduce the light absorption, scattering, as well as the electromagnetic field distribution of NPs with arbitrary shapes and sizes in theoretical modeling.[57] In comparison to the previous Mie theory,[58, 59] this approach can properly resolve the complex systems, such as coupled NPs, multi-composite nano-assemblies, and so on.[60] In DDA simulation, NP is divided into small grids, which are interrelating with each other through the dipole-dipole interactions. The optical properties of NPs can be simulated through the self-consistent field calculation of the whole system.
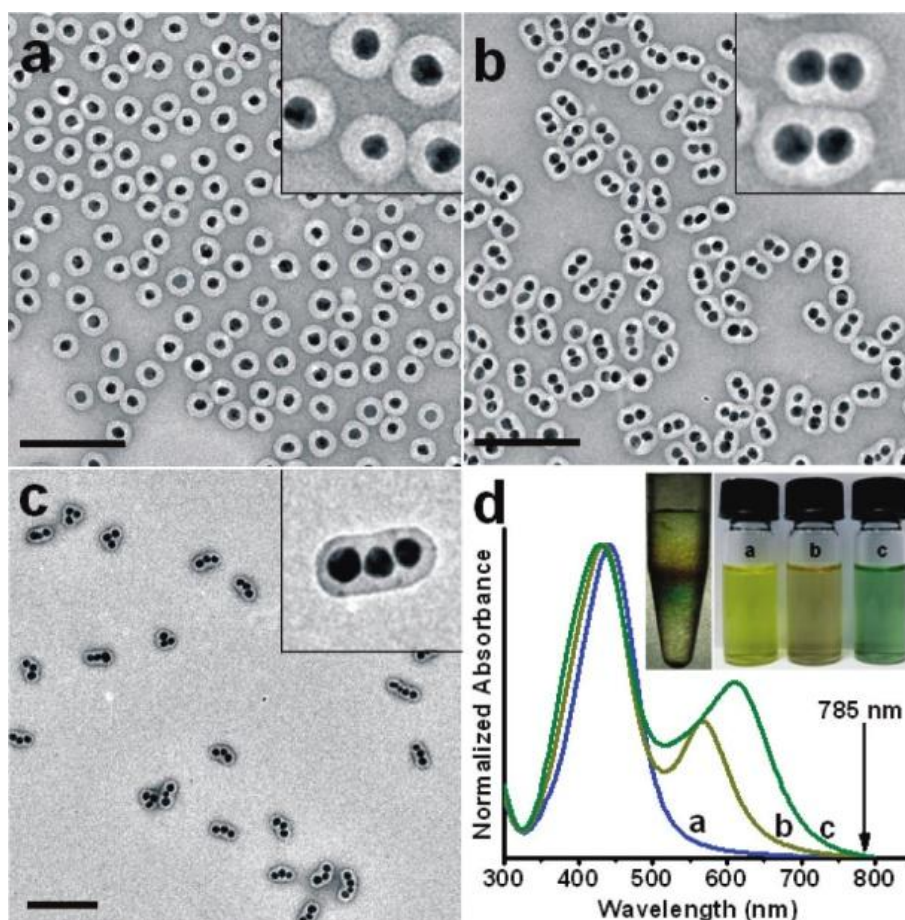
Figure 1-2 (a-c) TEM images and (d) UV-Vis spectra of the samples enriched with Au@Ag monomers (a), dimers (b), and trimers (c). The inset in (d) shows

a typical outcome of the differential centrifugation, where monomers, dimers, and trimers were enriched in distinct yellow, brown, and green bands, respectively. Scale bars: 200 nm. Reprinted with permission from ref. [41]. Copyright (2005) American Chemical Society.

Because the SPR is highly size-dependent, the absorption peak of the SPR will shift along with the aggregation of the NPs, resulting in the colloid solution color change. This optical speciality can be directly adopted for the fast DNA analysis and detection.[12, 61, 62] Another application is the cancer therapy and detection owing to the near-infrared absorption.[63-65] Designed nano-composites can absorb near-infrared radiation, while the tissue of human body usually cannot absorb this low energy radiation. When the nano-composites are targeted to the tumors, and irradiated, they can play the role of nanoscale heating source, killing the cancer cells by the generating heat.

Surface Raman Enhancement Scattering (SERS), is named for the phenomenon that Raman signal can be enhanced when the molecules are absorbed on the metal surface.[13, 42, 66-70] One important contribution to this effect is the electromagnetic enhancement, which is owing to the SPR property of the NPs. When the SPR appears, strong electrons collection and oscillation will arise on some special area of the NPs, generating strong localized electromagnetic field.

One important application of SERS is the labelling and sensing.[71, 72] Several Raman reporters can be assembled on the same metal surface simultaneously, and excited with a single light source to give multiple sets of characteristic fingerprint of the individual analytes. Moreover, in comparison to the

fluorescence technique, the reporters close to the NPs have good photostability. These advantages lead SERS labels as the ideal material in multi-complex bio-systems.[73-75] Our group have developed one general strategy to bind the Raman analytes onto the surface of polymer encapsulated noble NPs.[76] As the polymer encapsulation method is very general to all of the noble NPs, and the polymer shell is easy to be further functionalized, this kind of SERS labels is promised to be widely applied.

1.2.2 Catalytic Property

For catalytic reaction, the catalytic activity is almost dependent on the surface atoms of the metallic catalysts. At nanoscale, the surface/volume ratio is very high, thus NPs always exhibit more excellent catalytic properties, such as Pt NPs usually showing higher catalytic activity than the traditional Pt black. Generally, metallic catalysts can be catalogued to two kinds: metallic NP catalysts; supported metallic NP catalysts. For the metallic NP itself, there are usually two strategies to improve the catalytic activity: component, determining the electronic structure;[24, 77] shape of the NP, organizing the surface atoms.[78] Many researchers have devoted their great efforts on exploring the new catalysts and improving the activity based on these two aspects.

One important approach is the shape control of the NPs. It is proved that NPs with high index facets usually show higher catalytic activity than that with normal low index facets.[78-81] The high index facets contain abundant atomic steps and kinks, which can be used as active sites for the chemical bonds

splitting.[82] Sun and Wang group have reported the tetrahexahedral platinum nanocrystals enclosed by high index facets like {730} represented high activity. Such NPs have high intensity of atomic steps and dangling bonds, which can largely enhance the catalytic activity of formic acid oxidation.[78] Recently, two types of Au-Pd core-shell NPs enclosed by high-index facets also have prepared through hetero-epitaxial growth of Pd shell on high-index-faceted AuNPs. They also show high catalytic activity for the Suzuki coupling reaction.[80] Dendritic nanostructures also show excellent catalytic properties.[24, 83-86] The typical example is the Pd-Pt bimetallic dendritic nanostructures, which were synthesized by depositing Pt on the Pd seed in aqueous solution (Figure 1-3). These NPs show high activity for oxygen reduction reaction.[24]
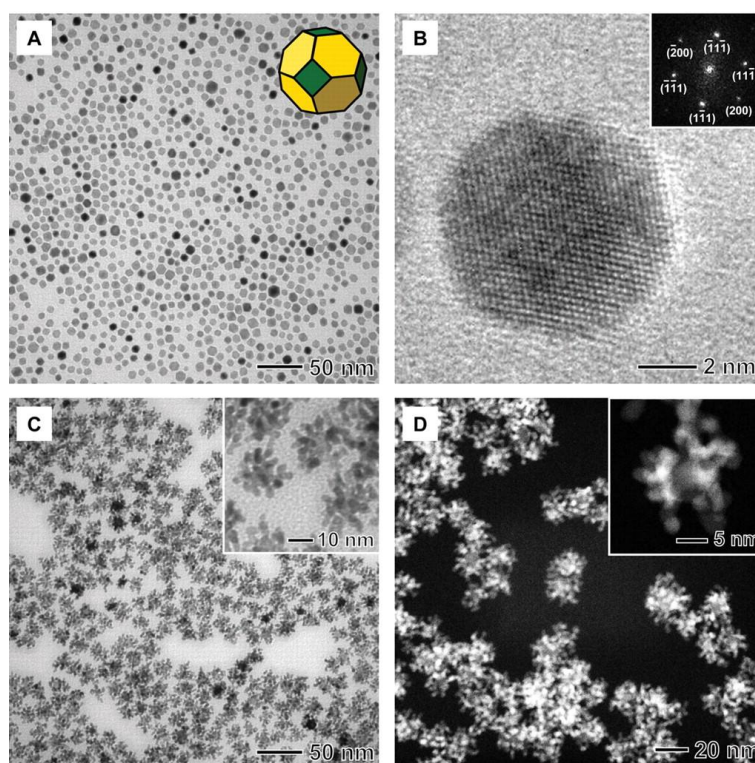
Figure 1-3 (A) TEM image of truncated octahedral Pd NCs. The inset shows a geometrical model of the truncated octahedron, where the green and yellow

colors denote the {100} and {111} facets, respectively. (B) HRTEM image of a single truncated octahedron of Pd recorded along the [011] zone axis and the corresponding FT pattern (inset). (C) TEM image of Pd-Pt nanodendrites. (D) HAADF-STEM image of Pd-Pt nanodendrites. (permission from ref. [24], copyright 2009 American Association for the Advancement of Science)

The other approach is the synthesis of multi-component nanostructures. Bimetallic core-shell NPs or alloys have exhibited wonderful catalytic activity.[23, 24, 86-90] As Pt and Pd have good catalytic activity, many bimetallic NPs with Pt or Pd were synthesized, in which the activity has been enhanced due to the low relative quantity of noble metal usage and the improvement of high active facets. Yang and co-workers have demonstrated that Pd can be localized deposited on the cubic Pt nanocrystals, which showed enhanced electrocatalytic oxidation of formic acid.[88] Recently, Han and co-workers selectively deposited Pt on the AuNPs with different shapes (cube, rod, and octahedron). These Au@Pt core-shell nanostructures showed excellent enhancement of electrocatalytic activity toward oxygen reduction reaction. Meanwhile, they concluded that the different enhancement degree is relied on the specific facet of the seed, which can induce different nucleation and growth of the shell.[23] Ultra-long Pd NWs also can be served as seed for the Pt overgrowth. This kind of core-shell nanodendritic structure can enhance electrocatalytic activity significantly.[87] Very recently, one type of Ag@Pd core-shell structures have been used for the producing hydrogen from the

decomposition of formic acid at room temperature. The results also showed that the core-shell structure was crucial and better than the alloys.[91]

Metallic NPs are often produced in colloidal solution with the help of surfactants. However, the surfactant molecules may influence the catalytic properties of the NPs. El-Sayed and co-workers found that the catalytic activity of PVP coated Pd NPs was weakened for the catalysed Suzuki reaction. This is because the surfactant on the NPs can prevent the NPs from adsorbing new atoms to perform the reaction.[92]

1.3 Strategies for the Manufacture of Nanomaterials

With the development of nanotechnology, more and more NPs with morphology control, well-tuning component and scale-up quantities are required. Thus numerous strategies towards abundant kinds of NPs are developing. Generally, there are two big species: physical method and chemical method. For the physical method, special techniques or instruments (such as molecular beam epitaxy,[93] scanning probe microscope,[94, 95] and so on) are usually required, which dependent on severe conditions. Thus, the physical method is usually used for the accurate materials and cannot expand to large regions. In contrast, chemical method can offer wide platform for the NPs synthesis under friendly conditions. In chemical method, the idea "bottom-up" is usually used; it contains the NPs synthesis from atoms and the assembly of NPs.[96-98] In the following, I will briefly introduce the chemical strategies.

1.3.1 Synthesis of Nanoparticles

Since the advancement of characterization means and nanotechnology, numerous methods have been developed to synthesize NPs, especially for the metallic NPs. One famous approach is the chemical vapor deposition (CVD) method, in which the precursor was evaporate at high temperature firstly, and deposited on the substrate to form solid materials with high-purity and high-performance. This method is often used for the semiconductor fabrication.[99-107]

Another widely used method is wet chemistry synthesis, in which the NPs were synthesized in colloidal solution, guaranteeing the scale up possibility. For metallic NPs, the wet chemistry synthesis set-up usually is very simple: reducing agent was added into the solution containing metallic precursor and stabilizer to reduce the metal ions to atoms, followed by aggregating the atoms to NPs. The typical and well-known method for the synthesis of AuNPs was developed by Fens.[108] Varying sizes of sodium citrate stabilized Au nanospheres (AuNSs) have been synthesized by using sodium citrate to reduce the $HAuCl_4$ in boiling water. This method can be used to synthesize small AuNSs (<20 nm) with narrow distribution, and large AuNSs with the help of seeds.[109-111] Similarly, AgNSs also can be synthesized by reducing $AgNO_3$ with ascorbic acid in the presence of seeds.[41] Metallic NPs (Au, Ag, and Au3Pd) capped with hydrophobic ligand, which can be dispersed in organic solvent also have been synthesized at either high or room temperature.[112, 113]

Many anisotropic metallic nanostructures have been widely used for bio-sensing, imaging, and cancer treatment based on the specific SPR. Seed-mediated growth approach is the most popular method for the AuNRs since Prof. El-Sayed, and Murphy first reported.[114, 115] The aspect ratio, diameter, and shape of the AuNRs can be easily tuning through the addition of $AgNO_3$ or the control of pH, concentration, seeds amount, and so on.[116-119] By using the similar method, AgNRs and NWs also have been synthesized.[120] In one recent review, metallic NPs with various shapes synthesized via wet chemical method have been discussed.[121] The seeds and the surfactant play import roles in controlling the shape of final products.

Recently, some ultrathin metallic NWs (Au, Pt, PtFe) have been synthesized in non-polar solvent using oleylamine as the capping agent and reducing agent.[122] These NWs have been used for the fabrication of multi-component nanomaterials with excellent properties.[123] The application of these NWs may be limited due to the hydrophobic capping agent. However, the synthesis of ultrathin NWs in polar solvent is still very rare.[124, 125] So it is critical to develop new synthesis strategy. In Chapter 3, I will discuss one new type of ultrathin Au-Ag NWs.

Finally, template-mediated synthesis is also a powerful method. Very recently, silver microcoil has been synthesized through one biotemplate.[126] This left-handed coil structure may be applied in electromagnetic-responsive fields. Several other kinds of helical metallic nanosprings were synthesized

with the help of template,[127, 128] which will be discussed in detail later. It is also demonstrated that metallic NRs (Au, Ag, Pt, Pd) can be fabricated in silica nanotube template.[129]

1.3.2   Assembly of Nanoparticles

With the primitive structural control that has been developed so far, NP assemblies have shown great promise in photonic crystals, sensors, nanowire growth (as catalysts), and for exploring fundamental electronic and optical properties.[14, 106, 130-135] However, the future fabrication of advanced nanodevices will require sophisticated assembly techniques. To this end, it is critical to develop methodologies to assemble heterologous nano-objects with finite size and precise stoichiometry.

Previously, homo-aggregates of AuNPs such as dimers and trimers were prepared by exploiting either aggregation kinetics[40, 136, 137] or steric effects.[133, 138, 139] Specific bonding of heterologous NPs was achieved only through the use of atypical NPs with anisotropic surface functionalities (*e.g.*, NP with a single DNA molecule).[140-147]

Our group has paid more attention to assembling NPs into nanoclusters with smaller size. The idea of our homo-aggregation is to control the charge repulsion of the NPs by tuning the ionic strength of the solution.[40, 41, 136, 148] Copolymer was added to stop the aggregation, and encapsulate the clusters, consequently protect them from further dissociation during purification (Figure 1-4).
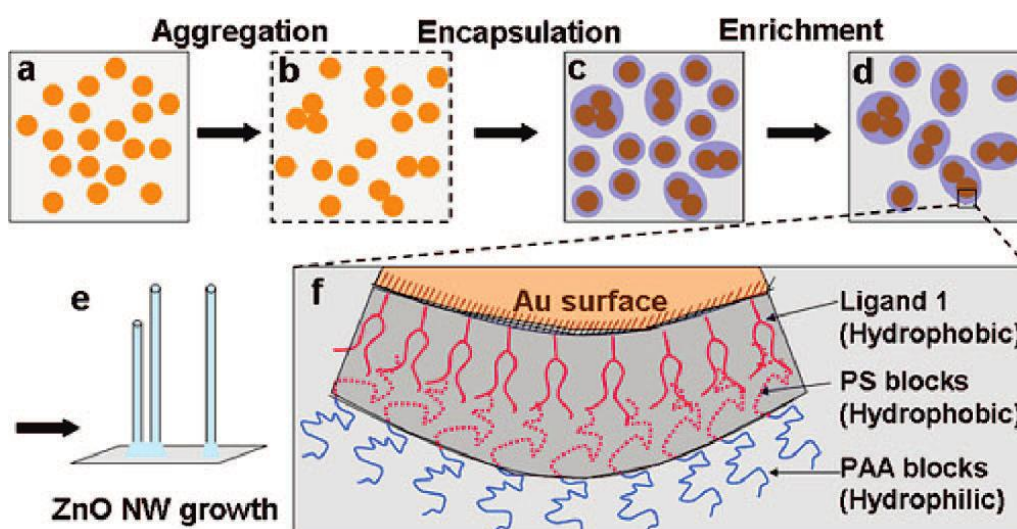
Figure 1-4 Illustration for the preparation of dimeric AuNPs and Dimeric ZnO NWs. (Reprinted with permission from ref. [136]. Copyright (2008) American Chemical Society.)

The previous strategies for the hetero-assembly is mainly based on the synthesis of anisotropic functionalization of the NPs. Usually NPs were stuck on the surface of substrate via DNA or small molecule linkers, and then functionalized by another linkers. Thus Janus NPs were produced by remove the NPs from substrate, and used for the performance of hetero-assembly (Figure 1-5). The hetero-assembly is believed to be the development orientation towards the fabrication of future nanodevices. However, these methods developed so far have some disadvantages: more expensive DNA molecules are used; the substrates are often in small scale. To improve the restricted applications, more intelligent technique is highly demanded.
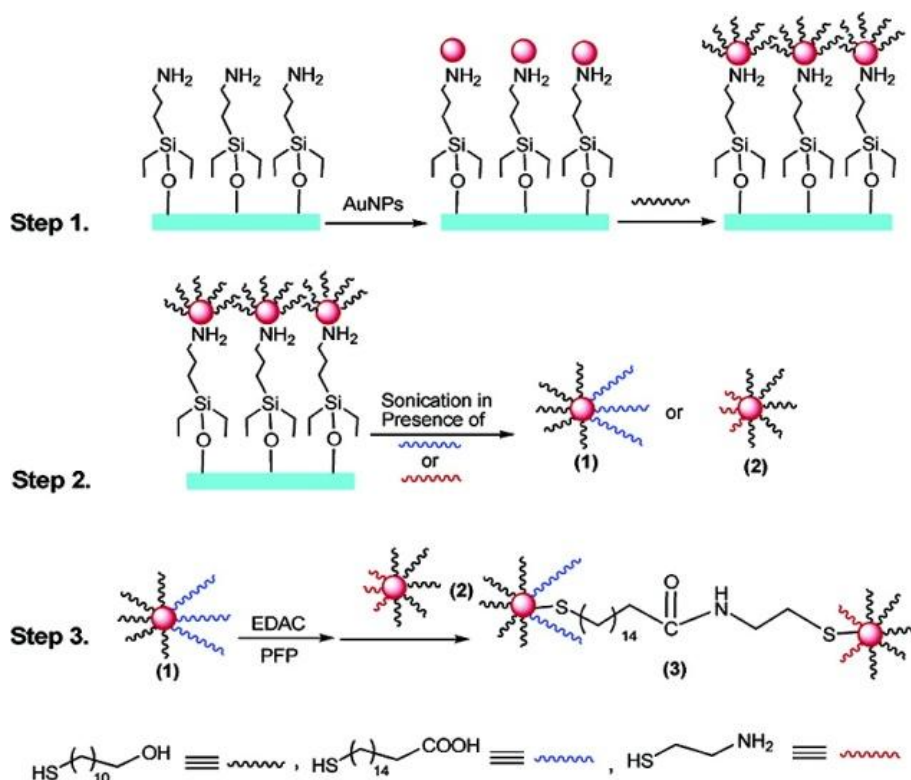
Figure 1-5 Scheme for the synthesis of gold nanoparticle dimmers. (Reprinted with permission from ref. [145]. Copyright (2007) American Chemical Society.)

1.4 Helical Nanostructures

As we know many biomolecules, such as RNA, DNA, protein, and so on contain the helical stuctures. Thus, the chirality is highly associated with the life sciences. Meanwhile, chirality is usually the active element of drugs. Thus, chirality is one major theme in organic chemistry and has been adequately studied. However, for the nanoscience, it still stays at the beginning step due to the challenge of the manufacture of helical nanostructures. Once you open a watch or a machine, macroscopic chiral components such as gears, springs, propellers and scissors will appear. In contrast, chiral nano-objects are of great importance for fabricating future nanodevices. Primary studies have demonstrated that the asymmetric structures are more useful for asymmetric

15

catalysis,[149, 150] chiral separation,[151, 152] and novel optical properties.[153-159] For these applications, metallic nanostructures have clear advantages. In the following, the strategies for the fabrication of helical nanostructures will be reviewed.

1.4.1 Syntheses of Helical Nanostructures

Some groups have devoted their great efforts to reduce the symmetry of NPs, even for the pursuing of chiral nanostructures. Up to now, most of the chiral nanostructures have been synthesized using CVD method.[99-104] Based on the characterization and the growth conditions analyses, several growth mechanisms have been proposed, which can be further consulting for the fabrication of analogous structures.

Helical carbon nanotubes have been synthesized through CVD method in the presence of metal NPs, which were served as the catalysts. Due to the different extrusion rate of the catalytic NPs, the velocity of carbon deposition is different. Consequently, helix-shape carbon nanotubes formed.[101] Screw dislocation induced growth mechanism can be applied to explain some helical structures. For the helical semiconductors, one surface charge imbalance mechanism was proposed. As shown in Figure 1-6, left- and right-handed ZnO nanohelices have been synthesized. Because the wurtzite-structured ZnO crystal contains the positive charged Zn^{2+} and negative charge O^{2-} polar surfaces, the ZnO can grow with the helical structures to minimize the total energy.[99]
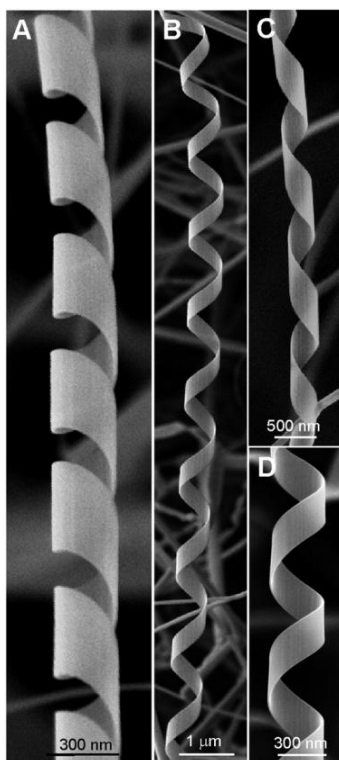
Figure 1-6 Morphology of nanohelices. (A to C) Typical SEM images of the left- and right-handed ZnO nanohelices. (D) High-magnification SEM image of a right-handed ZnO nanohelix, showing a uniform and perfect shape. (permission from ref. [99], copyright 2005 American Association for the Advancement of Science).

Another important strategy is template-mediated synthesis. Stucky and co-workers found that the confined channels (SiO_2 loaded in anodic aluminum oxide (AAO)) can be used as the hard template for the formation of chiral AgNWs through the electrochemical deposition performance (Figure 1-7). The shapes and morphologies of the chiral nanostructures also can be controlled by tuning the diameter of these channels.[127] Another research group also used the similar method to synthesize the Pd nanosprings, in which AAO membrane was used as the template and Cu was used as the helper.[128] Very recently, silver microcoil has been synthesized through the spiral vessels in lotus root as

bio-template.[126] It can be predicted that this left-handed coil structure derived from the bio-template can be applied in electromagnetic-responsive fields.
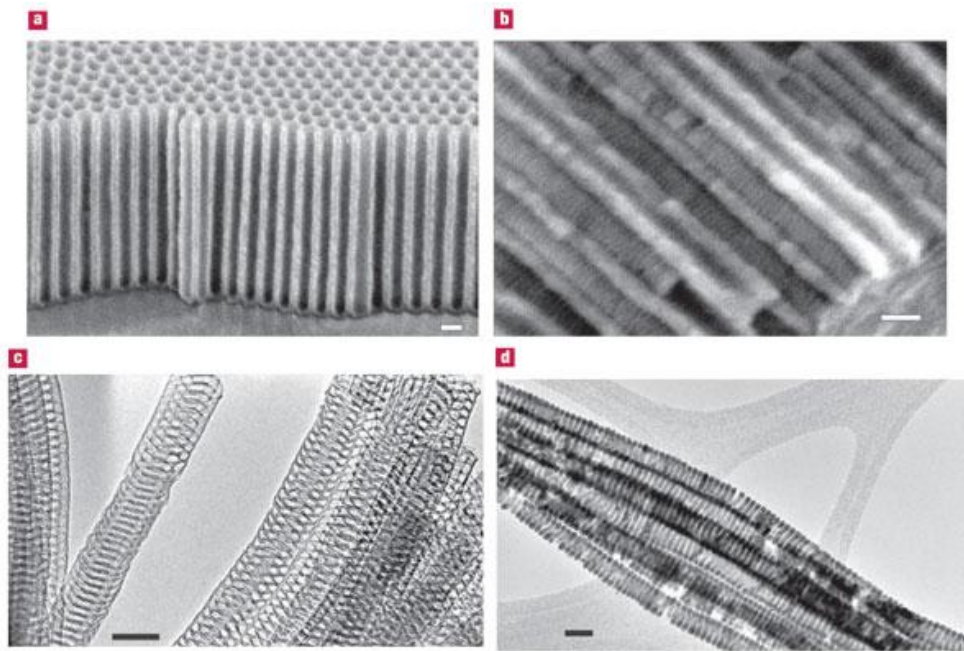
Figure 1-7 SEM images of PAA membrane and TEM images of free-standing mesoporous silica fibres and silver mesostructured nanowires.a, SEM image of the starting PAA membrane. b, SEM image of the PAA membrane cross-section after loading with mesoporous silica. c, TEM image of free-standing mesoporous silica fibres. d, TEM image of Ag nanowires with inverted mesostructures after their release from the oxide matrix. Scale bars: 100 nm in a and b, and 50 nm in c and d. (Reprinted with permission from ref. [127]. Copyright 2004, Macmillan Publishers Ltd./Nature Publishing Group.)

A kind of Au-Ag NWs with the intrinsic chirality have been produced several months ago.[160] The synthesis process is similar to the ultrathin AuNWs synthesis, just Ag precursor is added and high temperature is adopted. These NWs are usually 2 nm in width and 50~100 nm in length, with uniform distribution of both Au and Ag elements. These NWs are proposed to be the packing structures of several Boerdijk-Coxeter-Bernal helices, which is consistent with the simulation of electron micrograph. However, the growth

mechanism is still not clear.

1.4.2 Helical Nanostructures Formation *via* Assembly

Although helical nanostructures have been synthesized via various methods, these methods have some disadvantages, which limit the widely application of different chiral nanostructures formation. CVD method usually requires very high temperature and bulk substrates, thus the products are typically large and nonmetallic. The template in the template-mediated method usually needs complex synthesis or treatment. So it is needed to develop new methodologies to improve the helical nanostructures. Rational assembly of non-chiral nano-object into chiral nanocomposite is one essential choice.
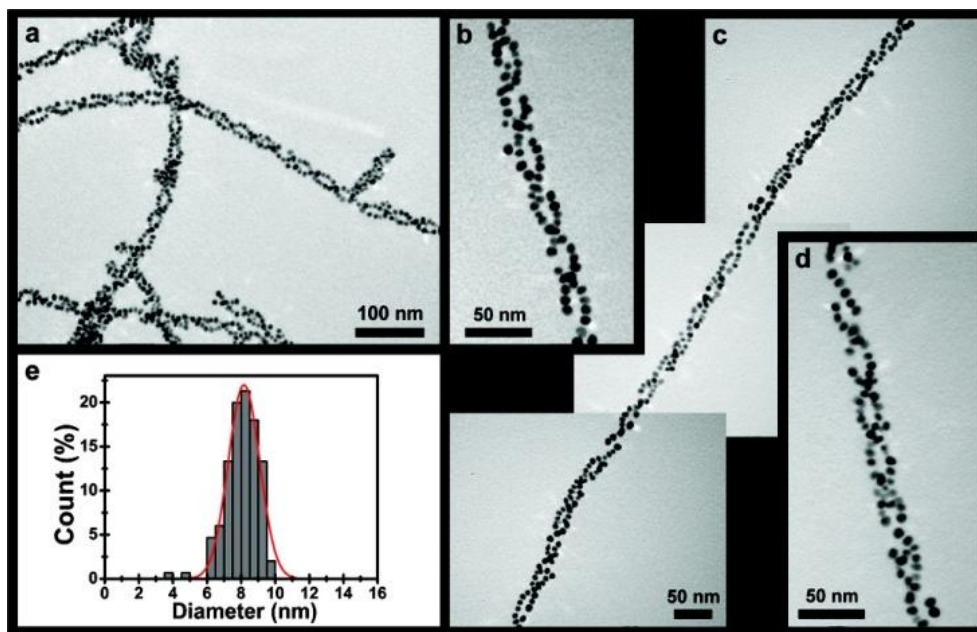
Figure 1-8 TEM characterization of gold nanoparticle double helices. Structurally regular gold nanoparticle double helices form when a solution of chloroauric acid is added to HEPES buffer solutions containing C_{12}−PEPAu, as evidenced by TEM analysis (a−d). The sizes of the gold nanoparticles are uniform (8.2 ± 1.0 nm; based on 150 counts) (e). (Reprinted with permission from ref. [158]. Copyright (2008) American Chemical Society.)

In colloidal solution, some chiral biomolecules have been used as the templates for the surface assembly of NPs.[153, 158, 161, 162] Chiral NPs assembles are easily fabricated, although these formations are not coherent. In one typical example, functionalized peptide was firstly assembled into left-handed double helical structures. Then this helical structure was used as the template for the AuNPs nucleation and growth. Figure 1-8 showed the double helical AuNPs assembly. This type of nanostructure can enhance the intensity of circular dichroism (CD) response due to the SPR coupling of the NPs.[154] Amino Acid based coordination polymers also can exhibit the chiral transformation during long time incubation.[157]
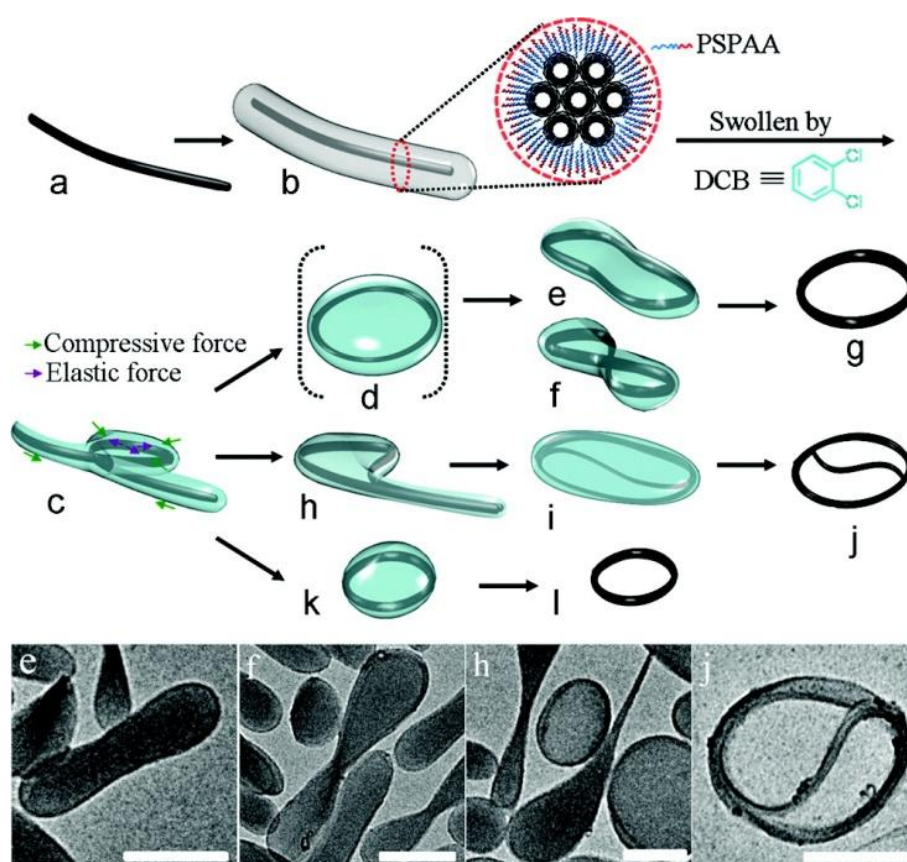
Figure 1-9 (top) Schematics illustrating the fabrication and structural transformation of CNT rings. Bundles of CNTs (a) were encapsulated in PSPAA shells (b). With the addition of DCB and water, the polymer shell

contracted and coiled the embedded CNTs via intermediates (c) to racket-shaped (h) and ring structures. While the small CNT rings (k) remained, the large circular rings (d) were further compressed to "peanut-shaped" (e) and "8-shaped" (f) structures. After removal of the polymer shells, the CNT rings did not uncoil (g, j, and l). (bottom) TEM images of the typical structures. All scale bars represent 200 nm. (Reprinted with permission from ref. [163]. Copyright (2011) American Chemical Society.)

Our group is also interested in the environment-responsive shape transformation of nanostructures. Recently, we have demonstrated that the polymer coated AuNWs and carbon nanotubes can coil into ring structures.[163, 164] The idea is that the polymer coating can swell and deswell when the solution conditions changes (Figure 1-9). When H_2O is added, the polymer can contract and so as to induce the embedded nanofilaments coiling. Although these nanosprings are packed closely, they could be with the chiral arrangement. This system can be potentially used in further nanodevices because the mechanical energy can be stored and released easily.

1.5 Bibliography

[1] Feynman, R. P., There's Plenty of Room at the Bottom. *Eng. & Sci.*, **23**, 22 (1960).

[2] Binnig, G. and Rohrer, H., Scanning Tunneling Microscopy. *IBM J. Res. & Dev.*, **30**, 355 (1986).

[3] Zhu, M., Lanni, E., Garg, N., Bier, M. E., and Jin, R., Kinetically Controlled, High-Yield Synthesis of Au-25 Clusters. *J. Am. Chem. Soc.*, **130**, 1138 (2008).

[4] Hulkko, E., Lopez-Acevedo, O., Koivisto, J., Levi-Kalisman, Y., Kornberg, R. D., Pettersson, M., and Hakkinen, H., Electronic and Vibrational

Signatures of the Au(102)(P-Mba)(44) Cluster. *J. Am. Chem. Soc.*, **133**, 3752 (2011).

[5] Keuleyan, S., Lhuillier, E., and Guyot-Sionnest, P., Synthesis of Colloidal Hgte Quantum Dots for Narrow Mid-Ir Emission and Detection. *J. Am. Chem. Soc.*, **133**, 16422 (2011).

[6] Wang, X., Zhuang, J., Peng, Q., and Li, Y. D., A General Strategy for Nanocrystal Synthesis. *Nature*, **437**, 121 (2005).

[7] Lu, X. M., Rycenga, M., Skrabalak, S. E., Wiley, B., and Xia, Y. N., *Chemical Synthesis of Novel Plasmonic Nanoparticles*, in *Annu. Rev. Phys. Chem.* 2009. p. 167.

[8] Rycenga, M., Cobley, C. M., Zeng, J., Li, W. Y., Moran, C. H., Zhang, Q., Qin, D., and Xia, Y. N., Controlling the Synthesis and Assembly of Silver Nanostructures for Plasmonic Applications. *Chem. Rev.*, **111**, 3669 (2011).

[9] Xia, Y. N., Yang, P. D., Sun, Y. G., Wu, Y. Y., Mayers, B., Gates, B., Yin, Y. D., Kim, F., and Yan, Y. Q., One-Dimensional Nanostructures: Synthesis, Characterization, and Applications. *Adv. Mater.*, **15**, 353 (2003).

[10] Zhang, J. A., Langille, M. R., and Mirkin, C. A., Photomediated Synthesis of Silver Triangular Bipyramids and Prisms: The Effect of Ph and Bspp. *J. Am. Chem. Soc.*, **132**, 12502 (2010).

[11] Taton, T. A., Mirkin, C. A., and Letsinger, R. L., Scanometric DNA Array Detection with Nanoparticle Probes. *Science*, **289**, 1757 (2000).

[12] Elghanian, R., Storhoff, J. J., Mucic, R. C., Letsinger, R. L., and Mirkin, C. A., Selective Colorimetric Detection of Polynucleotides Based on the Distance-Dependent Optical Properties of Gold Nanoparticles. *Science*, **277**, 1078 (1997).

[13] Kneipp, J., Kneipp, H., and Kneipp, K., Sers - a Single-Molecule and Nanoscale Tool for Bioanalytics. *Chem. Soc. Rev.*, **37**, 1052 (2008).

[14] Rosi, N. L. and Mirkin, C. A., Nanostructures in Biodiagnostics. *Chem. Rev.*, **105**, 1547 (2005).

[15] Wilson, R., The Use of Gold Nanoparticles in Diagnostics and Detection. *Chem. Soc. Rev.*, **37**, 2028 (2008).

[16] Jeong, U., Teng, X. W., Wang, Y., Yang, H., and Xia, Y. N., Superparamagnetic Colloids: Controlled Synthesis and Niche Applications. *Adv. Mater.*, **19**, 33 (2007).

[17] Lu, A. H., Salabas, E. L., and Schuth, F., Magnetic Nanoparticles: Synthesis, Protection, Functionalization, and Application. *Angew. Chem., Int. Ed.*, **46**, 1222 (2007).

[18] Dubertret, B., Calame, M., and Libchaber, A. J., Single-Mismatch Detection Using Gold-Quenched Fluorescent Oligonucleotides. *Nat. Biotechnol.*, **19**, 365 (2001).

[19] Imahori, H. and Fukuzumi, S., Porphyrin Monolayer-Modified Gold Clusters as Photoactive Materials. *Adv. Mater.*, **13**, 1197 (2001).

[20] Henglein, A., Small-Particle Research-Physicochemical Properties of Extremely Small Colloidal Metal and Semiconductor Particles. *Chem. Rev.*, **89**, 1861 (1989).

[21] Hayward, R. C., Saville, D. A., and Aksay, I. A., Electrophoretic Assembly of Colloidal Crystals with Optically Tunable Micropatterns. *Nature*, **404**, 56 (2000).

[22] Hu, J. T., Ouyang, M., Yang, P. D., and Lieber, C. M., Controlled Growth and Electrical Properties of Heterojunctions of Carbon Nanotubes and Silicon Nanowires. *Nature*, **399**, 48 (1999).

[23] Kim, Y., Hong, J. W., Lee, Y. W., Kim, M., Kim, D., Yun, W. S., and Han, S. W., Synthesis of Aupt Heteronanostructures with Enhanced Electrocatalytic Activity toward Oxygen Reduction. *Angew, Chem., Int. Ed.*, **49**, 10197 (2010).

[24] Lim, B., Jiang, M. J., Camargo, P. H. C., Cho, E. C., Tao, J., Lu, X. M., Zhu, Y. M., and Xia, Y. N., Pd-Pt Bimetallic Nanodendrites with High Activity for Oxygen Reduction. *Science*, **324**, 1302 (2009).

[25] Guo, C. X., Wang, M., Chen, T., Lou, X. W., and Li, C. M., A Hierarchically Nanostructured Composite of Mno(2)/Conjugated Polymer/Graphene for High-Performance Lithium Ion Batteries. *Adv. Energy Mater.*, **1**, 736 (2011).

[26] Chen, T., Guai, G. H., Gong, C., Hu, W., Zhu, J., Yang, H., Yan, Q., and Li, C. M., Thermoelectric Bi2te3-Improved Charge Collection for High-Performance Dye-Sensitized Solar Cells. *Energy & Environmental Science*, DOI: 10.1039/C1EE02385C (2012).

[27] Wang, C., Hu, Y. J., Lieber, C. M., and Sun, S. H., Ultrathin Au Nanowires and Their Transport Properties. *J. Am. Chem. Soc.*, **130**, 8902 (2008).

[28] Alkilany, A. M. and Murphy, C. J., Toxicity and Cellular Uptake of Gold Nanoparticles: What We Have Learned So Far? *Journal of Nanoparticle Research*, **12**, 2313 (2010).

[29] Singh, A., Mody, H., Siwale, R., and Mody, V., Introduction to Metallic Nanoparticles. *Journal of Pharmacy & BioAllied Sciences*, **2**, 282 (2010).

[30] Murphy, C. J., Sau, T. K., Gole, A. M., Orendorff, C. J., Gao, J., Gou, L.,

Hunyadi, S. E., and Li, T., Anisotropic Metal Nanoparticles: Synthesis, Assembly, and Optical Applications. *J. Phys. Chem. B*, **109**, 13857 (2005).

[31] Collin, R., *Field Theory of Guided Waves*. 2nd ed. 1990, New York: Wiley.

[32] Liz-Marzán, L. M., Tailoring Surface Plasmons through the Morphology and Assembly of Metal Nanoparticles. *Langmuir*, **22**, 32 (2005).

[33] Kelly, K. L., Coronado, E., Zhao, L. L., and Schatz, G. C., The Optical Properties of Metal Nanoparticles: The Influence of Size, Shape, and Dielectric Environment. *J. Phys. Chem. B*, **107**, 668 (2002).

[34] Van de Hulst, H. C., *Light Scattering by Small Particles*. 1981, New York: Dover.

[35] Jin, R. C., Cao, Y. W., Mirkin, C. A., Kelly, K. L., Schatz, G. C., and Zheng, J. G., Photoinduced Conversion of Silver Nanospheres to Nanoprisms. *Science*, **294**, 1901 (2001).

[36] Sonnichsen, C., Franzl, T., Wilk, T., von Plessen, G., Feldmann, J., Wilson, O., and Mulvaney, P., Drastic Reduction of Plasmon Damping in Gold Nanorods. *Phys. Rev. Lett.*, **88**,   (2002).

[37] Sosa, I. O., Noguez, C., and Barrera, R. G., Optical Properties of Metal Nanoparticles with Arbitrary Shapes. *J. Phys. Chem. B*, **107**, 6269 (2003).

[38] Orendorff, C. J., Sau, T. K., and Murphy, C. J., Shape-Dependent Plasmon-Resonant Gold Nanoparticles. *Small*, **2**, 636 (2006).

[39] Eustis, S. and El-Sayed, M. A., Why Gold Nanoparticles Are More Precious Than Pretty Gold: Noble Metal Surface Plasmon Resonance and Its Enhancement of the Radiative and Nonradiative Properties of Nanocrystals of Different Shapes. *Chem. Soc. Rev.*, **35**, 209 (2006).

[40] Chen, G., Wang, Y., Tan, L. H., Yang, M. X., Tan, L. S., Chen, Y., and Chen, H. Y., High-Purity Separation of Gold Nanoparticle Dimers and Trimers. *J. Am. Chem. Soc.*, **131**, 4218 (2009).

[41] Chen, G., Wang, Y., Yang, M. X., Xu, J., Goh, S. J., Pan, M., and Chen, H. Y., Measuring Ensemble-Averaged Surface-Enhanced Raman Scattering in the Hotspots of Colloidal Nanoparticle Dimers and Trimers. *J. Am. Chem. Soc.*, **132**, 3644 (2010).

[42] Ko, H., Singamaneni, S., and Tsukruk, V. V., Nanostructured Surfaces and Assemblies as Sers Media. *Small*, **4**, 1576 (2008).

[43] Haes, A. J. and Van Duyne, R. P., A Unified View of Propagating and Localized Surface Plasmon Resonance Biosensors. *Anal. Bioanal. Chem.*, **379**, 920 (2004).

[44] Willets, K. A. and Van Duyne, R. P., *Localized Surface Plasmon*

Resonance Spectroscopy and Sensing, in *Annu. Rev. Phys. Chem.* 2007. p. 267.

[45] Zhao, J., Zhang, X. Y., Yonzon, C. R., Haes, A. J., and Van Duyne, R. P., Localized Surface Plasmon Resonance Biosensors. *Nanomedicine*, **1**, 219 (2006).

[46] Li, W., Camargo, P. H. C., Au, L., Zhang, Q., Rycenga, M., and Xia, Y., Etching and Dimerization: A Simple and Versatile Route to Dimers of Silver Nanospheres with a Range of Sizes. *Angew, Chem., Int. Ed.*, **49**, 164 (2010).

[47] Rycenga, M., Cobley, C. M., Zeng, J., Li, W., Moran, C. H., Zhang, Q., Qin, D., and Xia, Y., Controlling the Synthesis and Assembly of Silver Nanostructures for Plasmonic Applications. *Chem. Rev.*, **111**, 3669 (2011).

[48] Cortie, M. B. and McDonagh, A. M., Synthesis and Optical Properties of Hybrid and Alloy Plasmonic Nanoparticles. *Chem. Rev.*, **111**, 3713 (2011).

[49] Jones, M. R., Osberg, K. D., Macfarlane, R. J., Langille, M. R., and Mirkin, C. A., Templated Techniques for the Synthesis and Assembly of Plasmonic Nanostructures. *Chem. Rev.*, **111**, 3736 (2011).

[50] Mayer, K. M. and Hafner, J. H., Localized Surface Plasmon Resonance Sensors. *Chem. Rev.*, **111**, 3828 (2011).

[51] Halas, N. J., Lal, S., Chang, W.-S., Link, S., and Nordlander, P., Plasmons in Strongly Coupled Metallic Nanostructures. *Chem. Rev.*, **111**, 3913 (2011).

[52] Morton, S. M., Silverstein, D. W., and Jensen, L., Theoretical Studies of Plasmonics Using Electronic Structure Methods. *Chem. Rev.*, **111**, 3962 (2011).

[53] Skrabalak, S. E., Chen, J. Y., Sun, Y. G., Lu, X. M., Au, L., Cobley, C. M., and Xia, Y. N., Gold Nanocages: Synthesis, Properties, and Applications. *Acc. Chem. Res.*, **41**, 1587 (2008).

[54] Zhang, J., Li, S. Z., Wu, J. S., Schatz, G. C., and Mirkin, C. A., Plasmon-Mediated Synthesis of Silver Triangular Bipyramids. *Angew. Chem., Int. Ed.*, **48**, 7787 (2009).

[55] Li, S. Z., Pedano, M. L., Chang, S. H., Mirkin, C. A., and Schatz, G. C., Gap Structure Effects on Surface-Enhanced Raman Scattering Intensities for Gold Gapped Rods. *Nano Lett.*, **10**, 1722 (2010).

[56] Turkevich, J., Garton, G., and Stevenson, P. C., The Color of Colloidal Gold. *Journal of Colloid Science*, **9**, S26 (1954).

[57] Draine, B. T. and Flatau, P. J., User Guide for the Discrete Dipole Approximation Code Ddscat 7.0. http://arxiv.org/abs/0809.0337 (2008).

[58] Mie, G., Beiträge Zur Optik Trüber Medien, Speziell Kolloidaler Metallösungen. *Annalen der Physik*, **330**, 377 (1908).

[59] Mie, G., Contribution to the Optics of Turbid Media, Particularly of Colloidal Metal Solutions. *Royal Aircraft Establishment*, Library Translation (1976).

[60] Liz-Marzán, L. M., Tailoring Surface Plasmons through the Morphology and Assembly of Metal Nanoparticles. *Langmuir*, **22**, 32 (2006).

[61] Mirkin, C. A., Letsinger, R. L., Mucic, R. C., and Storhoff, J. J., A DNA-Based Method for Rationally Assembling Nanoparticles into Macroscopic Materials. *Nature*, **382**, 607 (1996).

[62] Cao, Y. W., Jin, R., and Mirkin, C. A., DNA-Modified Core-Shell Ag/Au Nanoparticles. *J. Am. Chem. Soc.*, **123**, 7961 (2001).

[63] Lal, S., Clare, S. E., and Halas, N. J., Nanoshell-Enabled Photothermal Cancer Therapy: Impending Clinical Impact. *Acc. Chem. Res.*, **41**, 1842 (2008).

[64] Bardhan, R., Lal, S., Joshi, A., and Halas, N. J., Theranostic Nanoshells: From Probe Design to Imaging and Treatment of Cancer. *Acc. Chem. Res.*, **44**, 936 (2011).

[65] Wang, J., Byrne, J. D., Napier, M. E., and DeSimone, J. M., More Effective Nanomedicines through Particle Design. *Small*, **7**, 1919 (2011).

[66] Han, X. X., Zhao, B., and Ozaki, Y., Surface-Enhanced Raman Scattering for Protein Detection. *Anal. Bioanal. Chem.*, **394**, 1719 (2009).

[67] Camden, J. P., Dieringer, J. A., Zhao, J., and Van Duyne, R. P., Controlled Plasmonic Nanostructures for Surface-Enhanced Spectroscopy and Sensing. *Acc. Chem. Res.*, **41**, 1653 (2008).

[68] Gordon, R., Sinton, D., Kavanagh, K. L., and Brolo, A. G., A New Generation of Sensors Based on Extraordinary Optical Transmission. *Acc. Chem. Res.*, **41**, 1049 (2008).

[69] Lal, S., Grady, N. K., Kundu, J., Levin, C. S., Lassiter, J. B., and Halas, N. J., Tailoring Plasmonic Substrates for Surface Enhanced Spectroscopies. *Chem. Soc. Rev.*, **37**, 898 (2008).

[70] Lombardi, J. R. and Birke, R. L., A Unified View of Surface-Enhanced Raman Scattering. *Acc. Chem. Res.*, **42**, 734 (2009).

[71] Doering, W. E., Piotti, M. E., Natan, M. J., and Freeman, R. G., Sers as a Foundation for Nanoscale, Optically Detected Biological Labels. *Adv. Mater.*, **19**, 3100 (2007).

[72] Cao, Y. W. C., Jin, R. C., and Mirkin, C. A., Nanoparticles with Raman

Spectroscopic Fingerprints for DNA and Rna Detection. *Science*, **297**, 1536 (2002).

[73] Porter, M. D., Lipert, R. J., Siperko, L. M., Wang, G., and Narayanan, R., Sers as a Bioassay Platform: Fundamentals, Design, and Applications. *Chem. Soc. Rev.*, **37**, 1001 (2008).

[74] Hu, Q., Tay, L.-L., Noestheden, M., and Pezacki, J. P., Mammalian Cell Surface Imaging with Nitrile-Functionalized Nanoprobes: Biophysical Characterization of Aggregation and Polarization Anisotropy in Sers Imaging. *J. Am. Chem. Soc.*, **129**, 14 (2006).

[75] Kneipp, K., Kneipp, H., Itzkan, I., Dasari, R. R., and Feld, M. S., Ultrasensitive Chemical Analysis by Raman Spectroscopy. *Chem. Rev.*, **99**, 2957 (1999).

[76] Yang, M. X., Chen, T., Lau, W. S., Wang, Y., Tang, Q. H., Yang, Y. H., and Chen, H. Y., Development of Polymer-Encapsulated Metal Nanopartictes as Surface-Enhanced Raman Scattering Probes. *Small*, **5**, 198 (2009).

[77] Zhang, J., Sasaki, K., Sutter, E., and Adzic, R. R., Stabilization of Platinum Oxygen-Reduction Electrocatalysts Using Gold Clusters. *Science*, **315**, 220 (2007).

[78] Tian, N., Zhou, Z.-Y., Sun, S.-G., Ding, Y., and Wang, Z. L., Synthesis of Tetrahexahedral Platinum Nanocrystals with High-Index Facets and High Electro-Oxidation Activity. *Science*, **316**, 732 (2007).

[79] Tian, N., Zhou, Z.-Y., and Sun, S.-G., Platinum Metal Catalysts of High-Index Surfaces: From Single-Crystal Planes to Electrochemically Shape-Controlled Nanoparticles. *J. Phys. Chem. C*, **112**, 19801 (2008).

[80] Wang, F., Li, C., Sun, L.-D., Wu, H., Ming, T., Wang, J., Yu, J. C., and Yan, C.-H., Heteroepitaxial Growth of High-Index-Faceted Palladium Nanoshells and Their Catalytic Performance. *J. Am. Chem. Soc.*, **133**, 1106 (2010).

[81] Zhou, Z.-Y., Huang, Z.-Z., Chen, D.-J., Wang, Q., Tian, N., and Sun, S.-G., High-Index Faceted Platinum Nanocrystals Supported on Carbon Black as Highly Efficient Catalysts for Ethanol Electrooxidation. *Angew, Chem., Int. Ed.*, **49**, 411 (2010).

[82] Somorjai, G. A. and Blakely, D. W., Mechanism of Catalysis of Hydrocarbon Reactions by Platinum Surfaces. *Nature*, **258**, 580 (1975).

[83] Wilson, O. M., Knecht, M. R., Garcia-Martinez, J. C., and Crooks, R. M., Effect of Pd Nanoparticle Size on the Catalytic Hydrogenation of Allyl Alcohol. *J. Am. Chem. Soc.*, **128**, 4510 (2006).

[84] Garcia-Martinez, J. C., Lezutekong, R., and Crooks, R. M., Dendrimer-Encapsulated Pd Nanoparticles as Aqueous, Room-Temperature Catalysts for the Stille Reaction. *J. Am. Chem. Soc.*, **127**, 5097 (2005).

[85] Scott, R. W. J., Wilson, O. M., and Crooks, R. M., Synthesis, Characterization, and Applications of Dendrimer-Encapsulated Nanoparticles. *J. Phys. Chem. B*, **109**, 692 (2004).

[86] Lim, B. and Xia, Y. N., Metal Nanocrystals with Highly Branched Morphologies. *Angew. Chem., Int. Ed.*, **50**, 76 (2011).

[87] Guo, S., Dong, S., and Wang, E., Ultralong Pt-on-Pd Bimetallic Nanowires with Nanoporous Surface: Nanodendritic Structure for Enhanced Electrocatalytic Activity. *Chem. Commun.*, **46**, 1869 (2010).

[88] Lee, H. J., Habas, S. E., Somorjai, G. A., and Yang, P. D., Localized Pd Overgrowth on Cubic Pt Nanocrystals for Enhanced Electrocatalytic Oxidation of Formic Acid. *J. Am. Chem. Soc.*, **130**, 5406 (2008).

[89] Wang, D. and Li, Y., Bimetallic Nanocrystals: Liquid-Phase Synthesis and Catalytic Applications. *Adv. Mater.*, **23**, 1044 (2011).

[90] Lee, Y. M., Garcia, M. A., Huls, N. A. F., and Sun, S. H., Synthetic Tuning of the Catalytic Properties of Au-Fe3o4 Nanoparticles. *Angew. Chem., Int. Ed.*, **49**, 1271 (2010).

[91] Tedsree, K., Li, T., Jones, S., Chan, C. W. A., Yu, K. M. K., Bagot, P. A. J., Marquis, E. A., Smith, G. D. W., and Tsang, S. C. E., Hydrogen Production from Formic Acid Decomposition at Room Temperature Using a Ag-Pd Core-Shell Nanocatalyst. *Nat Nano*, **6**, 302 (2011).

[92] Narayanan, R. and El-Sayed, M. A., Effect of Catalysis on the Stability of Metallic Nanoparticles: Suzuki Reaction Catalyzed by Pvp-Palladium Nanoparticles. *J. Am. Chem. Soc.*, **125**, 8340 (2003).

[93] Ploog, K., Microscopical Structuring of Solids by Molecular Beam Epitaxy—Spatially Resolved Materials Synthesis. *Angewandte Chemie International Edition in English*, **27**, 593 (1988).

[94] Eigler, D. M. and Schweizer, E. K., Positioning Single Atoms with a Scanning Tunnelling Microscope. *Nature*, **344**, 524 (1990).

[95] Sato, A. and Tsukamoto, Y., Nanometre-Scale Recording and Erasing with the Scanning Tunnelling Microscope. *Nature*, **363**, 431 (1993).

[96] Kloke, A., von Stetten, F., Zengerle, R., and Kerzenmacher, S., Strategies for the Fabrication of Porous Platinum Electrodes. *Adv. Mater.*, **23**, 4976 (2011).

[97] Ruiz-Hitzky, E., Aranda, P., Darder, M., and Ogawa, M., Hybrid and

Biohybrid Silicate Based Materials: Molecular Vs. Block-Assembling Bottom-up Processes. *Chem. Soc. Rev.*, **40**, 801 (2011).

[98] Balzani, V., Credi, A., and Venturi, M., Light Powered Molecular Machines. *Chem. Soc. Rev.*, **38**, 1542 (2009).

[99] Gao, P. X., Ding, Y., Mai, W., Hughes, W. L., Lao, C., and Wang, Z. L., Conversion of Zinc Oxide Nanobelts into Superlattice-Structured Nanohelices. *Science*, **309**, 1700 (2005).

[100] Zhu, J., Peng, H., Marshall, A. F., Barnett, D. M., Nix, W. D., and Cui, Y., Formation of Chiral Branched Nanowires by the Eshelby Twist. *Nat Nano*, **3**, 477 (2008).

[101] Amelinckx, S., Zhang, X. B., Bernaerts, D., Zhang, X. F., Ivanov, V., and Nagy, J. B., A Formation Mechanism for Catalytically Grown Helix-Shaped Graphite Nanotubes. *Science*, **265**, 635 (1994).

[102] Wang, H. T., Wu, J. C., Shen, Y. Q., Li, G. P., Zhang, Z., Xing, G. Z., Guo, D. L., Wang, D. D., Dong, Z. L., and Wu, T., Crsi2 Hexagonal Nanowebs. *J. Am. Chem. Soc.*, **132**, 15875 (2010).

[103] Bierman, M. J., Lau, Y. K. A., Kvit, A. V., Schmitt, A. L., and Jin, S., Dislocation-Driven Nanowire Growth and Eshelby Twist. *Science*, **320**, 1060 (2008).

[104] Zhang, H. F., Wang, C. M., and Wang, L. S., Helical Crystalline Sic/Sio2 Core−Shell Nanowires. *Nano Lett.*, **2**, 941 (2002).

[105] Huang, M. H., Wu, Y., Feick, H., Tran, N., Weber, E., and Yang, P., Catalytic Growth of Zinc Oxide Nanowires by Vapor Transport. *Adv. Mater.*, **13**, 113 (2001).

[106] Fan, H. J., Werner, P., and Zacharias, M., Semiconductor Nanowires: From Self-Organization to Patterned Growth. *Small*, **2**, 700 (2006).

[107] Wang, Z. L., Zinc Oxide Nanostructures: Growth, Properties and Applications. *Journal of Physics-Condensed Matter*, **16**, R829 (2004).

[108] Frens, G., Controlled Nucleation for Regulation of Particle-Size in Monodisperse Gold Suspensions. *Nature Phys. Sci.*, **241**, 20 (1973).

[109] Brown, K. R., Walter, D. G., and Natan, M. J., Seeding of Colloidal Au Nanoparticle Solutions. 2. Improved Control of Particle Size and Shape. *Chem. Mater.*, **12**, 306 (2000).

[110] Wang, Y., Chen, G., Yang, M., Silber, G., Xing, S., Tan, L. H., Wang, F., Feng, Y., Liu, X., Li, S., and Chen, H., A Systems Approach Towards the Stoichiometry-Controlled Hetero-Assembly of Nanoparticles. *Nature Communications*, **1**, 87 (2010).

[111] Feng, Y., Wang, Y., Wang, H., Chen, T., Tay, Y. Y., Yao, L., Yan, Q., Li, S., and Chen, H., Engineering "Hot" Nanoparticles for Surface-Enhanced Raman Scattering by Embedding Reporter Molecules in Metal Layers. *Small*, **8**, 246 (2012).

[112] Shen, C., Hui, C., Yang, T., Xiao, C., Tian, J., Bao, L., Chen, S., Ding, H., and Gao, H., Monodisperse Noble-Metal Nanoparticles and Their Surface Enhanced Raman Scattering Properties. *Chem. Mater.*, **20**, 6939 (2008).

[113] Sugie, A., Somete, T., Kanie, K., Muramatsu, A., and Mori, A., Triethylsilane as a Mild and Efficient Reducing Agent for the Preparation of Alkanethiol-Capped Gold Nanoparticles. *Chem. Commun.*, 3882 (2008).

[114] Nikoobakht, B. and El-Sayed, M. A., Preparation and Growth Mechanism of Gold Nanorods (Nrs) Using Seed-Mediated Growth Method. *Chem. Mater.*, **15**, 1957 (2003).

[115] Jana, N. R., Gearheart, L., and Murphy, C. J., Wet Chemical Synthesis of High Aspect Ratio Cylindrical Gold Nanorods. *J. Phys. Chem. B*, **105**, 4065 (2001).

[116] Gao, J. X., Bender, C. M., and Murphy, C. J., Dependence of the Gold Nanorod Aspect Ratio on the Nature of the Directing Surfactant in Aqueous Solution. *Langmuir*, **19**, 9065 (2003).

[117] Gole, A. and Murphy, C. J., Seed-Mediated Synthesis of Gold Nanorods: Role of the Size and Nature of the Seed. *Chem. Mater.*, **16**, 3633 (2004).

[118] Sau, T. K. and Murphy, C. J., Room Temperature, High-Yield Synthesis of Multiple Shapes of Gold Nanoparticles in Aqueous Solution. *J. Am. Chem. Soc.*, **126**, 8648 (2004).

[119] Wang, C. G., Wang, T. T., Ma, Z. F., and Su, Z. M., Ph-Tuned Synthesis of Gold Nanostructures from Gold Nanorods with Different Aspect Ratios. *Nanotechnology*, **16**, 2555 (2005).

[120] Murphy, C. J. and Jana, N. R., Controlling the Aspect Ratio of Inorganic Nanorods and Nanowires. *Adv. Mater.*, **14**, 80 (2002).

[121] Sau, T. K. and Rogach, A. L., Nonspherical Noble Metal Nanoparticles: Colloid-Chemical Synthesis and Morphology Control. *Adv. Mater.*, **22**, 1781 (2010).

[122] Wang, C. and Sun, S. H., Facile Synthesis of Ultrathin and Single-Crystalline Au Nanowires. *Chemistry-an Asian Journal*, **4**, 1028 (2009).

[123] Sánchez-Iglesias, A., Grzelczak, M., Pérez-Juste, J., and Liz-Marzán, L. M., Binary Self-Assembly of Gold Nanowires with Nanospheres and

Nanorods. *Angew, Chem., Int. Ed.*, **49**, 9985 (2010).

[124] Krichevski, O., Tirosh, E., and Markovich, G., Formation of Gold-Silver Nanowires in Thin Surfactant Solution Films. *Langmuir*, **22**, 867 (2006).

[125] He, J. T., Wang, Y. W., Feng, Y. H., Qi, X. Y., Zeng, Z. Y., Teo, W. S., Zhang, H., and Chen, H. Y., in preparation (2011).

[126] Kamata, K., Suzuki, S., Ohtsuka, M., Nakagawa, M., Iyoda, T., and Yamada, A., Fabrication of Left-Handed Metal Microcoil from Spiral Vessel of Vascular Plant. *Adv. Mater.*, **23**, 5509 (2011).

[127] Wu, Y. Y., Cheng, G. S., Katsov, K., Sides, S. W., Wang, J. F., Tang, J., Fredrickson, G. H., Moskovits, M., and Stucky, G. D., Composite Mesostructures by Nano-Confinement. *Nat. Mater.*, **3**, 816 (2004).

[128] Liu, L. C., Yoo, S. H., Lee, S. A., and Park, S., Wet-Chemical Synthesis of Palladium Nanosprings. *Nano Lett.*, **11**, 3979 (2011).

[129] Gao, C., Zhang, Q., Lu, Z., and Yin, Y., Templated Synthesis of Metal Nanorods in Silica Nanotubes. *J. Am. Chem. Soc.*, **133**, 19706 (2011).

[130] Vlasov, Y. A., Bo, X. Z., Sturm, J. C., and Norris, D. J., On-Chip Natural Assembly of Silicon Photonic Bandgap Crystals. *Nature*, **414**, 289 (2001).

[131] Ge, J. P., Hu, Y. X., and Yin, Y. D., Highly Tunable Superparamagnetic Colloidal Photonic Crystals. *Angew. Chem., Int. Ed.*, **46**, 7428 (2007).

[132] Porter, M. D., Lipert, R. J., Siperko, L. M., Wang, G., and Narayanana, R., Sers as a Bioassay Platform: Fundamentals, Design, and Applications. *Chem. Soc. Rev.*, **37**, 1001 (2008).

[133] Dadosh, T., Gordin, Y., Krahne, R., Khivrich, I., Mahalu, D., Frydman, V., Sperling, J., Yacoby, A., and Bar-Joseph, I., Measurement of the Conductance of Single Conjugated Molecules. *Nature*, **436**, 677 (2005).

[134] Lee, J., Hasan, W., Stender, C. L., and Odom, T. W., Pyramids: A Platform for Designing Multifunctional Plasmonic Particles. *Acc. Chem. Res.*, **41**, 1762 (2008).

[135] Velev, O. D. and Gupta, S., Materials Fabricated by Micro- and Nanoparticle Assembly-the Challenging Path from Science to Engineering. *Adv. Mater.*, **21**, 1897 (2009).

[136] Wang, X. J., Li, G. P., Chen, T., Yang, M. X., Zhang, Z., Wu, T., and Chen, H. Y., Polymer-Encapsulated Gold-Nanoparticle Dimers: Facile Preparation and Catalytical Application in Guided Growth of Dimeric Zno-Nanowires. *Nano Lett.*, **8**, 2643 (2008).

[137] Li, W. Y., Camargo, P. H. C., Lu, X. M., and Xia, Y. N., Dimers of Silver Nanospheres: Facile Synthesis and Their Use as Hot Spots for

Surface-Enhanced Raman Scattering. *Nano Lett.*, **9**, 485 (2009).

[138] Brousseau, L. C., Novak, J. P., Marinakos, S. M., and Feldheim, D. L., Assembly of Phenylacetylene-Bridged Gold Nanocluster Dimers and Trimers. *Adv. Mater.*, **11**, 447 (1999).

[139] Chen, T., Yang, M. X., Wang, X. J., Tan, L. H., and Chen, H. Y., Controlled Assembly of Eccentrically Encapsulated Gold Nanoparticles. *J. Am. Chem. Soc.*, **130**, 11858 (2008).

[140] Alivisatos, A. P., Johnsson, K. P., Peng, X. G., Wilson, T. E., Loweth, C. J., Bruchez, M. P., and Schultz, P. G., Organization of 'Nanocrystal Molecules' Using DNA. *Nature*, **382**, 609 (1996).

[141] Loweth, C. J., Caldwell, W. B., Peng, X. G., Alivisatos, A. P., and Schultz, P. G., DNA-Based Assembly of Gold Nanocrystals. *Angew. Chem., Int. Ed.*, **38**, 1808 (1999).

[142] Xu, X. Y., Rosi, N. L., Wang, Y. H., Huo, F. W., and Mirkin, C. A., Asymmetric Functionalization of Gold Nanoparticles with Oligonucleotides. *J. Am. Chem. Soc.*, **128**, 9286 (2006).

[143] Huo, F. W., Lytton-Jean, A. K. R., and Mirkin, C. A., Asymmetric Functionalization of Nanoparticles Based on Thermally Addressable DNA Interconnects. *Adv. Mater.*, **18**, 2304 (2006).

[144] DeVries, G. A., Brunnbauer, M., Hu, Y., Jackson, A. M., Long, B., Neltner, B. T., Uzun, O., Wunsch, B. H., and Stellacci, F., Divalent Metal Nanoparticles. *Science*, **315**, 358 (2007).

[145] Sardar, R., Heap, T. B., and Shumaker-Parry, J. S., Versatile Solid Phase Synthesis of Gold Nanoparticle Dimers Using an Asymmetric Functionalization Approach. *J. Am. Chem. Soc.*, **129**, 5356 (2007).

[146] Pal, S., Deng, Z., Wang, H., Zou, S., Liu, Y., and Yan, H., DNA Directed Self-Assembly of Anisotropic Plasmonic Nanostructures. *J. Am. Chem. Soc.*, **133**, 17606 (2011).

[147] Tikhomirov, G., Hoogland, S., Lee, P. E., Fischer, A., Sargent, E. H., and Kelley, S. O., DNA-Based Programming of Quantum Dot Valency, Self-Assembly and Luminescence. *Nat Nano*, **6**, 485 (2011).

[148] Yang, M., Chen, G., Zhao, Y., Silber, G., Wang, Y., Xing, S., Han, Y., and Chen, H., Mechanistic Investigation into the Spontaneous Linear Assembly of Gold Nanospheres. *Phys. Chem. Chem. Phys.*, **12**, 11850 (2010).

[149] Baiker, A., Progress in Asymmetric Heterogeneous Catalysis: Design of Novel Chirally Modified Platinum Metal Catalysts. *Journal of Molecular Catalysis a-Chemical*, **115**, 473 (1997).

[150] Thomas, J. M. and Raja, R., Exploiting Nanospace for Asymmetric Catalysis: Confinement of Immobilized, Single-Site Chiral Catalysts Enhances Enantioselectivity. *Acc. Chem. Res.*, **41**, 708 (2008).

[151] Hazen, R. M. and Sholl, D. S., Chiral Selection on Inorganic Crystalline Surfaces. *Nat. Mater.*, **2**, 367 (2003).

[152] Che, S., Liu, Z., Ohsuna, T., Sakamoto, K., Terasaki, O., and Tatsumi, T., Synthesis and Characterization of Chiral Mesoporous Silica. *Nature*, **429**, 281 (2004).

[153] Shemer, G., Krichevski, O., Markovich, G., Molotsky, T., Lubitz, I., and Kotlyar, A. B., Chirality of Silver Nanoparticles Synthesized on DNA. *J. Am. Chem. Soc.*, **128**, 11006 (2006).

[154] Oh, H. S., Liu, S., Jee, H., Baev, A., Swihart, M. T., and Prasad, P. N., Chiral Poly(Fluorene-Alt-Benzothiadiazole) (Pfbt) and Nanocomposites with Gold Nanoparticles: Plasmonically and Structurally Enhanced Chirality. *J. Am. Chem. Soc.*, **132**, 17346 (2010).

[155] Nakashima, T., Kobayashi, Y., and Kawai, T., Optical Activity and Chiral Memory of Thiol-Capped Cdte Nanocrystals. *J. Am. Chem. Soc.*, **131**, 10342 (2009).

[156] Mastroianni, A. J., Claridge, S. A., and Alivisatos, A. P., Pyramidal and Chiral Groupings of Gold Nanocrystals Assembled Using DNA Scaffolds. *J. Am. Chem. Soc.*, **131**, 8455 (2009).

[157] Li, C., Deng, K., Tang, Z. Y., and Jiang, L., Twisted Metal-Amino Acid Nanobelts: Chirality Transcription from Molecules to Frameworks. *J. Am. Chem. Soc.*, **132**, 8202 (2010).

[158] Chen, C. L., Zhang, P. J., and Rosi, N. L., A New Peptide-Based Method for the Design and Synthesis of Nanoparticle Superstructures: Construction of Highly Ordered Gold Nanoparticle Double Helices. *J. Am. Chem. Soc.*, **130**, 13555 (2008).

[159] Chen, W., Bian, A., Agarwal, A., Liu, L. Q., Shen, H. B., Wang, L. B., Xu, C. L., and Kotov, N. A., Nanoparticle Superstructures Made by Polymerase Chain Reaction: Collective Interactions of Nanoparticles and a New Principle for Chiral Materials. *Nano Lett.*, **9**, 2153 (2009).

[160] Velázquez-Salazar, J. J., Esparza, R., Mejía-Rosales, S. J., Estrada-Salas, R. n., Ponce, A., Deepak, F. L., Castro-Guerrero, C., and José-Yacamán, M., Experimental Evidence of Icosahedral and Decahedral Packing in One-Dimensional Nanostructures. *ACS Nano*, **5**, 6272 (2011).

[161] Chen, C. L. and Rosi, N. L., Preparation of Unique 1-D Nanoparticle

Superstructures and Tailoring Their Structural Features. *J. Am. Chem. Soc.*, **132**, 6902 (2010).

[162] Chen, C. L. and Rosi, N. L., Peptide-Based Methods for the Preparation of Nanostructured Inorganic Materials. *Angew, Chem., Int. Ed.*, **49**, 1924 (2010).

[163] Chen, L. Y., Wang, H., Xu, J., Shen, X. S., Yao, L., Zhu, L. F., Zeng, Z. Y., Zhang, H., and Chen, H. Y., Controlling Reversible Elastic Deformation of Carbon Nanotube Rings. *J. Am. Chem. Soc.*, **133**, 9654 (2011).

[164] Xu, J., Wang, H., Liu, C. C., Yang, Y. M., Chen, T., Wang, Y. W., Wang, F., Liu, X. G., Xing, B. G., and Chen, H. Y., Mechanical Nanosprings: Induced Coiling and Uncoiling of Ultrathin Au Nanowires. *J. Am. Chem. Soc.*, **132**, 11920 (2010).

Chapter 2   A Systems Approach Towards the Stoichiometry Controlled Hetero-assembly of Nanoparticles

2.1 Introduction

Colloidal growth of nanoparticles (NPs) has been a major focus in nanoscience over the past decades. It provides a scalable and versatile approach to control the size and morphology of NPs, which are critical for their properties. NPs with simple geometries, such as spheres, rods, cubes, and triangular prisms, have been prepared with excellent control.[1-5] In contrast, colloidal assembly of NPs has been less studied, though it could conceivably offer novel synthetic controls for multi-component nanoclusters. The key challenge is to develop general methodologies to assemble colloidal nano-objects with precise stoichiometry. Previously, homo-aggregates such as dimers and trimers were prepared by exploiting either random aggregation,[6-8] steric effects,[9-12] or specific control over surface ligands (*e.g.*, divalent NPs).[13-16] Compared to these "homo-coupling" nanoreactions, controlling

stoichiometry in the "cross-coupling" of NPs presents different and arguably greater challenges. It was only achieved through the brilliant design and pre-fabrication of NPs with anisotropic surface functionalities (*e.g.*, NP with a single DNA molecule).[17-22]

In a sense, the assembly of NPs in a colloidal solution is analogous to molecular reactions. Rationally controlled organic syntheses, completed with coupling, protection and separation schemes, have brought about complex molecules with precise structural control. From this perspective, a complete nanoreaction system emulating the concepts and strategies of molecular reactions may offer a systematic approach to sophisticated nanostructures.

A major problem in assembling NPs is the preservation of the product nanoclusters against both disintegration and aggregation, which is often exacerbated by ligand dissociation and exchange over long periods of time. We have recently demonstrated that encapsulation of nanoclusters in polystyrene-*block*-poly(acrylic acid) (PSPAA) micelles is a way to overcome these problems, and afford sufficient stability for the nanoclusters to be separated using concentrated CsCl solutions.[7, 23, 24] We now combine the protection and purification schemes with the hetero-assembly of NPs, making it possible to recover pure nanoclusters with long-term stability. The systems approach led to complete nanoreactions with new structural controls, which is also an ideal platform to study the interactions of NPs, just as the studies of molecular reactions provide insights in the chemical nature of atoms.

2.2 Materials and Methods

2.2.1 Materials

All chemical reagents were obtained from commercial suppliers and used without further purification. Hydrogen tetrachloroaurate(III) hydrate ($HAuCl_4 \cdot H_2O$), 99.9% (metals basis Au 49%) was purchased from Alfa Aesar; amphiphilic diblock copolymer polystyrene-block-poly(acrylic acid) (PS_{154}-*b*-PAA_{60}, M_n = 16000 for the polystyrene block and M_n = 4300 for the poly(acrylic acid) block, M_w/M_n=1.15) was obtained from Polymer Source, Inc.; DMF, 99.8% was purchased from Tedia Company, Inc.; Pentaerythritol tetrakis(3-mercapto-propionate), **1**, was purchased from Aldrich; 1,2-dipalmitoyl-*sn*-glycero-3-phosphothioethanol (Sodium Salt), **2**, was purchased from Avanti Polar Lipids. Deionized water (resistance > 18 $M\Omega \; cm^{-1}$) was used in all of our reactions. All other chemicals were purchased from Aldrich. Copper specimen grids (200 mesh) with formvar/carbon support film (referred to as TEM grids in the text) were purchased from Electron Microscopy Sciences.
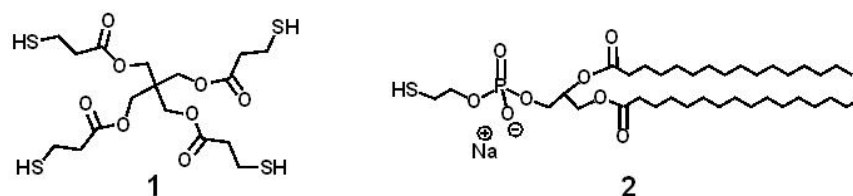
Scheme 2-1 Ligands used in this chapter.

2.2.2 Methods

Methods of Characterization. Transmission Electron Microscopy (TEM) images were collected from a JEM-1400 Transmission Electron Microscopy

(JEOL) operated at 120 kV. Ultraviolet-visible (UV-vis) spectra were collected on a Cary 100 UV-Vis spectrophotometer.

Preparation of TEM Samples. $(NH_4)_6Mo_7O_{24}$ was used as a negative stain (3.4 mM) in all TEM images reported in this chapter, so that polymer shells appeared white against a dark background. TEM grids were treated by oxygen plasma in a Harrick® plasma cleaner/sterilizer for 1 min to improve the surface hydrophilicity. A sample solution was carefully mixed with stain solution on the surface of a plastic petridish, forming a small bead; a TEM grid was then floated on the top of the bead with the hydrophilic face contacting the solution. The TEM grid was then carefully picked up by a pair of tweezers, wicked with filter paper to remove excess solution and finally dried in air for 20 min.

Interpretation of TEM results. TEM is a limited observation technique, as it only characterizes a fraction of the sample and does not measure the ensemble properties of nanoparticles. That was the reason we provided large-area TEM images in this Supplementary Information. Suppose one has a sample containing a variety of particles, among which only 50% of them are the desired product X. That is, in a randomly sampled TEM image, each particle has a 50% probability of being the right particle. If each TEM image shows only 5 particles, then the probability of all 5 particles being X is $0.5^5 = 3.1\%$. If each TEM image shows only 10 particles, then the probability of finding a randomly sampled image containing 10 X's is reduced to 0.098%. That is, one has to search though 1000 images of 10 particles each in order to find one right image.

If each TEM image shows 20 particles, then one has search through 1,000,000 images of 20 particles each in order to find one right image. The large numbers (> 20) of uniform nanostructures given in our TEM images makes it statistically close to impossible to find such images had the sample been not of high purity.

Synthesis of AuNPs by sodium citrate reduction. Small size AuNPs (~ 18 nm) were prepared following literature procedures by sodium citrate reduction of HAuCl$_4$,[25] with small modifications. In a representative synthesis, a 250 mL round bottom flask was charged with 100 ml aq. HAuCl$_4$. This solution was heated to 100 °C with vigorous stirring for 30 min, and then 2.62 mL of sodium citrate (38.7 mM) was added quickly ([Na$_3$citrate]$_{final}$ = 989 μM). After heating the mixture for an additional 60 min, a deep-red AuNP solution was obtained. The average particle diameter was measured to be 17.8 ± 1.6 nm from TEM images using ImageJ (http://rsb.info.nih.gov/ij/, last visited Jul 21st, 2009). The concentrations of the as-synthesized AuNP solution (1.62 nM) were estimated from the total amount of Au used during the synthesis, the density of Au (19.3 g cm^{-3}), and the average size of AuNPs (d$_{av}$ = 17.8 nm by TEM).

Synthesis of AuNPs by seeded growth. Larger AuNPs (~ 36 nm) were synthesized by using 15 nm AuNPs as seeds,[26] with small modifications. In a typical synthesis, a 250 mL round bottom flask was charged with 100 mL aq. HAuCl$_4$ (0.25 mM). The solution was refluxed with vigorous stirring for 10 min, and then 12 mL of AuNP seeds (d$_{AuNP}$ = 15 nm) and 500 μL of sodium citrate (38.7 mM) was added. After boiling the solution for 45 min, a deep-red AuNP

solution was obtained. The solution was cooled to room temperature, and sodium citrate was added so that $[Na_3citrate]_{final}$ = 989 μM, the same concentration as that of 18 nm AuNPs. The average diameter was measured to be 35.7 ± 4.4 nm from TEM images using ImageJ. The concentration of the as-synthesized AuNP solution was estimated to be 0.172 nM.

Synthesis of A-NPs (1-AuNPs). Firstly, 1.5 mL citrate-AuNPs (d_{AuNP} = 18 nm) was concentrated to 100 μL by centrifugation at 13,300 g for 15 min. Then the AuNPs solution was added dropwise to 300 μL **1** in ethanol (4 mg/mL). The mixture was incubated for 2 h and it remained red after the incubation. This solution contains A-NPs as well as excess **1**, which could cause citrate-AuNPs to aggregate if not removed. Thus, the A-NPs were purified twice by centrifugation in DMF to remove the excess **1**. For reacting with 18 nm B-NPs, 1/8 of the purified A-NPs solution was diluted to 100 μL by DMF; for reacting with 36 nm B-NPs, 1/32 of the purified A-NPs were used to make a 100 μL solution. These solutions were used within 15 min, otherwise partial ligand dissociation may lead to aggregation of the A-NPs. Assuming no AuNPs was lost during this process, the final [A] is 3.04 or 0.759 nM, respectively.

Preparation of B-NPs solution. B-NPs solution was prepared by concentrating the citrate-AuNPs solution so to remove the excess $Na_3citrate$ from the as-synthesized solution.

Setup of the nanoreactions. A main problem of the stoichiometry control of the NP assemblies: without restrictions multiple B-NPs could bond to each

A-NP and *vice versa*, leading to copolymerization of the two reactants. Our strategy is to react A-NPs with excess B-NPs, and to control the stoichiometry of the product AB_n by tuning the repulsion between the B-NPs. A DMF solution of A-NPs was prepared following the above procedure. The salt concentrations in the B-NPs solutions were carefully controlled in the following reactions, all other conditions were the same: the purified A-NPs in DMF (100 μL, d_{AuNP} = 18 nm) were slowly added to an aqueous solution containing large excess of B-NPs (200 μL). During the addition, the eppendorf tube was placed on a vigorous vortex to help the mixing of the AuNPs.

Calculation of the concentration of AuNPs. Weight of $HAuCl_4\,H_2O$ in the as-synthesized AuNP solution (100 mL) = 10 mg, weight of each 18 nm AuNP $= \rho_{Au} \times V_{Au} = 5.648 \times 10^{-14}$ mg

Then, the concentration of the as-prepared 18 nm AuNPs based on the number of NPs, M_{NP} = (10 × 196.97/ 357.80)) / (5.648 × 10^{-14} × 0.1 × 6.02 × 10^{23}) = 1.62 nM

So, for the concentrated 18 nm B-NPs solution, [B] = 1.62 nM × 3000/200 = 24.3 nM = 24.3 × 10^{-9} × 6.02 × 10^{23} = 1.46 × 10^{16} particles/liter;

The concentration of the AuNP solution based on the number of Au atoms, M_{atom} = 10/ 357.80/ 0.1 × 3000 / 200 = 4.19 mM

Preparation of AB nanoclusters. For 18 nm B-NPs, the citrate-AuNPs solution (3 mL) was concentrated to 10 μL by centrifugation at 13,300 *g* for 15

min, and then diluted by 190 μL H_2O. The residue [Na_3citrate] was estimated to be 49.5 μM and [B] = 24.3 nM.

For 36 nm B-NPs, the citrate-AuNPs (4.5 mL) was concentrated to 10 μL by centrifugation at 5,200 g for 15 min, and then diluted by 190 μL H_2O. The residue [Na_3citrate] was estimated to be 49.5 μM and [B] = 3.87 nM.

Preparation of AB$_2$ nanoclusters. For 18 nm B-NPs, the citrate-AuNPs (3 mL) was concentrated to 20 μL by centrifugation at 13,300 g for 15 min, and then diluted by 180 μL H_2O. The residue [Na_3citrate] was estimated to be 98.9 μM and [B] = 24.3 nM.

For 36 nm B-NPs, the citrate-AuNPs (4.5 mL) was concentrated to 10 μL by centrifugation at 5,200 g for 15 min, and then diluted by 190 μL aq. NaCl (3.16 mM). The residue [Na_3citrate] was estimated to be 49.5 μM; final concentrations: [NaCl] = 3 mM and [B] = 3.87 nM.

Preparation of AB$_3$ nanoclusters. Citrate-AuNPs (d_{av} = 18 nm, 3 mL) was concentrated to 20 μL by centrifugation at 13,300 g for 15 min, added back 150 μL supernatant, and then diluted by 30 μL H_2O. The residue [Na_3citrate] was estimated to be 841 μM and [B] = 24.3 nM.

Preparation of AB$_4$ nanoclusters. Citrate-AuNPs (d_{av} = 18 nm, 3 mL) was concentrated to 20 μL by centrifugation at 13,300 g for 15 min, added back 150 μL supernatant, and then added 30 μL aq. NaCl (20 mM). The residue [Na_3citrate] was estimated to be 841 μM; final concentrations: [NaCl] = 3 mM, and [B] = 24.3 nM.

Polymer encapsulation of the reaction products.[7, 27]**.** After the nanoreaction, the product AB_n nanoclusters and the excess B-NPs were stabilized by polymer encapsulation. This prevents the nanoclusters from disintegration and uncontrolled aggregation during the subsequent purification and characterization steps. In a typical procedure, 740 μL DMF was added to the reaction mixture, which contains 100 μL DMF and 200 μL H_2O, followed by 60 μL $PS_{154}PAA_{60}$ in DMF (8 mg/mL). Finally, 40 μL **2** in EtOH (2 mg/mL) was added. The mixture was then heated to 100 ℃ for 2 hrs and was then allowed to slowly cool down in the oil bath until room temperature was reached. The final solution is stable at room temperature for months.

The resulting solution contained AB_n@PSPAA, B@PSPAA, empty polymer micelles, DMF, and extra **2**. To isolate the nanoclusters from the excess reactants, the product solution was diluted (200 μL diluted by 1300 μL pH=10 aq. NaOH), and then centrifuged at 13,300 g (5,200 g for nanoclusters that 36 nm B-NPs were used) for 20 min to remove the supernatant. The collected purplish-red product at the bottom of centrifuge tubes was diluted by 100 μL pH=10 aq. NaOH, giving a stable solution that contained mainly AB_n@PSPAA and B@PSPAA.

Purification of AB_2@PSPAA, AB_3@PSPAA, and AB_4@PSPAA by differential centrifugation method (no concentration gradient was used).[24] A stock solution of saturated CsCl was prepared by dissolving excess CsCl in

pH =10 aq. NaOH; this solution has a density of 1.91 g•cm^{-3} and contained roughly 61.8% CsCl by weight.

In a typical separation, the mixture of AB$_n$@PSPAA and B@PSPAA (100 µL) was carefully layered on the top of 1000 µL saturated CsCl solution in an eppendorf tube, and the tube was centrifuged at 2,300 g for 25 min. The resulting solution showed two distinct bands of red and blue color, separated by a gap. The lower band was extracted, diluted by pH=10 aq. NaOH, and then centrifuged again to remove the excess CsCl.

Purification of AB$_2$@PSPAA nanoclusters by Ag growth/etching method. Instead, Ag was grown on the exposed A-NPs to enhance the difference between AB$_2$@PSPAA and B@PSPAA. Metallic Ag was formed by reducing AgNO$_3$ with ascorbic acid.[28] In a typical separation, the collected AB$_2$@PSPAA and B@PSPAA mixture in pH=10 aq. NaOH (100 µL) was added to 800 µL sodium citrate (1.161 mM), following by 400 µL AgNO$_3$ (1 mM). Then, 400 µL ascorbic acid (2 mM) was added and the mixture was incubated for 2 hrs on a shaker. The color of the solution changed from red to brown and TEM characterization showed Ag growth on the A-NPs but not on the PSPAA shells of B-NPs. The mixture solution was purified three times by centrifugation at 1,400 g for 15 min and the supernatants containing the unaffected B@PSPAA were removed. The concentrated brown solution was added to 1000 µL NH$_3$H$_2$O to etch the Ag blocks[29] and the mixture was incubated in an orbital shaker for 12 hrs with exposure to air. Finally, the

purified AB_2@PSPAA nanoclusters were collected by centrifugation at 2,200 g

for 15 min.

Purification of AB@PSPAA nanoclusters by Ag growth/etching method.

The separation of AB@PSPAA from B@PSPAA (d_A = 18 nm, d_B = 36 nm) is

nearly impossible using differential sedimentation, considering the small

weight/density difference between them. The purification of AB@PSPAA was

similar as that for AB_2 nanoclusters, except that different centrifugation speeds

were used. After Ag growth on the surface of the AB nanoclusters, the resulting

solution was purified three times by centrifugation at 200 g for 20 min. After

$NH_3 \cdot H_2O$ etching, the NPs were collected by centrifugation and etched again by

using 1000 μL $NH_3 \cdot H_2O$. Finally, the purified AB@PSPAA nanoclusters were

collected by centrifugation at 2,200 g for 20 min.

Calculation of extinction spectra of AB_n The extinction spectra of B@PSPAA

and AB_n@PSPAA (n = 2, 3 and 4, d_A = d_B = 18 nm) nanostructures were

calculated by discrete dipole approximations.[30] The DDSCAT7 program

(Draine, B. T.; Flatau, P. J. 2008, http://arxiv.org/abs/0809.0337) was used and

only metal parts were included. The grid spacing was fixed at 0.33 nm and the

dielectric constants of gold were from Johnson and Christy.[31] The extinction

spectra were averaged over all orientations of nanostructures. The refractive

index of medium is 1.4.

Theoretical considerations Depending on the particle size and the double layer thickness, two approaches are usually utilized to estimate the electrostatic repulsion potential V_{elec} of two NPs in an electrolyte.

The Derjaguin summation method (DSM)[32, 33] allows the determination of the electrostatic repulsion potential V_{elec} (*eq. 1*) for NPs that are separated by a minimum distance h_m, and where the double layer thickness is considered small compared to the particle radius a ($\kappa a > 5$). If $\kappa a < 5$ or the two NPs are separated by a distance, the V_{elec} is usually estimated by the linear superposition approximation method (LSA, *eq. 2*)[34-36].

$$V_{elec} = 4\pi\varepsilon\Psi_1\Psi_2 \frac{a_1 a_2}{a_1 + a_2} \ln\left(1 + e^{-h_m/Le}\right) \qquad \textit{eq. 1}$$

$$V_{elec} \approx \varepsilon\Psi_1\Psi_2 \frac{a_1 a_2}{h_m + a_1 + a_2} e^{-h_m/Le} \qquad \textit{eq. 2}$$

where $\qquad \kappa^{-1} = L_e = \left(\frac{\varepsilon kT}{2e^2 I}\right)^{1/2} \qquad \textit{eq. 3}$

Herein, $L_e = \kappa^{-1}$ is the Debye screening length, calculated from the dielectric permittivity ε, the Boltzmann constant k, the absolute temperature T, the elementary charge e and the ionic strength I of the electrolyte solution (*eq. 3*). Ψ_i is the surface potential of the NP; a_i is the radius of NP.

From *eq. 1*, it is apparent that for two spheres, an increase in the radii results in an increase of the term $\dfrac{a_1 a_2}{a_1 + a_2}$ and therefore a corresponding increase in the value of the V_{elec}. In *eq. 2*, the V_{elec} is proportional to $\dfrac{a_1 a_2}{h_m + a_1 + a_2}$, and thus the same conclusion would hold true. These analyses agree with the

experimental observations that as the size of the B-NPs increases from 18 to 36 nm, the yield of AB@PSPAA increased from 18.2% to 90.4% at the same ionic strength (entry 1 and 7 of Table 2-1).

Furthermore, since the term $e^{-h_m/Le}$ is proportional to $e^{-\sqrt{I}}$, V_{elec} would decrease at high ionic strength for both *eq. 1* and *eq. 2*.

In our system, the separation distances of the NPs are long, and the calculated κa is less than 5, so *eq. 2* is suitable for estimating the V_{elec} between the B-NPs.

2.3   Results and Discussions

2.3.1 Assembly of AB$_n$ Nanoclusters.

Two types of NPs were prepared as the basic reactants: group A was gold NPs (AuNPs) coated with a tetra-thiol molecule, **1** (A-NPs, Figure 2-1), while group B was citrate-stabilized AuNPs (B-NPs). To mimic molecular reactions, it is critical that these two types of NPs could react with each other but do not form aggregates of their own.
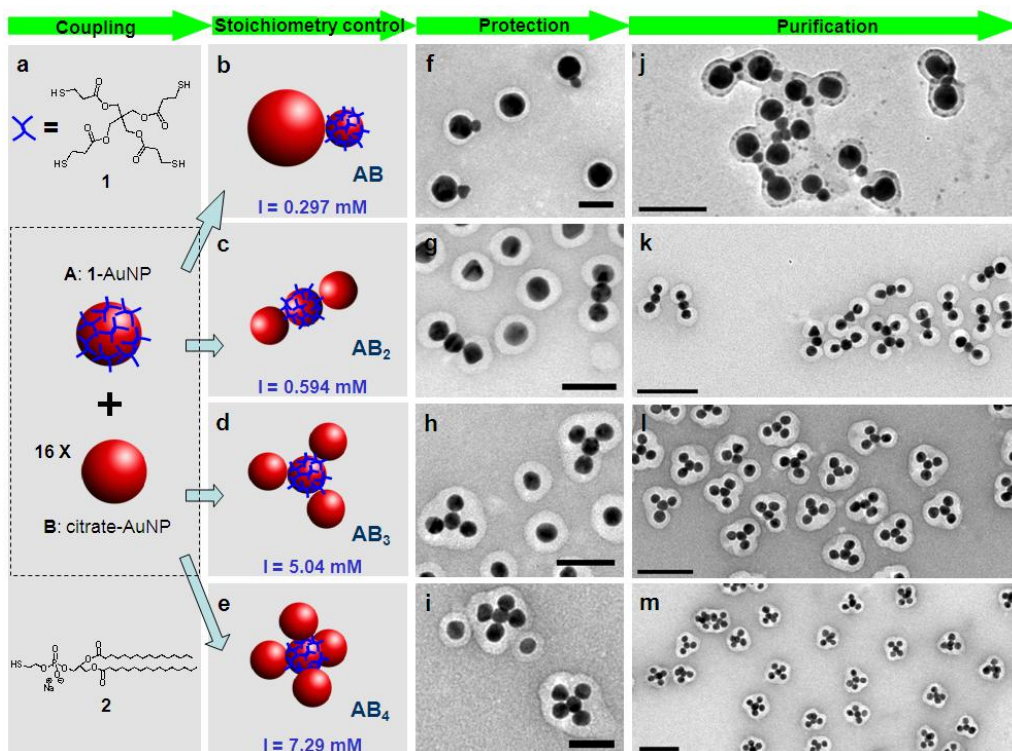
Figure 2-1. Stoichiometry-controlled nanoreactions. a-e, Schematics showing the syntheses of AB, AB_2, AB_3 and AB_4 nanoclusters, by tuning the charge repulsion (via the ionic strength of the reaction media) between the B-NPs. f-i, Transmission electron microscopy (TEM) images of the AB_n nanoclusters after protection by PSPAA, whereby the nanoclusters were treated with PSPAA and a thiol-ended hydrophobic ligand, 2-dipalmitoyl-*sn*-glycero-3-phosphothioethanol (sodium salt) (**2**). The surface of B-NP is rendered hydrophobic by ligand exchange, upon which the PSPAA self-assembles to form a uniform shell. The excess B-NPs are also encapsulated, but the A-NPs are not encapsulated due to persistence of the polar ligand **1**. See Table 1 for product analyses. j-m, TEM images of the purified nanoclusters. Scale bars are 50 nm for f–i, and 100 nm for j–m.

The thiol groups of **1** allowed the ligand to firmly anchor on a AuNP while presenting extra thiol groups that could bond to additional AuNPs (i.e., forming AuNP-**1**-AuNP bridges through the Au-S interactions). Hence, the A-NPs have to be completely covered with **1**, so that they would not provide exposed Au surface for bonding among themselves. These NPs were thus synthesized by

treating citrate-AuNPs with excess **1**, and the free ligands were then removed by centrifugation. If the unpurified A-NPs were treated with B-NPs, due to the excess ligand **1** in the solution, linear chain structure was obtained (Figure 2-2). Since excess **1** can replace sodium citrate on the surface of B-NPs quickly, the electrostatic repulsion of NPs decreased. Linear aggregation will kinetically form due to the kinetic energy of NPs can just overcome the repulsion potential. This is well consistent with our previous works and the literature about the formation mechanism of linear NP aggregates.[37-39] It indicates that the taking away the excess **1** is critical to the stoichiometry-controlled nanoreaction. The purified A-NPs were relatively stable in DMF, but they were used shortly after the synthesis. In the absence of excess **1**, the A-NPs could undergo partial ligand dissociation, which will lead to aggregation. Finally, the stoichiometry of the NP assemblies has to be controlled.

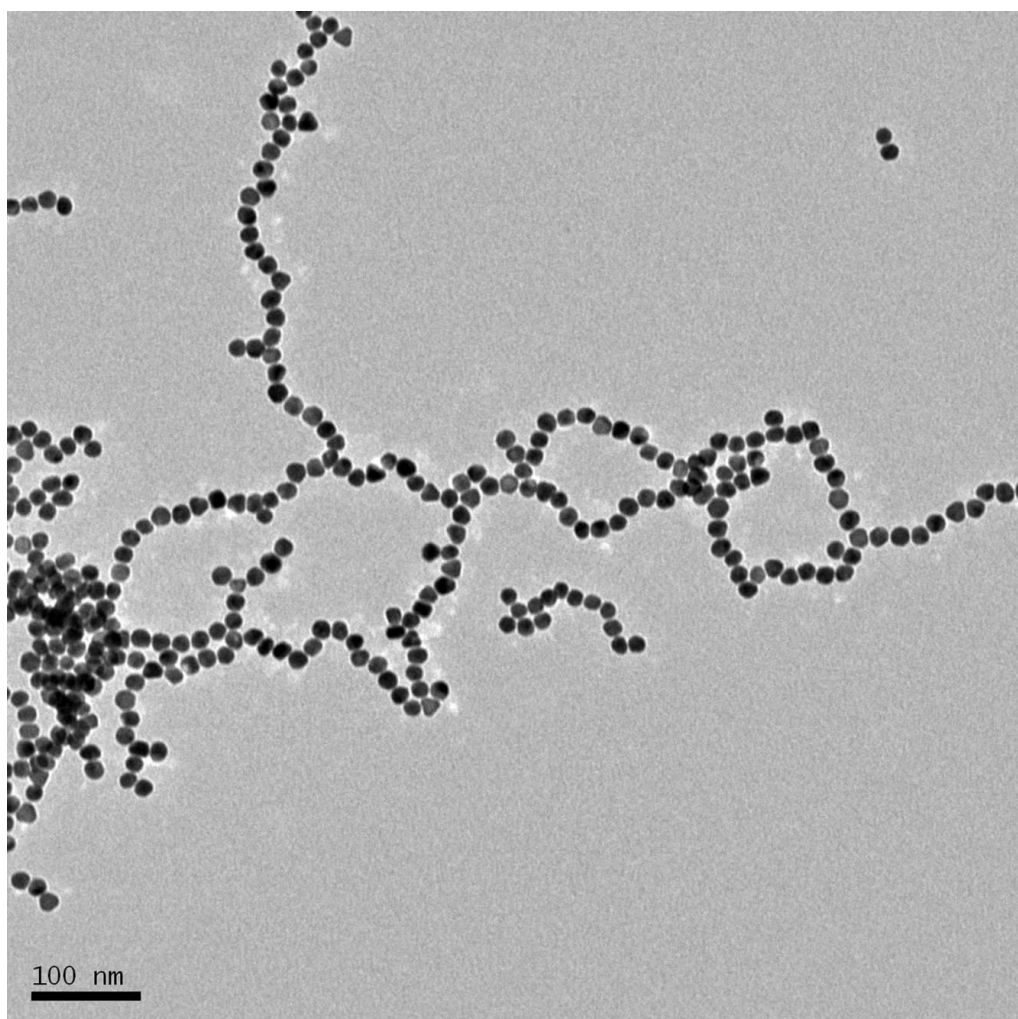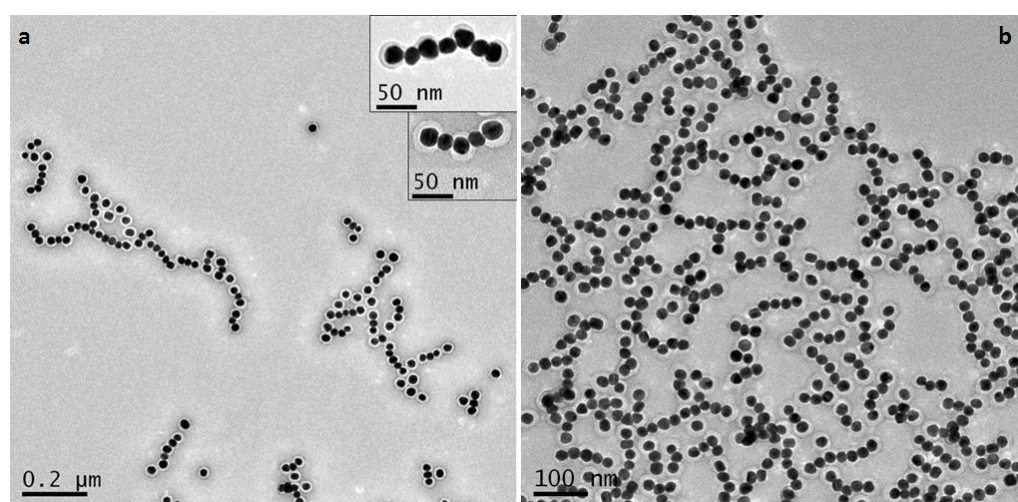**Figure 2-2** TEM images of the reaction between unpurified A-NPs and B-NPs.

Figure 2-3. TEM images of the 18 nm NP nanoreaction when the ratio of B-NPs to A-NPs was 8:1 (a) and 2:1 (b). Some linear chains composed of alternating A-NPs and B-NPs (*e.g.*, BABAB@PSPAA) existed, in addition to the AB$_2$@PSPAA nanoclusters. The linear chains in the sample b are longer and more than the sample a.

Without restrictions, multiple B-NPs could bond to each A-NP and *vise versa*, leading to extensive and un-controlled aggregation of the two reactants (Figure 2-3). Our strategy here is to treat A-NPs with excess B-NPs (the ratio of B-NPs to A-NPs was set as 16:1), and to control the stoichiometry of the product AB_n by fine-tuning the repulsion between the B-NPs via the varying of ionic strength of the reaction solution (Figure 2-3).

In a colloidal reaction, the purified A-NPs in DMF (100 µL, d_A = 18 nm) was slowly added to an aqueous solution containing large excess of B-NPs (200 µL, d_B = 18 nm, and final [A]:[B] = 1:16). The random collision between A- and B-NPs gives AB_n nanoclusters. However, the product solution cannot be directly characterized by TEM, as any drying or purification process would lead to significant aggregation of the solution species. Hence, both the product AB_n and the remaining B-NPs were protected by PSPAA encapsulation (Figure 2-1f-i), which basically involved the functionalization of the B-NP surface by a hydrophobic ligand (**2**), followed by PSPAA self-assembly[7, 27, 40]. Ligand **2** cannot replace the hydrophilic ligand **1** on the surface of A-NPs, which was thus not encapsulated. The resulting AB_n@PSPAA and B@PSPAA were readily isolated from the preparative solution by centrifugation, and then they were re-dispersed in water. With the polymer protection, the nanoclusters are stable against dissociation and aggregation. This allowed detailed product analysis of the nanoreactions by TEM characterization, giving a window for mechanistic insights.

Figure 2-1g and Figure 2-4 show the TEM images of a sample that contained trimeric nanoclusters, where the polymer shells only attached to the AuNPs on the ends but not the central one. The uniformity of this unique polymer coverage indicated that the trimeric clusters were not B_3@PSPAA, but rather (BAB)@PSPAA. This assignment is consistent with the expectations that **2** could replace citrate ions on B-NPs but not the multi-dentate **1** on A-NPs, and that PSPAA could only attach to regions covered with nonpolar and hydrophobic ligands like **2**.[12] Thus, the nanoreaction was successful in giving the AB_2 nanoclusters. The reaction product was surveyed based on the TEM images. Since excess B-NPs were used, the yield of the product AB_2 (89.4%, Table 2-1) was calculated based on the number of A-NPs. The by-products included a few AB, AB_3 and also A_xB_y nanoclusters which may result from aggregated A-NPs.
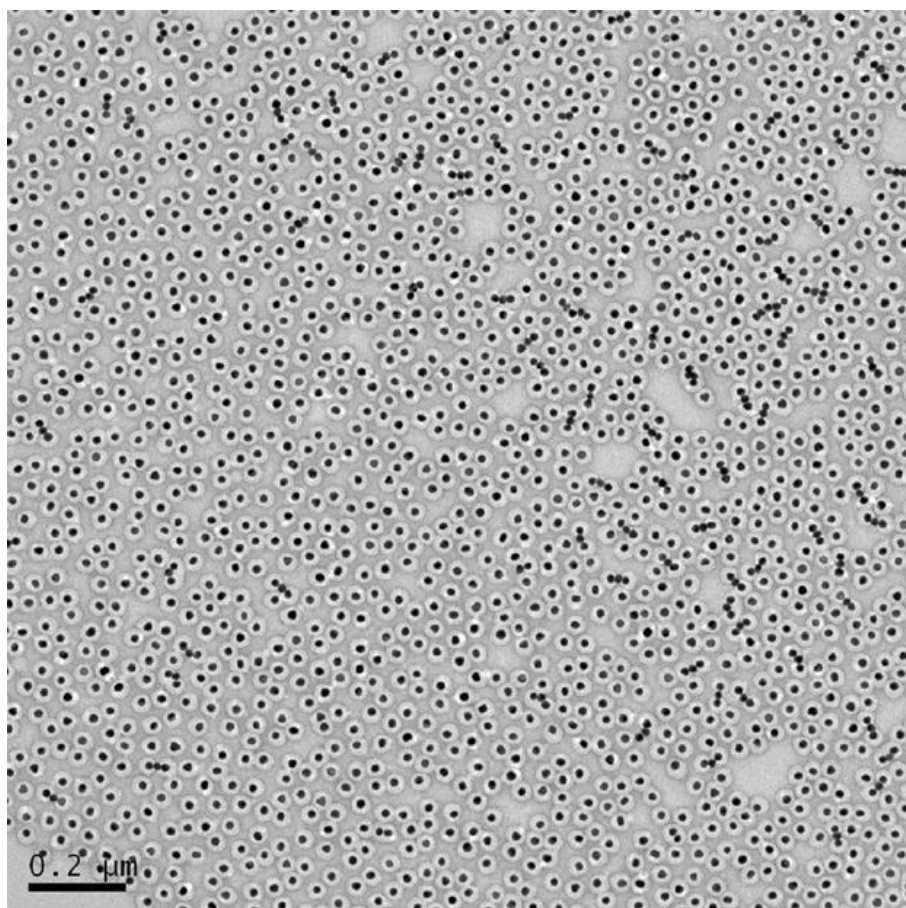
Figure 2-4. Large-area view of the AB_2@PSPAA nanoclusters and remaining B@PSPAA after the nanoreaction and polymer protection ($d_A = d_B = 18$ nm, entry 2 of Table 2-1).

Table 2-1. Product analyses of the nanoreactions.

Entry	**B**	I	Salt concentrations		Yield% based on **A**[a]				Isolated Purity%[a]
	(nm)	(mM)	Na$_3$citrate	Additional salt	AB	AB$_2$	AB$_3$	AB$_4$	
1	18	0.297	49.5 μM	-	18.2	74.0	1.98	0	-
2	18	0.594	98.9 μM	-	5.80	89.4	0.39	0	AB$_2$, 87.3[b], 85.9[c]
3	18	2.59	98.9 μM	2.00 mM NaCl	1.54	62.2	34.1	0.616	-
4	18	2.59	98.9 μM	2.00 mM NaNO$_3$	2.11	68.0	27.6	0.754	-
5	18	5.04	841 μM	-	2.10	18.9	65.6	6.88	AB$_3$, 64.1[b]
6	18	7.29	841 μM	2.25 mM NaCl	0	0.817	16.0	64.9	AB$_4$, 67.5[b]
7	36	0.297	49.5 μM	-	90.4	1.92	0	0	AB, 83.2[c]
8	36	3.30	49.5 μM	3.00 mM NaCl	10.1	85.7	0	0	-

[a] The synthetic yield was based on A-NPs (at least 500 counts) in randomly sampled TEM images of product solutions after removal of empty micelles and before the removal of B@PSPAA; the excess B@PSPAA were not included in the calculations. The isolated purity was calculated from randomly sampled TEM images of purified nanoclusters (at least 1000 counts); both the nanoclusters and the excess B@PSPAA were counted.

[b] Purified using the differential centrifugation method, as illustrated in Figure 2-14a-c.

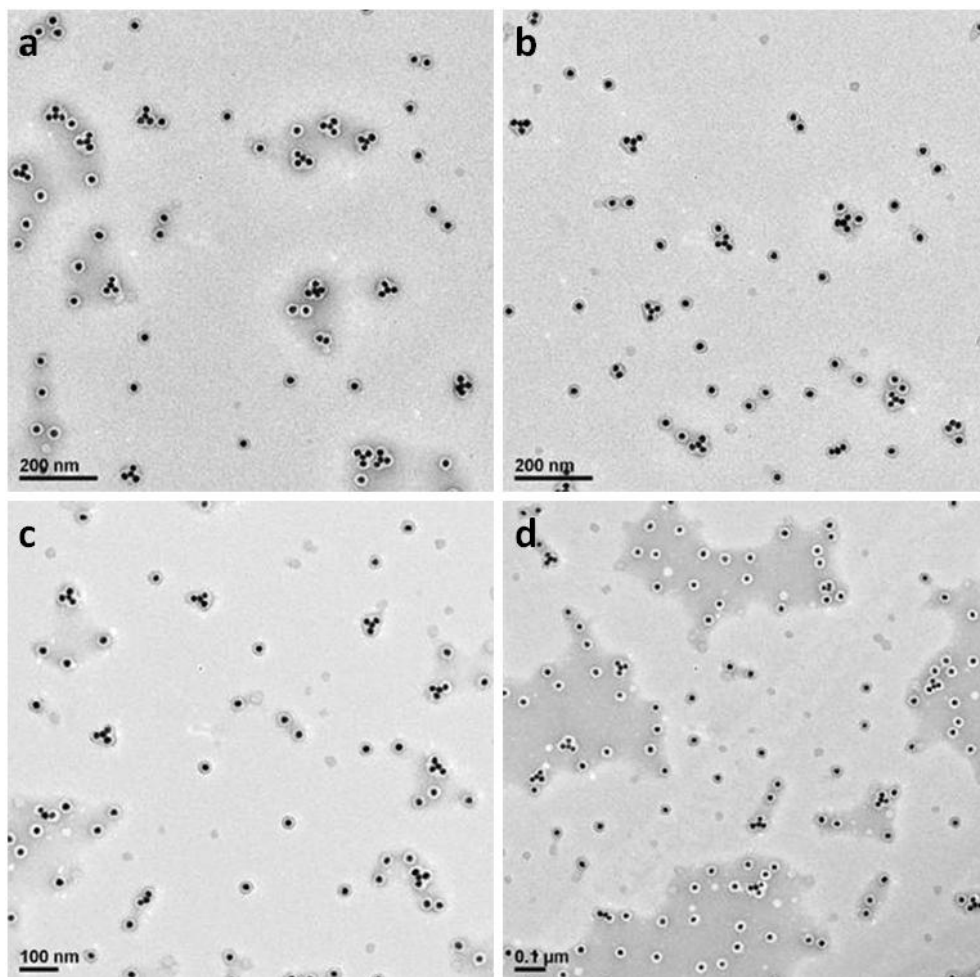[c] Purified using the Ag growth/etching method, as illustrated in Figure 2-14d-f.

Figure 2-5. Large-area view of the AB$_3$@PSPAA nanoclusters and remaining B@PSPAA ($d_A = d_B = 18$ nm, entry 5 of Table 2-1).

It was intriguing that the nanoreaction terminated at AB_2 despite the presence of excess B-NPs. As a NP in close packing has a coordination number of 12, there was sufficient space on the AB_2 for additional bonding with B-NPs. Obviously, some form of repulsion other than steric hindrance was responsible for the stoichiometry control. Since strong electric or magnetic dipoles are unlikely for the large spherical AuNPs (> 5 nm),[41] the most likely candidate is charge repulsion. Moreover, the linear AB_2 is reminiscent of the linear aggregates of AuNPs reported earlier,[38, 42] where charge and dipole interactions were proposed to be the main factors in the geometric control.
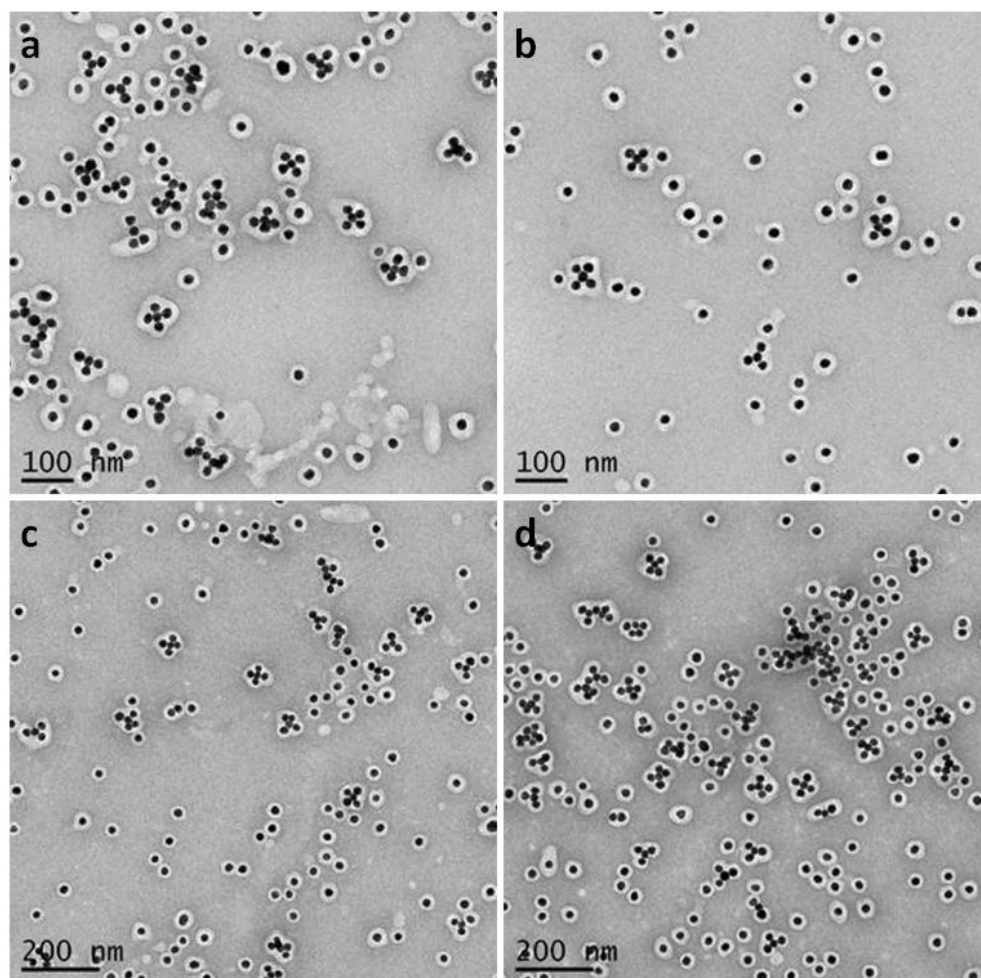

Figure 2-6 Large-area view of the AB_4@PSPAA nanoclusters and remaining B@PSPAA ($d_A = d_B = 18$ nm, entry 6 of Table 2-1).

To test this proposal, the colloidal reactions were carried out in solutions with varying ionic strengths (Table 2-1), which are known to modulate the charge repulsion between NPs. While it was difficult to adjust the ionic strength using a single salt owing to the stability requirements for the reactant NPs, it was clear that the size of AB_n nanoclusters increased with increasing [Na_3citrate] or [NaCl] (Figure 2-1). In particular, the sole increase of [NaCl] from 0 to 2.25 mM (entry 5 and 6) changed the major product of the nanoreaction from AB_3 (65.6%) to AB_4 (64.9%). In entry 4 of Table 2-1, $NaNO_3$ was shown to have a similar effect as NaCl, indicating that the Cl^- ions were not particularly important. Thus, the stoichiometry control of AB_n was probably more relevant to the general ionic strength of the solution than other effects.

Clear distance existed between the neighboring B-NPs in all AB_n nanoclusters, leading to linear (AB_2), triangular (AB_3), or tetrahedron (AB_4) geometries. While the large nanoclusters such as AB_3 and AB_4 were often completely engulfed by the polymer shell (Figure 2-1-l, m), their structural uniformity indicated that the hetero-assembly were successful and that the central NPs were all A-NPs. Notably, the ~18 nm separation of the B-NPs in AB_2 is a testament for the strong long-range repulsion during the formation of the nanoclusters. Such a force is most probably charge repulsion. It is hence likely that the increase in ionic strength led to more effective shielding of the surface charges, allowing more B-NPs to bond to each A-NP.

2.3.2 Mechanism of the Stoichiometry Control.

Interestingly, at low salt conditions (Table 2-1, entry 1) some heterodimers AB@PSPAA (18.2%) were observed in addition to AB_2@PSPAA (74.0%) (d_A = d_B = 18 nm, Figure 2-7). The partial polymer coverage demonstrated that these dimers were not B_2@PSPAA. The fact that the AB nanoclusters only occurred in the low-salt reactions indicated that they probably did not originate from the dissociation of AB_2.
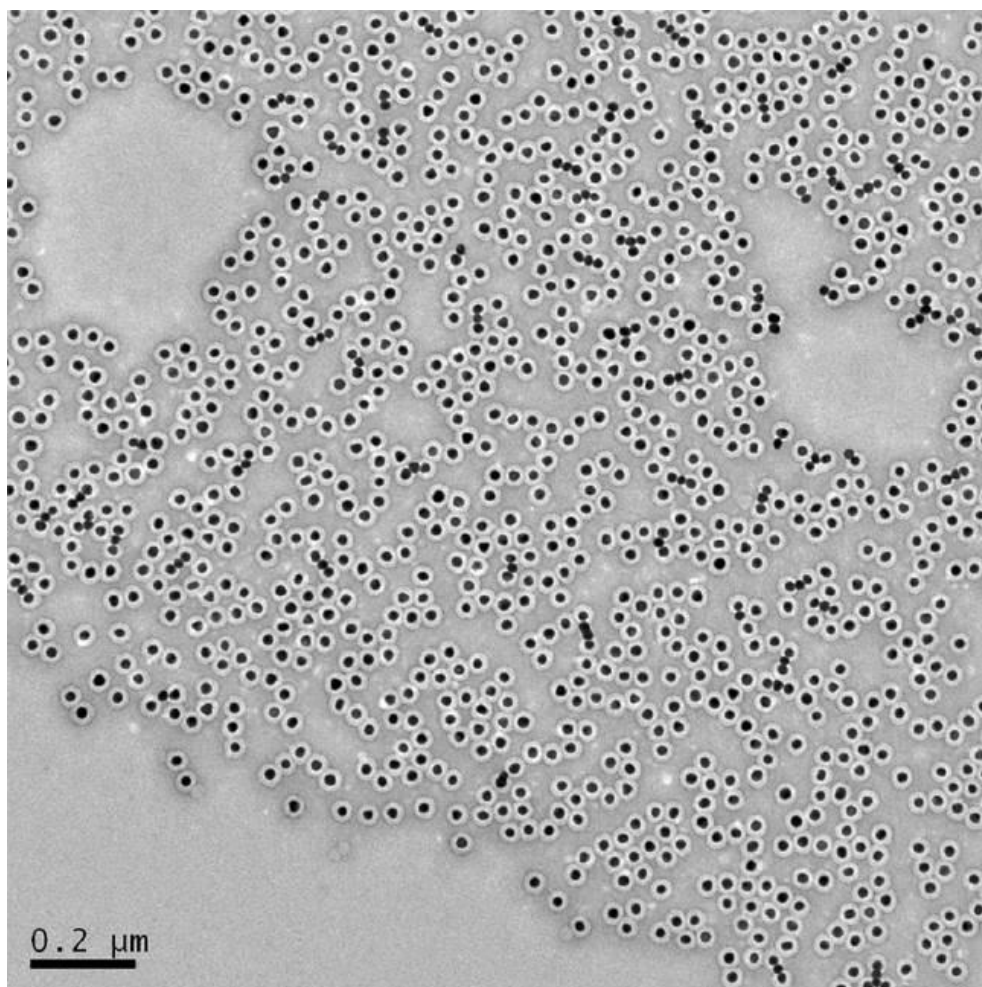
Figure 2-7. Large-area view of the AB@PSPAA nanoclusters, AB_2@PSPAA nanoclusters, and remaining B@PSPAA (d_A = d_B = 18 nm, entry 1 of Table 2-1).
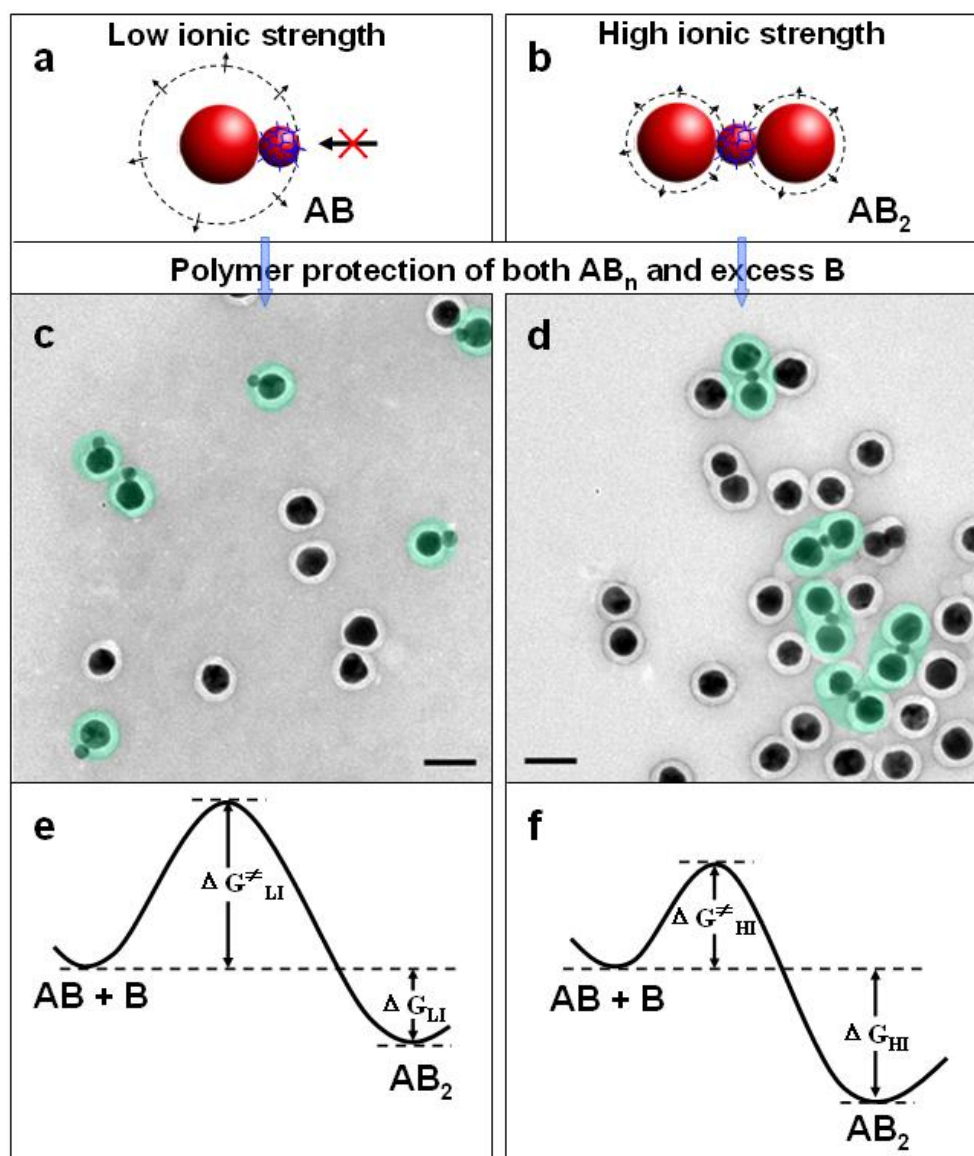
Figure 2-8. Mechanistic investigation of valency control in the nanoreactions, where long-range charge repulsion was identified as the key factor. (a, b) Schematic diagrams showing the creation of AB and AB_2 nanoclusters by tuning the charge repulsion between the B-NPs; larger radius of the dashed circle means stronger repulsion. (c, d) TEM images of the two samples in a and b, respectively, after polymer encapsulation (d_{A-NP} = 36 nm, d_{B-NP} = 18 nm). All scale bars are 50 nm. (e, f) Schematics showing the reaction coordinates of eq. 3 at low and high ionic strengths, respectively.
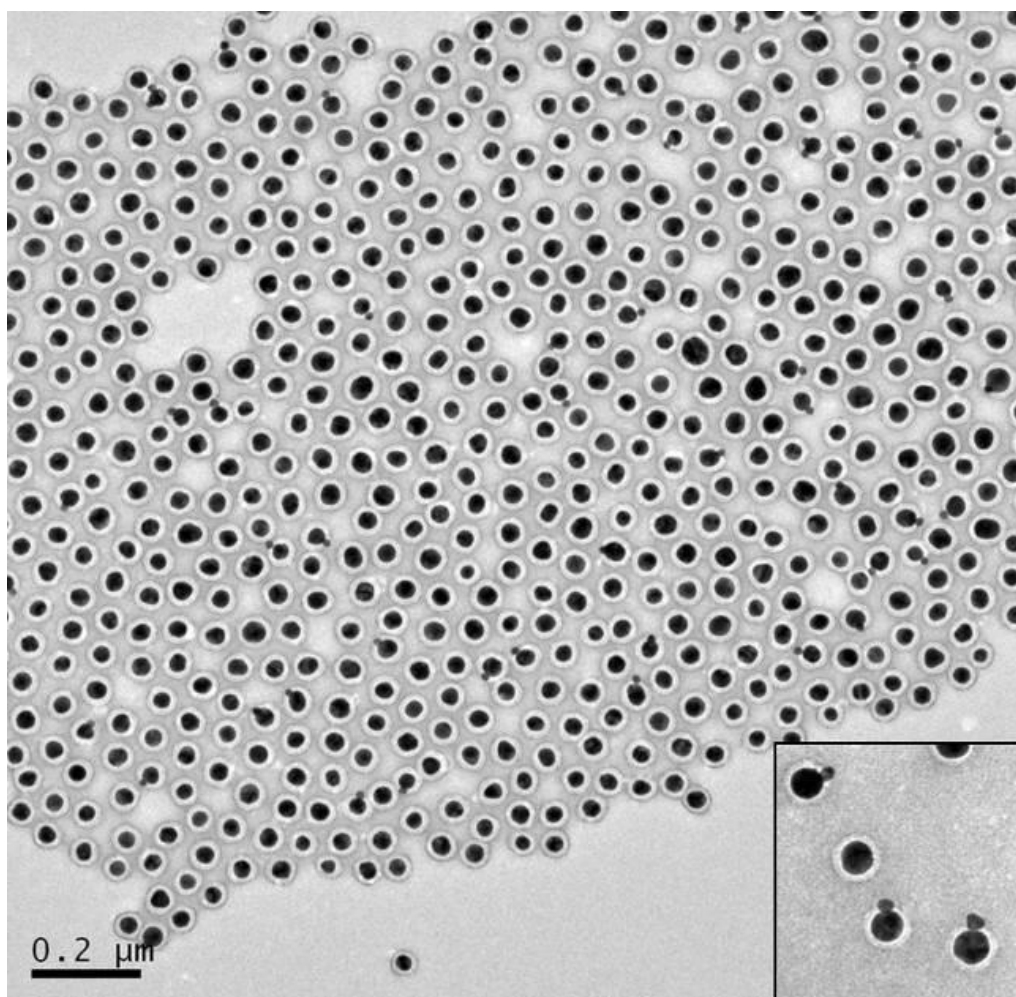
Figure 2-9. Large-area view of the AB@PSPAA nanoclusters and remaining B@PSPAA (d_A = 18 nm, d_B = 36 nm, entry 7 of Table 1); inset: high magnification.
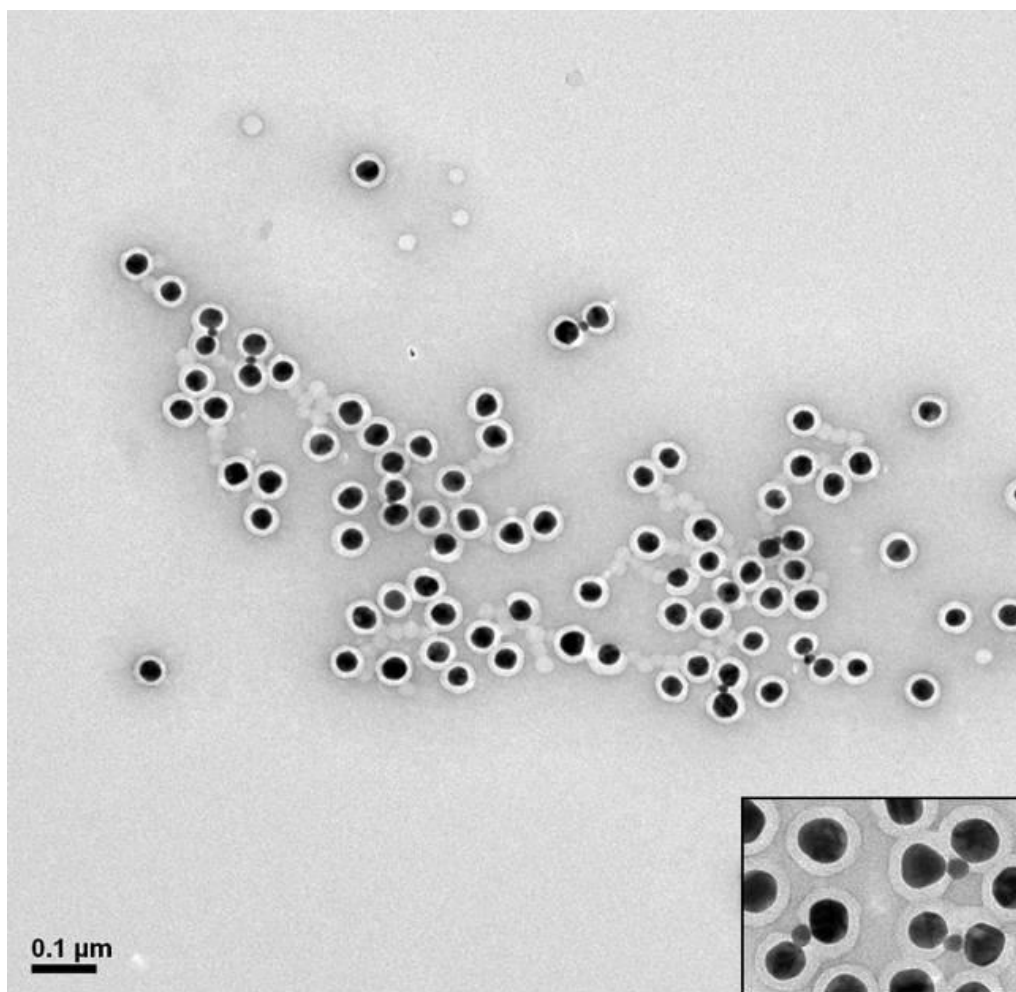
Figure 2-10 Large-area view of the AB$_2$@PSPAA nanoclusters and remaining B@PSPAA (d_A = 18 nm, d_B = 36 nm, entry 8 of Table 1); inset: high magnification.

Instead, they could be considered as an intermediate before the formation of AB$_2$. Should charge repulsion between the B-NPs be a dominant factor in controlling this nanoreaction, larger B-NPs are expected to trap more AB nanoclusters owing to their larger size and stronger charge repulsion. As expected, reacting 18 nm A-NPs with 36 nm B-NPs under otherwise similar experimental conditions gave heterodimers AB@PSPAA in excellent yield (90.4%, Figure 2-1f, j, Figure 2-8c, and Figure 2-9). Synthesis of heterodimers is a major challenge in colloidal assembly. Our simple approach has achieved

the same level of specificity as those of DNA-based assembly techniques.[21, 43]

The AB heterodimers could also be categorized as "Janus" NPs[12, 44] in that

they possess two diametric faces of different chemical functionalities.

By increasing ionic strength in this reaction ([NaCl] = 3.00 mM),

AB_2@PSPAA (85.7%, Figure 2-8d, and Figure 2-10) resulted instead. These

two reactions ruled out electric or magnetic dipoles as the key controlling

factors: while it is possible to argue that transient or static dipoles dictate the

linear encounter of AB with a B-NP in forming the AB_2 nanocluster (Figure

2-1g and Figure 2-8d), the dipoles cannot explain the non-reactivity of AB at

low ionic strength (Figure 2-8c, and entry 7 of Table 2-1). Any charge-dipole or

dipole-dipole interaction would have facilitated the reaction of *eq. 4* rather than

impeding it. Alternatively, long-range (> 18 nm) charge repulsion between the

B-NPs could best explain the non-reactivity of AB; it is also consistent with the

formation of AB_2 at increased ionic strength. Though it is hard to determine the

charge of A-NPs, it is clear that the charge interaction between A- and B-NP

plays a minor role since AB clusters readily formed even at lowest ionic

strength.

$$AB + B \rightarrow AB_2 \qquad\qquad eq. 4$$

To understand how charge interactions affect the nanoreactions, it is critical

to determine whether the reactions are thermodynamically or kinetically

controlled. In *eq. 4*, the covalent bonding between A- and B-NPs should be the

main driving force for the reaction, although other factors, such as

charge-charge interactions (V_{elec}), Van de Waals interactions, solvophobic effects, and possibly also charge-dipole or dipole-dipole interactions, may contribute to the ΔG. On the other hand, the transition state should occur at a point before the chemical bond formation (Figure 2-8e, f), where the long-range charge interaction would dominate. Thus, the V_{elec} has to be overcome before effective collision could take place, making it a major contributor of $\Delta G^{\neq}$. Hence, both ΔG and $\Delta G^{\neq}$ should decrease at high ionic strength due to weak charge repulsion. This leads to two scenarios that could explain the non-reactivity of AB at low ionic strength. If the reactions are thermodynamically controlled, the kinetic energy of the NPs (KE) should exceed the activation barrier ($\Delta G^{\neq}$), while ΔG_{HI} (HI stands for high ionic strength) should be < 0 at high ionic strength (forward reaction), and $\Delta G_{LI} > 0$ at low ionic strength (backward reaction). That is, the system was at or close to equilibrium at the end of reaction and the AB nanoclusters formed because they were the most stable state. In contrast, kinetically controlled reactions would mean that KE > $\Delta G^{\neq}_{HI}$ (forward reaction) but KE < $\Delta G^{\neq}_{LI}$ (no reaction); both ΔG_{LI} and ΔG_{HI} should be < 0. Hence, the AB nanoclusters accumulated because the kinetic energy of the reactants was insufficient to cross the activation barrier to make AB_2.

Experiments were carried out to distinguish these two possibilities. After the formation of AB_3 clusters ($d_A = d_B = 18$ nm), the colloid was diluted and incubated in an aqueous solution at low ionic strength (0.297 mM) before

PSPAA encapsulation. However, few AB$_2$ or AB clusters were obtained, even when the incubation was carried out at elevated temperature or under sonication (Figure 2-11). Therefore, it is unlikely that the nanoreactions were reversible. Furthermore, the AB$_3$@PSPAA in Figure 2-1-l often deviated from perfect triangles and sometimes appeared T shape, suggesting the addition of a B-NP to a linear BAB intermediate during its formation. This observation is generally consistent with a non-reversible and kinetically controlled reaction.
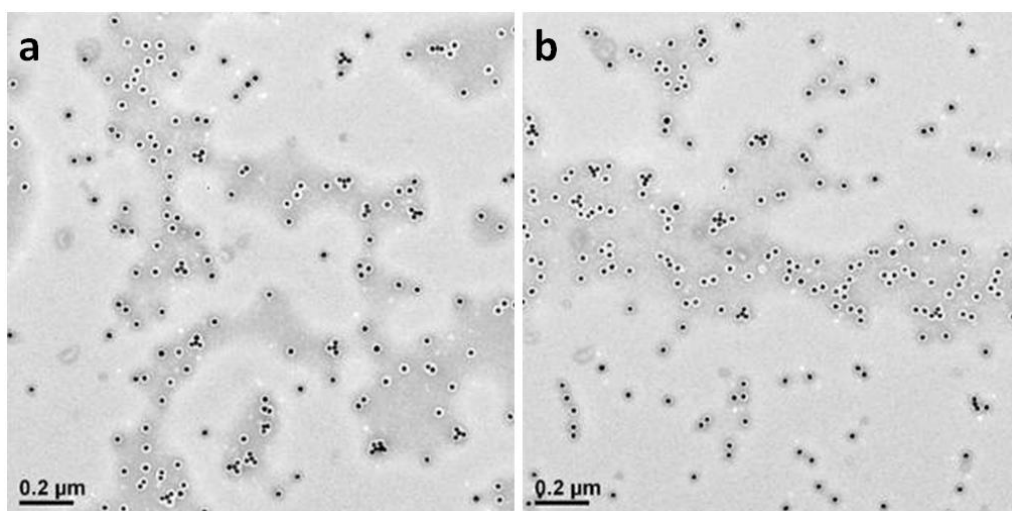
Figure 2-11. After reacting A-NPs with B-NPs ($d_A = d_B = 18$ nm, same conditions as those of entry 5 of Table 1), the reaction mixture was diluted to lower the ionic strength to 0.297 mM, and then heated at 80 °C for 30 min. Finally, the nanoclusters were encapsulated by PSPAA and the products were concentrated before TEM characterization. The products showed similar ratio of AB$_3$@PSPAA as those of entry 5 of Table 2-1, indicating that the B-NPs did not dissociate from the AB$_3$ nanoclusters after the decrease of ionic strength. Repeating this experiment with additional sonication step gave similar results.

As theoretical considerations were performed in the method section, the electrostatic repulsion potential (V_{elec}) between the B-NPs can be estimated by linear superposition approximation (LSA)[34-36]:

$$V_{elec} \approx \varepsilon \Psi_i^2 \frac{a_i^2}{h_m + 2a_i} e^{-h_m/Le} \qquad\qquad \textbf{\textit{eq. 2}}$$

$$L_e = \kappa^{-1} = \left(\frac{\varepsilon k T}{2e^2 I} \right)^{1/2} \qquad\qquad \textbf{\textit{eq. 3}}$$

where $L_e = \kappa^{-1}$ is the Debye screening length, calculated from the dielectric constant ε of the medium, the Boltzmann constant k, the temperature T, the elementary charge e and the ionic strength I of the electrolyte (***eq. 3***); a_i is the particle radius; h_m is the separation distance of the interacting B-NPs; and Ψ_i is the surface potential of the particle. Therefore, an increase in the radius of B-NPs results in an increase in $a_i^2/(h_m + 2a_i)$ and thus a correspondingly larger repulsion potential V_{elec}. Furthermore, as V_{elec} is proportional to $exp(-\sqrt{I})$, high ionic strength leads to weak repulsion potential, consistent with the experimental results (Table 2-1).

In Figure 2-1, the initial bonding of A-NP and B-NP is favorable, but further attachment of a B-NP on the resulting AB cluster has to overcome the repulsion between the B-NPs, which becomes stronger as the AB_n cluster increases in size. At a specific ionic strength, the growth of AB_n stops when the kinetic energy of the colliding NPs could not exceed the repulsion potential V_{elec}. High ionic strength lowers the V_{elec} and thus allowing more B-NPs to react with each A-NP (Figure 2-1a-e). Understandably, the size variation among the A-NPs and B-NPs will cause unequal charge repulsions and thus lead to non-uniformity in the stoichiometry of the product nanoclusters. This is in

drastic contrast to molecular reactions where all atoms or molecules are perfectly uniform.

2.4 Purification

2.4.1 Differential Centrifugation Separation

The development of purification strategy of nanoparticles or small nanoparticles aggregates is a hot theme in nanotechnology.[45-49] This is because the precisely controlled nanostructure is the primary step on the way to the scalable fabrication of nanodevice. However, up to now, it is still a cry to produce pure clusters of two or three NPs directly in colloidal solution. Moreover, it is difficult to separate the selective nanostructure in a mixture solution due to the possible dissociation or further aggregation during the isolation process. Our group has developed copolymer encapsulation method to resolve this problem.[7, 12, 23, 27, 48, 50] However, in our previous assembly techniques as well as the method presented in this chapter, the yields of clusters are still very low. So it is critical to develop new purification method to isolate the selective products from the mixture.

Recently, our group has developed one differential centrifugation method, which can be used to isolate dimers and trimers of AuNPs aggregates in high purity.[24] For the gradient we used in this separation is high density CsCl solution (62%, 1.9 g·cm^{-3}), the polymer encapsulated nanoclusters were re-dispersed in high pH (>10) aqueous solution, which can provides sufficient surface charge to the PAA part.[12, 27] Thus the polymer encapsulated

nanoclusters can be stable under such adverse conditions.

As shown in Figure 2-12A, the differential centrifugation setup is easy: a concentrated nanoclusters solution was carefully put on the top of the 11+62% CsCl gradient. After centrifuged at 5800g for 20 min, two bands of red and purple color were appeared (Figure 2-12B). The b2 band solution was carefully transferred and purified to remove the concentrated CsCl, and characterized by TEM. Figure 2-12b2 showed the high purity of NPs dimers (>95%). The solution under the b2 band was purified to remove the CsCl, and then separated by another 11+62% CsCl gradient. The results were shown in Figure 2-12C. TEM image of c3 band was shown in Figure 2-12c3, in which 81% trimers were obtained. Because of the large size distribution of NPs, the weight of some dimers and trimers may overlap.
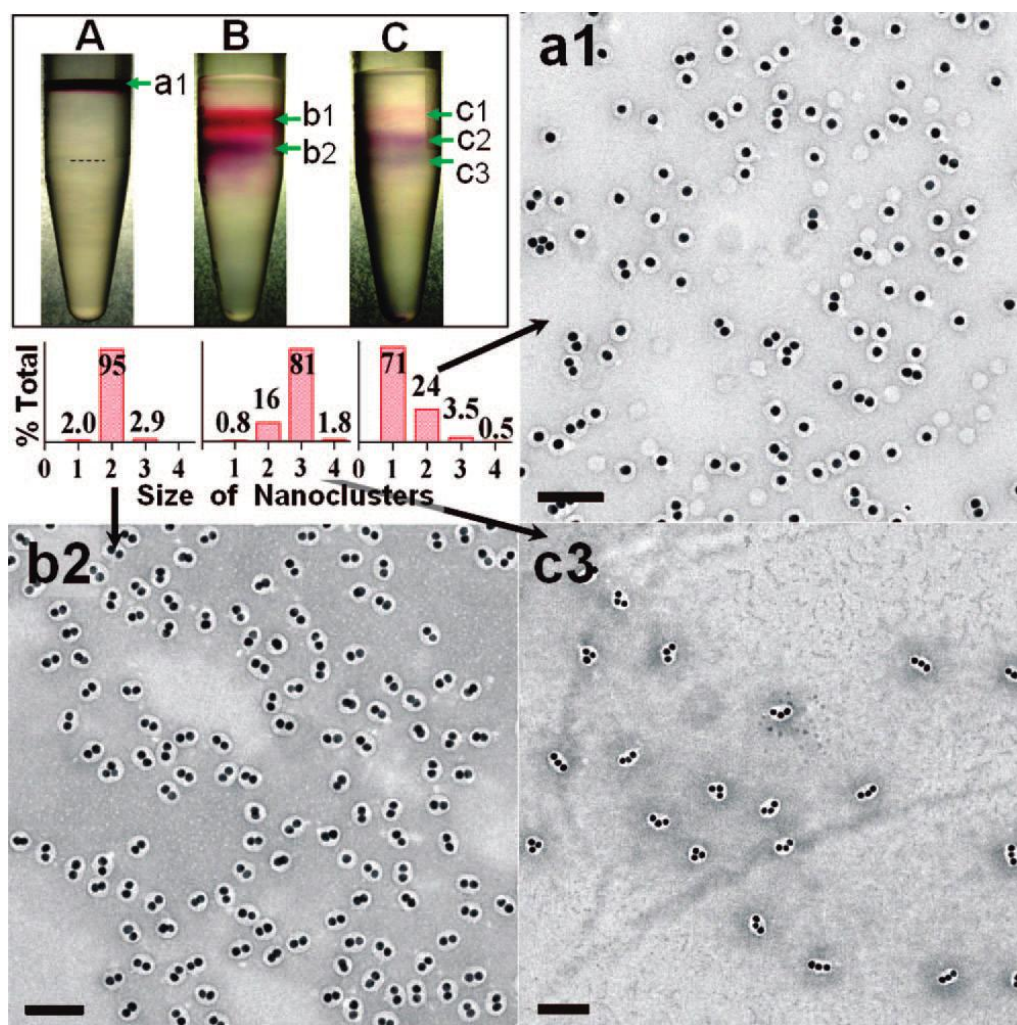
Figure 2-12 (A) A typical setup of differential centrifugation, where 62% and 11% aq. CsCl and then $AuNP_n$@PSPAA in water were layered from bottom to top. (B) The result of A after 20 min centrifugation. (C) Separation result of a pre-enriched trimer sample. (a1, b2, and c3) TEM images of the respective fractions indicated in A-C; the histograms are shown in the insets. Scale bars: 100 nm. Reprinted with permission from ref. [24]. Copyright 2009 American Chemical Society.

Figure 2-13 (A, B, D, E) Separation of AuNP$_n$@PSPAA by differential centrifugation, before (0 min) and after 20, 40, and 60 min. (F, G) All conditions are same as those for B and E, except that the CsCl gradient was precentrifuged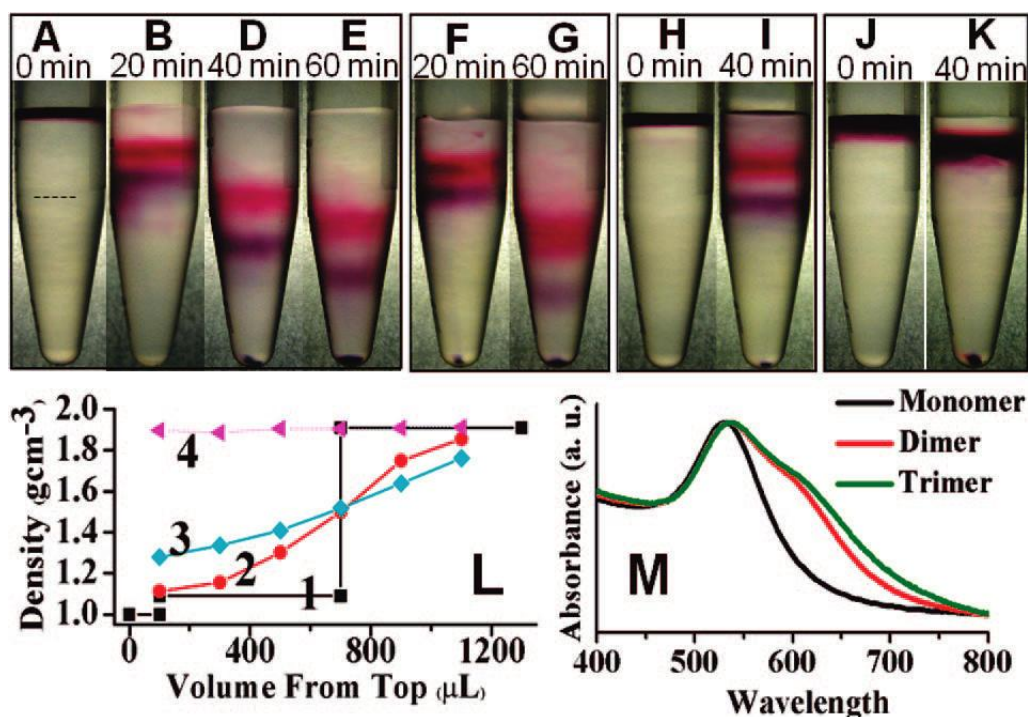 for 20 min before loading AuNP$_n$@PSPAA. (H, I) AuNP$_n$@ PSPAA was loaded on top of 62% CsCl solution, before and after 40 min centrifugation. (J, K) AuNP$_n$@PSPAA was loaded on top of 50% sucrose solution, before and after 40 min centrifugation. (L) Density trace of the 11 + 62% gradient before (line 1) and after 20 and 120 min (line 2 and 3) centrifugation and density trace of solution I (line 4). (M) UV-vis spectra of monomer, dimer, and trimer samples. Reprinted with permission from ref. [24]. Copyright 2009 American Chemical Society.

If the solution was centrifuged for a long time, it can be found that the monomer and dimer bands moved towards the bottom of centrifuge tube, and the gap between them increased (Figure 2-13A-E). So the separation was possible due to the different sedimentation velocity of various nanoclusters. From Figure 2-13H-I, we can found that the monomers still can move downward in saturated CsCl solution. It indicated that the averaged density of AuNP$_n$@PSPAA was higher than the saturated CsCl solution ($\rho_{NPs} > \rho_{solvent}$),

and thus the gradient is not necessary to the separation. Figure 2-13L showed the density changing of the mixture after centrifugation. The initial sharp gradient has smoothed under longer centrifugation time. One control experiment that the gradient solution was centrifuged for 20 min before the separation setup showed that the separation was not affected too much (Figure 2-13F-G). Consequently, the movement of the NP bands was mainly independent of any sharp density gradient. Figure 2-13J-K showed that in a sucrose solution (50%), the nanoclusters cannot separate efficiently. In comparison to 62% the CsCl solution, this sucrose solution is with a lower density but higher viscosity.

When a NP reached steady-state during centrifugation, the friction force (F $_{friction}$) should be equal to centripetal force (F$_{centrifugal}$) minus buoyancy (F$_{buoyancy}$); it can be re

$$fv = m\omega^2 r - m\omega^2 r(\rho_{solvent}/\rho_{NP})$$

where f is the frictional coefficient, v is the steady-state sedimentation velocity, m is the mass of NP, m is the angular velocity, and r is the distance from the center of rotation. Because the mass of a dimer is about twice of a monomer, as well as the similar polymer coating, the F $_{friction}$ (F$_{centrifugal}$ - F$_{buoyancy}$) of a dimer is larger than that of a monomer (close to two times). The frictional coefficient, f, which is related to the cross section, should be larger for a dimer. However, due to the close packing of two NPs in a dimer, the cross section difference between a dimer and monomer would be much small (more

less than two times). So the sedimentation velocity of a dimer is larger than that of a monomer if $\rho_{solvent} < \rho_{NP}$. On the other hand, our experience demonstrated that lower density solvent such as pure water could not work for the NPs separation. So the CsCl solution with higher density and viscosity could slow down the nanoclusters. Thus, the difference of sedimentation velocity of various clusters can be enhanced relatively.

In comparison to the previous cases, the advantage of our method is the effectiveness. Such as, in Dai's work, different size of AuNPs (5, 10, and 20 nm) was separated, in which the weight difference is 1:8:64; in our case, the weight difference of monomer, dimer, trimer is 1:2:3. Furthermore, almost all the NPs can be encapsulated in the copolymer shell, thus this separation method is more general. Our method will play more important role in the purification of nanoclusters.

2.4.2 Purification of the Products of Nanoassembly

To mimic molecular reactions, the products of the nanoreactions have to be purified by removing the excess B@PSPAA. Since the overall densities of AB_n@PSPAA (n = 2~4) are significantly larger than that of B@PSPAA, the former was easily isolated by differential centrifugation.[24] Figure 2-14a-c shows a typical purification, where the product solution containing AB_3@PSPAA was carefully layered on top of a saturated CsCl solution (no concentration gradient was used). After centrifugation, the B@PSPAA and AB_3@PSPAA were separated into two distinct bands of red and blue color,

respectively. The blue band was enriched in AB_3@PSPAA, and its color indicated surface plasmon coupling among the AuNPs of AB_3. This band was isolated, diluted by aq. NaOH (pH=10), and then centrifuged again to remove the excess CsCl. The purity of the resulting AB_2-, AB_3-, and AB_4@PSPAA, as based on the surveys of over 1000 nanoclusters in TEM images, were 87.3%, 64.1% and 67.5%, respectively (Figure 2-1k-m, Figure 2-15, Figure 2-16, and Figure 2-17). Most of the impurities in these samples were AB_n@PSPAA nanoclusters. The non-ideal purities achieved here could be attributed to the imperfect uniformity in the size of the original AuNPs, which affects both the yield of the nanoreactions and also the efficacy of the purification.
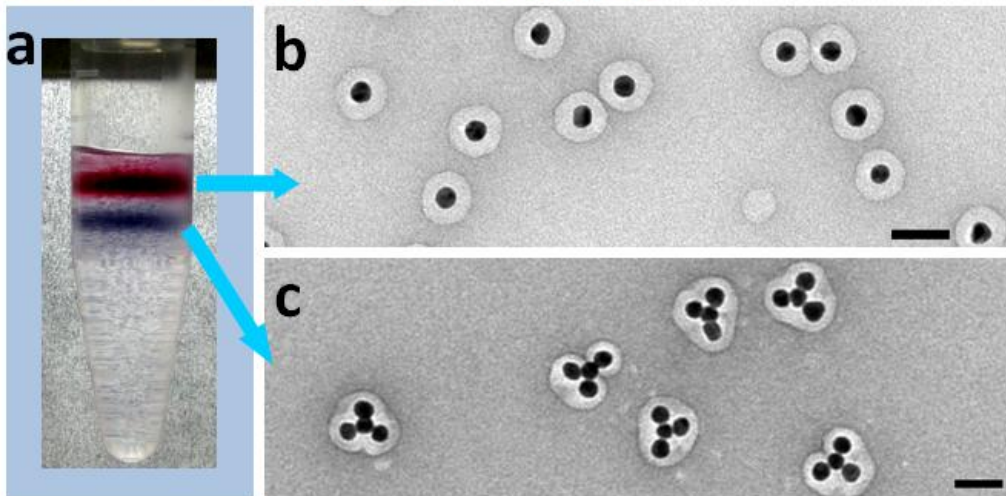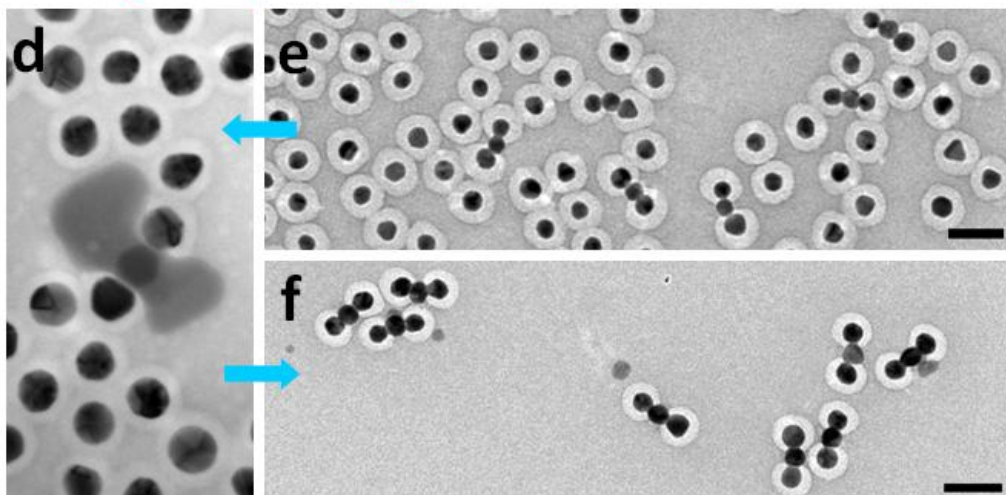
Figure 2-14 Purification of the AB_n@PSPAA nanoclusters. a, Photographs of a sample solution after differential centrifugation. b, c, TEM images of the separated B@PSPAA and AB_3@PSPAA partitions. e, d, TEM images of the AB_2@PSPAA and B@PSPAA mixture before and after Ag growth on the A-NPs. f, TEM image of the sample in f after centrifugation and etching Ag. All scale bars are 50 nm.

Figure 2-15 Large-area view of the purified AB$_2$@PSPAA nanoclusters, isolated by using the differential centrifugation method.
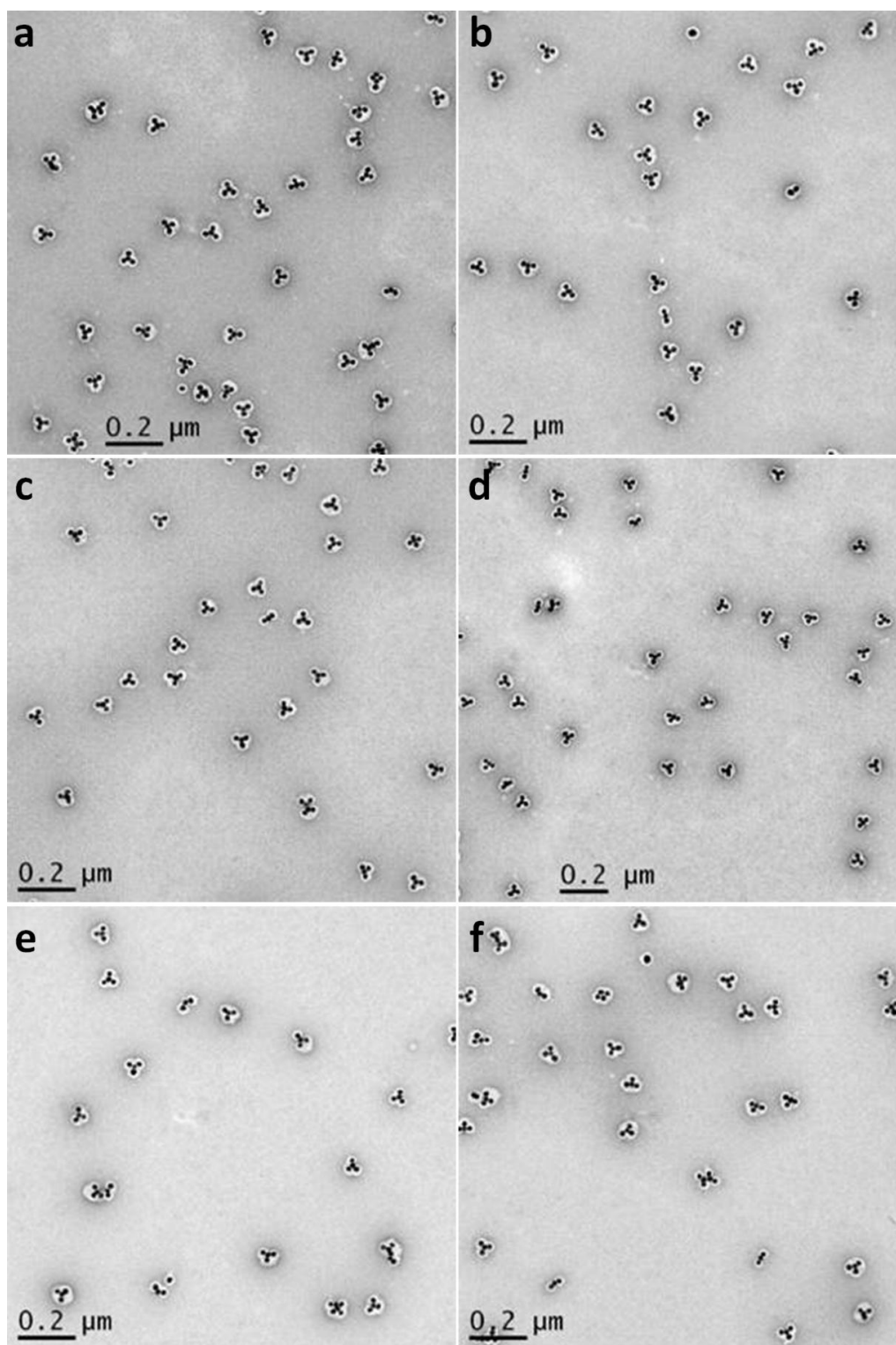
Figure 2-16 Large-area view of the purified AB$_3$@PSPAA, isolated by using the differential centrifugation method.
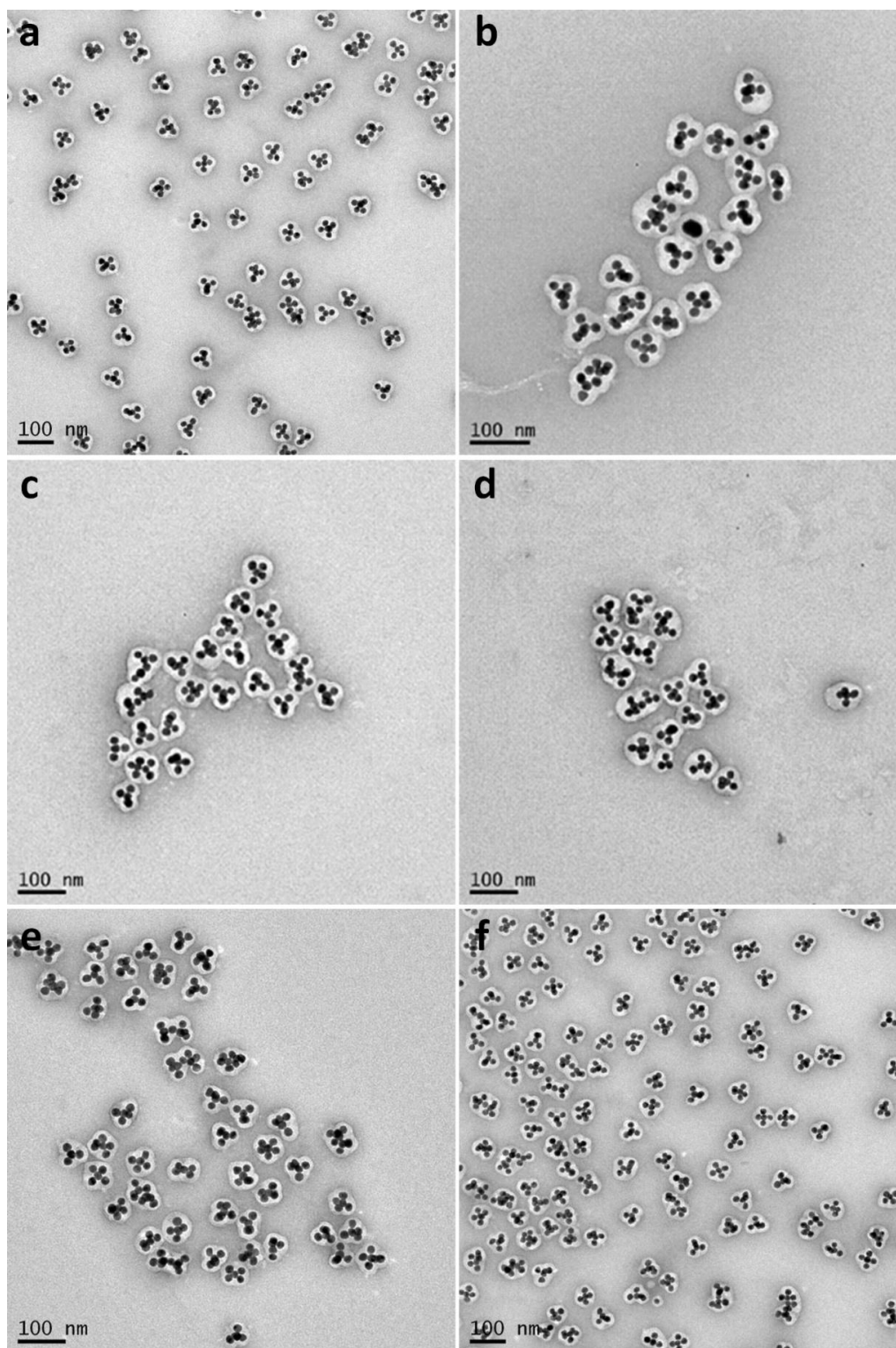
Figure 2-17 Large-area view of the purified AB$_4$@PSPAA, isolated by using the differential centrifugation method.

Figure 2-18. TEM images of the AB$_2$@PSPAA sample after Ag growth, which occurred on the exposed A-NPs but not on the B@PSPAA.

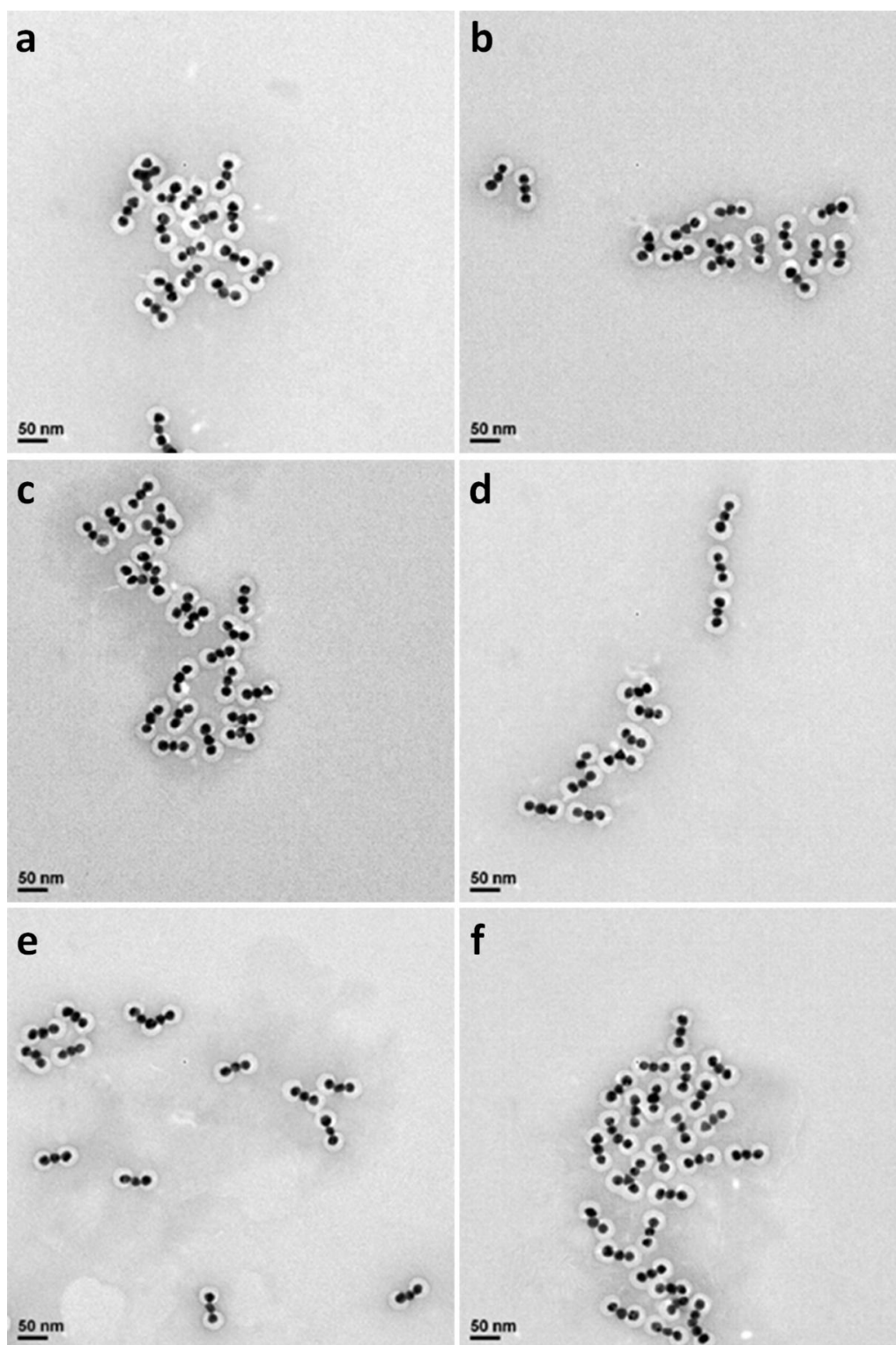**Figure 2-19**. Large-area view of the purified AB$_2$@PSPAA nanoclusters isolated by using the Ag growth/etching separation method; inset: high magnification.

The AB- and AB$_2$@PSPAA nanoclusters, especially the AB@PSPAA may aggregate in the saturated CsCl aq. solution due to the exposure of A-NPs. An alternative method was adapted for the separation of AB- and AB$_2$@PSPAA (Table 2-1, entry 2 and 7), where the exposed A-NPs were exploited as seeds for growing metallic Ag (Figure 2-14d-f). This method was analogous to the separation of (6,5) single-walled carbon nanotubes, which were sunk downward by metallic nanoparticles deposition.[51] In contrast, no Ag growth occurred on the PSPAA shells. As a result, the AB$_2$@PSPAA grew significantly heavier

than the fully-encapsulated B@PSPAA, and they could be easily isolated from the latter by centrifugation at low speed in water. Subsequently, the isolated Ag-(AB$_2$@PSPAA) were washed with NH$_3\cdot$H$_2$O to etch the Ag blocks, and then centrifuged to remove the excess reactants. Using this method, AB$_2$@PSPAA were isolated in 85.9% purity (Figure 2-19). This technique was essential for the purification of AB@PSPAA (Figure 2-1-j and Figure 2-21, purity 83.2%, d$_A$ = 18 nm, d$_B$ = 36 nm), as there was only a small density difference between the AB- and B@PSPAA. As such, it is nearly impossible to separate them by the differential centrifugation method. For AB$_3$- and AB$_4$@PSPAA, however, the polymer shell tends to enclose the whole nanoclusters without exposing the A-NPs; this prevents Ag attachment and thus renders the purification method ineffective. Hence, the two purification methods are complementary in recovering the nanoreaction products and may allow flexibility in designing future synthetic routes.
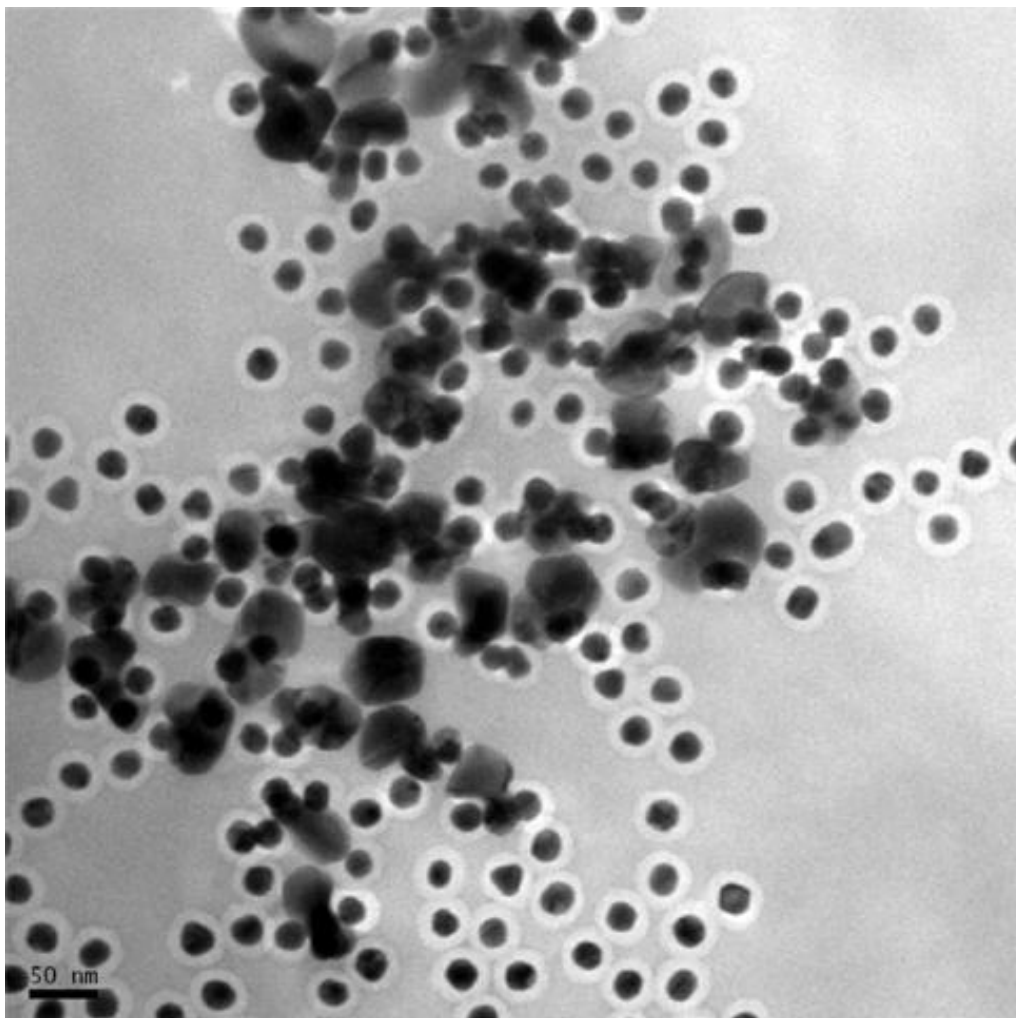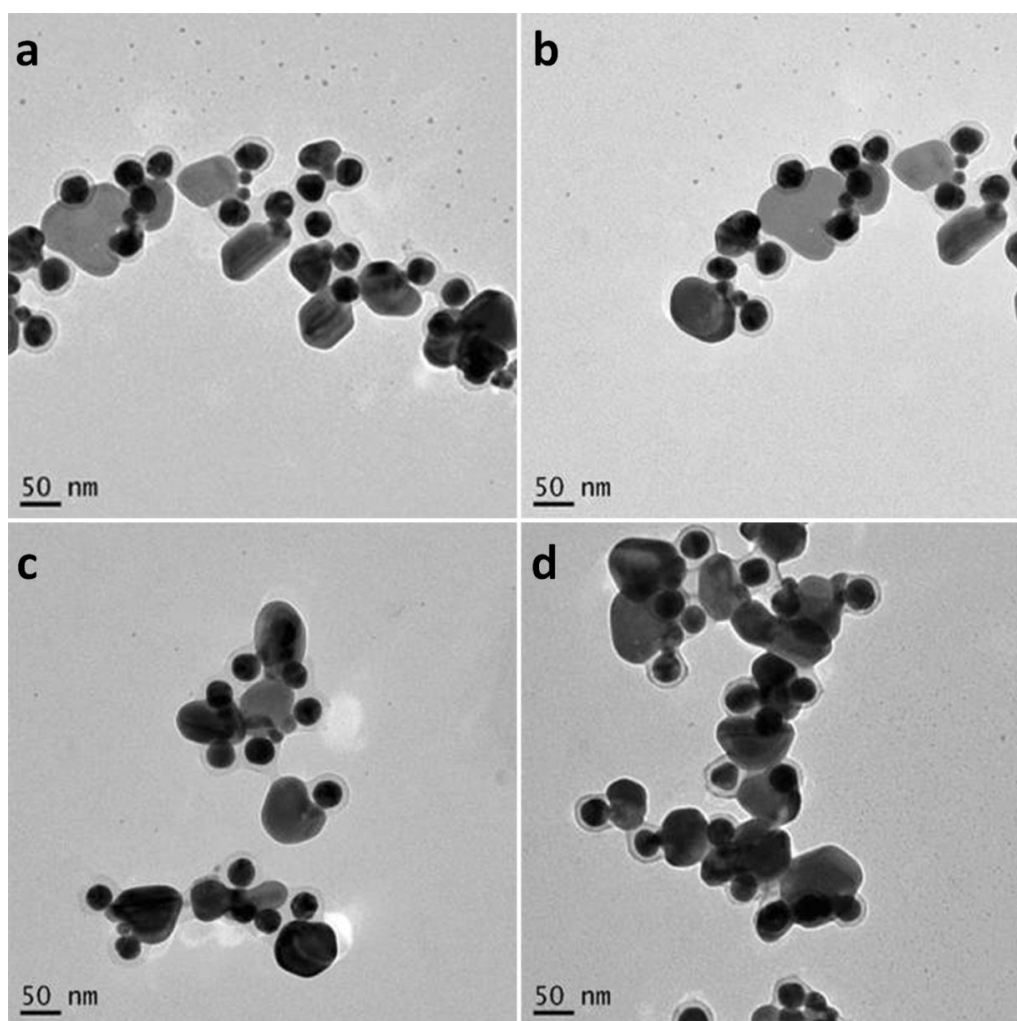
Figure 2-20 TEM images of the AB@PSPAA sample after Ag growth, which occurred on the exposed A-NPs but not on the B@PSPAA.
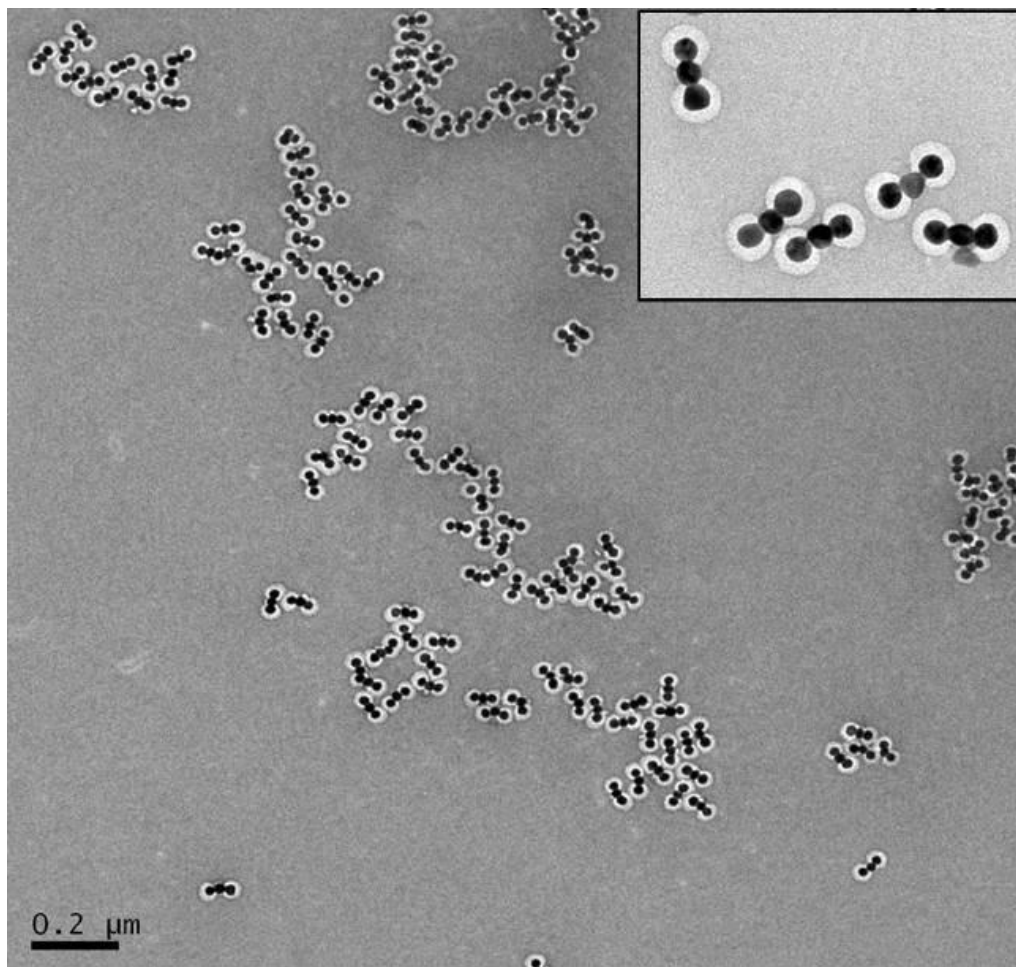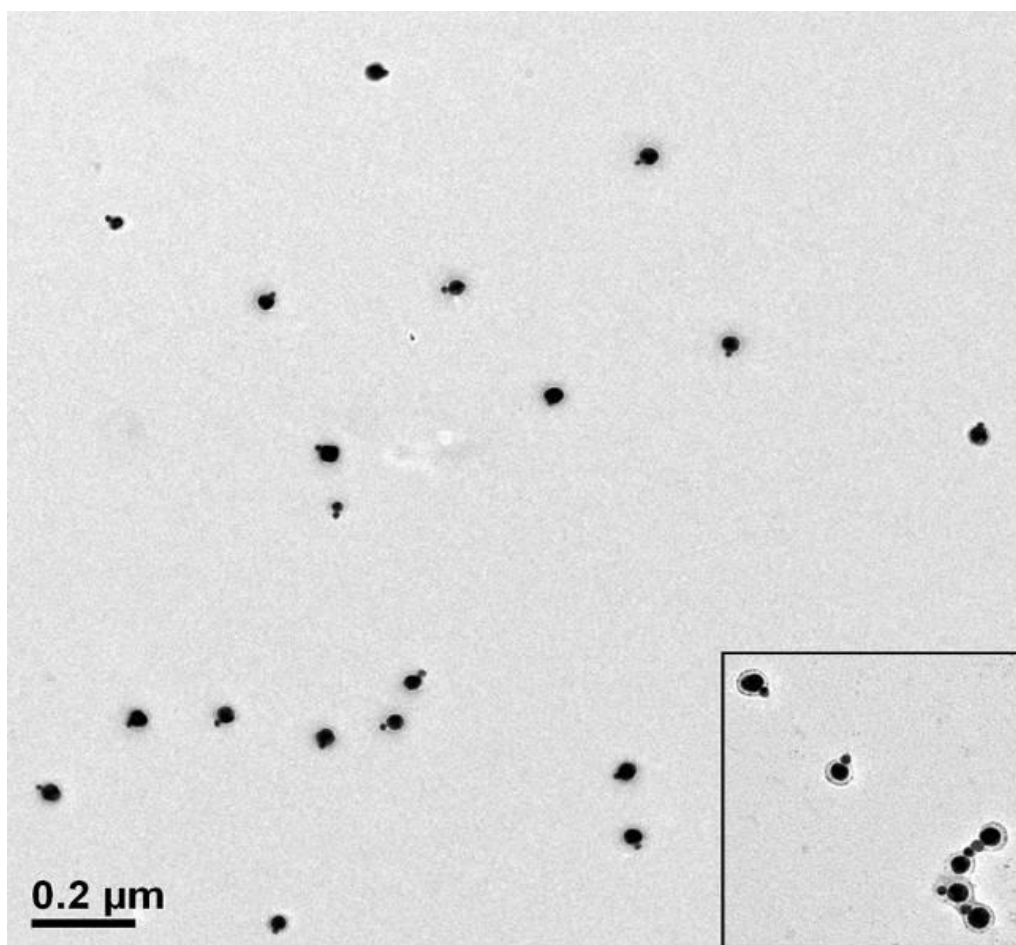
Figure 2-21. Large-area view of the purified AB@PSPAA by using the Ag growth/etching separation method (d_A = 18 nm, d_B = 36 nm); inset: high magnification.

So far, in our nanoreactions, the size of the B-NPs is always larger than or equal to the size of A-NPs. This setup effectively utilized the charge repulsion between B-NPs for the stoichiometry control. Reacting large A-NPs (36 nm) with small B-NPs (18 nm) is also feasible. But the stoichiometry of the resulting nanoclusters was less uniform, most likely due to the fact that the repulsion between B-NPs was not far enough to affect all neighbors on the large surface of A-NPs. Nevertheless, controlling the ionic strength still by and large control the stoichiometry of the AB_n nanoclusters.
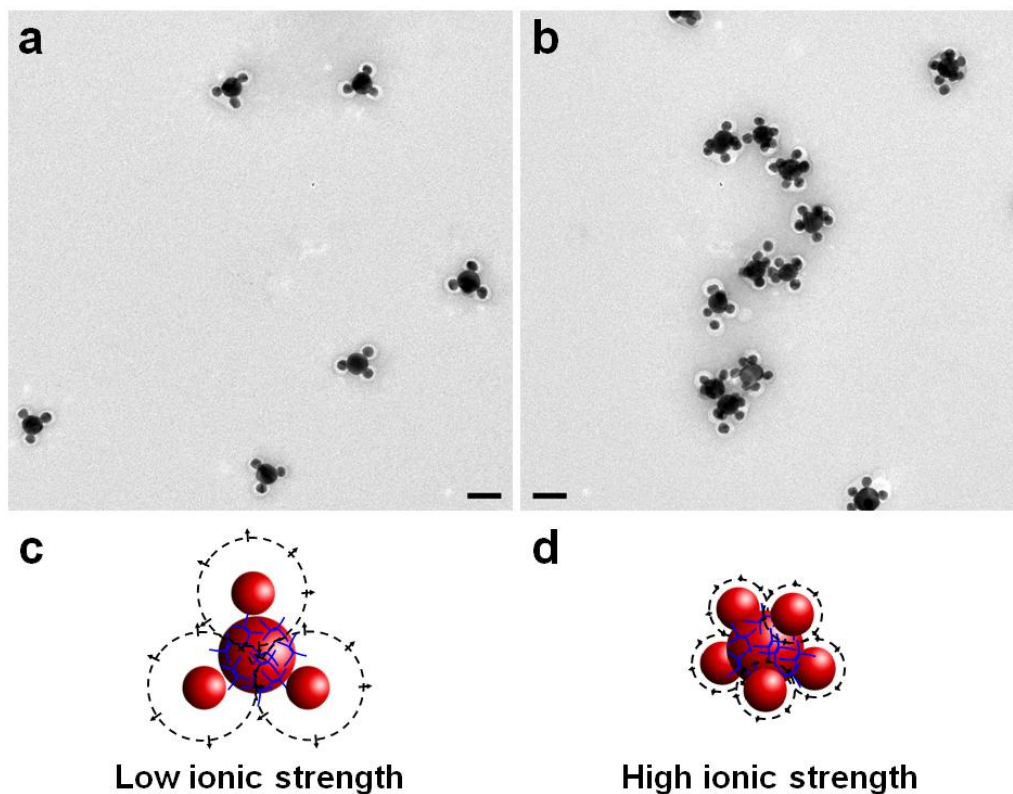
Figure 2-22. (a) TEM image of AB_n@PSPAA ($n \leq 4$) nanoclusters and remaining B@PSPAA. These nanoclusters were assembled in low ionic strength aqueous solution. ($d_A = 36$ nm, $d_B = 18$ nm, I = 0.594 mM). (b) TEM image of AB_n@PSPAA ($n \geq 4$) nanoclusters and remaining B@PSPAA. These nanoclusters were assembled in high ionic strength aqueous solution. ($d_A = 36$ nm, $d_B = 18$ nm, I = 3.30 mM). (c, d) Schematic diagrams showing the creation of AB_n@PSPAA ($n \leq 4$ and ≥ 4) nanoclusters by tuning the charge repulsion between the B-NPs; larger radius of the dashed circle means stronger repulsion.

2.5 Complex Nanostructure Based on This Nanoreaction System

2.5.1 Nano-lens Model Nanostructure Formation

One understandable advantage of our nanoreaction system is the usage for multistep assembly of nanoobjects. Nano-lens, one kind of controlled nanoparticle aggregates with giant local optical fields, has been well studied by using simulation methods for many years.[52-54] However, till now, there is still

no effective method to synthesize this kind of nano-optics. Using our nanoreaction strategy, this kind of structures may be achieved easily by treating the medium size A-NPs with the large and small size B-NPs. When the NPs surfaces or the gaps are functionalized with Raman-active molecule,[8, 12, 55-58] the optical properties of the nano-optics could be studied by single particle or ensample measuring.
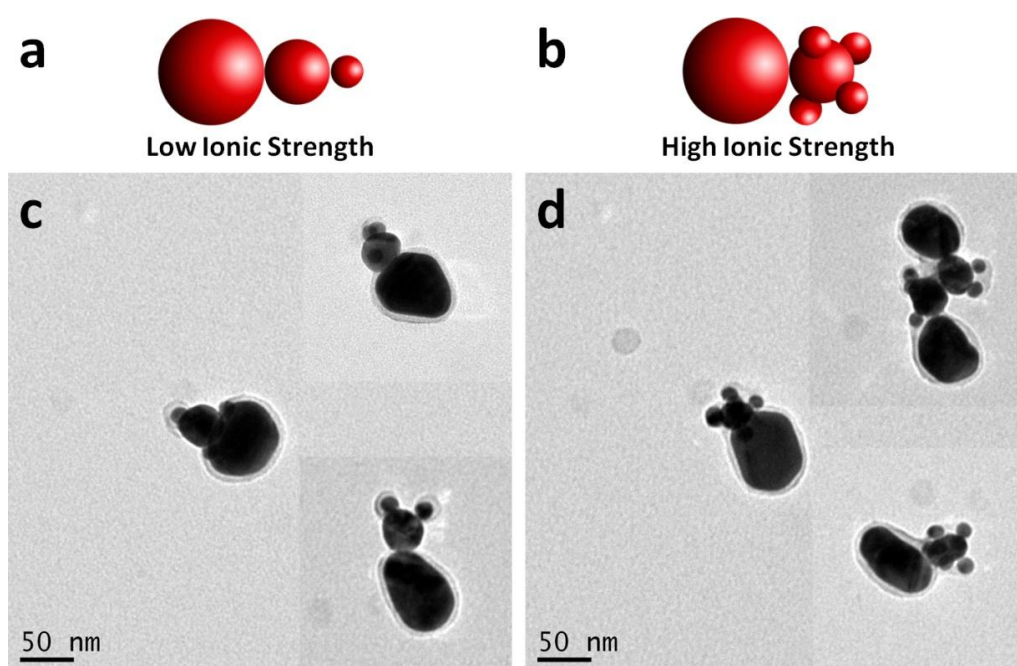
Figure 2-23 (a, b) Schematic diagrams showing the formation of BAB'$_n$@PSPAA ($n \leq 2$ and ≥ 3) nanoclusters by tuning the charge repulsion between the B (B')-NPs; (c, d) TEM image of BAB'$_n$@PSPAA nanoclusters. These nanoclusters were assembled in different ionic strength aqueous solution. ($d_A = 36$ nm, $d_B = 60$ nm, $d_{B'} = 18$ nm)

As we discussed before, when the A-NPs react with large B-NPs at low ionic strength, the heterodimer structure can be obtained (Figure 2-8c, Figure 2-9, and Figure 2-21). So it is reasonable that B'AB like structure can be synthesized by incubating smaller B'-NPs with this AB heterodimer products. Figure 2-23 shows the formation schemes and TEM images of the

BAB'$_n$@PSPAA nanoclusters. Firstly, A-NPs (d_A = 36 nm) were synthesized, purified and redispersed in DMF as normal procedure. Then large B-NPs (d_B = 60 nm) were added before the addition of B'-NPs ($d_{B'}$ = 18 nm). The ionic strength of the B-NPs and B'-NPs aqueous solution was fine tuned: at low ionic strength, no more than two B'-NPs attached to each A-NP, which was stuck by one B-NP, thus the linear BAB' hetero-trimer structure was formed. Because this kind of hetero-trimer was easy to be synthesized and further functionalized in colloidal solution, it should be one excellent nano-lens model for the theoretic study or practical application; when the ionic strength increased, several B'-NPs were close to each A-NP, thus more than three B'-NPs were docked, and complex hetero nanocomposites were formed.

2.5.2 Toothed Club Nanostructure Formation
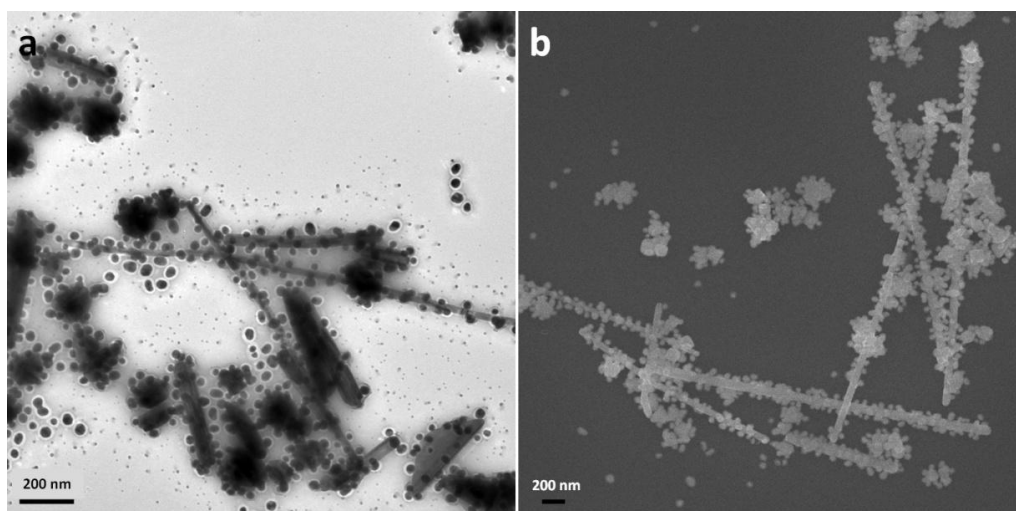
Figure 2-24 TEM and SEM images of the toothed club nanostructure fabricated by AgNWs and AuNPs.

When the AgNWs were chosen as A-NPs and reacted with small B-NPs (d_B = 36 nm), toothed club nanostructures were obtained (Figure 2-24). From the

83

TEM and SEM images, we found that the B-NPs were attached on the NWs uniformly owing to the large charge repulsion. It can be predicted that by fine tuning the ionic strength of the reaction solution, the density of small NPs can be controlled. This toothed club structures is also one useful physical model to study the electromagnetic field as well as the SPR properties.[59]

2.6 Spectra Characterization of the AB_n Nanoclusters.

Figure 2-25a shows the normalized UV-Vis spectra of B@PSPAA and AB_n@PSPAA (n = 2, 3 and 4) with 18 nm A- and B-NPs. The spectrum of AB@PSPAA ($d_A = d_B = 18$ nm) is not shown owing to the low purity. The 530 nm peak of AB_2 could be assigned to the transverse mode of the LSPR. A second LSPR absorption at 620 nm was observed for AB_2@PSPAA, which can be attributed to the longitudinal resonance of the linear BAB cluster.[31] However, the spectra of AB_3@PSPAA (64.1% purity) and AB_4@PSPAA (67.5% purity) were very similar to that of AB_2@PSPAA and no extra absorption band was observed.

To investigate this phenomenon, we calculated the extinction spectra of the AB_n nanoclusters using discrete dipole approximation.[30, 60] The results agree well with our observations. In particular, the LSPR positions of AB_3 are almost the same as those of AB_2 (Figure 2-25b). This suggests that the four-body coupling in AB_3 structure is weaker than the three-body coupling in the same system. In addition, the extinction spectra of AB_2 nanoclusters are similar when the $\angle$ BAB angle varies from 120 to 180 degree (Figure 2-25c). These results

show that the extinction spectra of AB_2 are not sensitive to the structural deformation. This phenomenon actually has been previously observed in the absorption spectra of trimers and quadrumers of 21 nm silver spheres by Nordlander and co-workers.[61] Therefore, our experimental observations are in agreement with theoretic predictions.
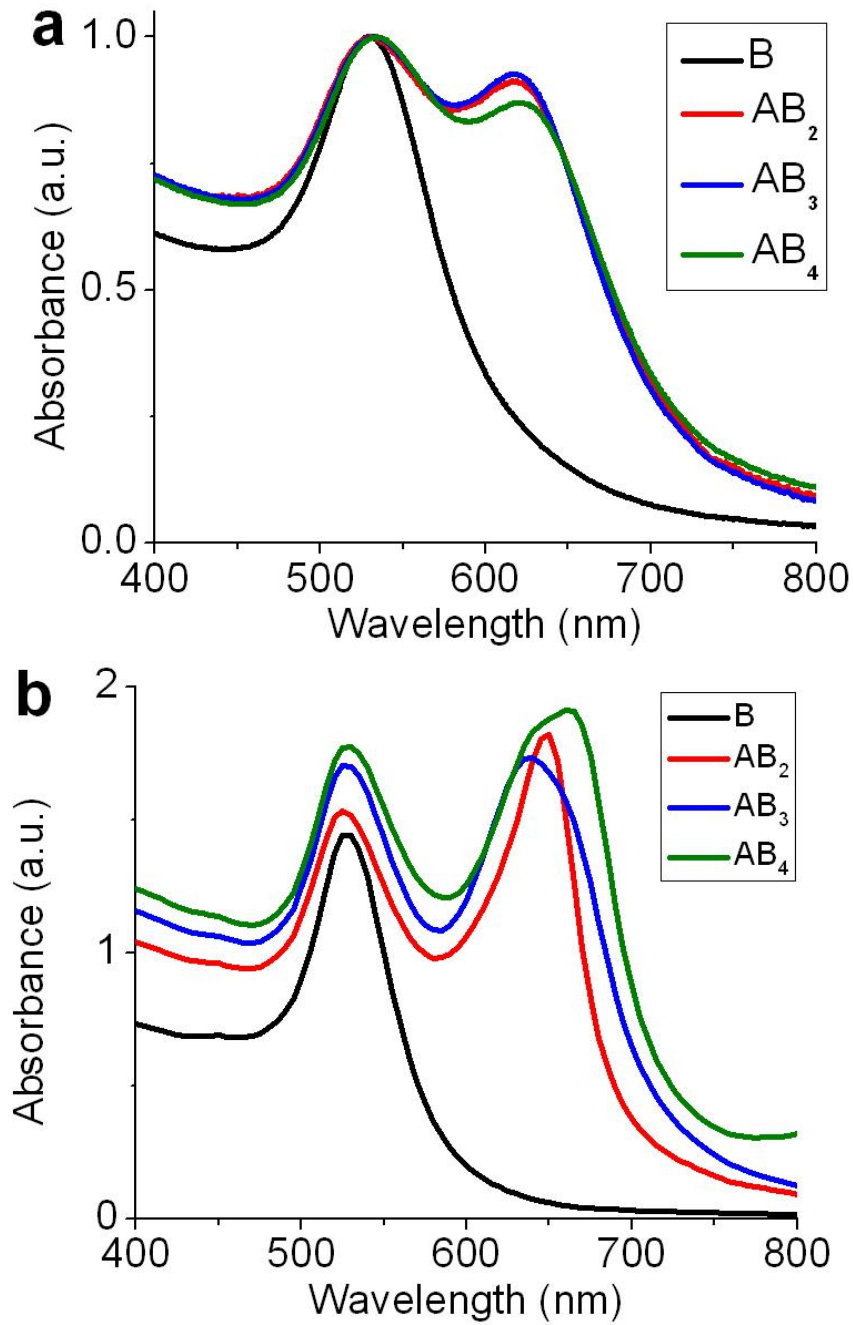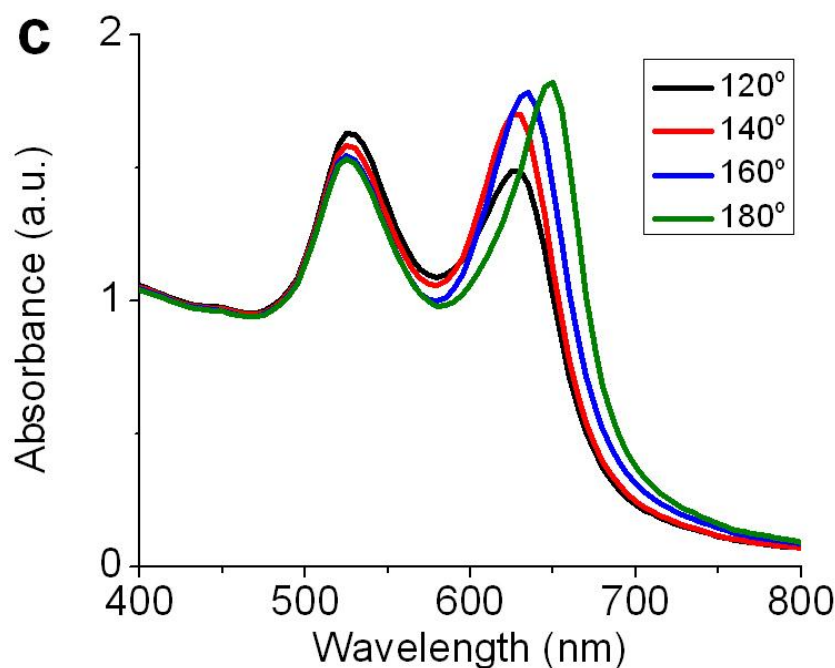
Figure 2-25. (a) UV-Vis spectra of B@PSPAA and AB_n@PSPAA (n = 2, 3 and 4, $d_A = d_B = 18$ nm); (b) Calculated extinction spectra of B, linear AB_2, equilateral triangular AB_3, and regular tetrahedral AB_4 ($d_A = d_B = 18$ nm, all gaps between AuNPs are 1 nm); and (c) Calculated extinction spectra of AB_2 with varying $\angle BAB$ angles.

2.7 Conclusion

We demonstrated a systems approach to colloidal assembly of Au nanoparticles. By understanding and directing the reaction kinetics, the stoichiometry of the product nanoclusters was controlled simply by modulating the ionic strength of the reaction media. Colloidal synthesis is generally scalable and easy to control; and the polymer protection led to the recovery of pure nanoclusters with long-term stability. Hence, this initial platform of nanoparticle-based reactions permits further development of synthetic methodologies and allows insights into the interactions of nanoparticles. Specifically, charge repulsion has been identified as the major factor in the stoichiometry control in our system, while charge or magnetic dipoles were

ruled out. The nanoreactions were found to be kinetically controlled: the reaction proceeds at high ionic strength but strong charge repulsion at low ionic strength gives rise to an insurmountable barrier that diminishes effective collision.

2.8 Bibliography

[1] Grzelczak, M., Perez-Juste, J., Mulvaney, P., and Liz-Marzan, L. M., Shape Control in Gold Nanoparticle Synthesis. *Chem. Soc. Rev.*, **37**, 1783 (2008).

[2] Lu, X. M., Rycenga, M., Skrabalak, S. E., Wiley, B., and Xia, Y. N., Chemical Synthesis of Novel Plasmonic Nanoparticles. *Annu. Rev. Phys. Chem.*, **60**, 167 (2009).

[3] Peng, X. G., Manna, L., Yang, W. D., Wickham, J., Scher, E., Kadavanich, A., and Alivisatos, A. P., Shape Control of Cdse Nanocrystals. *Nature*, **404**, 59 (2000).

[4] Murray, C. B., Norris, D. J., and Bawendi, M. G., Synthesis and Characterization of Nearly Monodisperse Cde (E = S, Se, Te) Semiconductor Nanocrystallites. *J. Am. Chem. Soc.*, **115**, 8706 (1993).

[5] Wang, F., Han, Y., Lim, C. S., Lu, Y. H., Wang, J., Xu, J., Chen, H. Y., Zhang, C., Hong, M. H., and Liu, X. G., Simultaneous Phase and Size Control of Upconversion Nanocrystals through Lanthanide Doping. *Nature*, **463**, 1061 (2010).

[6] Li, W. Y., Camargo, P. H. C., Lu, X. M., and Xia, Y. N., Dimers of Silver Nanospheres: Facile Synthesis and Their Use as Hot Spots for Surface-Enhanced Raman Scattering. *Nano Lett.*, **9**, 485 (2009).

[7] Wang, X. J., Li, G. P., Chen, T., Yang, M. X., Zhang, Z., Wu, T., and Chen, H. Y., Polymer-Encapsulated Gold-Nanoparticle Dimers: Facile Preparation and Catalytical Application in Guided Growth of Dimeric Zno-Nanowires. *Nano Lett.*, **8**, 2643 (2008).

[8] Chen, G., Wang, Y., Yang, M. X., Xu, J., Goh, S. J., Pan, M., and Chen, H. Y., Measuring Ensemble-Averaged Surface-Enhanced Raman Scattering in the Hotspots of Colloidal Nanoparticle Dimers and Trimers. *J. Am. Chem.*

Soc., **132**, 3644 (2010).

[9] Brousseau, L. C., Novak, J. P., Marinakos, S. M., and Feldheim, D. L., Assembly of Phenylacetylene-Bridged Gold Nanocluster Dimers and Trimers. *Adv. Mater.*, **11**, 447 (1999).

[10] Dadosh, T., Gordin, Y., Krahne, R., Khivrich, I., Mahalu, D., Frydman, V., Sperling, J., Yacoby, A., and Bar-Joseph, I., Measurement of the Conductance of Single Conjugated Molecules. *Nature*, **436**, 677 (2005).

[11] Lee, J. H., Wernette, D. P., Yigit, M. V., Liu, J., Wang, Z., and Lu, Y., Site-Specific Control of Distances between Gold Nanoparticles Using Phosphorothioate Anchors on DNA and a Short Bifunctional Molecular Fastener. *Angew. Chem., Int. Ed.*, **46**, 9006 (2007).

[12] Chen, T., Yang, M. X., Wang, X. J., Tan, L. H., and Chen, H. Y., Controlled Assembly of Eccentrically Encapsulated Gold Nanoparticles. *J. Am. Chem. Soc.*, **130**, 11858 (2008).

[13] Alivisatos, A. P., Johnsson, K. P., Peng, X. G., Wilson, T. E., Loweth, C. J., Bruchez, M. P., and Schultz, P. G., Organization of 'Nanocrystal Molecules' Using DNA. *Nature*, **382**, 609 (1996).

[14] Sung, K. M., Mosley, D. W., Peelle, B. R., Zhang, S. G., and Jacobson, J. M., Synthesis of Monofunctionalized Gold Nanoparticles by Fmoc Solid-Phase Reactions. *J. Am. Chem. Soc.*, **126**, 5064 (2004).

[15] DeVries, G. A., Brunnbauer, M., Hu, Y., Jackson, A. M., Long, B., Neltner, B. T., Uzun, O., Wunsch, B. H., and Stellacci, F., Divalent Metal Nanoparticles. *Science*, **315**, 358 (2007).

[16] Nakata, K., Hu, Y., Uzun, O., Bakr, O., and Stellacci, F., Chains of Superparamagnetic Nanoplarticles. *Adv. Mater.*, **20**, 4294 (2008).

[17] Loweth, C. J., Caldwell, W. B., Peng, X. G., Alivisatos, A. P., and Schultz, P. G., DNA-Based Assembly of Gold Nanocrystals. *Angew. Chem., Int. Ed.*, **38**, 1808 (1999).

[18] Xu, X. Y., Rosi, N. L., Wang, Y. H., Huo, F. W., and Mirkin, C. A., Asymmetric Functionalization of Gold Nanoparticles with Oligonucleotides. *J. Am. Chem. Soc.*, **128**, 9286 (2006).

[19] Sardar, R., Heap, T. B., and Shumaker-Parry, J. S., Versatile Solid Phase Synthesis of Gold Nanoparticle Dimers Using an Asymmetric Functionalization Approach. *J. Am. Chem. Soc.*, **129**, 5356 (2007).

[20] Mastroianni, A. J., Claridge, S. A., and Alivisatos, A. P., Pyramidal and Chiral Groupings of Gold Nanocrystals Assembled Using DNA Scaffolds. *J. Am. Chem. Soc.*, **131**, 8455 (2009).

[21] Maye, M. M., Nykypanchuk, D., Cuisinier, M., van der Lelie, D., and Gang, O., Stepwise Surface Encoding for High-Throughput Assembly of Nanoclusters. *Nat. Mater.*, **8**, 388 (2009).

[22] Maneeprakorn, W., Malik, M. A., and O'Brien, P., Developing Chemical Strategies for the Assembly of Nanoparticles into Mesoscopic Objects. *J. Am. Chem. Soc.*, **132**, 1780 (2010).

[23] Yang, M. X., Chen, T., Lau, W. S., Wang, Y., Tang, Q. H., Yang, Y. H., and Chen, H. Y., Development of Polymer-Encapsulated Metal Nanopartictes as Surface-Enhanced Raman Scattering Probes. *Small*, **5**, 198 (2009).

[24] Chen, G., Wang, Y., Tan, L. H., Yang, M. X., Tan, L. S., Chen, Y., and Chen, H. Y., High-Purity Separation of Gold Nanoparticle Dimers and Trimers. *J. Am. Chem. Soc.*, **131**, 4218 (2009).

[25] Frens, G., Controlled Nucleation for Regulation of Particle-Size in Monodisperse Gold Suspensions. *Nature Phys. Sci.*, **241**, 20 (1973).

[26] Brown, K. R., Walter, D. G., and Natan, M. J., Seeding of Colloidal Au Nanoparticle Solutions. 2. Improved Control of Particle Size and Shape. *Chem. Mater.*, **12**, 306 (2000).

[27] Chen, H. Y., Abraham, S., Mendenhall, J., Delamarre, S. C., Smith, K., Kim, I., and Batt, C. A., Encapsulation of Single Small Gold Nanoparticles by Diblock Copolymers. *ChemPhysChem*, **9**, 388 (2008).

[28] Templeton, A. C., Wuelfing, W. P., and Murray, R. W., Monolayer-Protected Cluster Molecules. *Acc. Chem. Res.*, **33**, 27 (2000).

[29] Xing, S. X., Tan, L. H., Chen, T., Yang, Y. H., and Chen, H. Y., Facile Fabrication of Triple-Layer (Au@Ag)@Polypyrrole Core-Shell and (Au@H2o)@Polypyrrole Yolk-Shell Nanostructures. *Chem. Commun.*, 1653 (2009).

[30] Skrabalak, S. E., Chen, J. Y., Sun, Y. G., Lu, X. M., Au, L., Cobley, C. M., and Xia, Y. N., Gold Nanocages: Synthesis, Properties, and Applications. *Acc. Chem. Res.*, **41**, 1587 (2008).

[31] Link, S., Mohamed, M. B., and El-Sayed, M. A., Simulation of the Optical Absorption Spectra of Gold Nanorods as a Function of Their Aspect Ratio and the Effect of the Medium Dielectric Constant. *J. Phys. Chem. B*, **103**, 3073 (1999).

[32] Derjaguin, B., Analysis of Friction and Adhesion Iv the Theory of the Adhesion of Small Particles. *Kolloid-Zeitschrift*, **69**, 155 (1934).

[33] Derjaguin, B., On the Repulsive Forces between Charged Colloid Particles and on the Theory of Slow Coagulation and Stability of Lyophobe Sols.

Trans. Faraday Soc., **35**, 0203 (1940).

[34] Bell, G. M., Levine, S., and McCartney, L. N., Approximate Methods of Determining the Double-Layer Free Energy of Interaction between Two Charged Colloidal Spheres. *J. Colloid Interface Sci.*, **33**, 335 (1970).

[35] Aizenberg, J., Braun, P. V., and Wiltzius, P., Patterned Colloidal Deposition Controlled by Electrostatic and Capillary Forces. *Phys. Rev. Lett.*, **84**, 2997 (2000).

[36] Adamczyk, Z., Jaszczolt, K., Michna, A., Zembala, M., and Barbasz, J., *Particle Deposition as a Tool for Studying Hetero-Interactions*, in *Colloid Stabilizty: The Role of Surface Forces, Part Ii*, T.F. Tadros, Editor. 2007, WILEY: Weinheim. p. 250.

[37] Zhang, H., Fung, K.-H., Hartmann, J. r., Chan, C. T., and Wang, D., Controlled Chainlike Agglomeration of Charged Gold Nanoparticles Via a Deliberate Interaction Balance. *J. Phys. Chem. C*, **112**, 16830 (2008).

[38] Zhang, H. and Wang, D. Y., Controlling the Growth of Charged-Nanoparticle Chains through Interparticle Electrostatic Repulsion. *Angew. Chem., Int. Ed.*, **47**, 3984 (2008).

[39] Yang, M., Chen, G., Zhao, Y., Silber, G., Wang, Y., Xing, S., Han, Y., and Chen, H., Mechanistic Investigation into the Spontaneous Linear Assembly of Gold Nanospheres. *Phys. Chem. Chem. Phys.*, **12**, 11850 (2010).

[40] Kang, Y. J. and Taton, T. A., Core/Shell Gold Nanoparticles by Self-Assembly and Crosslinking of Micellar, Block-Copolymer Shells. *Angew. Chem., Int. Ed.*, **44**, 409 (2005).

[41] Crespo, P., Litran, R., Rojas, T. C., Multigner, M., de la Fuente, J. M., Sanchez-Lopez, J. C., Garcia, M. A., Hernando, A., Penades, S., and Fernandez, A., Permanent Magnetism, Magnetic Anisotropy, and Hysteresis of Thiol-Capped Gold Nanoparticles. *Phys. Rev. Lett.*, **93**, 087204 (2004).

[42] Xing, S. X., Tan, L. H., Yang, M. X., Pan, M., Lv, Y. B., Tang, Q. H., Yang, Y. H., and Chen, H. Y., Highly Controlled Core/Shell Structures: Tunable Conductive Polymer Shells on Gold Nanoparticles and Nanochains. *J. Mater. Chem.*, **19**, 3286 (2009).

[43] Fu, A. H., Micheel, C. M., Cha, J., Chang, H., Yang, H., and Alivisatos, A. P., Discrete Nanostructures of Quantum Dots/Au with DNA. *J. Am. Chem. Soc.*, **126**, 10832 (2004).

[44] Walther, A. and Muller, A. H. E., Janus Particles. *Soft Matter*, **4**, 663 (2008).

[45] Qiu, P. H. and Mao, C. B., Viscosity Gradient as a Novel Mechanism for

the Centrifugation-Based Separation of Nanoparticles. *Adv. Mater.*, **23**, 4880 (2011).

[46] Steinigeweg, D., Schutz, M., Salehi, M., and Schlucker, S., Fast and Cost-Effective Purification of Gold Nanoparticles in the 20-250 Nm Size Range by Continuous Density Gradient Centrifugation. *Small*, **7**, 2443 (2011).

[47] Xiong, B., Cheng, J., Qiao, Y. X., Zhou, R., He, Y., and Yeung, E. S., Separation of Nanorods by Density Gradient Centrifugation. *Journal of Chromatography A*, **1218**, 3823 (2011).

[48] Wang, Y., Chen, G., Yang, M., Silber, G., Xing, S., Tan, L. H., Wang, F., Feng, Y., Liu, X., Li, S., and Chen, H., A Systems Approach Towards the Stoichiometry-Controlled Hetero-Assembly of Nanoparticles. *Nature Communications*, **1**, 87 (2010).

[49] Sun, X., Tabakman, S. M., Seo, W.-S., Zhang, L., Zhang, G., Sherlock, S., Bai, L., and Dai, H., Separation of Nanoparticles in a Density Gradient: Feco@C and Gold Nanocrystals. *Angew, Chem., Int. Ed.*, **48**, 939 (2009).

[50] Xu, J., Wang, H., Liu, C. C., Yang, Y. M., Chen, T., Wang, Y. W., Wang, F., Liu, X. G., Xing, B. G., and Chen, H. Y., Mechanical Nanosprings: Induced Coiling and Uncoiling of Ultrathin Au Nanowires. *J. Am. Chem. Soc.*, **132**, 11920 (2010).

[51] Kato, Y., Niidome, Y., and Nakashima, N., Efficient Separation of (6,5) Single-Walled Carbon Nanotubes Using a "Nanometal Sinker". *Angew. Chem., Int. Ed.*, **48**, 5435 (2009).

[52] Li, K. R., Stockman, M. I., and Bergman, D. J., Self-Similar Chain of Metal Nanospheres as an Efficient Nanolens. *Phys. Rev. Lett.*, **91**, 227402 (2003).

[53] Stockman, M. I., Nanofocusing of Optical Energy in Tapered Plasmonic Waveguides. *Phys. Rev. Lett.*, **93**, 137404 (2004).

[54] Dai, J. H., Cajko, F., Tsukerman, I., and Stockman, M. I., Electrodynamic Effects in Plasmonic Nanolenses. *Physical Review B*, **77**, (2008).

[55] Chen, T., Wang, H., Chen, G., Wang, Y., Feng, Y. H., Teo, W. S., Wu, T., and Chen, H. Y., Hotspot-Induced Transformation of Surface-Enhanced Raman Scattering Fingerprints. *ACS Nano*, **4**, 3087 (2010).

[56] Feng, Y., Wang, Y., Wang, H., Chen, T., Tay, Y. Y., Yao, L., Yan, Q., Li, S., and Chen, H., Engineering "Hot" Nanoparticles for Surface-Enhanced Raman Scattering by Embedding Reporter Molecules in Metal Layers. *Small*, n/a (2011).

[57] Feng, Y., Xing, S., Xu, J., Wang, H., Lim, J. W., and Chen, H., Probing the Kinetics of Ligand Exchange on Colloidal Gold Nanoparticles by Surface-Enhanced Raman Scattering. *Dalton Trans.*, **39**, 349 (2010).

[58] Chen, T., Du, C., Tan, L. H., Shen, Z., and Chen, H., Site-Selective Localization of Analytes on Gold Nanorod Surface for Investigating Field Enhancement Distribution in Surface-Enhanced Raman Scattering. *Nanoscale*, **3**, 1575 (2011).

[59] Hutchison, J. A., Centeno, S. P., Odaka, H., Fukumura, H., Hofkens, J., and Uji-i, H., Subdiffraction Limited, Remote Excitation of Surface Enhanced Raman Scattering. *Nano Lett.*, **9**, 995 (2009).

[60] Zhang, J., Li, S. Z., Wu, J. S., Schatz, G. C., and Mirkin, C. A., Plasmon-Mediated Synthesis of Silver Triangular Bipyramids. *Angew. Chem., Int. Ed.*, **48**, 7787 (2009).

[61] Brandl, D. W., Mirin, N. A., and Nordlander, P., Plasmon Modes of Nanosphere Trimers and Quadrumers. *J. Phys. Chem. B*, **110**, 12302 (2006).

Chapter 3   Chiral Transformation: from Single Nanowire to Double Helix

3.1   Introduction

Chirality is a major theme in organic chemistry, but it has yet to be fully explored in nanoscience. Chiral nano-objects are of great importance for fabricating future nanodevices, as clearly demonstrated by macroscopic chiral components such as gears, springs, propellers and scissors. The asymmetric organization of the surface atoms or ligands on small (< 5 nm) nanoparticles (NPs) is useful for asymmetric catalysis,[1, 2] chiral separation,[3, 4] and novel optical properties.[5-11] For these applications, metallic nanostructures have clear advantages.

Great efforts have been devoted to reducing the high symmetry of NPs. In contrast to the syntheses of Janus (two-sided) NPs,[12] the available synthetic strategies for less symmetric chiral nano-objects are very limited. Most of the chiral nanostructures in the literature were fabricated using chemical vapor deposition (CVD).[13-15] Because of the high temperature growth on bulk substrates, they were typically large and non-metallic. In colloids, a popular approach was to use chiral biomolecules or polymers as templates for the

surface assembly of NPs.[5, 6, 8, 10, 11] Chiral NWs were also made in confined

environments.[16-19] But intrinsic chiral NWs were extremely rare.[20, 21]

To date, the majority of the reported nanostructures were of single

component,[22, 23] but this simplicity limits their structural variety. We are

interested in multi-component systems that offer new synthetic strategies and

novel architectures.[17, 18, 24-27] Of particular interest to us is the

environment-responsive shape transformation of nanostructures, which is of

critical importance for developing smart nanodevices. Previously, we showed

that the polymer shells on Au NWs[17] or carbon nanotubes[18] could be induced

to contract, coiling the embedded nanofilaments into ring structures. It was the

first system that can transform the entire population of colloidal nanostructures.

Here, we report a new system where an entire population of nanostructures

undergoes predictable shape transformation. Ultrathin Au-Ag alloy NWs are

first fabricated using a new method. Upon growth of an additional metal layer

(Pd, Pt, or Au), the NWs wind around themselves to form double helices

(93.5% yield for Pd). By systematic analysis of reaction conditions, we show

that the rate of metal deposition was a critical factor in inducing the winding of

NWs. The winding action probably originates from the chirality within the

as-synthesized Au-Ag alloy NWs, which likely have the

Boerdijk-Coxeter-Bernal (BCB) type twisted lattice.[21]

3.2 Materials and Methods

3.2.1 Materials

All chemical reagents were used as purchased without further purification. Hydrogen tetrachloroaurate(III) hydrate ($HAuCl_4 \cdot 3H_2O$), 99.9% (metal basis Au 49%), pyrrole (98%), aniline (99%), sodium dodecylsulfate (SDS, 99%), and ammonium persulfate (APS, $(NH_4)_2S_2O_8$, 98%) were purchased from Alfa Aesar; silver nitrate (99+%) and polyvinylpyrrolidone (PVP, M_w: 40,000) were purchased from Sigma Aldrich; 2-propanol (HPLC grade) and ethanol (analytical grade) were purchased from Fisher Scientific; all other chemicals were purchased from Aldrich. Deionized water (resistance > 18 $M\Omega \cdot cm^{-1}$) was used in all reactions. Copper specimen grids (300 meshes) with formvar/carbon support film (referred to as TEM grids in the text) were purchased from Beijing XXBR Technology Co, Ltd.

3.2.2 Methods

TEM images were collected from a JEM-1400 transmission electron microscope (JEOL) operated at 100 kV. High-resolution TEM was performed on an FEI Titan Cubed S-Twin transmission electron microscopy operated at 80 kV with image Cs corrector applied. High-resolution scanning transmission electron microscopy (STEM) and energy-dispersive X-ray spectroscopy (EDS) were performed on an FEI aberration-corrected Titan Cubed S-Twin transmission electron microscope operated at 200 kV. Probe Cs corrector was applied to get better spatial resolution. In a typical experiment, high-resolution

STEM imaging was conducted at a 2-us/pixel scanning rate with 70 um C2 aperture, spot size 9, a high-angle annular dark-filed (HAADF) detector, and 146 mm camera length. Under such conditions, a spatial resolution of ~1.0 Å was obtained. EDS spectra were collected with 150 μm C2 aperture, spot size 6, and 240 s collection time. SEM images were collected from a JEOL-6700F Scanning Electron Microscopy operated at 10/15 kV. UV–Visible spectra were collected on a Cary 100 UV-Vis spectrophotometer.

Preparation of TEM samples: TEM grids were treated with oxygen plasma in a Harrick plasma cleaner/sterilizer for 1 min to improve the surface hydrophilicity. The grid was placed face-down on a droplet of as-synthesized sample laid on a plastic Petri dish. A filter paper was used to wick off the excess solution on the TEM grid, which was then dried in air for 5 min. $(NH_4)_6Mo_7O_{24}$ was used as the negative stain in the TEM images of polypyrrole and polyaniline encapsulated double helices samples, so that the polymer shells appear white against the stained background.

Preparation of ultrathin Au-Ag alloy NWs: In 800 μL DMF solution, 100 μL PVP (500 mM in DMF), 20 μL HAuCl$_4$ (50 mM in DMF), 20 μL AgNO$_3$ (50 mM in H$_2$O) were added in the order given. Then, 100 μL ascorbic acid (400 mM in H$_2$O) was added into the mixture by vortex mixing. Finally, the solution was left undisturbed at room temperature for 10 days (the long time incubation is necessary). The ultrathin Au-Ag nanowires could be precipitated out by acetone, washed by H$_2$O to remove the DMF and PVP, and isolated by

centrifugation. The product can be re-dispersed in 1 mL H$_2$O without aggregation.

Deposition of metal (Pd, Au, Pt, or Ag) on the Au-Ag NWs: Metallic double helices could be obtained by growing a thin metal layer on the surface of the Au-AgNWs. Taking Pd layer growth for instance, typically, into 640 μL of aqueous ascorbic acid solution (1.875 mM), 50 μL of as-synthesized Au-Ag NWs solution was added. The mixture was gently shaken, followed by addition of 60 μL of aqueous H$_2$PdCl$_4$ solution (1 mM). The final mixture was left undisturbed at room temperature for 2 h to complete the Pd growth reaction.

Preparation of (Au-Ag)@Pd double helices with NaBH$_4$ as the reducing agent: The conditions used were similar to the above method using ascorbic acid, except that NaBH$_4$ (with a same concentration) dissolved in ice/water mixture was used to replace ascorbic acid.

Preparation of (Au-Ag)@M (M = Pd, Au, Pt, or Ag) double helices using pyrrole as the reducing agent:[24] Taking Pd layer growth for instance, typically, into 500 μL aqueous pyrrole solution (10 mM), 50 μL aqueous SDS solution (40 mM), and 50 μL of the as-synthesized Au-Ag NWs solution were added in the order given. The solution was gently shaken, followed by addition of 60 μL of aqueous H$_2$PdCl$_4$ solution (1 mM). The mixture was left undisturbed at room temperature overnight (about 10 h) to complete the Pd growth reaction.

Preparation of ultrathin (Au-Ag)@M (M = Pd, Au, Pt, or Ag) double helices using aniline as the reducing agent:[25] The conditions used were similar to the pyrrole reduction method above, except that aniline of the same concentration was used as the reducing agent to replace pyrrole.

Polypyrrole encapsulation of the Au-Ag NWs:[27] Typically, to 200 μL of aqueous pyrrole solution (20 mM), 50 μL of aqueous SDS solution (40 mM), and 50 μL of the as-synthesized Au-Ag nanowires solution were added in the order given. The solution was vortexed for 5 s, followed by addition of 200 μL acidic APS solution (the final concentration of [APS]: 5 mM; [HCl]: 7.5 mM). After vortexing for 10 s, the reaction mixture was incubated at room temperature overnight.

SiO$_2$ encapsulation of the metal deposition induced double helices: The encapsulation was carried out by using Stöber method with modifications.[28-30] Typically, 1 mL 2-propanol was added into 440 uL synthesized double helices solution under vigorous stirring. 5 minute later, 0.8 uL TEOS was added followed by the addition of 35 uL of ammonia. The mixture was shaken gently. After 12 hrs reaction, the product was collected by centrifugation. The collected product was redispersed into the SiO$_2$ shell growth solution for the fully coating.

Determining the yields reported in the main text: The yields of different samples were determined from the surveys of figures in the supporting information, as well as additional TEM images of different samples. As shown

in Table 3-1, different samples were labelled by the reducing agents and the metal precursors.

Table 3-1 Determining the yields of double helices.

	Double helices	Unwound NWs	Total	Yield
Ascorbic acid-H_2PdCl_4[a]	230	16	246	93.5%
Ascorbic acid-H_2PdCl_4[b]	98	30	128	76.6%
Ascorbic acid-H_2PdCl_4[c]	100	11	111	90.1%
Ascorbic acid-$HAuCl_4$	9	76	85	10.6%
Ascorbic acid-K_2PtCl_4	129	27	156	82.7%
Pyrrole-$HAuCl_4$	91	12	103	88.3%
Aniline-$HAuCl_4$	88	10	98	89.8%
Pyrrole-H_2PdCl_4	104	10	114	91.2%

[a]As-synthesized Au-AgNWs were used for the Pd layer growth;

[b]Purified Au-AgNWs were dispersed in pure water, and used for the Pd layer growth;

[c]Purified Au-AgNWs were dispersed in DMF/water mixture (v/v = 1:13.7, or 0.88 M DMF), and used for the Pd layer growth;

3.3 Results and Discussion

3.3.1 Synthesis of Au-Ag NWs

The Au-Ag alloy NWs were synthesized by incubating $HAuCl_4$, $AgNO_3$ (Au/Ag mole ratio 1:1), ascorbic acid, and polyvinylpyrrolidone (PVP) in a DMF/water mixture (v/v = 7.7:1) at room temperature for 10 days. The product NWs exhibited a brown red color. To purify the NWs, they were precipitated by acetone, washed by water to remove the excess PVP, and finally isolated by centrifugation. From the transmission electron microscopy (TEM) images, the NWs have an averaged diameter of 2 nm and overall length of several microns.

They often have thicker tails of 4-10 nm in diameter and 70-200 nm in length. Energy dispersive X-ray spectroscopy (EDS) revealed that the central thin section was composed of 50.8% Au and 49.2% Ag (about 2:1 in atomic ratio, uniformly distributed), different from the tails (80.2% Au, 20.8% Ag) (Figure 3-2, Figure 3-3, and Figure 3-4). These water-soluble ultrathin NWs were similar in diameter to the hydrophobic ones synthesized in nonpolar solvents using oleylamine as the ligand.[21, 31-33] In polar solvent, there were only two known cases of ultrathin NWs.[30, 34] Like those in the literature, our ultrathin NWs were easily broken upon heating[17] or under TEM electron beam.[35]
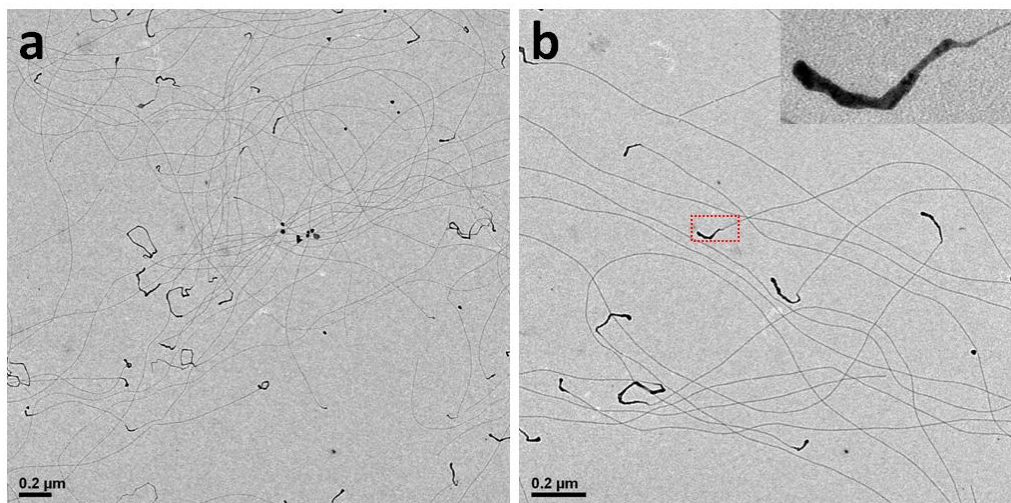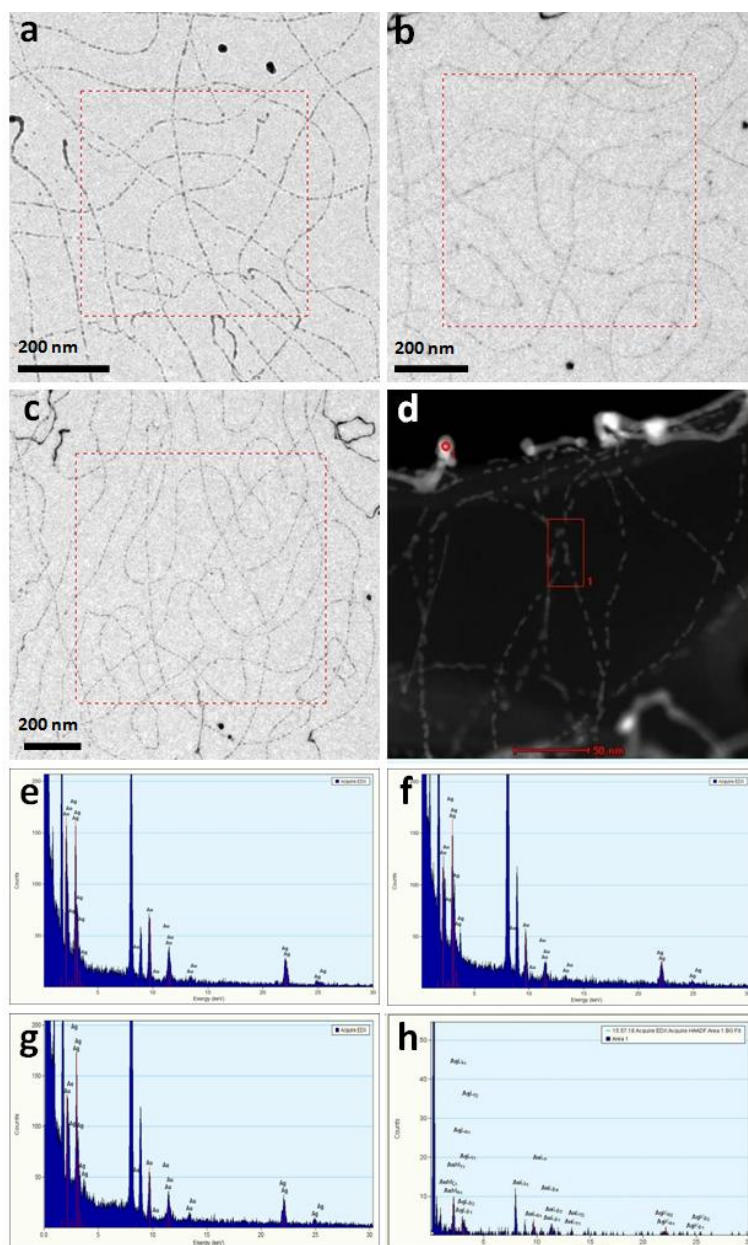

Figure 3-1 (a) A large-area TEM image of the as-synthesized Au-Ag NWs. (b) slightly higher magnification TEM image of the as-synthesized Au-Ag NWs (inset: one typical thick tail of the Au-Ag NW).

	a	b	c	d	Average
Ag (L)	50.40%	60.51%	50.28%	35.76%	**49.2%**
Au (L)	49.59%	39.48%	49.71%	64.23%	**50.8%**

The EDS analyses of the central thin sections of the as-synthesized Au-Ag nanowires: (a-d) the (S)TEM images with the selected area marked (d: the rectangle area); (e-h) the corresponding EDS spectra of the selected areas in a-d. The EDS analyses (atomic ratio) have been summarized in the above table.

Figure 3-2 EDS analysis of the central parts of the as-synthesized Au-AgNWs.
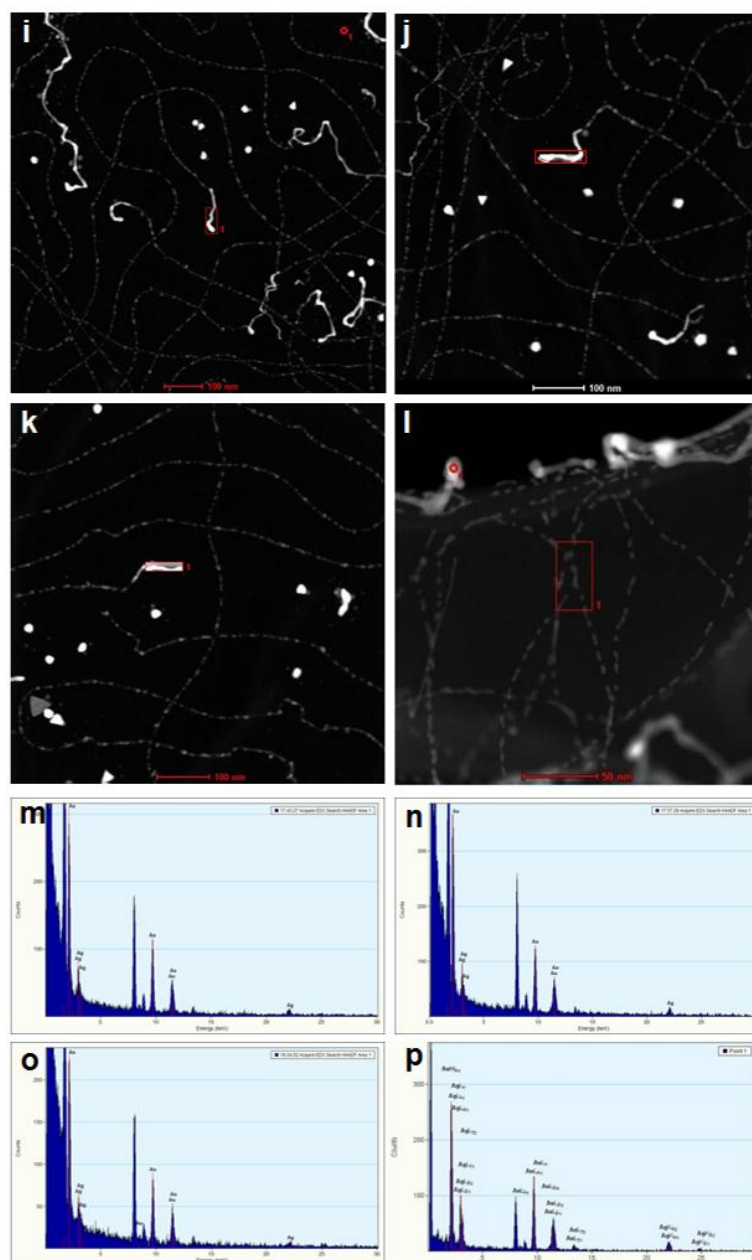
	i	j	k	l	Average
Ag (L)	17.95%	19.11%	21.13%	24.97%	**20.8%**
Au (L)	82.04%	80.88%	78.86%	75.02%	**80.2%**

The EDS analyses of the tails of the as-synthesized Au-Ag nanowires: (i-l) STEM images with the selected areas marked (l: the circle area); (m-p) the corresponding EDS spectra of the selected areas in i-l. The EDS analyses (atomic ratio) have been summarized in the above table.

Figure 3-3 EDS analysis of the large tail of the as-synthesized Au-AgNWs.
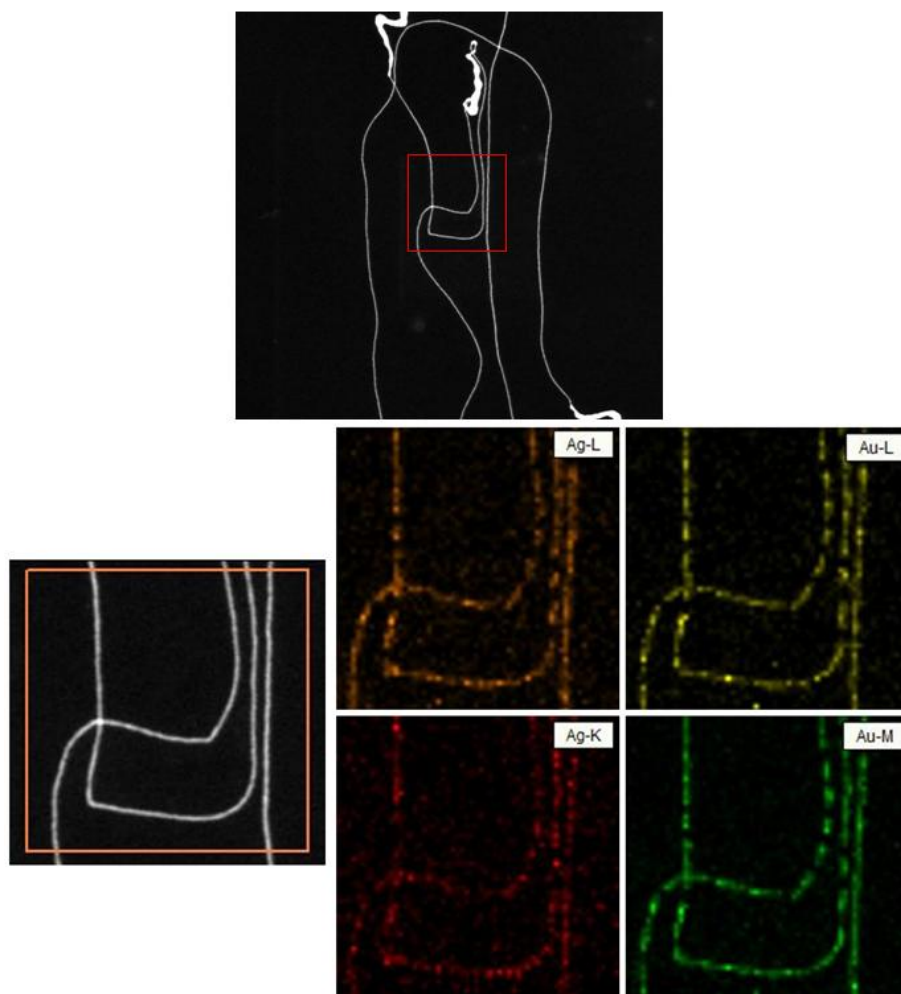
Figure 3-4 HAADF-STEM images of the Au-Ag NWs, and the corresponding element mapping of gold and silver. These two elements show homogeneously distribution, although the NWs were broken under the electron beam.

Although our 2 nm Au-Ag NWs were very fragile under the electron beam in high-resolution TEM (HRTEM), we managed to capture quite a number of images where the "fan"-like contrast was a recurring feature (Figure 3-5). These ordered patterns provide strong support against the possibility of random polycrystalline structure in the NWs.
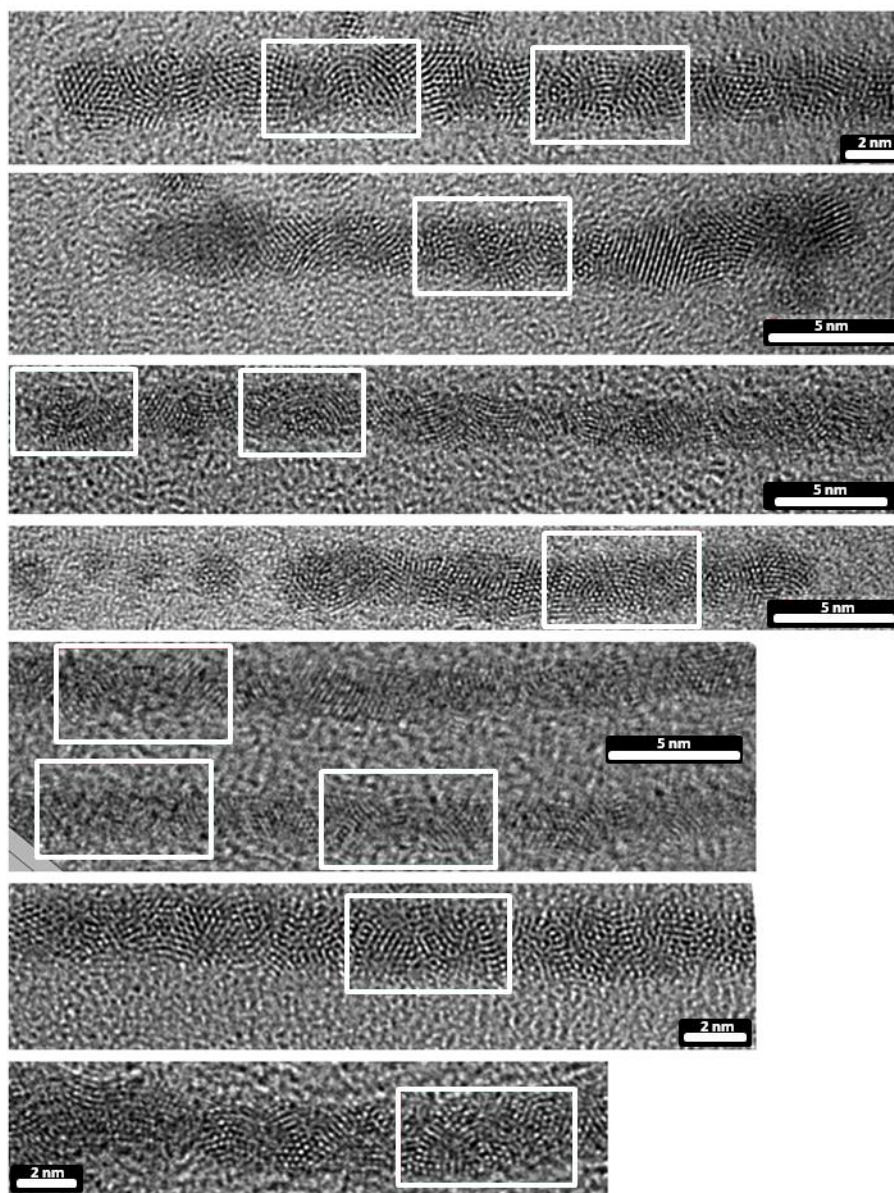
Figure 3-5 HRTEM images of the as-synthesized Au-Ag NWs; the "fan"-like contrast is highlighted in brackets.

A seminal work published very recently by José-Yacamán and coworkers showed that Au-Ag alloy can form ultrathin NWs (d = 2-5 nm, Au:Ag = 1:3) with BCB type twisted lattice (the twisting was not a result of strain).[21] The authors showed that 2 or more BCB type spirals can be roped together to give interpenetrated icosahedron segments, which give characteristic "fan"-like contrast under electron microscopy resembling that of half-spheres.[21, 36] On the

basis of their close resemblance to the "fan"-like contrast observed and simulated by José-Yacamán's team, it is likely that our Au-Ag NWs also have twisted lattice consisting of BCB type spirals.

3.3.2 Formation of Double Helices.

To our great interest, the alloy NWs formed double helices upon deposition of an additional metal layer at room temperature. The best results occurred with Pd deposition: Briefly, the as-synthesized Au-Ag NWs were added into an aqueous solution of ascorbic acid, followed by Pd precursor (aq. H_2PdCl_4). The mixture (DMF/water = 1:13.7, v/v) was gently mixed and then incubated for 1 h without stirring (to rule out the effect of swirling solution). The color of the solution changed from brown red to dark brown, indicating the reduction of Pd^{2+}. The samples were directly dried on TEM grids without purification, in order to gain accurate survey without losing nanostructures.

Figure 3-6 showed the double helix formation scheme and a typical TEM image of the resulting NWs after the Pd growth. The average diameter of the NWs increased to 3.5 nm (Figure 3-7), and the NWs tightly wound around themselves to give double helices. They were highly periodic, with uniform pitch length of 47 ± 7 nm and 2.7 nm gap separating the two intertwined NW sections. Only the helical region near the two ends (one with a U turn and one with two open strands) had irregular and longer pitch periods. To confirm the materials composition in the NWs, we carried out high-angle annular dark-field scanning TEM (HAADF-STEM) and EDS analyses (Figure 3-8). Each strand

of the double helix consisted of coaxial core-shell (Au-Ag)@Pd NWs, with Pd

forming a non-uniform coating.
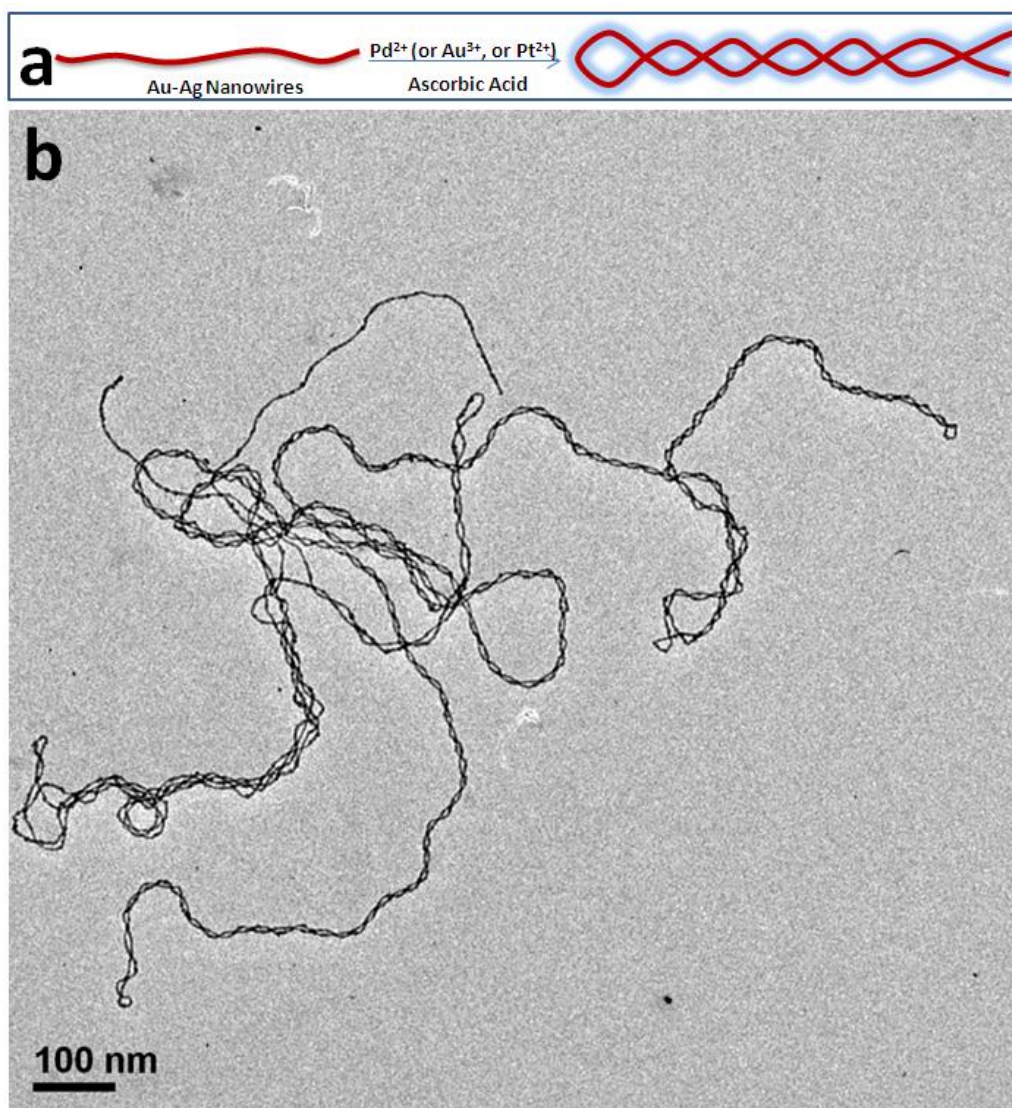
Figure 3-6 (a) Schematics illustrating the formation of double helix by growing a metal layer on Au-Ag alloy NW; (b) TEM image of a typical (Au-Ag)@Pd double helix.
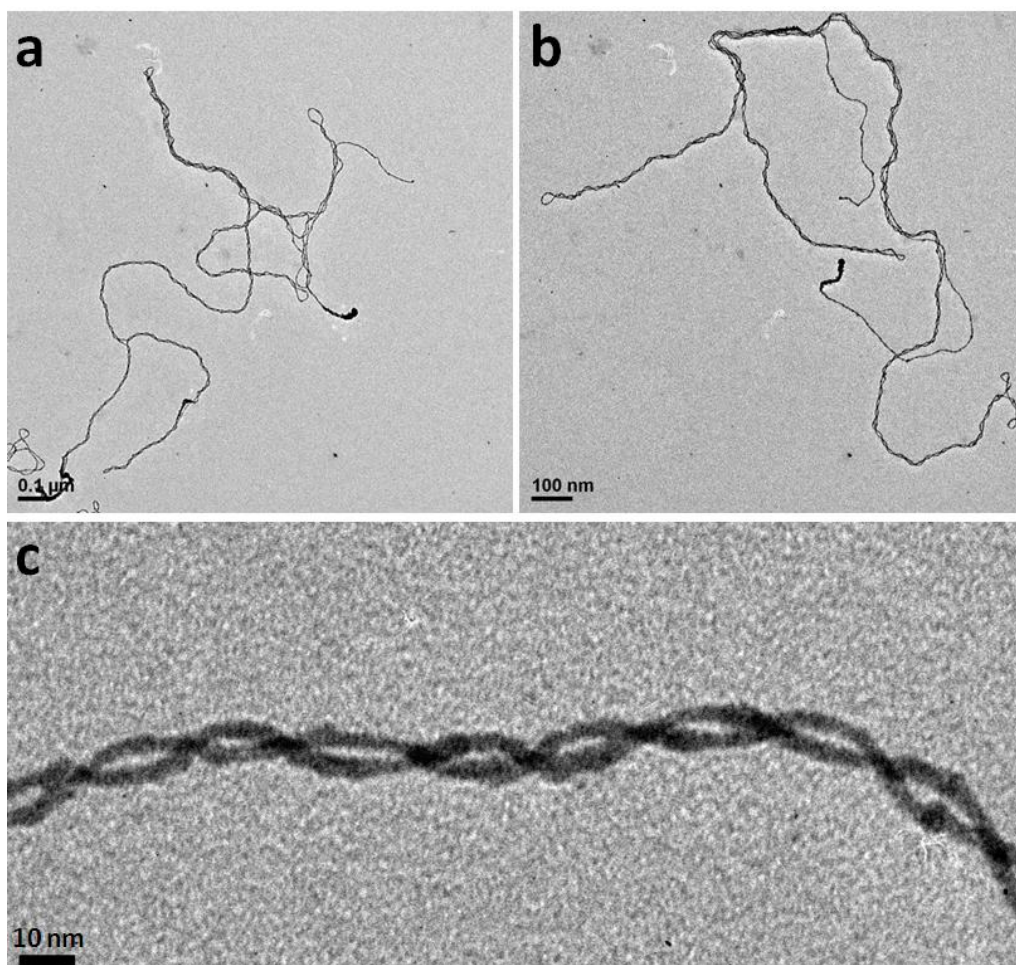
Figure 3-7 (a, b) Large-area and (c) high magnification TEM images of typical (Au-Ag)@Pd double helices obtained by ascorbic acid reducing H_2PdCl_4 (final concentration of H_2PdCl_4 is 80 μM.
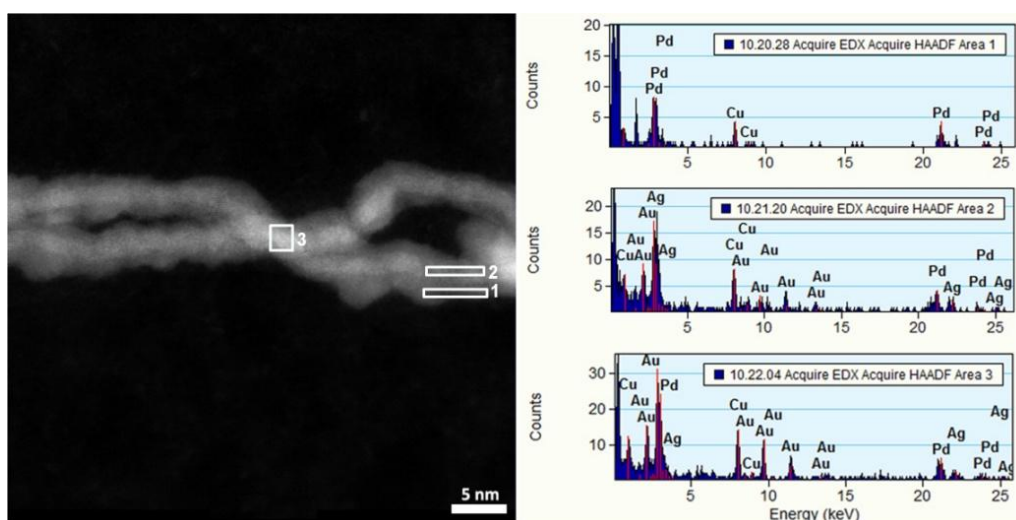
Figure 3-8 Magnified HAADF-STEM image of one typical (Au-Ag)@Pd double helix and the selected area EDS analyses at the bracketed regions.

Survey of the sample showed that most of the NWs transformed to double helices (93.5% out of 246 surveyed, Table 3-1). The rest 6.5% of NWs grew thicker without forming any helical region. As judged by the number of open strands (Figure 3-6b), the NWs did not intertwine with each other, and nearly all helices were derived from the self-winding of individual NWs. Some NWs formed multiple U-turn ends (Figure 3-6b, and Figure 3-9), and some even formed quadruple helices (Figure 3-9, Figure 3-10). The latter should result from continued twisting of a double helix, which is mechanically stronger than a single NW. Scanning electron microscopy (SEM) study revealed that both left- and right-handed helices existed in the sample (Figure 3-9). However, in each helix the chirality was *always* consistent. The multiple U-turn ends in Figure 3-9b showed the same winding direction.
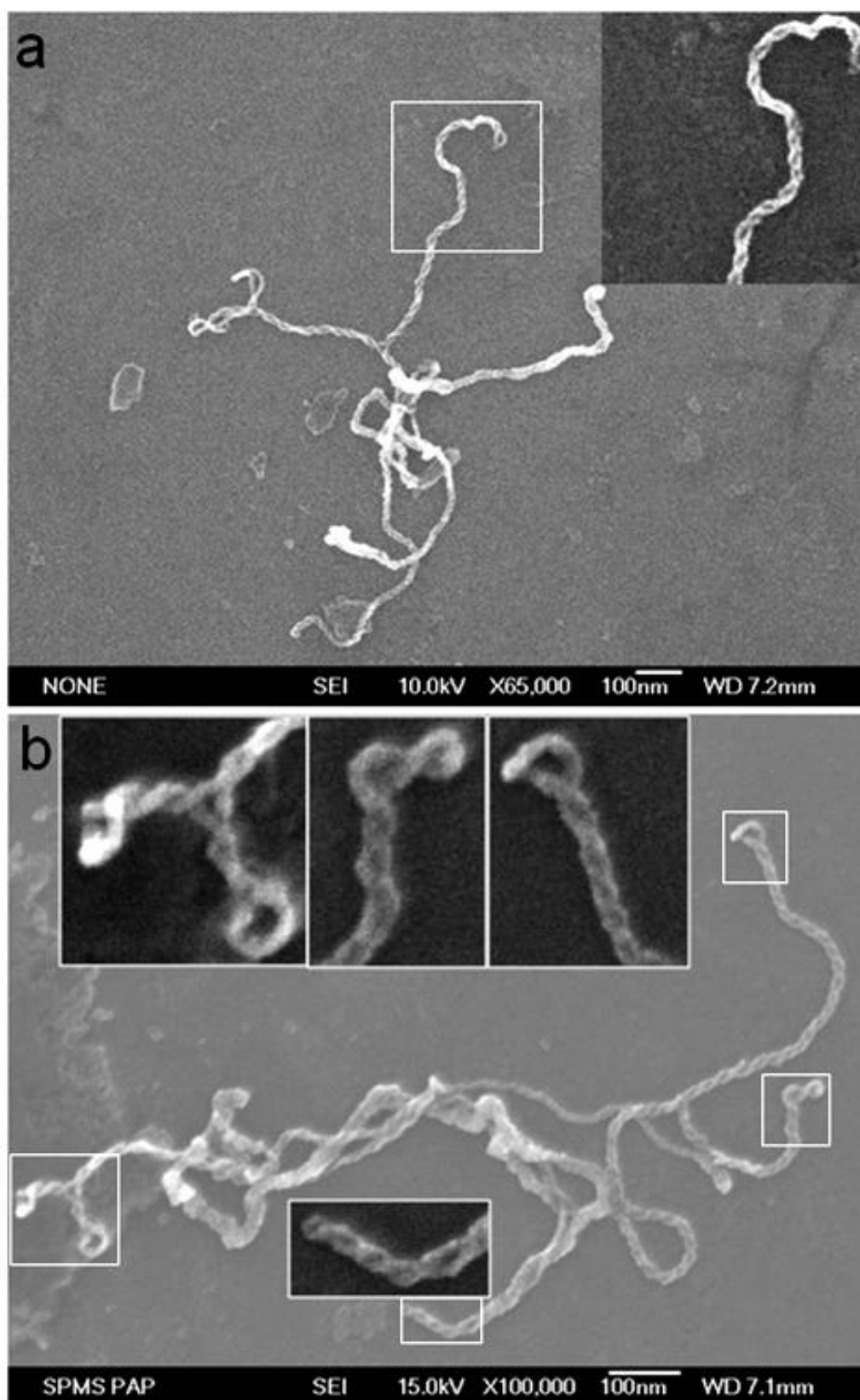
Figure 3-9 SEM images of (Au-Ag)@Pd double helices of different chirality: (a) right-handed; (b) left-handed: in this image, the 4 magnified regions show the same chirality.
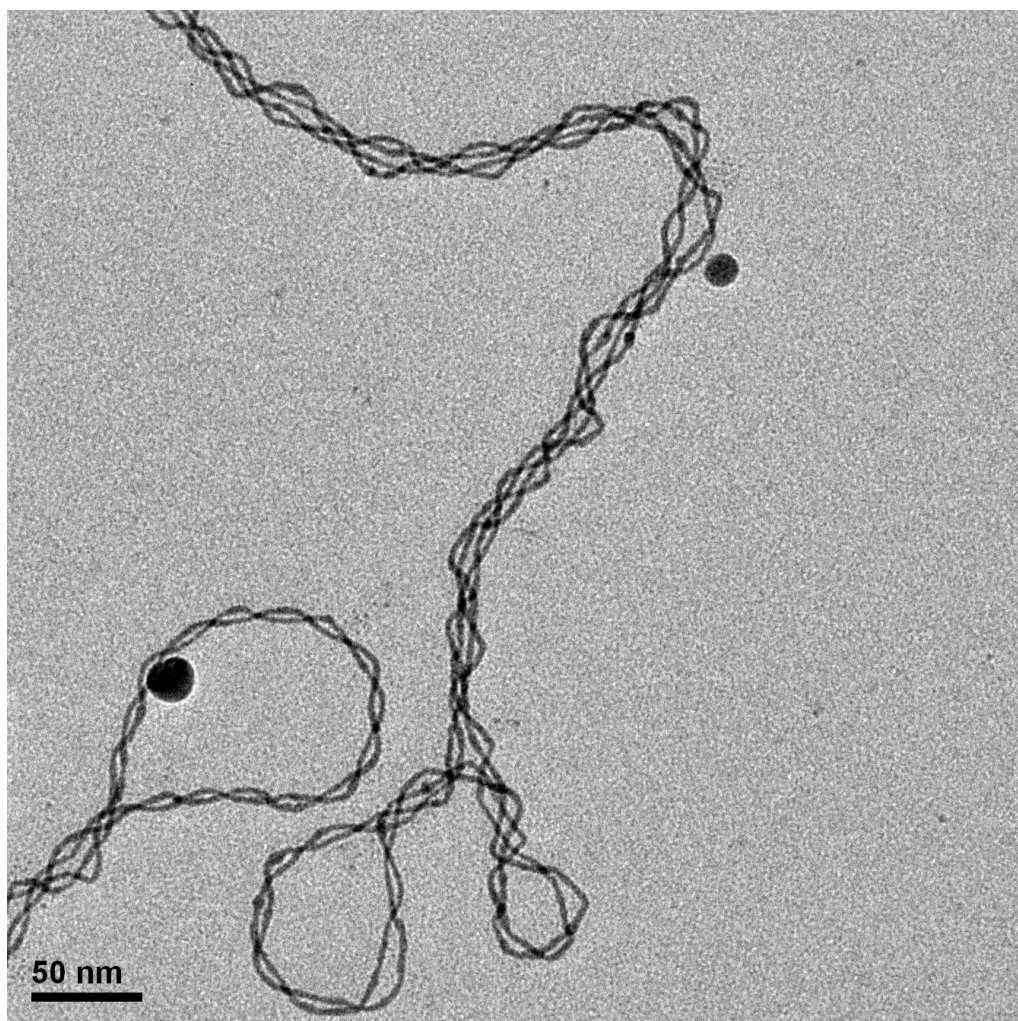
Figure 3-10 TEM image of a (Au-Ag)@Pd quadruple helix.

Further control experiments established that the NWs did not wind in the absence of H_2PdCl_4, with all other conditions unchanged (Figure 3-11). On the other hand, without ascorbic acid the purified Au-Ag NWs reacted with H_2PdCl_4 to give only straight NWs with small Pd NPs attached to their surface (Figure 3-12a and b). It was an expected result of the galvanic reaction between H_2PdCl_4 and Ag (the remaining Au/Ag ratio is 1.62, Figure 3-13). After reacting for 24 h, ascorbic acid was added to the mixture to reduce the remaining Pd^{2+}. The NWs were still able to form helices (Figure 3-12c and d), although they were loose with increased pitch period. Hence, the loss of Ag

from the ultrathin Au-Ag NWs seemed to have compromised their ability to wind, indicating the critical role played by the alloy NWs. Another important factor was the Pd deposition on the NWs, as opposed to the Pd-Ag galvanic exchange.
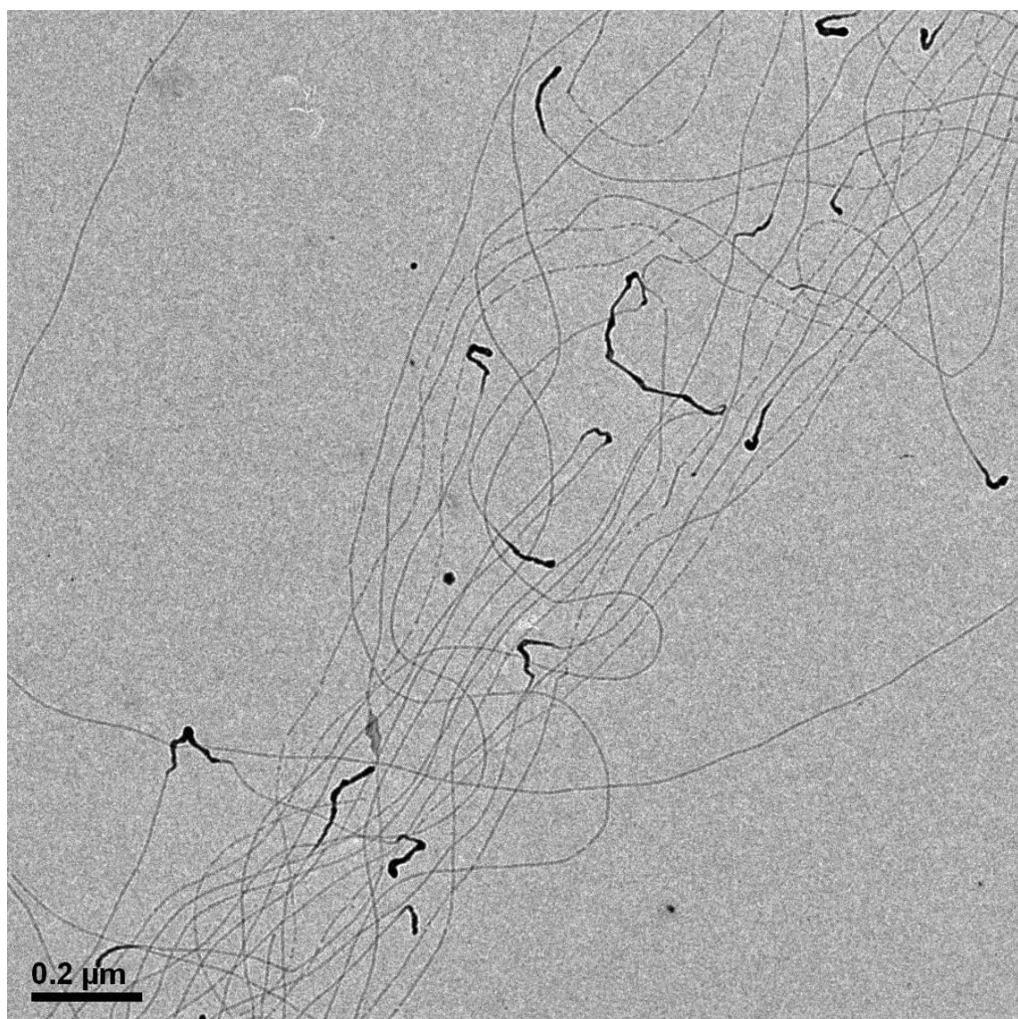
Figure 3-11 Large-area TEM image of the NWs incubated in the absence of H_2PdCl_4, with all other conditions unchanged. No obvious change was observed.
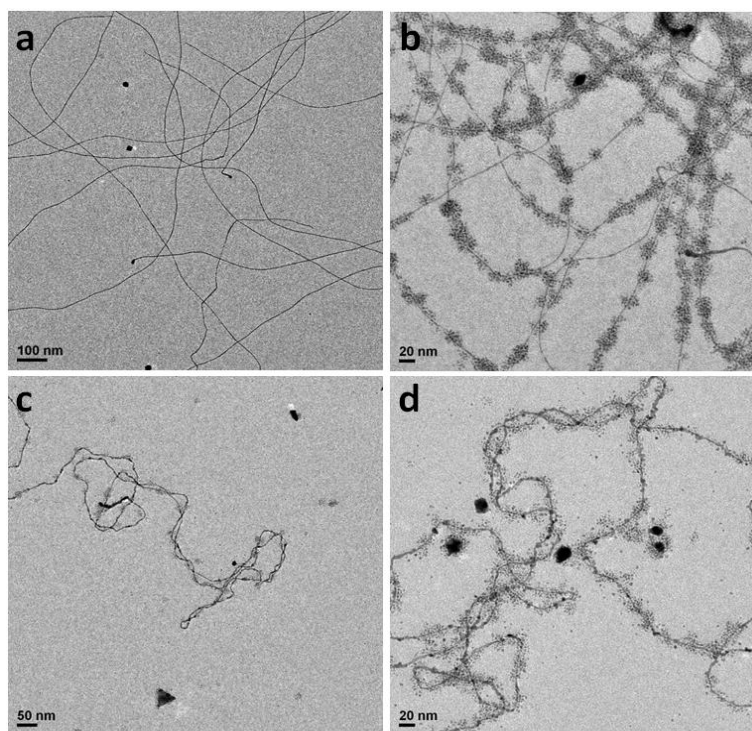
Figure 3-12 TEM images of NWs after the incubation of purified Au-Ag NWs with aq. H_2PdCl_4 solution for 20 min (a) and 24 h (b); (c, d) TEM images of the H_2PdCl_4 treated Au-Ag NWs sample (same as a and b) after addition of ascorbic acid. DMF was added back to follow the typical Pd growth condition.
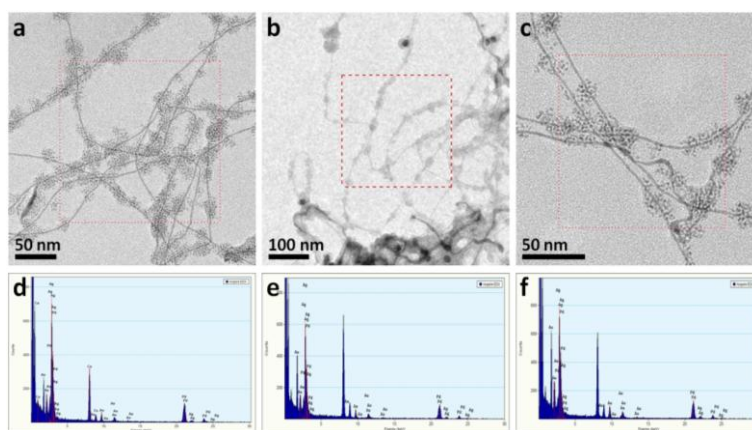
	a	b	c	Averaged Au/Ag ratio
Pd (K)	83.14%	78.18%	72.30%	
Ag (K)	5.47%	8.54%	11.32%	1.62
Au (L)	11.38%	13.26%	16.36%	

Figure 3-13 The selected-area EDS analyses of H_2PdCl_4 treated Au-Ag NWs in the absence of ascorbic acid: (a-c) the TEM images with the selected areas marked; (d-f) the corresponding EDS analyses of the selected areas. The EDS analyses are summarized in the above table.

As the H$_2$PdCl$_4$ concentration was increased from the original 80 μM to 270 and 540 μM, after its reduction the NWs in the resulting helices increased in thickness to 7 and 10 nm, respectively (Figure 3-14, and Figure 3-15). The NWs did not fuse together and the pitch length remained the same; only the gap distance between the NWs decreased significantly. Thus, the helix formation was finished after the initial Pd deposition.
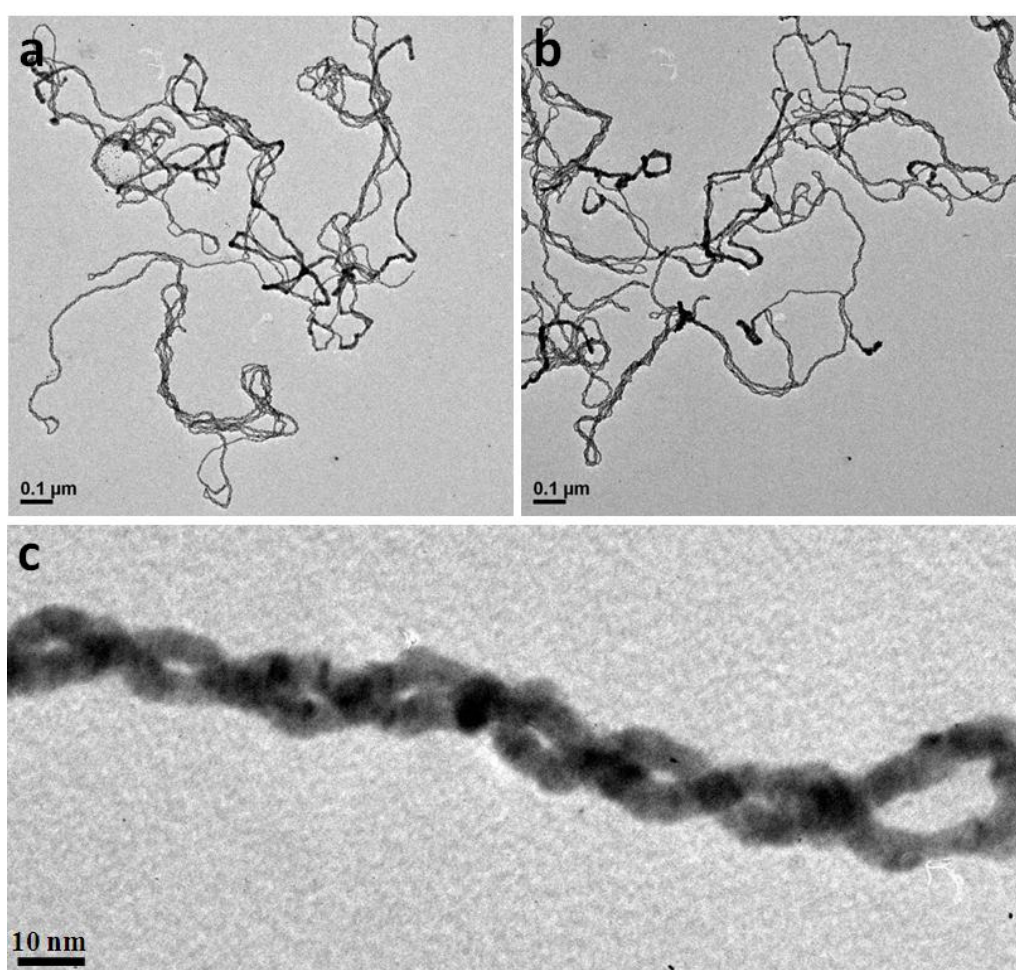
Figure 3-14 TEM images of the (Au-Ag)@Pd double helices obtained by ascorbic acid reducing H$_2$PdCl$_4$ (final concentration of H$_2$PdCl$_4$ is 270 μM).
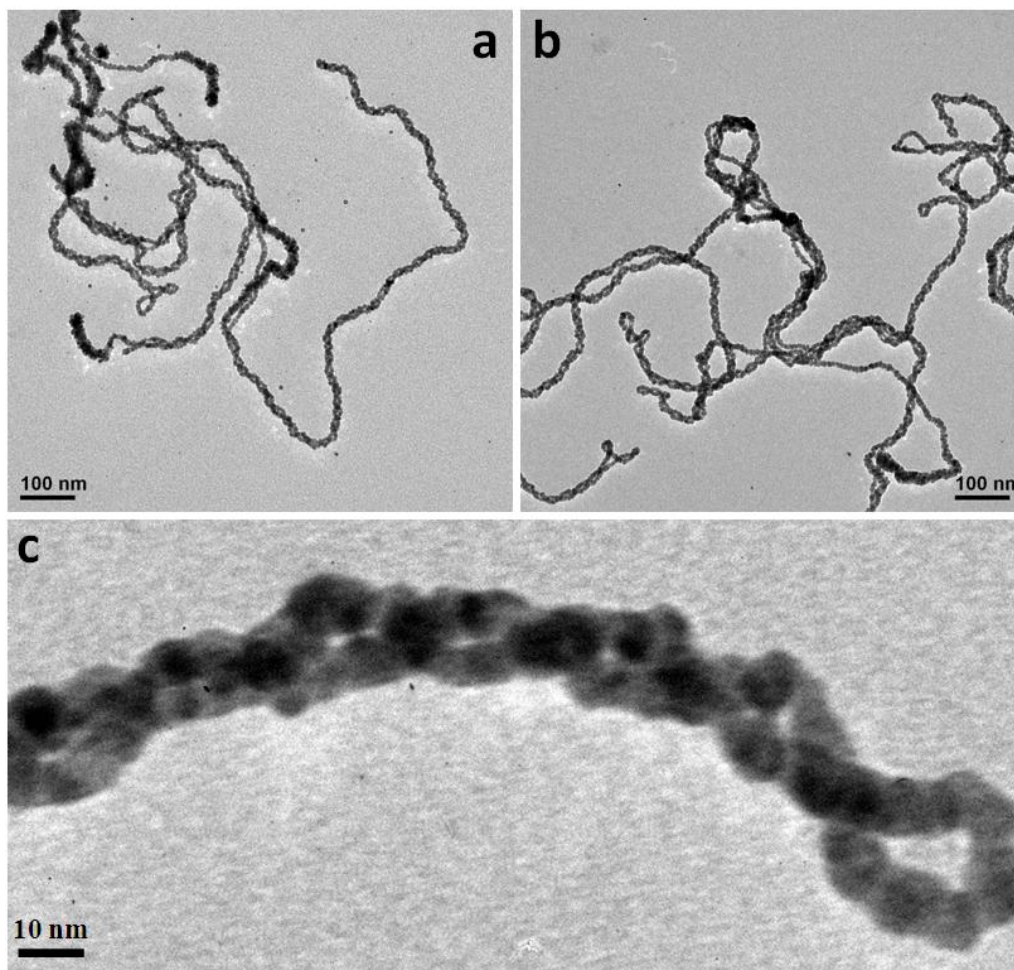
Figure 3-15 TEM images of the (Au-Ag)@Pd double helices obtained by ascorbic acid reducing H_2PdCl_4 (final concentration of H_2PdCl_4 is 540 μM).

To confirm the helices were formed in the growth solution, but not because of the contraction of the solvent during the TEM sample preparation, SiO_2 shell growth process was carried out after the Pd growth in the NWs solution. Figure 3-16 showed a typical TEM image of the helices coated with silica, which indicated that the double helices have already existed in the solution after the Pd deposition.
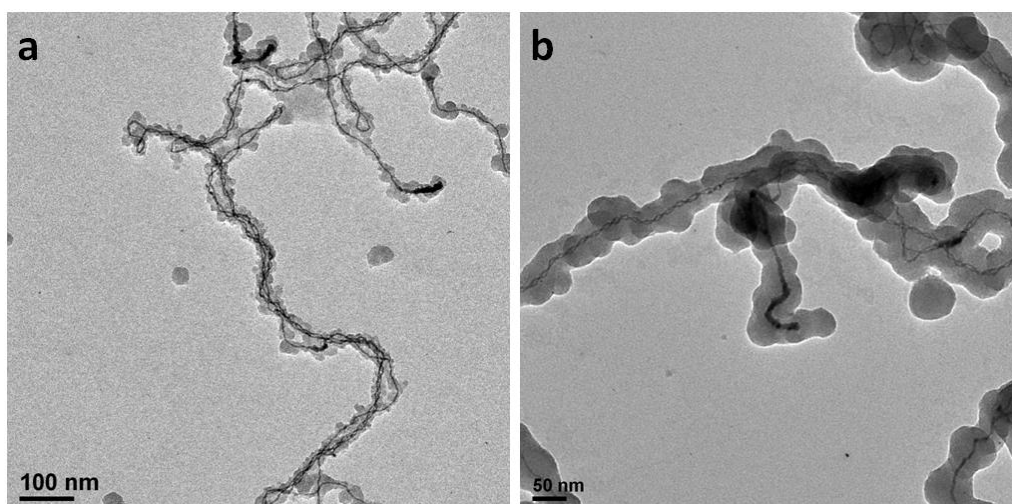
Figure 3-16 TEM images of the SiO$_2$ encapsulated double helices product: first round growth of SiO$_2$ shell (left), and grow SiO$_2$ shell twice (right).

3.3.3 Discussion

Pd was not unique in inducing the helix formation. In the following, we used a same batch of Au-Ag NWs for testing the reaction conditions. When H$_2$PdCl$_4$ was replaced by K$_2$PtCl$_4$, double helices were also obtained. There were tightly wound helices (Figure 3-17a and b) with the same average pitch length and gap separation as those in Figure 3-7, but there were also loose helices with kinks that have lost the potential to wind. When HAuCl$_4$ was used as the metal precursor, shortly after the addition of ascorbic acid (< 1 min) the color of the solution changed from brown red to the final light purple color, indicating the fast reaction. The yield of double helices was only 10.6% and they have irregular NW width (Figure 3-17c and d). Most of the NWs simply grew thicker and formed kinks, and this result was not improved when more HAuCl$_4$ was used. When AgNO$_3$ was used, no helix was formed. The Ag selectively

deposited at both ends of the NWs (Figure 3-17e and f) and there was no obvious change in diameter at the middle section.
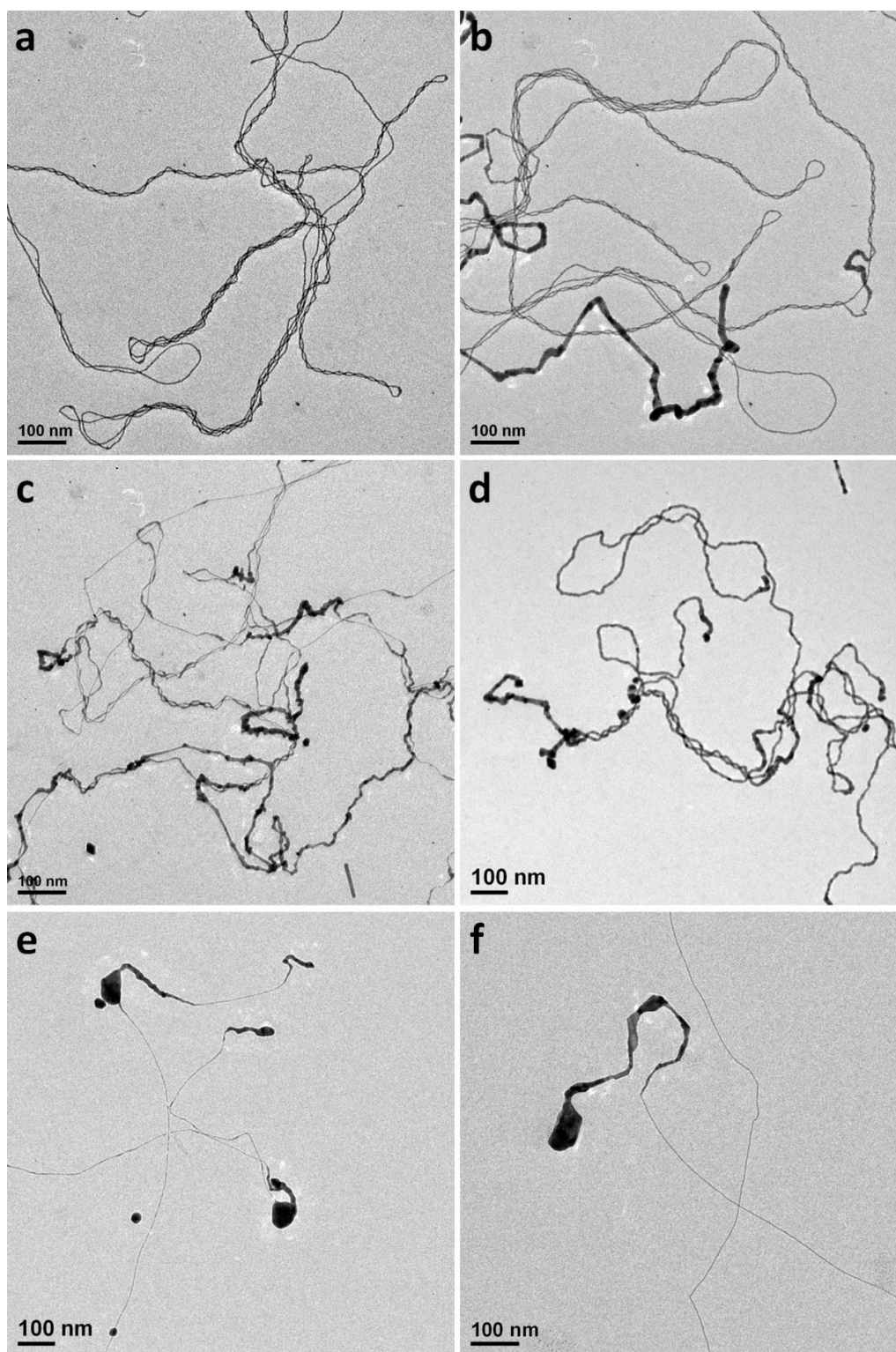
Figure 3-17 TEM images of the resulting NWs when (a, b) K_2PtCl_4 reacted with ascorbic acid; (c, d) $HAuCl_4$ reacted with ascorbic acid; (e, f) $AgNO_3$ reacted with ascorbic acid.
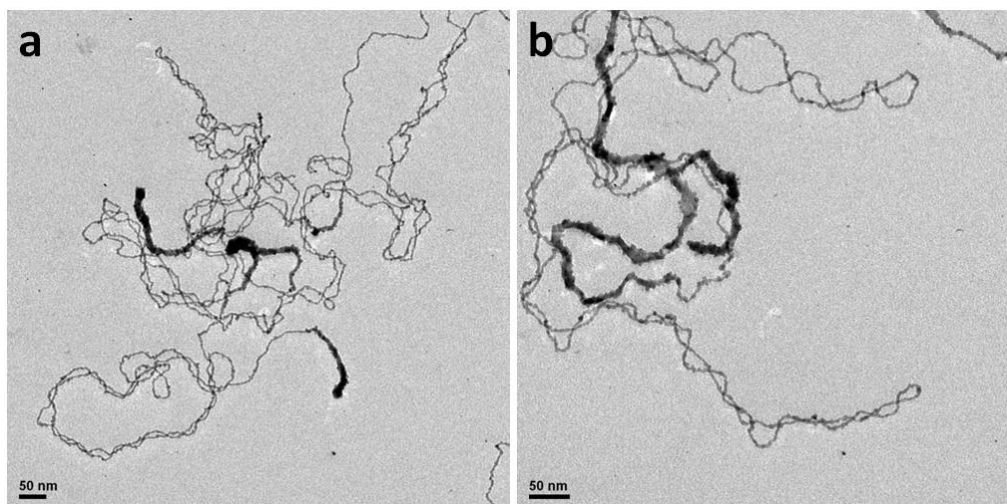
Figure 3-18 TEM images of the (Au-Ag)@Pd double helices obtained by ascorbic acid reducing H_2PdCl_4, in which the *purified* Au-Ag NWs were dispersed in *water*, leading to faster reaction. In a similar control experiment, purified Au-Ag NWs were dispersed in *DMF/water mixture* (v/v = 1:13.7), the result was the same as Figure 1c and S7 (thus not shown).

The above reaction conditions have already been optimized. After careful analysis of numerous initial reactions, we noticed that the yield of helix formation depended critically on the purification step. The residue DMF in the reaction mixture was found to a play an important role, probably via affecting the reaction rate (Figure 3-18). To illustrate this point, the purified Au-Ag NWs were dispersed in either water (0 M DMF) or DMF/water mixture (v/v = 1:13.7, *i.e.*, 0.88 M DMF). After mixing with H_2PdCl_4 and ascorbic acid, the solutions were incubated for 2 h. The rates of Pd reduction were clearly different as indicated by the color change and confirmed by UV-Vis kinetics (all reactions were finished within 8 min).
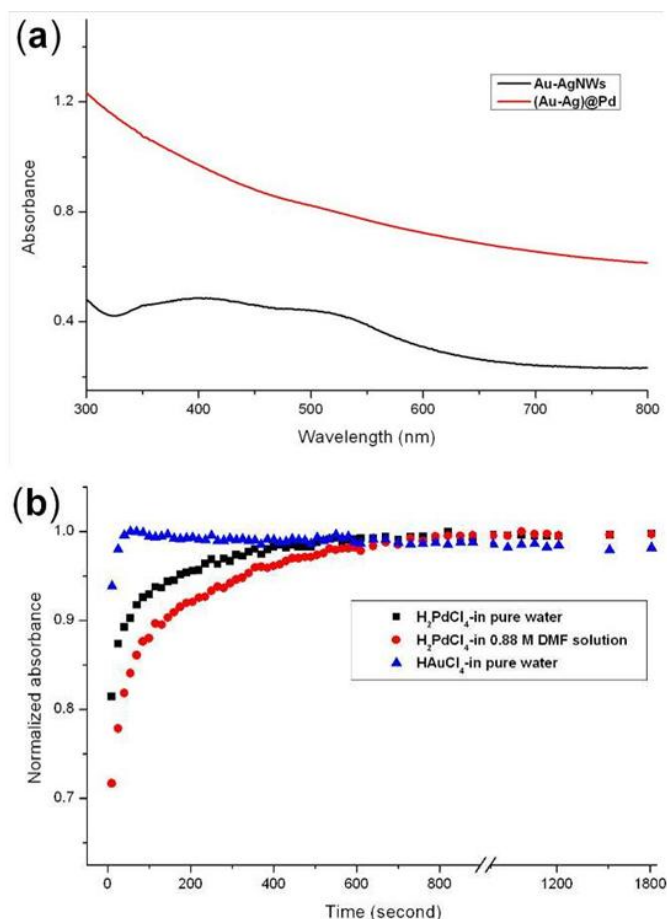
Figure 3-19 (a) UV-Vis spectra of the purified Au-Ag NWs, and (Au-Ag)@Pd double helices in aqueous solutions; (b) the normalized absorbance increase at 510 nm wavelength of Pd and Au growth in pure water or 0.88 M DMF aqueous solution.

The UV-Vis spectra of the as-synthesized Au-AgNWs and (Au-Ag)@Pd double helices (Figure 3-19a) showed that after the metal layer growth, the absorbance increased over the whole spectrum and the characteristic peaks around 400 nm and 500 nm disappeared. Nevertheless, the trend in the increase of absorbance was similar at different wavelengths, showing a plateau after initial increase in absorbance. The rates of metal deposition were reflected by the rates of increase in absorbance. In Figure 3-19b, the deposition reactions were studied by following the absorbance change at 510 nm. In the case of $HAuCl_4$ reduction in water, the reaction was too fast for us to move the cuvette

118

into the UV-vis spectrometer. All reactions reached a plateau within 8 min (for Au, less than 1 min).

The faster reaction in water gave kinked NWs and *loose* double helices (76.6% yield; no improvement after 24 h). In contrast, the presence of the 0.88 M of DMF residue led to slower reaction but higher yield (90.1%) of tightly wound helices. In comparison to the original reaction using the as-synthesized Au-Ag NWs (DMF/water = 1:13.7), these control experiments ruled out the effects of PVP and other residue chemicals.

We varied the reactants as an alternative approach to tune the rates of metal reduction in the presence of Au-Ag NWs. When $NaBH_4$ was used as the reductant for H_2PdCl_4 or K_2PtCl_4, the solution reached the final brown color instantaneously (< 1 s). Only a few loose double helices formed and the NWs contained many kinks (Figure 3-20). It appeared that the kink formation was correlated with the fast reaction rate, probably because the metal deposition was too fast for the NWs to respond by winding.
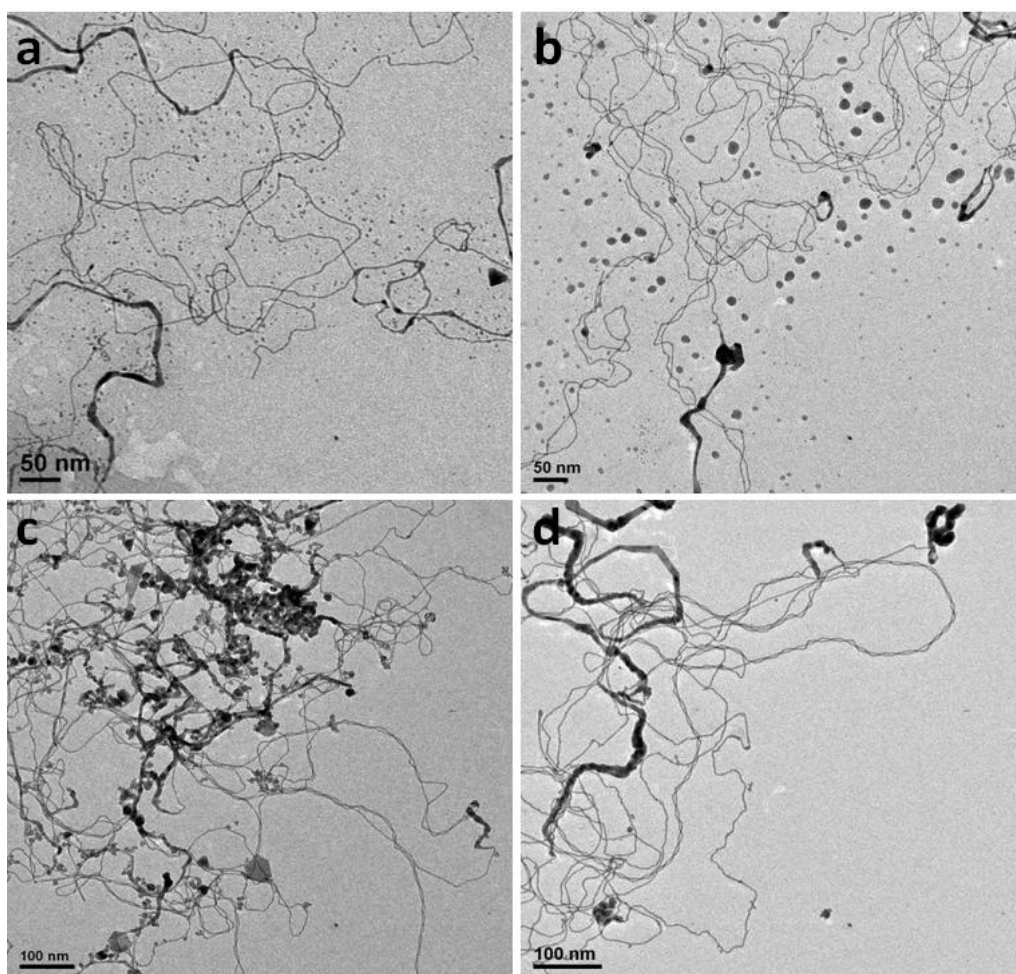
Figure 3-20 TEM images of the double helices induced by $NaBH_4$ arisen (a, b) Pd and (c, d) Pt deposition.

Figure 3-21 TEM images of the double helices induced by (a, b) pyrrole arisen Au deposition; (c, d) aniline arisen Au deposition; TEM images of the resulting NWs when AgNO$_3$ reacted with pyrrole.

On the other hand, aniline and pyrrole were known to cause slow reduction of AgNO$_3$ or HAuCl$_4$, leading to simultaneous formation of polymer

shells.[24-26] The reduction of $HAuCl_4$ by pyrrole was significantly slower than that using ascorbic acid. After 10 h, this slower reaction gave much improved yield of double helices (from 10.6% to 88.3%). Their structure was also improved in terms of tightly wound helices and uniform NW diameter (Figure 3-21a, b). Similarly, the reaction of $HAuCl_4$ with aniline was also slow, giving 89.8% yield (Figure 3-21c, d). Similar with the results of Ag deposition by the reductant of ascorbic acid, AgNPs also are docked on the tails of NWs in the pyrrole reducing case (Figure 3-21e, f).

The reaction of H_2PdCl_4 with pyrrole did not worsen or further improve the helix formation; after 10 h, tightly wound double helices were still obtained with good yield (Figure 3-22a, b). The similar results also exhibit in the pyrrole reduced K_2PtCl_4 case (Figure 3-22c, d). Control experiments showed that polymer coating without metal deposition cannot induce the helix formation: $(NH_4)_2S_2O_8$ was used to oxidize pyrrole, and the Au-Ag NWs remained straight after the polymer coating (Figure 3-22e).[27, 37]
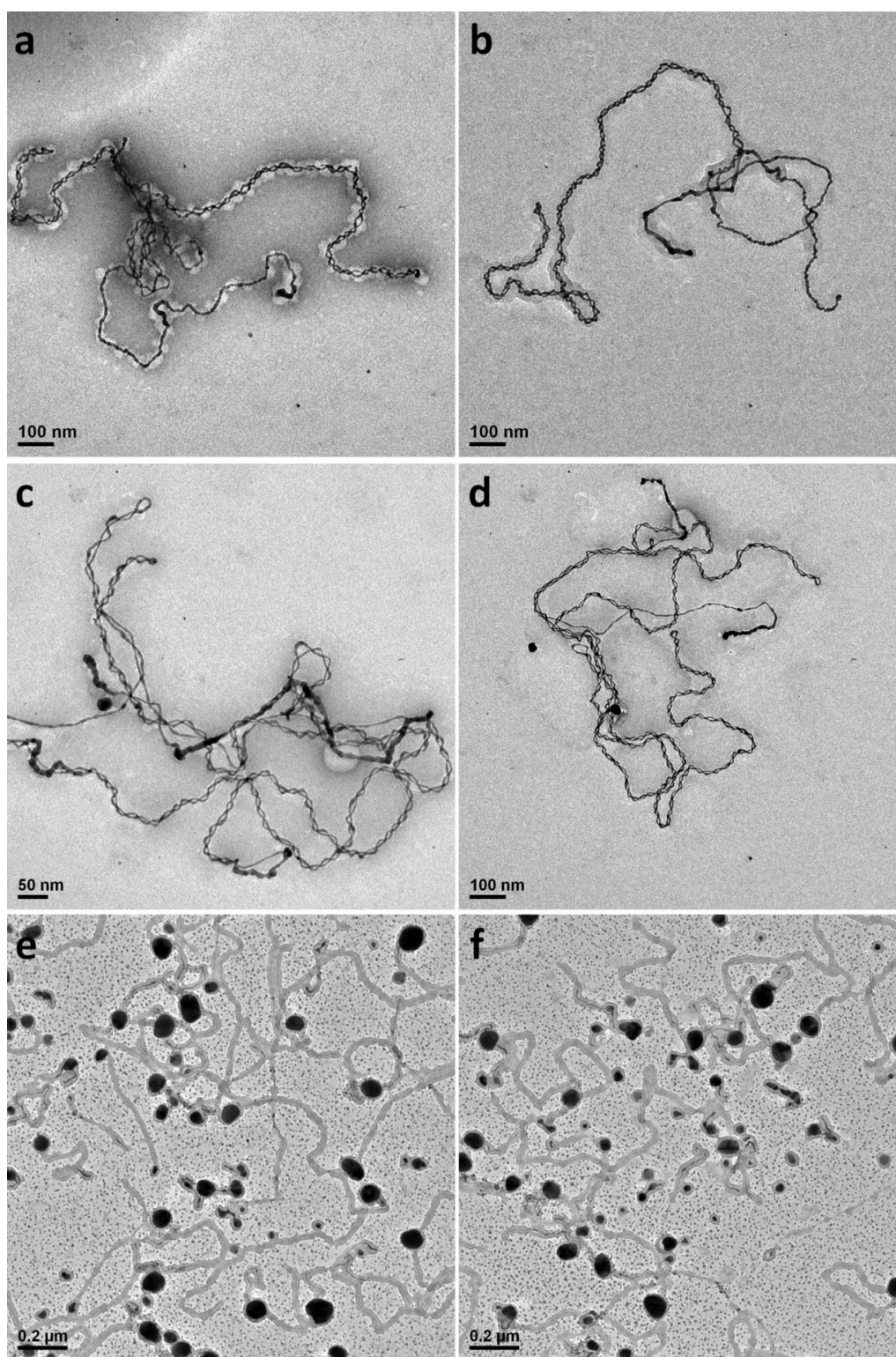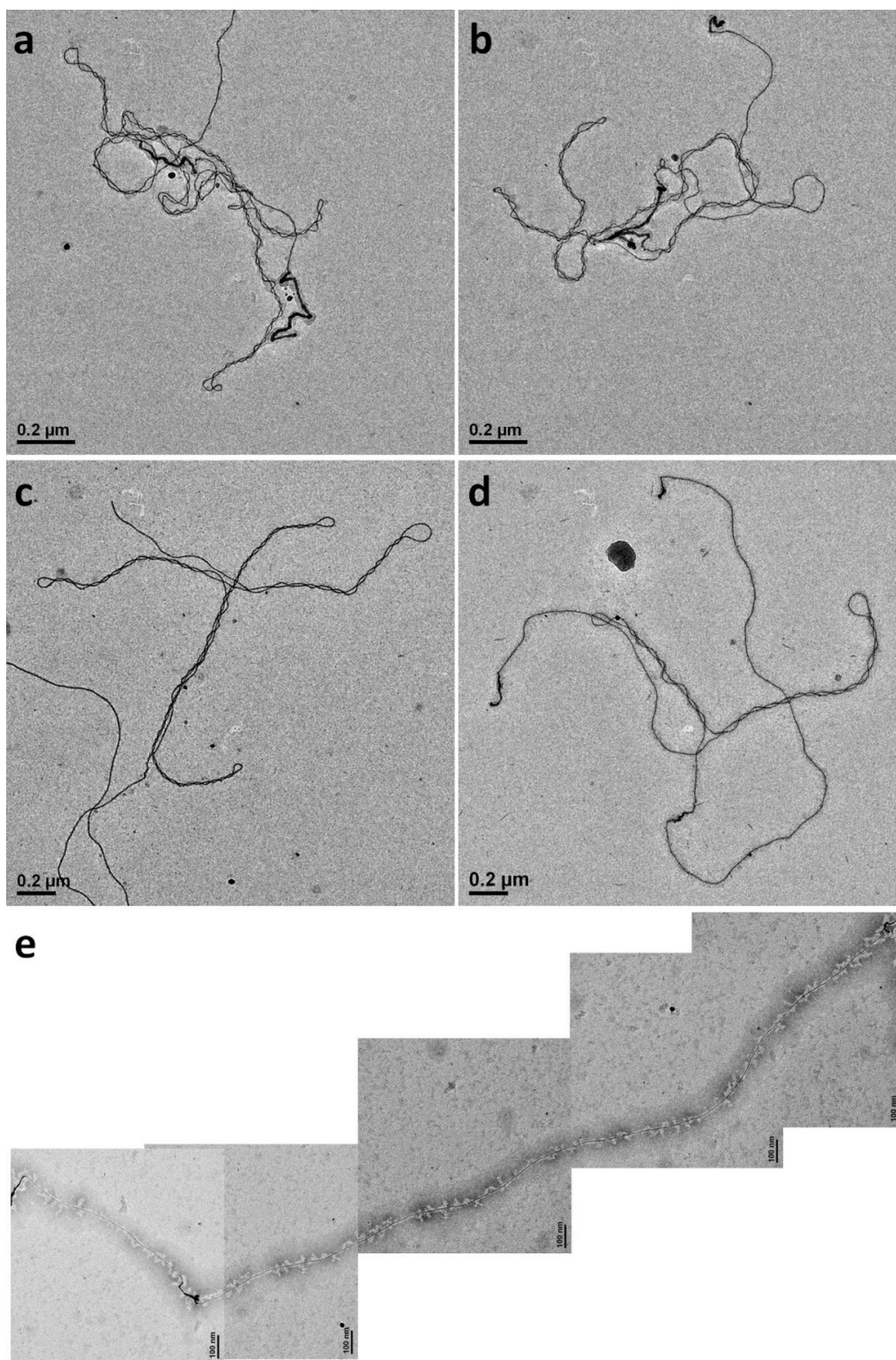
Figure 3-22 TEM images of the double helices induced by (a, b) pyrrole arisen Pd deposition; (c, d) pyrrole arisen Pt deposition; TEM images of the resulting NWs when $(NH_4)_2S_2O_8$ was used to oxide pyrrole to form the polypyrrole coating.

3.3.4 Mechanism Analysis

With our systematic study in the reaction conditions, the formation of double helices became highly reproducible and the yield improved significantly (such as, the yield of Au deposition induced double helices can increase from 10.6% to 88.3% by changing the reducing agents from ascorbic acid to pyrrole). Most importantly, the chemistry of the Au-Ag NWs offers mechanistic insights unattainable by physical characterization. The rate of metal deposition was clearly critical: Making the Pd reduction faster worsened the yield of double helices, whereas slowing the Au reduction improved the yield. Moreover, the formation of kinked NWs and loose double helices were correlated with the reaction rates as well as the depletion of Ag from the NWs. Hence, the NW winding must arise from the *interaction* between the metal coating and the embedded Au-Ag NW. On the other hand, Au and Ag have matching lattices (0.1% mismatch), but Au-Pd (4.71%) and Au-Pt (3.80%) have larger lattice mismatch.[38] The fact that both Pd and Au deposition can cause double helix formation suggests that the lattice matching was probably not a key factor.

The chirality of an individual double helix was remarkably consistent over microns in length (Figure 3-9b). It is impossible for random metal deposition on one end to influence that on the other. Hence, it is more likely that the embedded Au-Ag NW is the origin of the chiral action. Following the same logic, random defects in the NW cannot be the reason. Given the fast diffusion rate of noble metal atoms, high-density defects are unlikely in the ultrathin

Au-Ag NWs and random defects will most likely cancel out each other in terms of induced action. For random polycrystalline NWs, it is nearly impossible to achieve uniform width without using templates. Thus, *lattice order* in the Au-Ag NWs is the only conceivable explanation for the uniform NWs and their consistent action.

To study the origin of winding action of the NWs, it is obvious that their central ultrathin section (Au:Ag = 1:1) is more important that their thicker tails. As we discussed before, our NWs are similar to the recent published work, in which Au-Ag alloy showed the formation of ultrathin NWs (d = 2-5 nm, Au:Ag = 1:3) with BCB type twisted lattice (the twisting was not a result of strain).[21] The authors proposed that several BCB type spirals can be roped together to give interpenetrated icosahedron segments, which give characteristic "fan"-like contrast under electron microscopy. On the basis of their close resemblance to the "fan"-like contrast observed and simulated by José-Yacamán's team, it is likely that our Au-Ag NWs also have twisted lattice consisting of BCB type spirals. Though our NWs were much longer (5 μm *vs* 50 nm), a same chirality was maintained over an entire NW as indicated by the chirality in the resulting double helices (Figure 3-9b). Jointed segments with opposite chirality are expected to give non-helical section near the junction; this was not observed in the nicely wound double helices (e.g., the (Au-Ag)@Pd ones).

Icosahedron and the BCB-type lattice are made of tetrahedral units,[21] which cannot closely pack with each other. For example, when five tetrahedral stack

to form a decahedron, there is a misfit angle of 7.35°. The coating of metal on the BCB-type twisted lattice likely leads to the untwisting (twisting in the opposite direction of the BCB lattice) of the NWs to minimize the overall lattice energy. The increase in lateral dimension is expected to induce lattice strain, because the BCB-type packing cannot be maintained by growing on their sides (the constituent tetrahedra cannot expand in longitudinal direction).[21] While the open ends of a NW can twist without intertwining, the high aspect ratio (> 1000) makes it impossible to twist the entire NW strictly along a same axis. Thus, the NW winds around itself to form a double helix, in much the same way an electric cord winds around itself upon twisting. Multiple bending sites in a long NW thus give multiple U-turn ends. The pitch length of BCB type spirals (3.7 nm) is much shorter than that of the (Au-Ag)@Pd double helices. The excess twisting potential winds the double helix tightly together, leading to a constant pitch length. When Ag was partially removed from the Au-Ag NWs (Figure 3-12a, b), the reorganized lattice was largely compromised (Figure 3-12c, d). If the metal deposition was too fast, the additional layer hardened the NWs and the lattice strain was only relieved in a few spots in the form of kinks.

3.4 Conclusion

In summary, we report the synthesis of ultrathin Au-Ag NWs in polar solvent firstly. These flexible NWs are of 2 nm in width and several micrometers in length. In these NWs, Au and Ag elements distribute uniformly

(about 1:1 in atomic ratio). Then an unprecedented behabior of these NWs can be found in the colloidal solution: the NW winds around itself to form a metallic double helix. The chemistry of the NWs provides rich information for mechanistic inference. Their chiral action is a dramatic display of the chirality at atomic scale. The predictable motion of nanostructure upon chemical stimuli could be potentially exploited for developing smart nanodevices.

3.5 Bibliography

[1] Baiker, A., Progress in Asymmetric Heterogeneous Catalysis: Design of Novel Chirally Modified Platinum Metal Catalysts. *Journal of Molecular Catalysis a-Chemical*, **115**, 473 (1997).

[2] Thomas, J. M. and Raja, R., Exploiting Nanospace for Asymmetric Catalysis: Confinement of Immobilized, Single-Site Chiral Catalysts Enhances Enantioselectivity. *Acc. Chem. Res.*, **41**, 708 (2008).

[3] Hazen, R. M. and Sholl, D. S., Chiral Selection on Inorganic Crystalline Surfaces. *Nat. Mater.*, **2**, 367 (2003).

[4] Che, S., Liu, Z., Ohsuna, T., Sakamoto, K., Terasaki, O., and Tatsumi, T., Synthesis and Characterization of Chiral Mesoporous Silica. *Nature*, **429**, 281 (2004).

[5] Shemer, G., Krichevski, O., Markovich, G., Molotsky, T., Lubitz, I., and Kotlyar, A. B., Chirality of Silver Nanoparticles Synthesized on DNA. *J. Am. Chem. Soc.*, **128**, 11006 (2006).

[6] Oh, H. S., Liu, S., Jee, H., Baev, A., Swihart, M. T., and Prasad, P. N., Chiral Poly(Fluorene-Alt-Benzothiadiazole) (Pfbt) and Nanocomposites with Gold Nanoparticles: Plasmonically and Structurally Enhanced Chirality. *J. Am. Chem. Soc.*, **132**, 17346 (2010).

[7] Nakashima, T., Kobayashi, Y., and Kawai, T., Optical Activity and Chiral Memory of Thiol-Capped Cdte Nanocrystals. *J. Am. Chem. Soc.*, **131**, 10342 (2009).

[8] Mastroianni, A. J., Claridge, S. A., and Alivisatos, A. P., Pyramidal and

Chiral Groupings of Gold Nanocrystals Assembled Using DNA Scaffolds. *J. Am. Chem. Soc.*, **131**, 8455 (2009).

[9] Li, C., Deng, K., Tang, Z. Y., and Jiang, L., Twisted Metal-Amino Acid Nanobelts: Chirality Transcription from Molecules to Frameworks. *J. Am. Chem. Soc.*, **132**, 8202 (2010).

[10] Chen, C. L., Zhang, P. J., and Rosi, N. L., A New Peptide-Based Method for the Design and Synthesis of Nanoparticle Superstructures: Construction of Highly Ordered Gold Nanoparticle Double Helices. *J. Am. Chem. Soc.*, **130**, 13555 (2008).

[11] Chen, W., Bian, A., Agarwal, A., Liu, L. Q., Shen, H. B., Wang, L. B., Xu, C. L., and Kotov, N. A., Nanoparticle Superstructures Made by Polymerase Chain Reaction: Collective Interactions of Nanoparticles and a New Principle for Chiral Materials. *Nano Lett.*, **9**, 2153 (2009).

[12] Perro, A., Reculusa, S., Ravaine, S., Bourgeat-Lami, E. B., and Duguet, E., Design and Synthesis of Janus Micro- and Nanoparticles. *J. Mater. Chem.*, **15**, 3745 (2005).

[13] Amelinckx, S., Zhang, X. B., Bernaerts, D., Zhang, X. F., Ivanov, V., and Nagy, J. B., A Formation Mechanism for Catalytically Grown Helix-Shaped Graphite Nanotubes. *Science*, **265**, 635 (1994).

[14] Gao, P. X., Ding, Y., Mai, W., Hughes, W. L., Lao, C., and Wang, Z. L., Conversion of Zinc Oxide Nanobelts into Superlattice-Structured Nanohelices. *Science*, **309**, 1700 (2005).

[15] Wang, H. T., Wu, J. C., Shen, Y. Q., Li, G. P., Zhang, Z., Xing, G. Z., Guo, D. L., Wang, D. D., Dong, Z. L., and Wu, T., Crsi2 Hexagonal Nanowebs. *J. Am. Chem. Soc.*, **132**, 15875 (2010).

[16] Wu, Y. Y., Cheng, G. S., Katsov, K., Sides, S. W., Wang, J. F., Tang, J., Fredrickson, G. H., Moskovits, M., and Stucky, G. D., Composite Mesostructures by Nano-Confinement. *Nat. Mater.*, **3**, 816 (2004).

[17] Xu, J., Wang, H., Liu, C. C., Yang, Y. M., Chen, T., Wang, Y. W., Wang, F., Liu, X. G., Xing, B. G., and Chen, H. Y., Mechanical Nanosprings: Induced Coiling and Uncoiling of Ultrathin Au Nanowires. *J. Am. Chem. Soc.*, **132**, 11920 (2010).

[18] Chen, L. Y., Wang, H., Xu, J., Shen, X. S., Yao, L., Zhu, L. F., Zeng, Z. Y., Zhang, H., and Chen, H. Y., Controlling Reversible Elastic Deformation of Carbon Nanotube Rings. *J. Am. Chem. Soc.*, **133**, 9654 (2011).

[19] Liu, L. C., Yoo, S. H., Lee, S. A., and Park, S., Wet-Chemical Synthesis of Palladium Nanosprings. *Nano Lett.*, **11**, 3979 (2011).

[20] Kondo, Y. and Takayanagi, K., Synthesis and Characterization of Helical Multi-Shell Gold Nanowires. *Science*, **289**, 606 (2000).

[21] Velázquez-Salazar, J. J., Esparza, R., Mejía-Rosales, S. J., Estrada-Salas, R. n., Ponce, A., Deepak, F. L., Castro-Guerrero, C., and José-Yacamán, M., Experimental Evidence of Icosahedral and Decahedral Packing in One-Dimensional Nanostructures. *ACS Nano*, **5**, 6272 (2011).

[22] Rycenga, M., Cobley, C. M., Zeng, J., Li, W. Y., Moran, C. H., Zhang, Q., Qin, D., and Xia, Y. N., Controlling the Synthesis and Assembly of Silver Nanostructures for Plasmonic Applications. *Chem. Rev.*, **111**, 3669 (2011).

[23] Millstone, J. E., Hurst, S. J., Metraux, G. S., Cutler, J. I., and Mirkin, C. A., Colloidal Gold and Silver Triangular Nanoprisms. *Small*, **5**, 646 (2009).

[24] Xing, S. X., Tan, L. H., Chen, T., Yang, Y. H., and Chen, H. Y., Facile Fabrication of Triple-Layer (Au@Ag)@Polypyrrole Core-Shell and (Au@H2o)@Polypyrrole Yolk-Shell Nanostructures. *Chem. Commun.*, 1653 (2009).

[25] Xing, S. X., Feng, Y. H., Tay, Y. Y., Chen, T., Xu, J., Pan, M., He, J. T., Hng, H. H., Yan, Q. Y., and Chen, H. Y., Reducing the Symmetry of Bimetallic Au@Ag Nanoparticles by Exploiting Eccentric Polymer Shells. *J. Am. Chem. Soc.*, **132**, 9537 (2010).

[26] Pan, M., Xing, S. X., Sun, T., Zhou, W. W., Sindoro, M., Teo, H. H., Yan, Q. Y., and Chen, H. Y., 3d Dendritic Gold Nanostructures: Seeded Growth of a Multi-Generation Fractal Architecture. *Chem. Commun.*, **46**, 7112 (2010).

[27] Xing, S. X., Tan, L. H., Yang, M. X., Pan, M., Lv, Y. B., Tang, Q. H., Yang, Y. H., and Chen, H. Y., Highly Controlled Core/Shell Structures: Tunable Conductive Polymer Shells on Gold Nanoparticles and Nanochains. *J. Mater. Chem.*, **19**, 3286 (2009).

[28] Stober, W., Fink, A., and Bohn, E., Controlled Growth of Monodisperse Silica Spheres in Micron Size Range. *J. Colloid Interface Sci.*, **26**, 62 (1968).

[29] Chen, T., Chen, G., Xing, S. X., Wu, T., and Chen, H. Y., Scalable Routes to Janus Au-Sio2 and Ternary Ag-Au-Sio2 Nanoparticles. *Chem. Mater.*, **22**, 3826 (2010).

[30] Wong, Y. J., Zhu, L. F., Teo, W. S., Tan, Y. W., Yang, Y. H., Wang, C., and Chen, H. Y., Revisiting the StöBer Method: Inhomogeneity in Silica Shells. *J. Am. Chem. Soc.*, 11422 (2011).

[31] Wang, C. and Sun, S. H., Facile Synthesis of Ultrathin and

Single-Crystalline Au Nanowires. *Chemistry-an Asian Journal*, **4**, 1028 (2009).

[32] Hong, X., Wang, D. S., Yu, R., Yan, H., Sun, Y., He, L., Niu, Z. Q., Peng, Q., and Li, Y. D., Ultrathin Au-Ag Bimetallic Nanowires with Coulomb Blockade Effects. *Chem. Commun.*, **47**, 5160 (2011).

[33] Feng, H. J., Yang, Y. M., You, Y. M., Li, G. P., Guo, J., Yu, T., Shen, Z. X., Wu, T., and Xing, B. G., Simple and Rapid Synthesis of Ultrathin Gold Nanowires, Their Self-Assembly and Application in Surface-Enhanced Raman Scattering. *Chem. Commun.*, 1984 (2009).

[34] Krichevski, O., Tirosh, E., and Markovich, G., Formation of Gold-Silver Nanowires in Thin Surfactant Solution Films. *Langmuir*, **22**, 867 (2006).

[35] Lu, X. M., Yavuz, M. S., Tuan, H. Y., Korgel, B. A., and Xia, Y. N., Ultrathin Gold Nanowires Can Be Obtained by Reducing Polymeric Strands of Oleylamine-Aucl Complexes Formed Via Aurophilic Interaction. *J. Am. Chem. Soc.*, **130**, 8900 (2008).

[36] Ascencio, J. A., Gutierrez-Wing, C., Espinosa, M. E., Marin, M., Tehuacanero, S., Zorrilla, C., and José-Yacamán, M., Structure Determination of Small Particles by Hrem Imaging: Theory and Experiment. *Surf. Sci.*, **396**, 349 (1998).

[37] Yu, H., Chen, M., Rice, P. M., Wang, S. X., White, R. L., and Sun, S. H., Dumbbell-Like Bifunctional Au-Fe3o4 Nanoparticles. *Nano Lett.*, **5**, 379 (2005).

[38] Fan, F. R., Liu, D. Y., Wu, Y. F., Duan, S., Xie, Z. X., Jiang, Z. Y., and Tian, Z. Q., Epitaxial Growth of Heterogeneous Metal Nanocrystals: From Gold Nano-Octahedra to Palladium and Silver Nanocubes. *J. Am. Chem. Soc.*, **130**, 6949 (2008).

Chapter 4 One Pot Synthesis of Helical Gold Nanowires in Colloidal Solution

4.1 Introduction

As we discussed in Chapter 1 and Chapter 3, chirality is highly important in life science, medical science, and macro devices. Therefore it has been enthusiastically studied. However, the exploration of nano-chiral science is still very rare due to the challenge of the manufacture of helical nanostructures. It can be imaged that using chiral nano-objects as building blocks are of great significance for manufacturing future smart nanodevices. Primary studies have demonstrated that the asymmetric structures are more useful for asymmetric catalysis,[1, 2] chiral separation,[3, 4] and novel optical properties.[5-11] Moreover, for these applications, metallic nanostructures have clear advantages. So it is critical to develop new strategy to manufacture novel helical metallic nanostructures.

Till now, just a few cases of chiral metallic NWs have been synthesized.[12-16] The most popular strategy is the hard template-mediated NW synthesis. Stucky and co-workers found that the confined channels can be used as the hard template for the formation of chiral AgNWs.[12] The shapes and

morphologies of these chiral nanostructures can be controlled by tuning the diameters of these channels. Another research group also used the similar method to synthesize the Pd nanosprings with the help of simultaneous Cu deposition.[13] Very recently, silver microcoil has been synthesized through the spiral vessels in lotus root as biotemplate.[14] It has been demonstrated that this left-handed coil structure can be applied in electromagnetic-responsive fields. All these three cases are templates needed, and thus it is limited for the large-scale production. Couple months ago, bimetallic chiral Au-Ag NWs with the length of 50~100 nm, was synthesized in colloidal solution.[15] These NWs are proposed to be the stacking structures of several Boerdijk-Coxeter-Bernal helices. However, the growth mechanism is still unclear.

In Chapter 3, I have reported on ultrathin Au-Ag alloy NWs with intrinsic chirality, as well as the chiral transformation of ultrathin single NW to double helix.[16] As these NWs are very thin and the strategy of helices formation is complex, I would like to develop new method to synthesize helical metallic NWs directly in colloidal solution. In this chapter, I will introduce the formation of helical gold NWs in ethanol/H_2O mixture in the presence of small organic molecules.

4.2 Materials and Methods

4.2.1 Materials

All chemical reagents were used as purchased without further purification. Hydrogen tetrachloroaurate(III) hydrate ($HAuCl_4 \cdot 3H_2O$), 99.9% (metal basis

Au 49%) was purchased from Alfa Aesar; ethanol, analytical grade, was purchased from Fisher Scientific; Pentaerythritol tetrakis(3-mercapto-propionate), **1**, was purchased from Aldrich; 4-Mercaptobenzoic acid (4-MBA) technical grade, 90%, was purchased from Aldrich; L-Ascorbic acid, reagent grade, 99+%, was purchased from Sigma Aldrich. 4,4'-disulfanediyldibenzoic acid was purchased from Santa Cruz Biotechnology; Deionized water (resistance > 18 MΩ·cm^{-1}) was used in all reactions. Copper specimen grids (300 meshes) with formvar/carbon support film (referred to as TEM grids in the text) were purchased from Beijing XXBR Technology Co, Ltd.
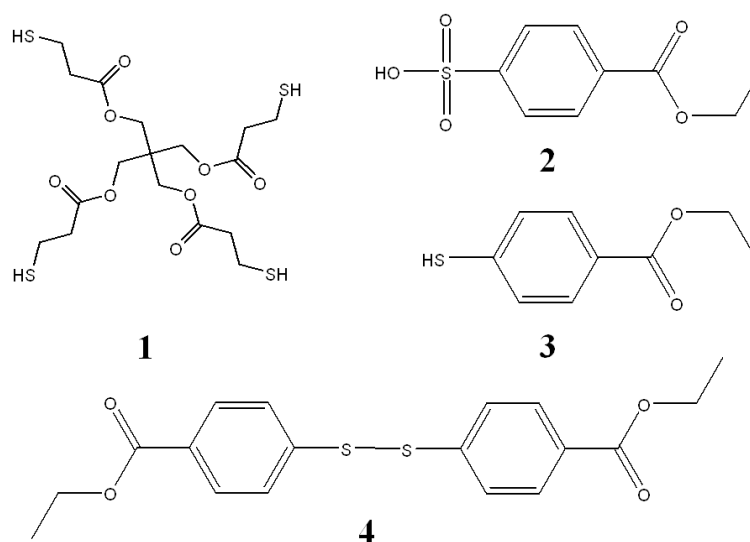
Scheme 4-1 Structures of the compounds used in this chapter

4.2.2 Methods

Characterization Methods: low magnification TEM images were collected from a JEM-1400 transmission electron microscope (JEOL) operated at 100 kV. High-resolution TEM image were collected from a JEM-2100F Transmission Electron Microscope (JEOL) operated at 200 kV.

Preparation of TEM samples: TEM grids were treated with oxygen plasma in a Harrick plasma cleaner/sterilizer for 1 min to improve the surface hydrophilicity. The grid was placed face-down on a droplet of as-synthesized sample laid on a plastic Petri dish. A filter paper was used to wick off the excess solution on the TEM grid, which was then dried in air for 5 min.

Synthesis of AuNPs by seeded growth: Larger AuNPs (36 ± 2.7 nm) were synthesized according to the method mentioned in chapter 2, but more 15 nm AuNPs was used as seeds.[17, 18] In a typical synthesis, a 250 mL round bottom flask was charged with 100 mL aq. $HAuCl_4$ (0.25 mM). The solution was refluxed with vigorous stirring for 10 min, and then 16 mL of AuNP seeds (d_{AuNP} = 15 nm) and 500 μL of sodium citrate (38.7 mM) was added. After boiling the solution for 45 min, a deep-red AuNP solution was obtained. The solution was cooled to room temperature. The average diameter was measured to be 36 ± 2.7 nm from TEM images using ImageJ.

Preparation of 1 functionalized AuNPs (1-AuNPs): In 1500 μL of as-synthesized AuNPs (36 nm), 100 μL of **1** (0.1 mM) was added, followed by continuing stirring for 3 hours. This solution was used as seeds directly without any further treatment.

Preparation of Au nanowires by using aged 4-MBA: Into 700 μL of 4-MBA (2 mM, aged for several months) ethanol solution, 100 μL of ascorbic acid (40 mM) aq. solution, 150 μL of $HAuCl_4$ (13.33 mM) aq. solution, 50 μL of **1**-AuNPs, were added in sequence with vortex mixing. Finally, the solution was

left undisturbed at room temperature for 16 hrs. The products were washed by ethanol to remove 4-MBA and the residual reactants, and isolated by centrifugation.

Preparation of 4-(ethoxycarbonyl)benzenesulfonic acid (2): 92.7 mg of potassium 4-carboxybenzenesulfonate was transferred into 5 mL of ethanol. The mixture was cooled in ice/H_2O mixture bath, followed by slow addition of 1 mL concentrated sulfuric acid. The mixture was then refluxed for 12 hrs. After cooling down to room temperature, ethyl acetate was used to extract the product. Finally the product was dried at reduced pressure.

Preparation of diethyl 4,4'-disulfanediyldibenzoate (3): The compound **3** was synthesized according to the literature.[19] Typically, 550 mg 4,4'-disulfanediyldibenzoic acid was added into 15 mL of ethanol. Into this suspension, 0.1 mL concentrated sulfuric acid was added. The mixture was then refluxed for 18 hrs, cooled down to room temperature, and concentrated under reduced pressure. The solution was combined with 25 mL of Dichloromethane, and washed with a saturated $NaHCO_3$ aq. (3×20 mL) and H_2O (3×20 mL). Finally the DCM solution was dried by anhydrous $MgSO_4$, and evaporated compound **3** appears as light yellow color oil.

Preparation of ethyl 4-mercaptobenzoate (4): Compound **4** was synthesized according to the previous literature.[19] Typically, 335 mg of compound **3** was added into 20 mL of ethanol/THF mixture (v/v = 1:1). The mixture was stirred and cooled in the ice/H_2O mixture bath for 10 min, followed by the slow

addition of 130 mg of NaBH$_4$. After the addition, the mixture was allowed to react for 4 hrs at room temperature. The mixture was then concentrated under reduced pressure. The solution was combined with 25 mL of ethyl acetate, and washed with a diluted HCl aq. (100 mM, 3×10 mL) and H$_2$O (3×10 mL). Finally the ethyl acetate solution was dried by anhydrous MgSO$_4$, and evaporated compound **4** appears as colorless oil.

Preparation of Au nanowires by using the mixture of 4-MBA and its deviates: Into 700 μL of the mixture of 4-MBA and its deviates (compound **3** or compound **4**) ethanol solution, 100 μL of ascorbic acid (40 mM) aq. solution, 150 μL of HAuCl$_4$ (13.33 mM) aq. solution, 50 μL of **1**-AuNPs, were added in sequence by vortex mixing. Finally, the solution was left undisturbed at room temperature for 16 hrs. The products were washed by ethanol to remove 4-MBA and the residual reactants, and isolated by centrifugation.

4.3 Results and discussion

4.3.1 Morphologies of Helical Gold Nanostructures

The helical Au NWs were synthesized by incubating HAuCl$_4$, ascorbic acid, 4-Mercaptobenzoic acid (4-MBA) in an ethanol/H$_2$O mixture (v/v = 7:3) at room temperature for 16 hrs. The products was black in color. To purify these products, they were washed by ethanol two times, and finally isolated by centrifugation. From the TEM images (Figure 4-1, 4-2, 4-3), the products in one pot of growth solution showed several kinds of helical structures with different

pitch length and width: single strand helices; double strands helices; multiple strands helices.
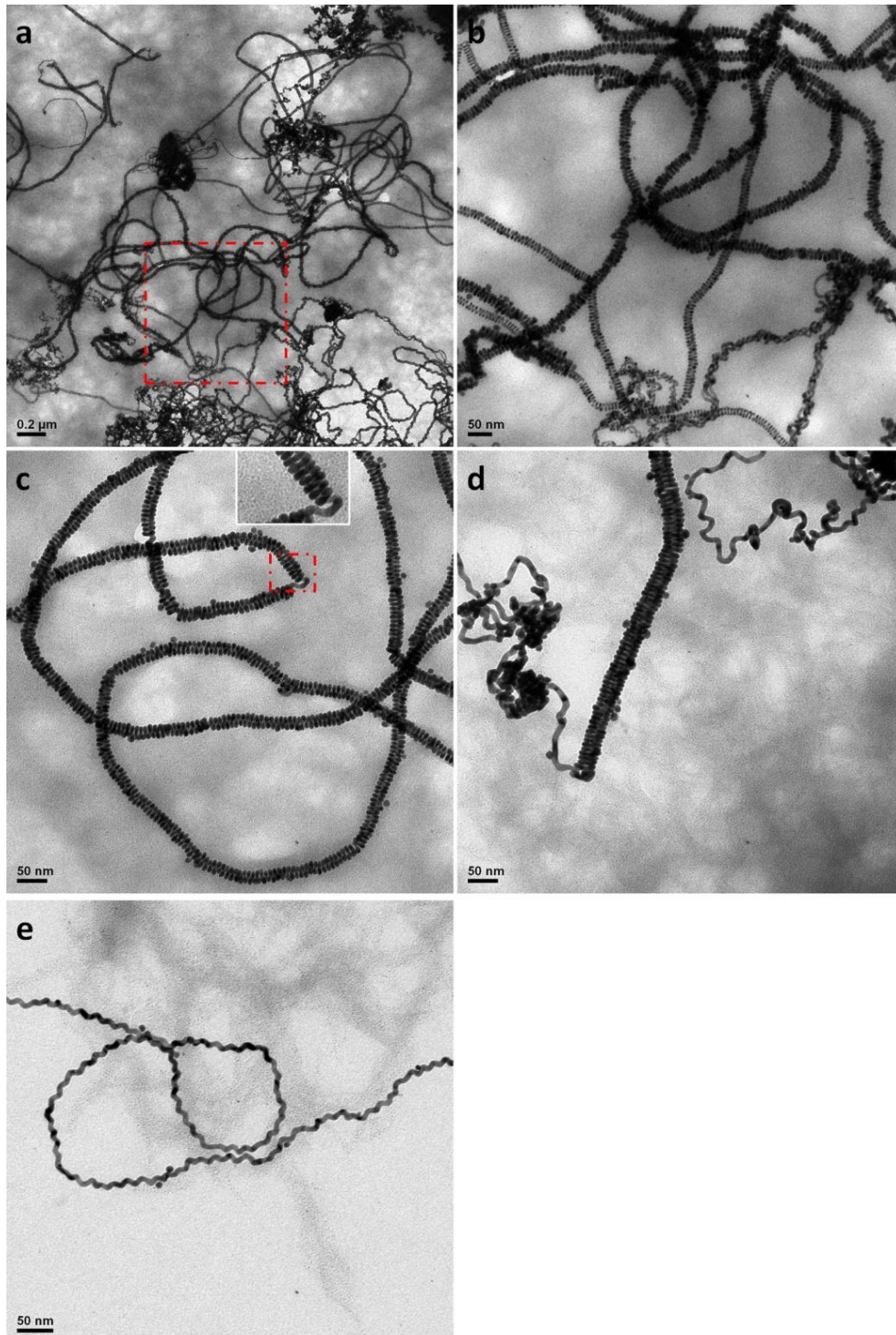

Figure 4-1 TEM images of single helical NWs with different width and pitch length. (a and b) large area and high magnification TEM images of the helical NWs, indicating the length of these helical NWs can reach to dozens of

micrometers, (c, d, and e) the TEM images of the helical NWs with different width (10~40 nm). Inset showed the magnified images of the single helices.

Figure 4-1 showed the TEM images of single helical NWs with different width and pitch length. From Figure 4-1a-d, we found that the helices were about tens of micrometers in length and with the same width in each single helix chain. It looked like that the growth of these NWs was highly dependent on the first step of growth. Once the helical NWs formed with a certain width, the whole helices will maintain this width, even while the length reached decades of micrometers. This was important information for this kind of helices, which would help us to understand the growth mechanism. As the NWs were stacked closely to form the helices, the pitch length almost equals to the diameter of these NWs (about 8~10 nm). The width of these single helices showed large range. Most of the single helices were shown in Figure 4-1a-c, in which the width of these helices was about 19~25 nm. Very few single helices, such as shown in Figure 4-1d, were with the width about 40 nm. In few cases, the pitch length increased to 15~23 nm; but the diameter was still about 9 nm (Figure 4-1e). Thus it seemed that this kind of single helices were formed by stretching the normal closely stacked helices. According to our previous results,[16, 20] we know that ultrathin gold NWs are always very flexible and elastic. It can be predicted that these NWs had excellent mechanical properties, which can be adopted as nanosprings in future smart nanodevices. Previously, the mechanical properties of carbon nanocoil have been well investigated.[21, 22] The characterization method can be applied for our helical NWs.
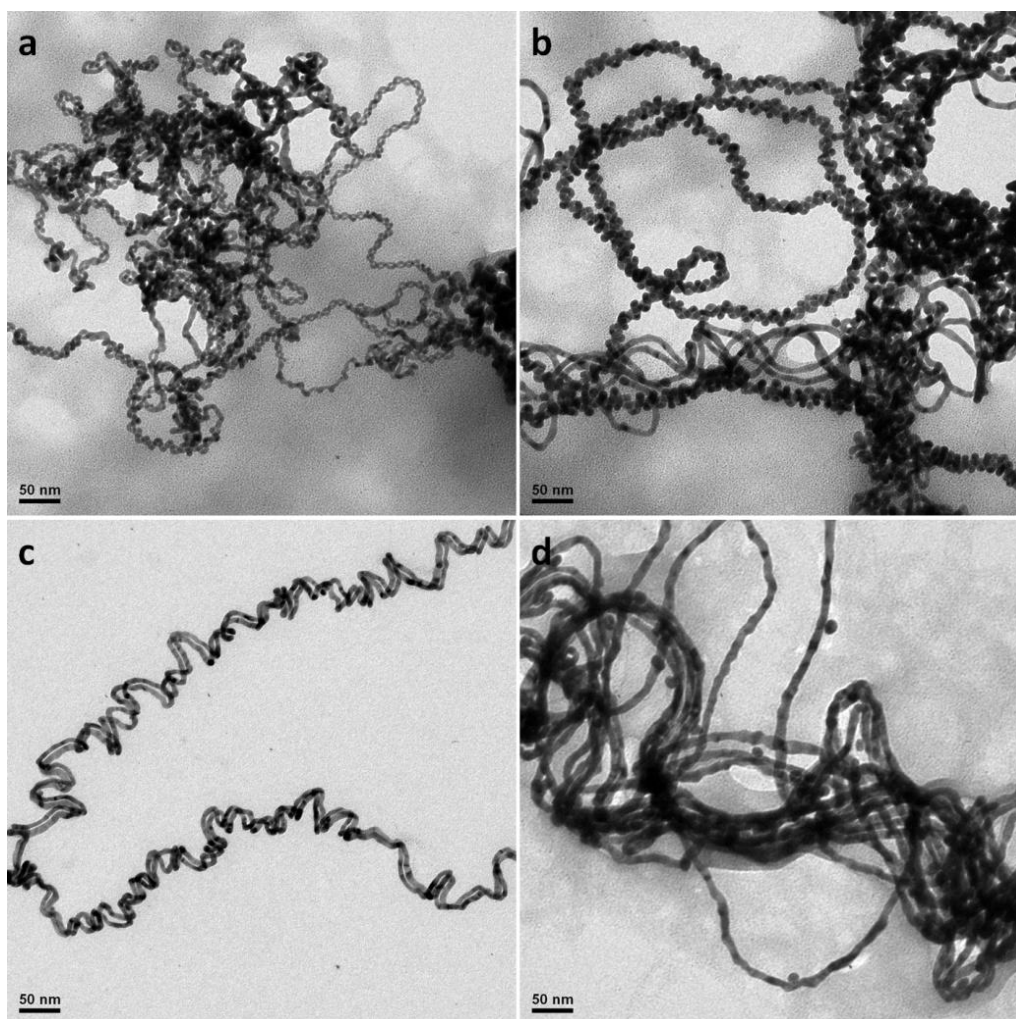
Figure 4-2 TEM images of double helical NWs with different width and pitch length. (a and b) the TEM images of double helices with different width (10~26 nm). (c) TEM images of double helices with irregular width, and pitch length, in which two NWs in the helices were stacked closely. (d) TEM image of one kind of single NWs coexisted in the product solution, in which the width was similar to the width of double helices in b.

Figure 4-2 showed the TEM images of several different kinds of double helices. In Figure 4-2a, the double helices represented the uniform width about 10 nm, and pitch length about 22.5~24.5 nm. In this case, the diameters of these NWs were about 4 nm, which was thinner than most of the NWs. In Figure 4-2b, the width of the double helices as well as the diameter of the NWs increased. The width of thinner segments was about 17.5 nm, in which two

NWs were wound uniformly. However, when the width increased to 26 nm, the double helices looked like one NW wound around the other straight NW. In this double helices case, the diameters of NWs were about 7~8.5 nm. Very few NWs exhibited the irregular twisting, as shown in Figure 4-2c. It's difficult to conclude the average width and pitch length owing to the highly rough packing. The diameters of these NWs were about 5~8 nm. Figure 4-2d showed single NWs with diameter about 10~12 nm, a little thicker than the NWs in the helices, but was very consistent with the width of double helices in Figure 4-2b. These NWs exhibited some curves and different TEM contrast along the NWs. The most possible reason was that these NWs were derived from the fusion of helical NWs during the NWs formation or TEM sample observation.

In these products, there were also some multiple helices, in which several NWs were intertwisting together. From the TEM images (Figure 4-3), several NWs wound around one NW or NW bundles. The width of these helices were in large range (about 50~80 nm), and the pitch length were about 110~150 nm. The diameters of the NWs in these multiple helices were about 5.5 nm. Comparing the diameters of NWs changing in all kinds of helices, we concluded that the NWs in the single strand helices were with thickest diameter (about 8~10 nm); when the diameter of NWs decreased to about 7~8 nm, the NWs showed double helical structures and continuing decreasing the diameter of NWs, double helices with smallest width or multiple strands helices appeared. Thus the thickness of NWs was associated with the formation of helices. This

may also be one breakthrough towards the optimization of the helices growth condition.
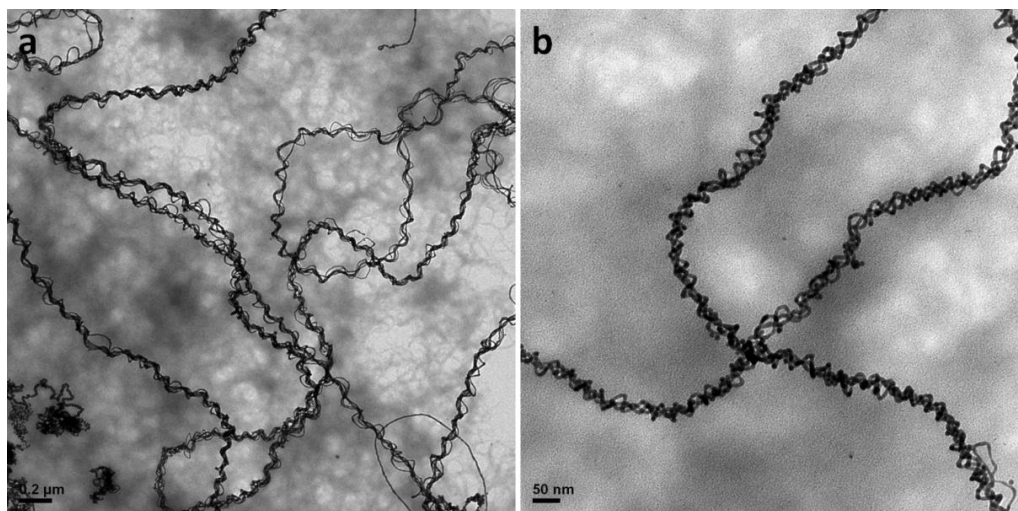
Figure 4-3 TEM images of multiple helical NWs formed by intertwisting several NWs together.

The separation of these products is obvious very important. The efficient method is to optimize the synthesis conditions after fully understanding the controlling factors to different morphologies. Of course, NWs also could be manipulated by optical tweezers,[23] optoelectronic tweezers,[24] or AFM probe[21] to accomplish the separation.

These helical NWs were very fragile either in the product solution or under the TEM beam irradiation. Figure 4-4a and b showed the TEM images of the double helices were fused together to form single NW. From Figure 4-4a, we found that the fused domains in the NWs showed two different thickness. The reason may be that the helices here had two different morphologies, similar to the inset of Figure 4-1c, in which some helices were close stacked, and some were stretched. After the electron beam irradiation, they fused to form two

different parts (*i* and *ii,* as shown in the inset of Figure 4-4a) with different thickness. From the magnified TEM image Figure 4-4b, the intermediate state of the helices fusion was trapped. Along the NWs, some segments have been fused together to form single NWs already, but some have no. The inset showed that these two NWs were going to fuse. After fusion, the NWs exhibited the single helical morphology, even straight NWs with few curves. If the product NWs haven't been isolated from the solution and purified after formation, these NWs would fuse by themselves (Figure 4-4c). This phenomenon indicated that these NWs were not thermodynamic stable due to the close packing of these NW strands in the helices. However, for the stretched helices, the intervals of the NWs were large, ensuring the stability of these helices.
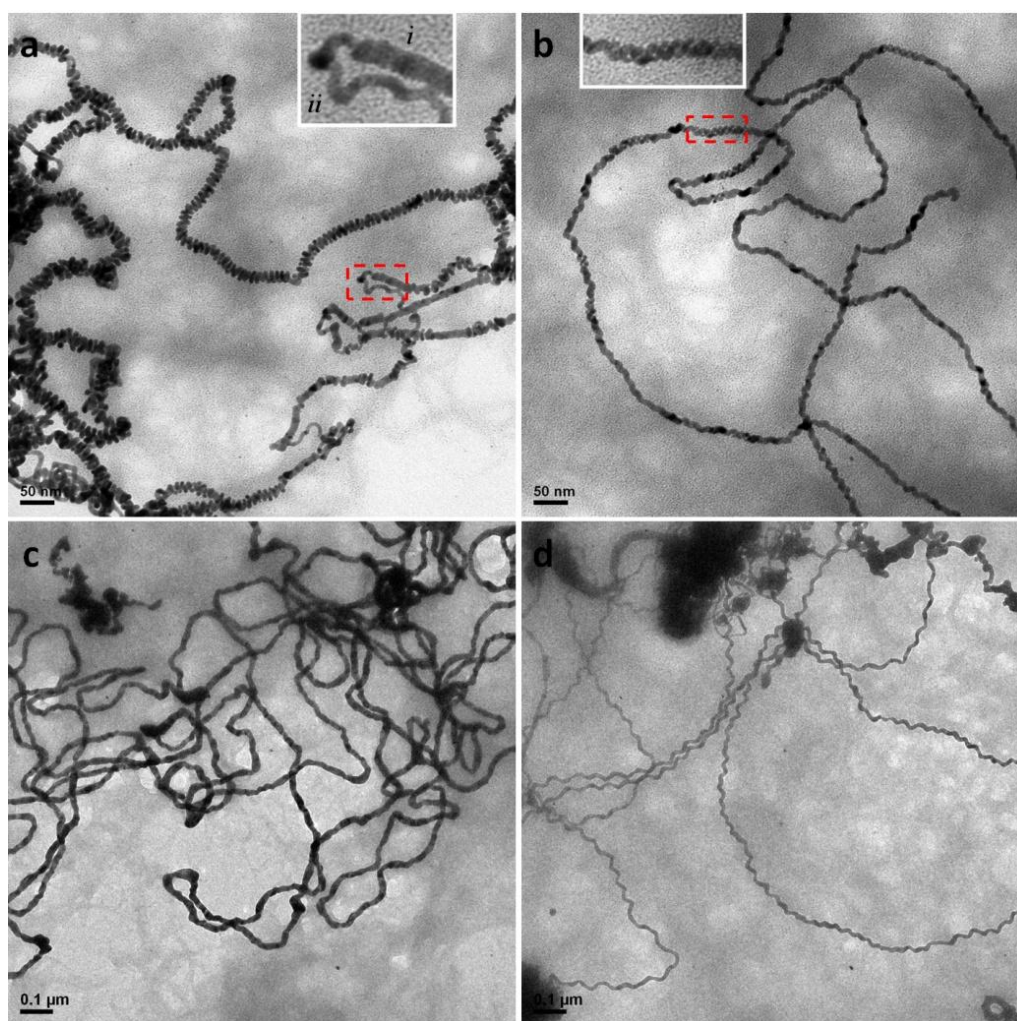
Figure 4-4 (a, and b) TEM images of helices fusion during the TEM observation. (c) TEM images of the helices products stored in the solution for three days, in which the helices formed with close arrangement of NWs were fused together to form the single NW, and the "stretched" helices remained their original structures. Insets showed the magnified TEM images corresponding to the red rectangles.

4.3.2 Optimization of Synthesis Condition

As the aged 4-MBA was used for the synthesis of helical gold nanostructures, and the freshly prepared 4-MBA didn't work, it was critical to find the optimal conditions. It is well known that thiophenol is very unstable and can even be oxidized by air.[19] The 4-MBA ethanol solution was prepared several months

ago and thus these 4-MBA could be oxidized to form the disulphide compound or continue oxidizing to form the sulfinate, and sulphonate compounds. Perhaps, the esterification reaction also took place under this long incubation time. From the LC-MS analysis (Figure 4-5, Figure 4-6, and Figure 4-7), we found that the main compound in 4-MBA ethanol solution changed quickly along with the incubation process. According to Figure 4-7, after 10 months incubation at room temperature, the main product of 4-MBA derivative should be 4-(ethoxycarbonyl)benzenesulfonic acid (**2**). Figure 4-8 showed the LC-MS analysis of the synthesized compound **2**. However, when this compound was used to perform the helical Au NWs growth, the solution color changed quickly. From TEM observation, there was no helical product. Thus the helical structure may be originated from others derivatives of 4-MBA, perhaps the mixture of these compounds.

So several derivatives of 4-MBA, such as 4,4'-disulfanediyldibenzoate (compound **3**), 4-mercaptobenzoate (compound **4**), as well as potassium 4-carboxybenzenesulfonate were synthesized or purchased for the helical NWs growth. The synthesized compounds also were confirmed by the LC-MS analyses (Figure 4-9, and Figure 4-10). All the growth conditions were similar to the previous case, except the derivatives instead of the aged 4-MBA solution.
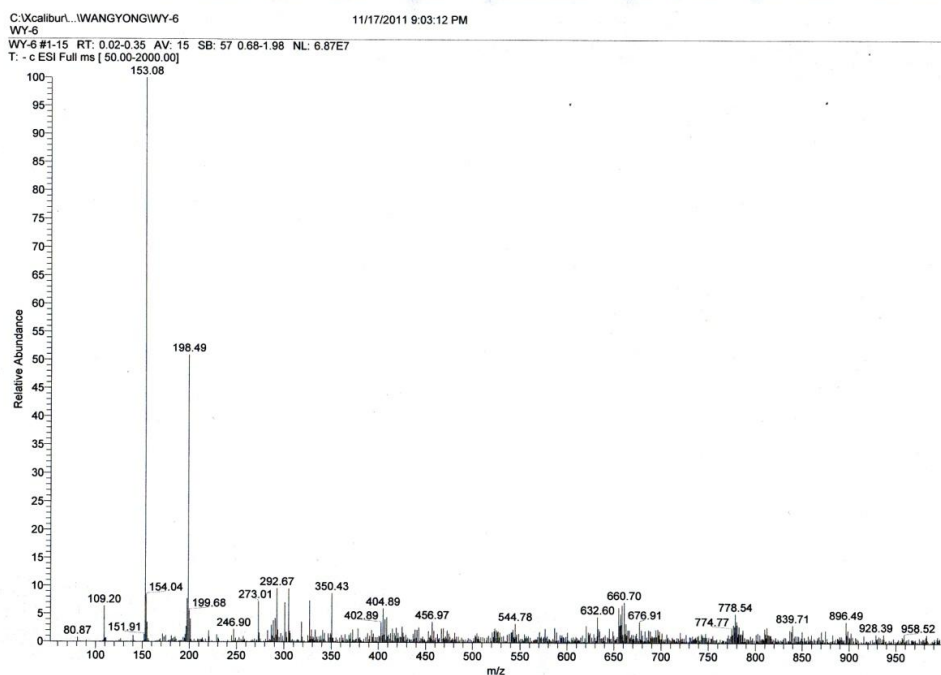
Figure 4-5 LC-MS of the fresh prepared 4-MBA ethanol solution.
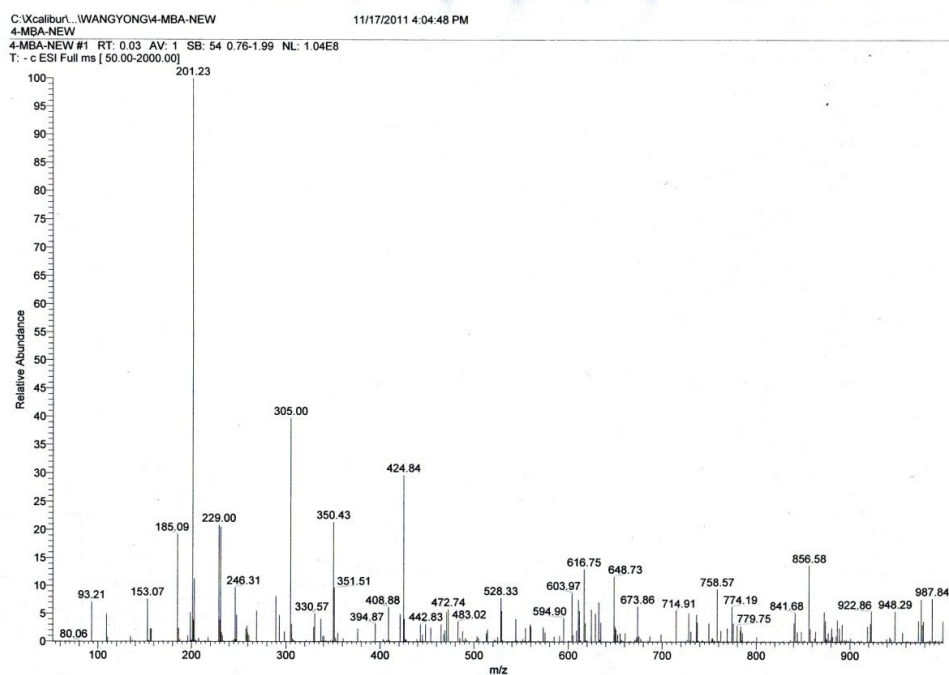
Figure 4-6 LC-MS of the 4-MBA ethanol solution incubated at room temperature for two weeks.
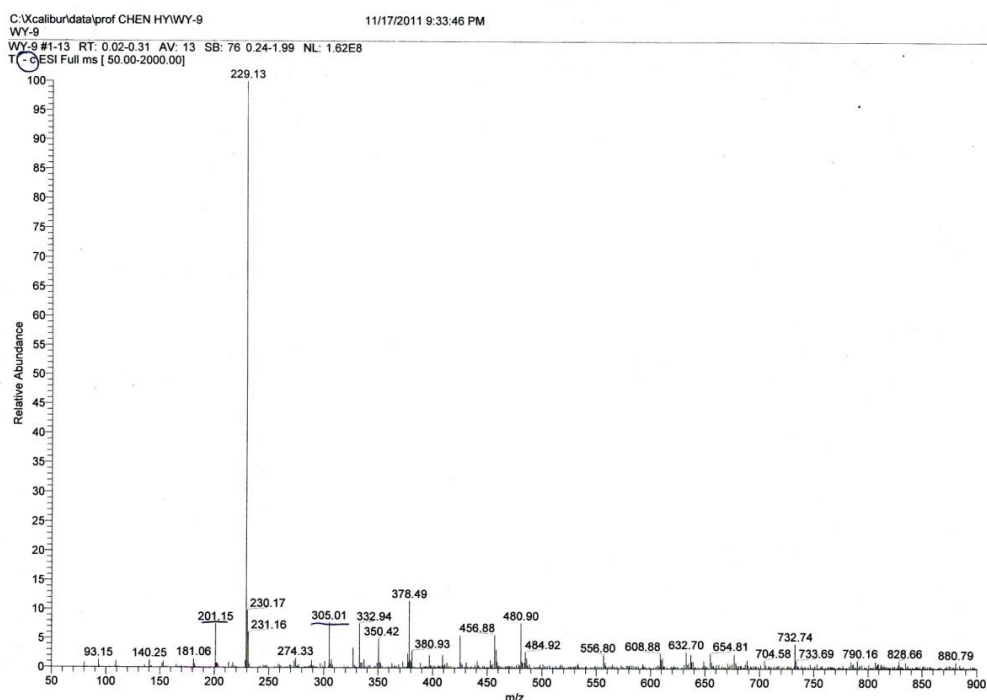
Figure 4-7 LC-MS of the 4-MBA ethanol solution incubated at room temperature for 10 months.
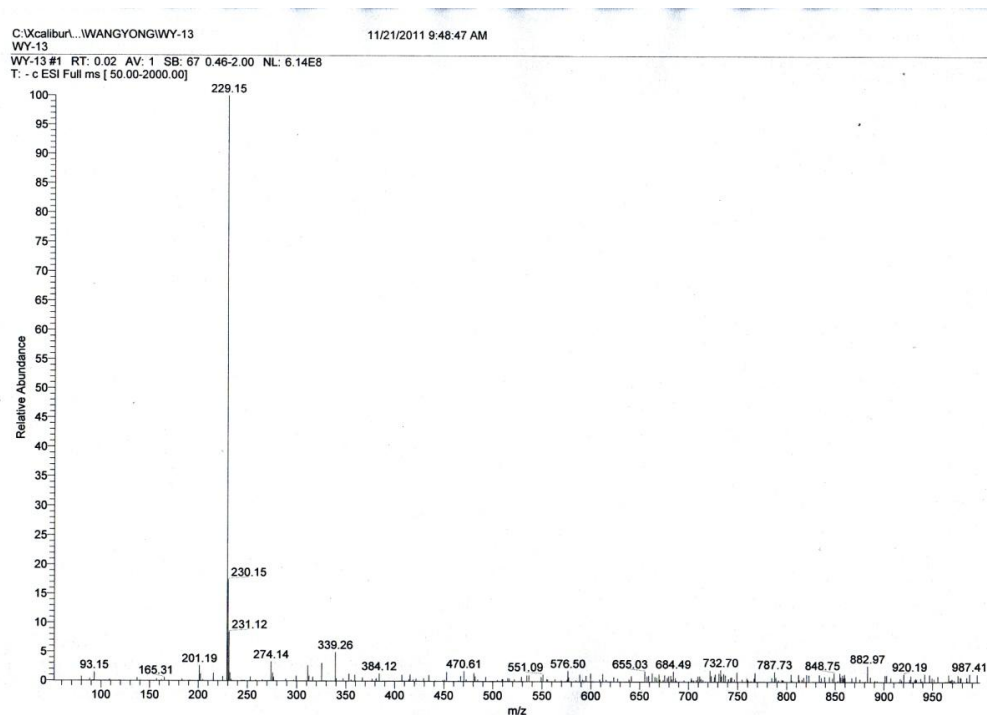
Figure 4-8 LC-MS of the compound **2**: 4-(ethoxycarbonyl)benzenesulfonic acid.
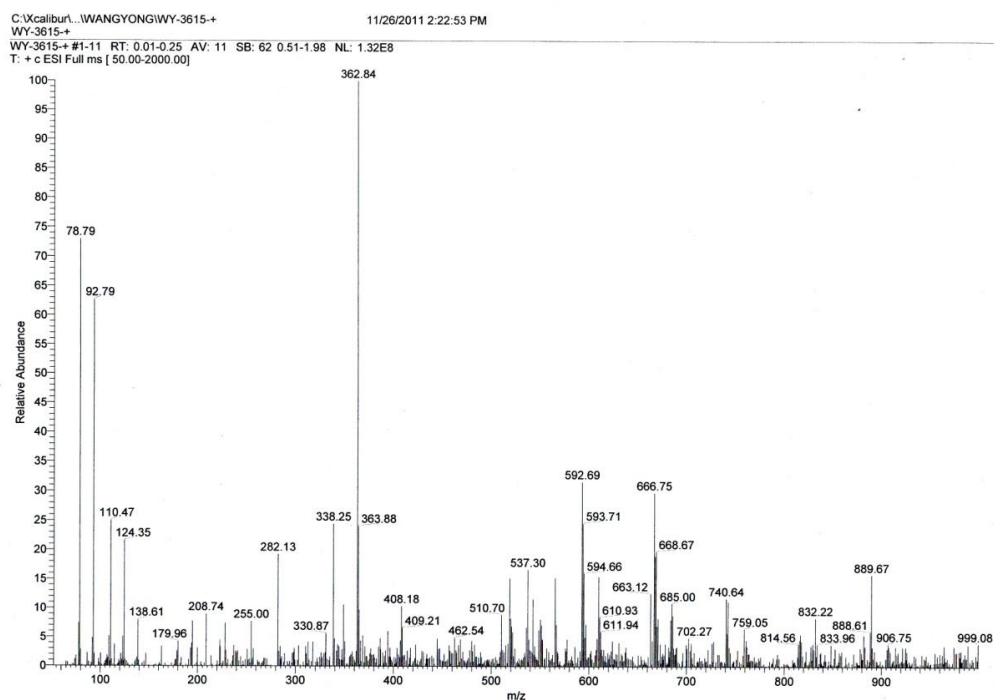
Figure 4-9 LC-MS of the compound **3**: diethyl 4,4'-disulfanediyldibenzoate.
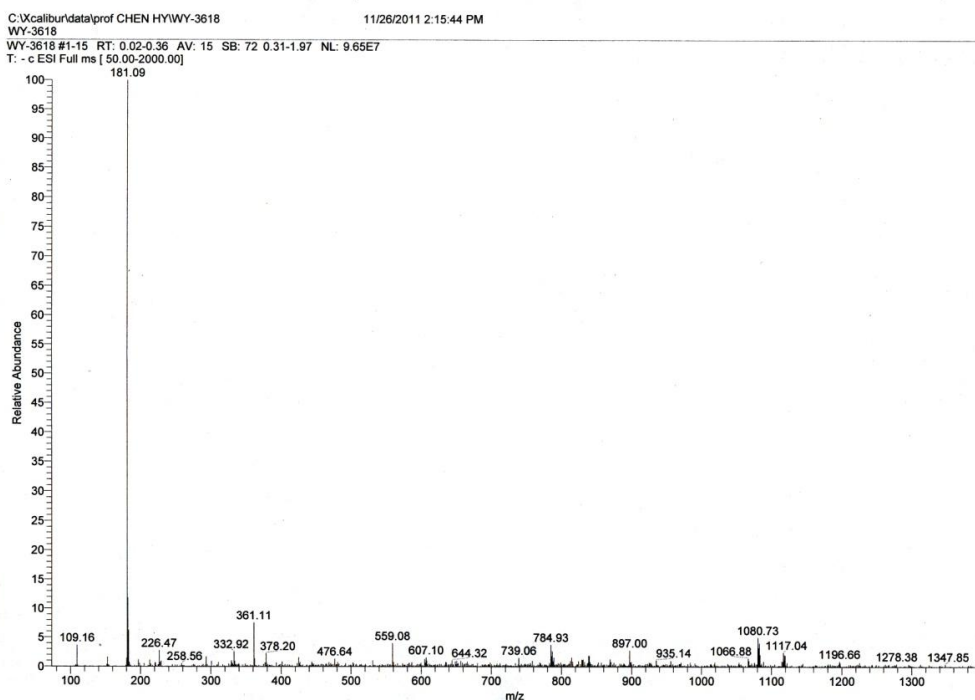
Figure 4-10 LC-MS of the compound **4**: ethyl 4-mercaptobenzoate.
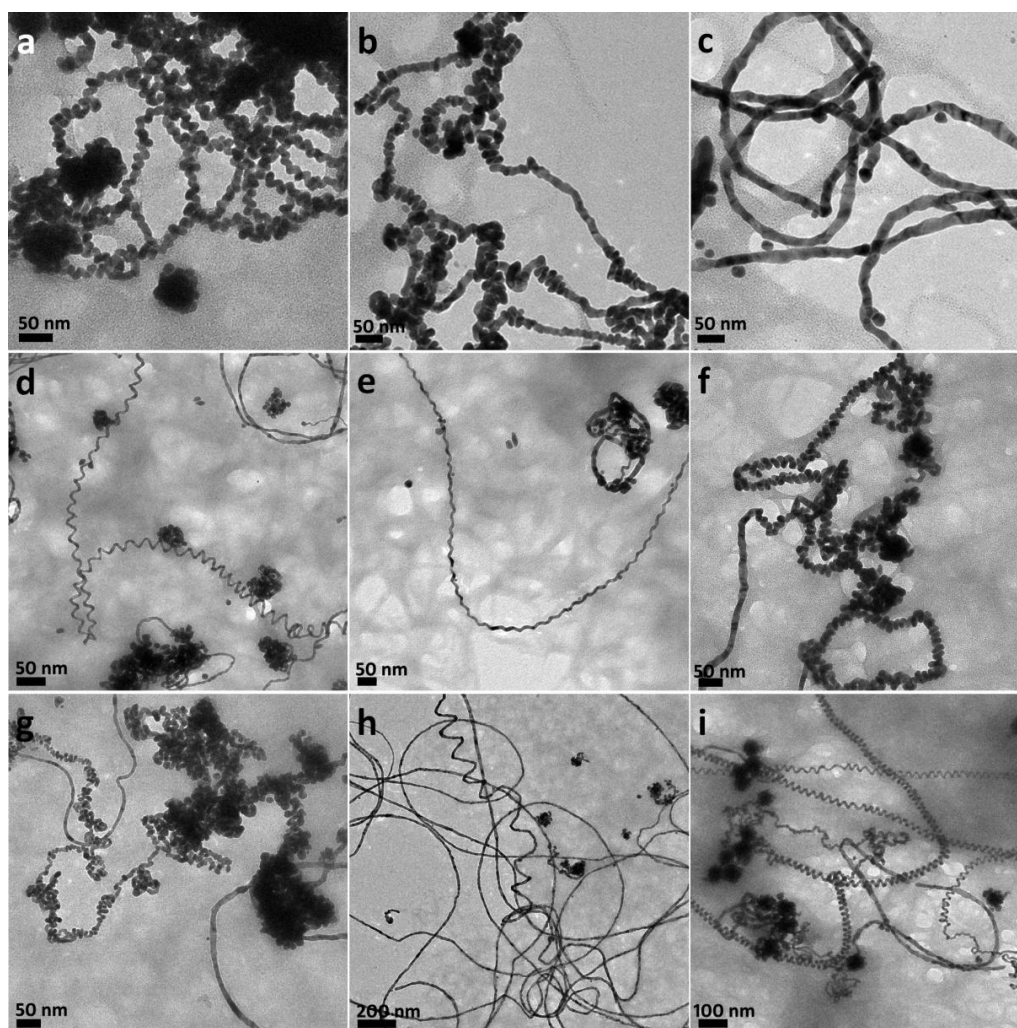
Figure 4-11 TEM images of the helical gold NWs synthesized in the mixture of 4-MBA derivates and 4-MBA at different final concentration: (a) compound **3** (50 μM) and 4-MBA (200 μM); (b, and c) compound **3** (100 μM) and 4-MBA (200 μM); (d, and e) compound **3** (200 μM) and 4-MBA (400 μM); (f) compound **4** (100 μM) and 4-MBA (200 μM); (g, and h) compound **4** (200 μM) and 4-MBA (200 μM); (i) compound **3** (100 μM), compound **4** (200 μM) and 4-MBA (200 μM).

When only compound **3** or compound **4** were used, no helical NW appeared in the solution. Even after tuning the concentration as well as the pH value of the growth solution, helical NW was not produced. Therefore, we hypothesized that the mixture of derivatives and 4-MBA may play the role. When compound **3** or compound **4** was used in the presence of fresh 4-MBA, there were some

helical NWs. However, these yields were still very low (Figure 4-11).

When small amount of compound **3** and 4-MBA were used as the capping agents, the main products were the straight NWs. These NWs also exhibited some curves, and different TEM contrast along the NWs, which were similar to the case presented previously (Figure 4-2d). The diameters of these NWs were in the range of 12~18 nm, which were little thicker than the previous ones. Some helical NWs can also be found in the product. As shown in Figure 4-11a, the TEM image represented the close packing helical NWs with the diameter of about 9 nm. However, the size of the helix in one NW was non-uniform, which is different from the aged 4-MBA induced helical NWs. The width and pitch length of these helices was about 16~22 nm, and 15~18 nm, respectively. When the amount of compound **3** was increased lightly, the products were similar to the Figure 4-11a case. The only difference was the repeating units in helices were stacking more closely, thus the fusion process can be observed when the sample was under the electron beam (Figure 4-11b). It still cannot be distinguished whether some NWs with many curves formed in the solution or fused from the helices (Figure 4-11c). These diameters were similar to the straight NWs discussed previously. By continuing increasing the amount of compound **3**, some uniform helices appeared with very low yield. There were two kinds of helices with different width and pitch length. As shown in Figure 4-11d, the diameter, width, and pitch length of these NWs were about 11 nm, 33nm, 48~55nm, respectively. The other kind of NWs were with the diameter,

width, and pitch length about 11 nm, 16 nm, 30~35 nm, respectively (Figure 4-11e). From this series of experiments, it was found that the amount of compound **3** in the growth solution could influence the product greatly. The thickness of these NWs was about 9~11 nm under different capping agent concentration. However, the pitch length and the width of the helices could change: more amount of compound **3**, resulted in longer pitch length and width. However, the yield of the helical NWs was still very low.

When compound **4** was used at very low concentration, the products were similar to the case of low concentration of compound **3** was used. One typical TEM image was shown in Figure 4-11f. The curving NWs formed owing to the fusion were also observed, which were not presented here. However, when the amount of compound **4** increased slightly, the products showed non-uniform helices. As shown in Figure 4-11g, the helices with different width and pitch length appeared in short distance of one NW. This may be because the structure of compound **4** being similar to 4-MBA, which could disturb the regular packing of these two kind of capping agents, thus influencing the NW growth. Other than this kind of helical NWs, some helices with width about 100 nm was also observed. The pitch length of these NWs could reach up to about 150 nm (Figure 4-11h).

Interestingly, when the mixture of compound 3, compound 4, and 4-MBA was used to perform the NWs growth, some uniform helices can be obtained. As shown in Figure 4-11i, the diameter of these helices was about 11 nm,

similar to the previous cases. The width of these helices was about 19 nm. At different areas of one helix, the pitch length could vary from 22 nm to 55 nm. This indicated that these helices were very flexible, ensuring the potential application as nanosprings in further nanodevices.

Comparing to the previous cases of the metallic helices, the advantages of our method are that the diameter, width as well as the pitch length are very small and can be tuned by changing the amount of capping agents easily in the colloidal solution. It is well known that in the previous cases, hard templates are compulsively used, which prevented scale up synthesis.[12, 13] However, until now, the yield and reproducibility of this process are both very poor. This also prevents us insight into the growth mechanism. However, the existing results can lead us some hypotheses. From Fig 4-1a, we can find that the length of the single strand gold helix can reach several micrometers, suggesting the very fast growth velocity. Moreover, the width is also uniform. So the possibilities that template-assistant growth or confined-environment growth are very small. It's hard to imagine that the small molecules can form so long template or confined-environment uniformly. However, we still cannot rule out this hypothesis. We also suppose that dislocation driven growth is possible to conduct the helices formation. But we still do not know the origination of the dislocation. Somehow, after adding the 4-MBA derivates, the dislocation was induced at the first stage of gold deposition. Then gold can grow under this driven force to form ultra-long helices. But this proposal requires further

experimental evidences. The yield issue is also one aspect to be improved in the further work.

4.3.1 Crystal Structure Analysis of the Gold Helices

The crystal structure of one typical helix has been studied by using the HRTEM characterization (Figure 4-12). Due to the low yield of the helices, the HRTEM sample preparation is highly challenged. Thus, the primary HRTEM characterization is still not satisfying. From the HRTEM image, combining the diagnostic angles of these planes, lattice fringes with the interplanar distances of 0.233 nm, 0.226 nm, and 0.213 nm could be assigned to {111}, {111}, and {200} planes of FCC gold, respectively. Thus the NW grew along the <100> direction. For the {200} planes, a small offset angle was observed along the growth direction, which may be due to the spiral of the NW. In the right side of the HRTEM image, the lattice spacing is about 0.191 nm. This value may be due to the inaccurate measurement caused by the helical pose of the NW. The complete characterization of these NWs will be carried out in the future after improving the yield of helices.
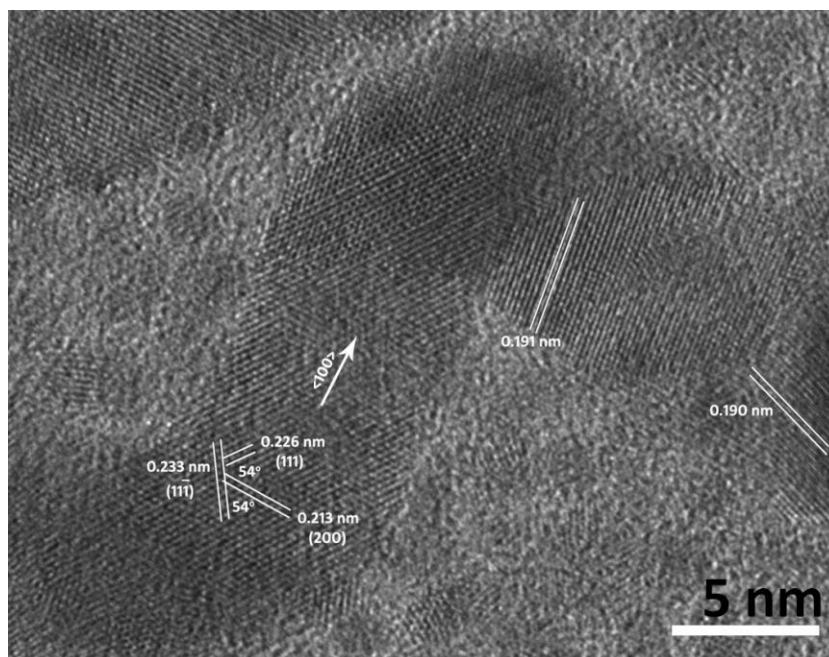
Figure 4-12 HRTEM image of one typical gold helix.

4.4 Conclusion

In this chapter, helical gold NWs were synthesized in colloidal solution in the presence of small organic molecules. Different kinds of helices, such as single strand helix, double strands helices, and multiple strands helices coexisted in one pot of growth solution. This is the first time to obtain metallic helices without the hard template, such as AAO channels. In our case, the helical NWs were formed owing to the mixture of 4-mercaptobenzoic acid and its deviates. This mixture may offer one novel soft template for the metallic helices growing. By tuning the amount of these organic molecules, the helices were primarily controlled. However, the yield was still very low. We could predicted that this kind of spring-like gold NWs could be potentially applied for the development of future smart nanodevices.

4.5 Bibliography

[1] Baiker, A., Progress in Asymmetric Heterogeneous Catalysis: Design of Novel Chirally Modified Platinum Metal Catalysts. *Journal of Molecular Catalysis a-Chemical*, **115**, 473 (1997).

[2] Thomas, J. M. and Raja, R., Exploiting Nanospace for Asymmetric Catalysis: Confinement of Immobilized, Single-Site Chiral Catalysts Enhances Enantioselectivity. *Acc. Chem. Res.*, **41**, 708 (2008).

[3] Hazen, R. M. and Sholl, D. S., Chiral Selection on Inorganic Crystalline Surfaces. *Nat. Mater.*, **2**, 367 (2003).

[4] Che, S., Liu, Z., Ohsuna, T., Sakamoto, K., Terasaki, O., and Tatsumi, T., Synthesis and Characterization of Chiral Mesoporous Silica. *Nature*, **429**, 281 (2004).

[5] Shemer, G., Krichevski, O., Markovich, G., Molotsky, T., Lubitz, I., and Kotlyar, A. B., Chirality of Silver Nanoparticles Synthesized on DNA. *J. Am. Chem. Soc.*, **128**, 11006 (2006).

[6] Oh, H. S., Liu, S., Jee, H., Baev, A., Swihart, M. T., and Prasad, P. N., Chiral Poly(Fluorene-Alt-Benzothiadiazole) (Pfbt) and Nanocomposites with Gold Nanoparticles: Plasmonically and Structurally Enhanced Chirality. *J. Am. Chem. Soc.*, **132**, 17346 (2010).

[7] Nakashima, T., Kobayashi, Y., and Kawai, T., Optical Activity and Chiral Memory of Thiol-Capped Cdte Nanocrystals. *J. Am. Chem. Soc.*, **131**, 10342 (2009).

[8] Mastroianni, A. J., Claridge, S. A., and Alivisatos, A. P., Pyramidal and Chiral Groupings of Gold Nanocrystals Assembled Using DNA Scaffolds. *J. Am. Chem. Soc.*, **131**, 8455 (2009).

[9] Li, C., Deng, K., Tang, Z. Y., and Jiang, L., Twisted Metal-Amino Acid Nanobelts: Chirality Transcription from Molecules to Frameworks. *J. Am. Chem. Soc.*, **132**, 8202 (2010).

[10] Chen, C. L., Zhang, P. J., and Rosi, N. L., A New Peptide-Based Method for the Design and Synthesis of Nanoparticle Superstructures: Construction of Highly Ordered Gold Nanoparticle Double Helices. *J. Am. Chem. Soc.*, **130**, 13555 (2008).

[11] Chen, W., Bian, A., Agarwal, A., Liu, L. Q., Shen, H. B., Wang, L. B., Xu, C. L., and Kotov, N. A., Nanoparticle Superstructures Made by Polymerase

Chain Reaction: Collective Interactions of Nanoparticles and a New Principle for Chiral Materials. *Nano Lett.*, **9**, 2153 (2009).

[12] Wu, Y. Y., Cheng, G. S., Katsov, K., Sides, S. W., Wang, J. F., Tang, J., Fredrickson, G. H., Moskovits, M., and Stucky, G. D., Composite Mesostructures by Nano-Confinement. *Nat. Mater.*, **3**, 816 (2004).

[13] Liu, L. C., Yoo, S. H., Lee, S. A., and Park, S., Wet-Chemical Synthesis of Palladium Nanosprings. *Nano Lett.*, **11**, 3979 (2011).

[14] Kamata, K., Suzuki, S., Ohtsuka, M., Nakagawa, M., Iyoda, T., and Yamada, A., Fabrication of Left-Handed Metal Microcoil from Spiral Vessel of Vascular Plant. *Adv. Mater.*, **23**, 5509 (2011).

[15] Velázquez-Salazar, J. J., Esparza, R., Mejía-Rosales, S. J., Estrada-Salas, R. n., Ponce, A., Deepak, F. L., Castro-Guerrero, C., and José-Yacamán, M., Experimental Evidence of Icosahedral and Decahedral Packing in One-Dimensional Nanostructures. *ACS Nano*, **5**, 6272 (2011).

[16] Wang, Y., Wang, Q., Sun, H., Zhang, W., Chen, G., Wang, Y., Shen, X., Han, Y., Lu, X., and Chen, H., Chiral Transformation: From Single Nanowire to Double Helix. *J. Am. Chem. Soc.*, **133**, 20060 (2011).

[17] Frens, G., Controlled Nucleation for Regulation of Particle-Size in Monodisperse Gold Suspensions. *Nature Phys. Sci.*, **241**, 20 (1973).

[18] Brown, K. R., Walter, D. G., and Natan, M. J., Seeding of Colloidal Au Nanoparticle Solutions. 2. Improved Control of Particle Size and Shape. *Chem. Mater.*, **12**, 306 (2000).

[19] Gentili, D., Ori, G., and Comes Franchini, M., Double Phase Transfer of Gold Nanorods for Surface Functionalization and Entrapment into Peg-Based Nanocarriers. *Chem. Commun.*, 5874 (2009).

[20] Xu, J., Wang, H., Liu, C. C., Yang, Y. M., Chen, T., Wang, Y. W., Wang, F., Liu, X. G., Xing, B. G., and Chen, H. Y., Mechanical Nanosprings: Induced Coiling and Uncoiling of Ultrathin Au Nanowires. *J. Am. Chem. Soc.*, **132**, 11920 (2010).

[21] Chen, X., Zhang, S., Dikin, D. A., Ding, W., Ruoff, R. S., Pan, L., and Nakayama, Y., Mechanics of a Carbon Nanocoil. *Nano Lett.*, **3**, 1299 (2003).

[22] Volodin, A., Buntinx, D., Ahlskog, M., Fonseca, A., Nagy, J. B., and Van Haesendonck, C., Coiled Carbon Nanotubes as Self-Sensing Mechanical Resonators. *Nano Lett.*, **4**, 1775 (2004).

[23] O'Neil, A. T. and Padgett, M. J. *Manipulation of Metallic Particles in Inverted Optical Tweezers*. in *Lasers and Electro-Optics, 1999. CLEO '99. Summaries of Papers Presented at the Conference on*. 1999.

[24] Jamshidi, A., Pauzauskie, P. J., Schuck, P. J., Ohta, A. T., Chiou, P.-Y., Chou, J., Yang, P., and Wu, M. C., Dynamic Manipulation and Separation of Individual Semiconducting and Metallic Nanowires. *Nat Photon*, **2**, 86 (2008).

Chapter 5 Heterodimer Synthesis Based on Seed-mediated Growth in Colloidal Solution

5.1 Introduction

Colloidal growth of nanoparticles (NPs) has made remarkable advances in the past several decades. Preparation of NPs with different shapes or surface facets planes is one significant theme, especially for the metallic NPs, in which the Surface Plasmon Resonance (SPR) can be fine tuned by the shape and size,[1-8] and the catalytic properties are extremely relied on the facets,[9-12] *etc*.

Great efforts have been devoted to synthesize various NPs based on the seed-mediated growth, because the formed NPs are dependent on the seeds morphologies and lattices.[13-20] However, most of these works are performed by using a single crystalline particle or twined particle as seeds, which have regular lattice stacking. However, there are few reports about NPs growth based on polycrystalline NPs, which are more easily to be synthesized than single crystalline NPs.[21]

In the last few years, multi-component nanostructures have attracted many researchers' attention due to not only the multifunctional properties of each

individual but also the new features derived from the interaction of the individuals.[13, 22-29] Beside the template growth strategy, the most popular method is the seed-mediated growth. Typically, Yang and co-workers reported that the PtNPs served as seeds for the localized growth of Pd, and epitaxial growth of Au, which were used for enhanced electrocatalytic applications.[13, 28] Xia and co-workers found that Pt NPs can be grown on CeO_2 surface to enhance the catalytic activity of reduction reaction.[29]

In this chapter, polycrystalline PtNPs and ligand functionalized AuNPs were used as the seeds for the growth of hetero-composites nanostructures. Sodium citrate, ascorbic acid, and hydroquinone were selected as the reducing agents, adopting the different reducibility. Au and Ag were grown on these seeds to form the heterodimeric structures due to the single nucleation site. Particularly, in the PtNPs seeds system, Ag triangle structures were obtained at higher $AgNO_3$ and hydroquinone concentration. This strategy will expand the NPs growth, in which polycrystalline NPs can be used as seeds for the heterodimer formation.

5.2 Materials and Methods

5.2.1 Materials

Materials: All chemical reagents were used as purchased without further purification. Hydrogen tetrachloroaurate(III) hydrate ($HAuCl_4 \cdot 3H_2O$), 99.9% (metal basis Au 49%), silver nitrate ($\geq$99+%), sodium citrate dihydrate ($\geq$ 99.0%), Hydroquinone (ReagentPlus®, $\geq$99%); polyvinylpyrrolidone (PVP,

M$_w$: 40,000); Hexadecyltrimethylammonium bromide (CTAB) were purchased from Sigma Aldrich; Pentaerythritol tetrakis(3-mercapto-propionate), **1**, was purchased from Aldrich; ethanol (analytical grade) was purchased from Fisher Scientific; all other chemicals were purchased from Aldrich. Deionized water (resistance > 18 MΩ·cm^{-1}) was used in all reactions. Copper specimen grids (300 meshes) with formvar/carbon support film (referred to as TEM grids in the text) were purchased from Beijing XXBR Technology Co, Ltd.
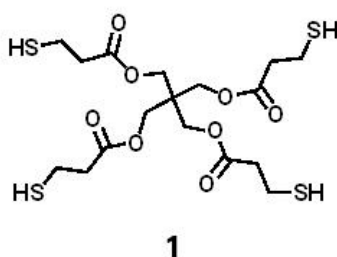
Scheme 5-1 ligand used in this chapter

Characterization Methods: TEM images were collected from a JEM-1400 transmission electron microscope (JEOL) operated at 100 kV. High-resolution TEM image were collected from a JEM-2100F Transmission Electron Microscope (JEOL) operated at 200 kV. SEM images were collected from a JEOL-6700F Scanning Electron Microscopy operated at 10 kV. UV–Visible spectra were collected on a Cary 100 UV-Vis spectrophotometer.

Preparation of TEM samples: TEM grids were treated with oxygen plasma in a Harrick plasma cleaner/sterilizer for 1 min to improve the surface hydrophilicity. The grid was placed face-down on a droplet of as-synthesized sample laid on a plastic Petri dish. A filter paper was used to wick off the excess

solution on the TEM grid, which was then dried in air for 5 min.

5.2.2 Methods

Synthesis of monodisperse polycrystalline PtNPs. All the PtNPs were synthesized following the literature procedures with little modification.[30] For the seeds solution, in a typical synthesis, a 250 mL round bottom flask was charged with 100 ml aq. $H_2PtCl_6 \cdot 6\,H_2O$ (0.278 mM). This solution was heated to 100 °C with vigorous stirring. Then 2.2 mL of a solution containing sodium citrate (1%) and citrate acid (0.05%) was added. After heating the mixture for half a min, 1.1 mL of a freshly prepared sodium borohydrate (21 mM) solution containing sodium citrate (1%) and citrate acid (0.05%) was quickly injected. The solution was cooled down to room temperature after heating for 10 min.

For the large PtNPs (27 $\pm$ 1.5 nm) solution, in a 250 mL round bottom flask, which was charged with 97 ml aq. $H_2PtCl_6 \cdot 6\,H_2O$ (0.6 mM), 3 mL of the previous Pt seeds solution was added at room temperature. 1.5 mL of an L-ascorbic acid solution (71 mM) containing sodium citrate (1%) was added into this mixture solution. The temperature was increased to the boiling point at the speed of 10 °C/min. The solution was stirred during the whole heating time (45 min). The average particle diameter was measured to be 27 $\pm$ 1.5 nm from TEM images using ImageJ.

Larger PtNPs (48.5 $\pm$ 1.8 nm) can be obtained by using the 27 nm PtNPs as seeds. In a typical synthesis, in a 250 mL round bottom flask, which was charged with 88 ml aq. $H_2PtCl_6 \cdot 6\,H_2O$ (0.66 mM), 12 mL of the previous Pt

seeds solution was added at room temperature. 1.5 mL of an L-ascorbic acid solution (71 mM) containing sodium citrate (1%) was added into this mixture solution. The temperature was increased to the boiling point at the speed of 10 °C/min. The solution was stirred during the whole heating time (45 min). The average particle diameter was measured to be 64.5 ± 4.5 nm from TEM images using ImageJ.

Synthesis of AuNPs by seeded growth. Larger AuNPs (36 ± 2.7 nm) were synthesized according to the method mentioned in chapter 2, but more 15 nm AuNPs was used as seeds.[21, 31] In a typical synthesis, a 250 mL round bottom flask was charged with 100 mL aq. $HAuCl_4$ (0.25 mM). The solution was refluxed with vigorous stirring for 10 min, and then 16 mL of AuNP seeds (d_{AuNP} = 15 nm) and 500 µL of sodium citrate (38.7 mM) was added. After boiling the solution for 45 min, a deep-red AuNP solution was obtained. The solution was cooled to room temperature. The average diameter was measured to be 36 ± 2.7 nm from TEM images using ImageJ.

Synthesis of Pt-M (M = Ag or Au) hetero-nanocomposites. The main idea of these syntheses of these hetero-nanocomposites is to reduce the metal precursors by using large Pt NP seeds (65 nm). With different reducing agents and stabilizers, different structures can be obtained:

Pt-M (M = Ag or Au) nanocomposites synthesized w/o PVP by the reduction of sodium citrate. In a typical synthesis, 750 µL of the as-synthesized PtNPs solution was centrifuged to 5 µL, and then transferred

into 2 mL aq. AgNO$_3$ (0.5 mM, or HAuCl$_4$) w/o PVP (100 mM). Under stirring, 150 μL of sodium citrate solution (1%, 33.3 mM) was added. Finally, the mixture was heated at 100 °C for 60 min.

Pt-M (M = Ag or Au) nanocomposites synthesized by the reduction of ascorbic acid or hydroquinone. In a typical synthesis, 750 μL of the as-synthesized PtNPs solution was centrifuged to 5 μL, and then transferred into 2 mL aq. AgNO$_3$ (0.5 mM, or HAuCl$_4$) in the presence of PVP (100 mM). Under stirring, 100 μL of ascorbic acid solution (10 mM, or hydroquinone, 10 mM) was added. Finally, the mixture was continued stirring for 60 min. For the producing of triangle Ag nanocomposites, more AgNO$_3$ and reducing agent were added (10 times concentration)

Pt-AuNR nanocomposites synthesis. The synthesis procedure is similar to the previous literature about the synthesis of AuNRs.[32] In a typical synthesis, into 4.875 mL of 0.1 M CTAB solution, 125 μL of aq. HAuCl$_4$ (10 mM), 13.75 μL of aq. ascorbic acid (100 mM) were added in sequence. The mixture was gently shaken and followed by the addition of PtNPs (375 μL of the as-synthesized PtNPs solution was centrifuged to 5 μL and redispersed into 20 μL of H$_2$O).

Synthesis of 1 functionalized AuNPs (1-AuNPs). Into 1.5 mL of sodium citrate stabilized AuNPs (d$_{AuNP}$ = 36 nm) solution, 100 uL of **1** ethanol solution (0.1 mM) was injected quickly. The mixture was incubated for 20 min on a shaker and it remained red after the incubation.

Au-M (M = Ag or Au) nanocomposites synthesis. The synthesis procedure is

similar to the synthesis of Pt-M (M = Ag or Au) nanocomposites. All the syntheses were carried out in the support of PVP. In a typical synthesis, into 1.6 mL of the **1-**AuNPs solution, 200 uL of PVP (0.5 M), 20 uL of AgNO$_3$ (50 mM), 20 uL of ascorbic acid (100 mM) were added in sequence. The mixture was stirred for several hr.

AuNP-AuNR nanocomposites synthesis. The synthesis procedure is similar to the synthesis of PtNP-AuNR. In a typical synthesis, into 4.875 mL of 0.1 M CTAB solution, 125 µL of aq. HAuCl$_4$ (10 mM), 13.75 µL of aq. ascorbic acid (100 mM) were added in this sequence. The mixture was gently shaken and followed by the addition of 300 uL of **1-AuNPs**.

5.3 Results and Discussion

5.3.1 Pt-M (M= Ag or Au) Heterodimers Formation

PtNPs with rough surface were synthesized according to the literature.[30] The particles sizes were about 65 nm and with a good distribution (Figure 5-1a). Based on the HRTEM characterization in the literature, the polycrystalline PtNPs surfaces consisted of numerous small clusters (3-10 nm) with close packing, and the lattices fringes of these clusters were assigned to (111) fringes. These NPs were chosen as the seeds to grow Ag and Au NPs with different reducing agents and stabilizers. For all the cases, the as-synthesized PtNPs were purified by centrifugation and then used as seeds.

Pt-Ag Heterodimers. Appropriate AgNO$_3$ was added into the purified PtNPs solution first, and then sodium citrate was added followed by heating. After 1h,

163

the solution color changed to brownish-yellow, indicating the formation of AgNPs. To purify the products, they were washed with ethanol to remove the excess PVP, and finally isolated by centrifugation. Because of the high contrast between Pt and Ag, it was easy to distinguish them from the TEM images. In Figure 5-1b, the TEM image showed that only one AgNP was grown from each PtNP seed, so as to exhibit the heterodimer structure. This assignment of one nucleation site on each seed was due to the large lattice mismatching.[15] There were two typical shapes of these grown AgNPs: sphere NPs with a diameter of about 50 nm; long rod NPs with a diameter of 20 nm and a length of 100~200 nm. It is well known that AgNPs shapes can be controlled by the addition of PVP owing to the favourable capping of Ag {100} by PVP.[33, 34] Thus, PVP was added into this reduction system. However, from the TEM image (Figure 5-1c), we found that there was little difference between them. This indicated that the formation of AgNPs was related on the PtNP seeds. The capping agent PVP played a minor role.
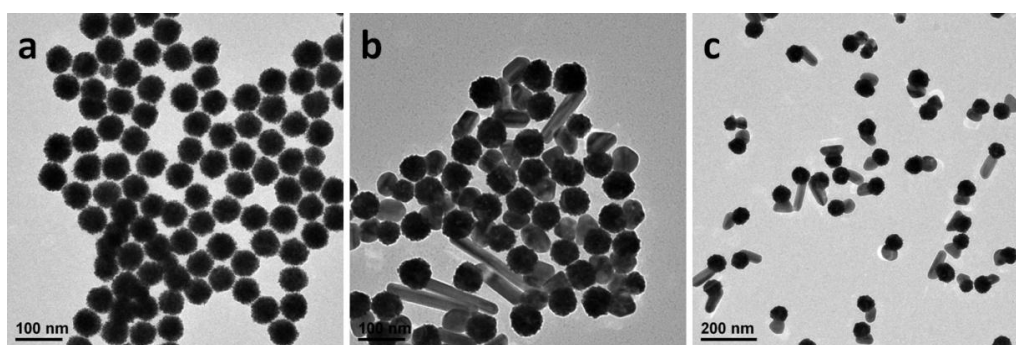

Figure 5-1 TEM images of the Pt seeds (a), Pt-Ag hetero-nanocomposites obtained by sodium citrate reducing $AgNO_3$ in the absence of PVP (b) and in the presence of PVP (c).

Xia and co-workers demonstrated that NPs shape can be controlled by choosing different reducing agents in seed mediated growth.[16] Ascorbic acid was chosen to reduce the $AgNO_3$ at room temperature. When ascorbic acid was added into the mixture solution, the color changed quickly to brownish-yellow in several seconds, reflecting that this reduction is very fast. As shown in Figure 5-2a, in the presence of PVP, uniform heterodimers were obtained and all the AgNPs showed spherical shapes, which is different from the sodium citrate reducing case. This phenomenon is also different from the literature that the ascorbic acid can cause the conformal overgrowth of Au on the Pd nanocubes, while sodium citrate guides the Au-Pd dimer formation.[16]

When this reduction took place without the PVP addition, irregular AgNPs were formed and the solution turned blue color (Figure 5-2b). Figure 5-2c showed the TEM image for 10 times $AgNO_3$ reduced in the presence of PVP. Besides the hetero-composites based on the seeded growth, many small AgNPs also coexisted, which arose from the homo-nucleation. In these seeded growth products, some Ag grew large and almost overgrew the whole seeds surface. Different shapes of AgNPs in the products also indicated that the AgNPs formation was still originated from the single nucleation site.
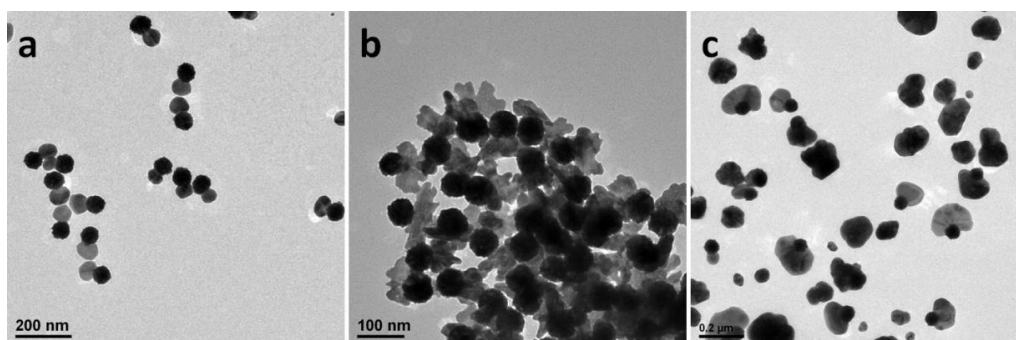
Figure 5-2 TEM images of Pt-Ag heterodimers obtained by ascorbic acid reducing AgNO₃ (20 uL of 50 mM) in the presence of PVP (a), in the absence of PVP (b), and 10 times of AgNO₃ (200 uL of 50 mM) was reduced in the presence of PVP (c).

Then hydroquinone with medium reducibility was used to reduce AgNO₃ in the presence of PVP. It was found that the solution color changed slower than in the ascorbic acid reducing case by bare eyes. The results were similar to that case, but maybe due to the lower reducibility of hydroquinone, the grown AgNPs were smaller (Figure 5-3a). Interestingly, when the AgNO₃ and hydroquinone concentration were increased 10 times, most of the grown AgNPs represented the triangle shape (Figure 5-3b-d). From Figure 5-3c, we observed that these triangle AgNPs were grown from each PtNP seed. Some of these seeds were fully encircled, and some were partial. It looked like the triangles were originated from the initial rod like AgNPs by expanding the surface. From the SEM image (Figure 5-3d), the thickness of these triangles was about 33 nm, and the edge length was about 300 nm. It also was found that PtNP seeds were encased in the triangles.
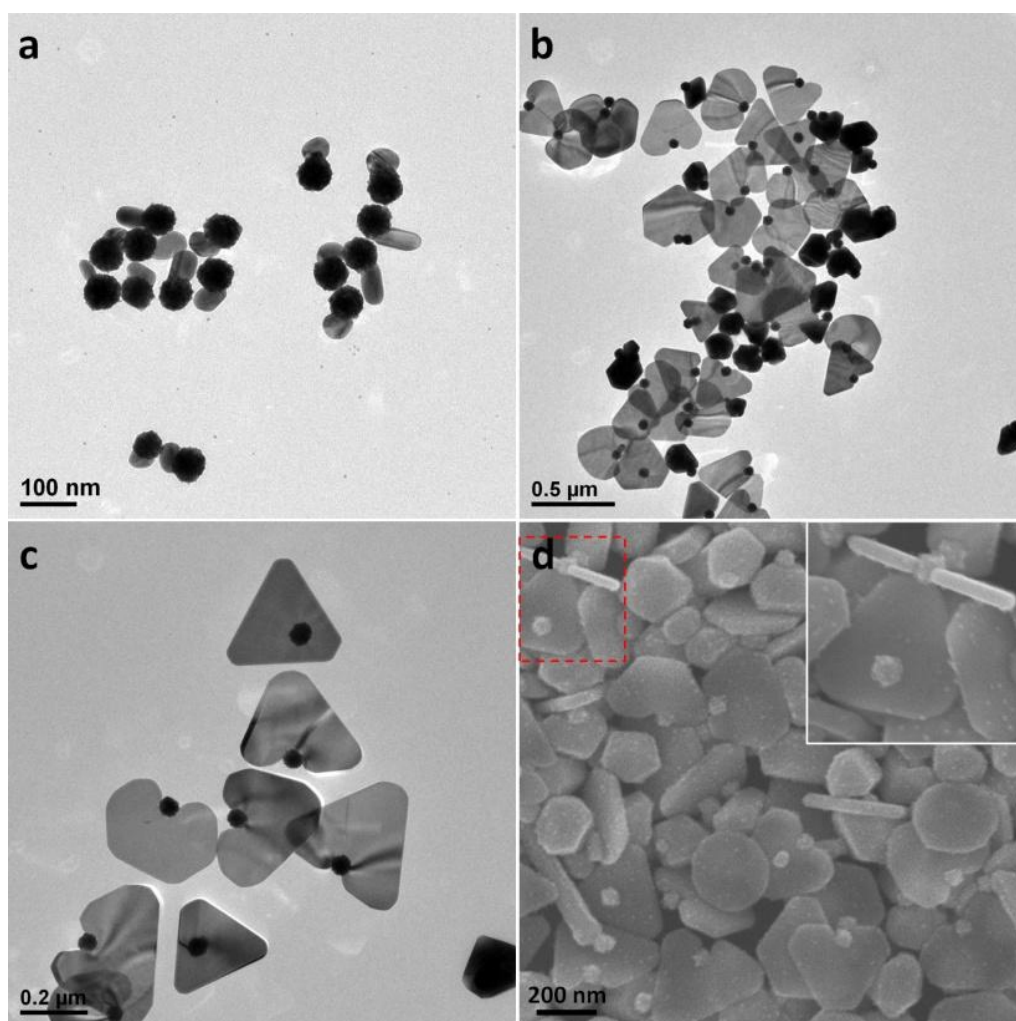
Figure 5-3 TEM images of Pt-Ag heterodimers obtained by hydroquinone reducing $AgNO_3$ in the presence of PVP (a), 10 times of $AgNO_3$ (200 uL of 50 mM) was reduced in the presence of PVP: low and high magnification (b and c), and the corresponding SEM image (d). Insert in d showed the magnification of the red rectangular section.
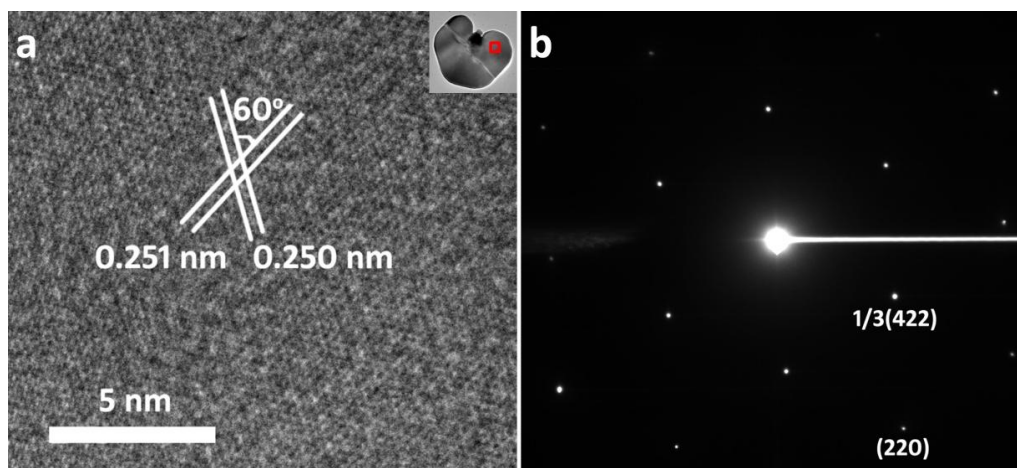
Figure 5-4 (a) HRTEM image of the Pt-Ag triangle heterodimers. Insert showed the low magnification TEM image of the corresponding sample (red rectangle area). (b) Electron diffraction analysis of the corresponding area.

Figure 5-4 showed the HRTEM and selected area electron diffraction (SAED) analysis of the Ag triangle segment of Pt-Ag heterodimer. The individual Ag triangle laid flat on the copper grid. Thus the electron beam was perpendicular to the top of Ag triangle, and irradiated from the [111] orientation of the Ag triangle. From the HRTEM image, we find that the lattice distance is about 0.25 nm, equal to three times the distance of {422} of face-centred cubic (FCC) silver. The 1/3{422} reflections was also confirmed by SAED characterization (Figure 5-4b). In the SAED image, these spots were assigned to the {220} and 1/3{422} Bragg reflections, corresponding to the lattice space of 0.144 and 0.251 nm, respectively. This result is consistent with the previous finding on nano-plate shape structure of FCC metals.[3, 35-37] So the formed Ag triangles were with (111) basal planes. The nucleation site on the Pt seed cannot be distinguished through the HRTEM.

Some control experiments were carried out to study the influence of PVP for

the AgNPs growth. Figure 5-5a and b showed the Pt-Ag hetero-composites synthesized at lower concentration of PVP. It was observed that the main products were also the triangles. However, the thickness increased (refer to the contrast of TEM images) and edge length decreased a little. Figure 5-5c showed that the sizes of PtNP seeds did not influence the products seriously.
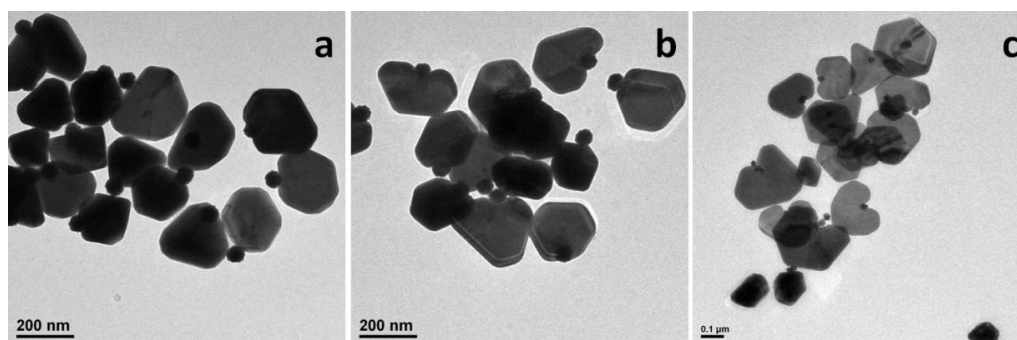
Figure 5-5 TEM images of Pt-Ag hetero-composites obtained by hydroquinone reducing AgNO$_3$ in different PVP concentration: a: 77 mM; b: 7.7 mM. c: TEM images of Pt-Ag hetero-composites obtained by using 29 nm PtNPs as seeds.

Pt-Au Heterodimers. AuNPs growth also was performed for this Pt seed-mediated growth. As shown in Figure 5-6a, when HAuCl$_4$ was reduced by sodium citrate in the presence of PVP, heterodimer structures were obtained. However, the surfaces of the grown AuNPs were rough and with several protuberances. This was different from the previous AgNPs growth case, maybe owing to the polycrystalline seeds and fast nucleation of Au. When the reducing agent was changed to ascorbic acid, spiky Pt@Au core-shell structures were obtained. Each core-shell structure consisted of dense packing of small NPs (diameter: about 15~25 nm). This arrangement was due to the fast formation of AuNPs, in which the polycrystalline PtNPs can act as multi-nucleation sites. These spiked NPs can be potentially used for the SERS applications because of

the coupling of these small NPs.[38-40]
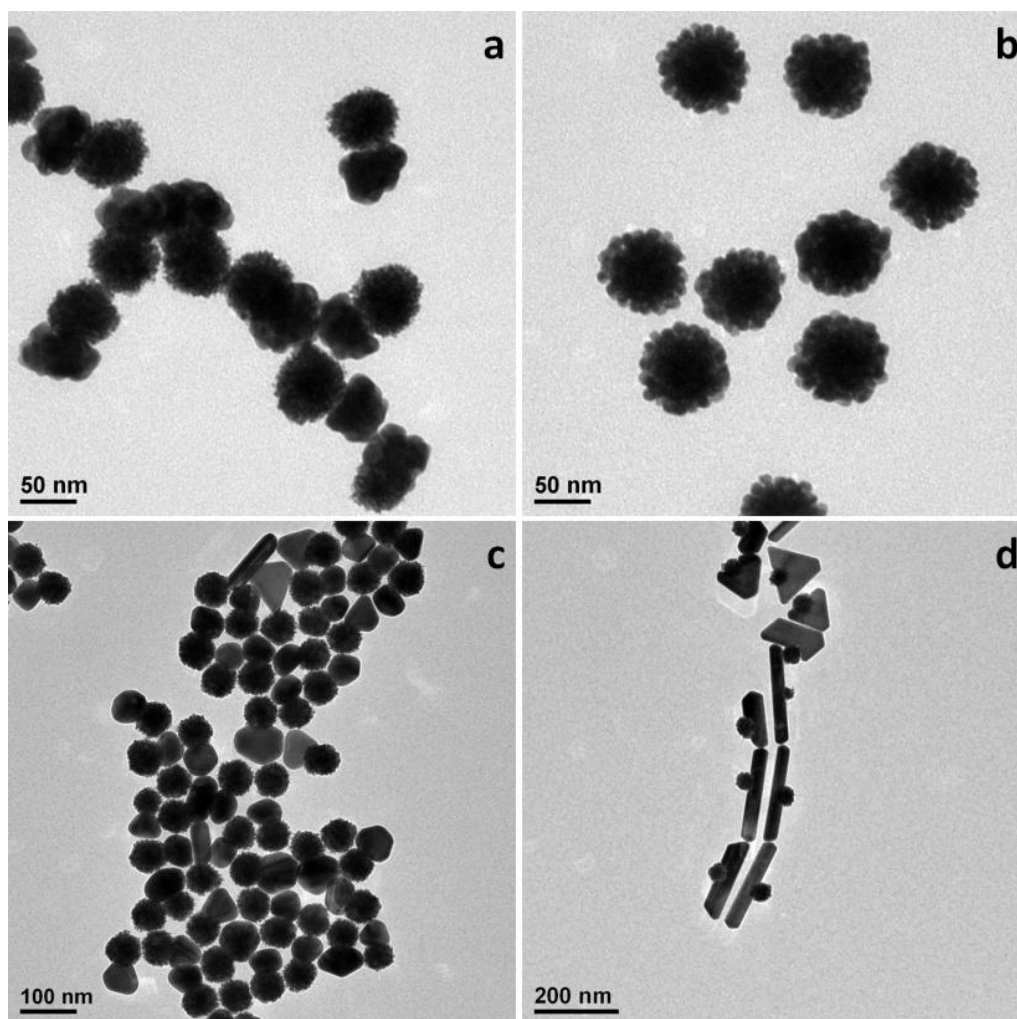
Figure 5-6 TEM images of Pt-Au heterodimers: in PVP solution (a) sodium citrate as reducing agent; (b) ascorbic acid as reducing agent; in CTAB solution (c) sodium citrate as reducing agent; (d) ascorbic acid as reducing agent.

The stabilizer was changed to CTAB in virtue of the perfect structure control of NPs syntheses.[41, 42] When sodium citrate was chosen to reduce $HAuCl_4$ under heating, heterodimers were obtained, in which the surfaces of the formed AuNPs were very slippery. Very few AuNRs also coexisted. In contrast, lots of AuNRs can be synthesized when ascorbic acid was used as reducing agent and the reaction was carried out at room temperature. In both cases, on each PtNP seed, AuNPs only nucleated at one site of the seed, which was different from

the PVP system. It looks like the change is due to the reaction speed: fast reaction rate causes the multi-sites nucleation; low reaction rate induces single-site nucleation.[16]

5.3.2 Au-M (M = Ag or Au) Heterodimers Formation

As discussed in the Chapter 4, AuNPs can be functionalized with ligand pentaerythritol tetrakis(3-mercapto-propionate) (**1**), and used as seeds. Because of the fully coating, **1** functionalized AuNPs (**1**-AuNPs) will be dispersed in aqueous solution without any aggregation. In this section, this kind of AuNPs will be used as the seed for the Ag and Au NPs growth to form the heterodimeric structures. It is well known that Ag and Au can be conformal grown on the bare Au seeds uniformly to form the core-shell structures owing to the excellent lattice matching.[15, 43, 44]

Au-Ag heterodimers. Firstly, the mixture containing 2 μL of 0.1 mM **1** and 1500 μL of the as-synthesized AuNPs solution was incubated for 15 min to prepare **1**-AuNPs. Then PVP was added as the stabilizer, followed by the addition of $AgNO_3$ and ascorbic acid. The solution color did not change for several hours after the addition of $AgNO_3$ and ascorbic acid. This may be because Ag^+ can react with ligand **1** to form stable complex thus the reduction potential will decrease.[45] So some amount of NaOH aqueous solution was added to increase the reducibility of ascorbic acid.[46] The solution color changed to brownish-yellow indicated the formation of AgNPs. TEM image showed that Ag can completely cover the seeds (Figure 5-7a). The core-shell

structures also exhibited a bit eccentric. The reason may be due to the coating of ligand, which can improve the metal-metal interfacial energy, similar to the large lattice mismatching influence.

When the amount of **1** was increased to 4 µL, a thin layer of Ag was grown on the AuNP seeds and then grown along one orientation to form the more eccentric structures (Figure 5-7b). When the amount of **1** reached 40 µL, Au-Ag heterodimers were obtained after two hrs incubation. As shown in Figure 5-7c, Ag plates, spheres and rods coexisted in the products with the diameter of about 60 nm. When the amount of **1** reached 100 µL, the result was similar to the previous case. The AgNPs in the heterodimers were uniform with the diameter of about 40 nm (Figure 5-7d).

A control experiment was carried out to study the role of incubation time. When the mixture of AuNPs and **1** was incubated just 1 min before the addition of $AgNO_3$ and ascorbic acid, the products were high eccentric, in which Ag shell fully covered the AuNP seeds due to the multi-sites nucleation. There was large area of connection between the formed AgNP and seed (Figure 5-7e). When incubation time increased to 30 min, heterodimers were obtained, in which Ag shell would not be observed on the AuNP seeds (Figure 5-7f). This pointed out that the ligand coating played an important role in determining the nucleation site.
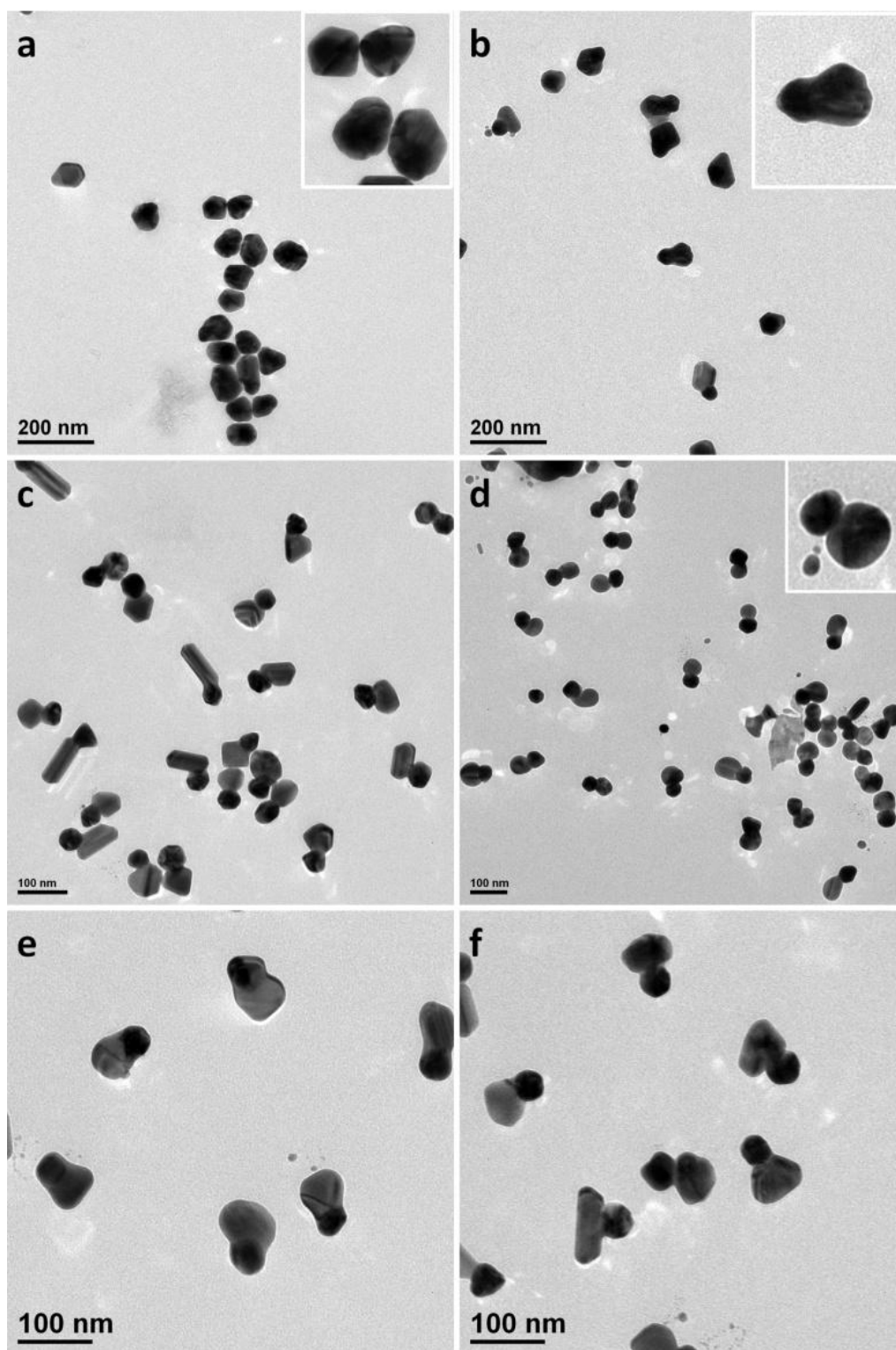
Figure 5-7 TEM images of the AgNPs growth based on the different syntheses of **1**-AuNPs: (a) 2 μL; (b) 4 μL; (c) 40 μL; (d) 100 μL of 0.1 mM **1** was added into 1500 μL as-synthesized AuNPs. The mixture was incubated for 15 min. TEM images of the AgNPs growth based on the different syntheses of 1-AuNPs (40 μL of 0.1 mM **1** was added into 1500 μL as-synthesized AuNPs soluiton): the incubation time for the mixture of **1** and AuNPs was (e) 1 min; (f) 30 min.

For all the syntheses, 20 μL of 50 mM AgNO$_3$ was reduced by 20 μL of 100 mM ascorbic acid. Inset of d showed magnified Au-Ag heterodimer.

HRTEM analyses were carried out to study the Au-Ag heterodimers growth. Figure 5-8a showed the TEM image of one typical Au-Ag heterodimer at low magnification. From the image, two important segments can be found: one is the Au seed; the other is the grown AgNP. Five twin boundaries were found in this Au seed, which can be confirmed from the HRTEM image (Figure 5-8b). By measuring the lattice fringes of these five areas, it can be found that the interplanar distances were about 0.233 nm, corresponding to the {111} fringes of FCC Au. Figure 5-8c exhibited the HRTEM image of the connection region of Au-Ag dimer. The dash curve showed the boundary of Au and Ag. It was found that the Ag followed the epitaxial growth from one segment of the five-twinned Au seed. From the dash boundary in Figure 5-8d, small region of Ag attached on the Au seed with the different lattice orientation. This reflected that the whole Ag segment just grown from one small nucleation site of the Au seed. When grown larger, Ag reached another segment of five-twinned Au seed. Figure 5-8e and f showed another case of the Au-Ag heterodimer. They showed a similar phenomenon, in which the Ag was with the epitaxial growth mode and nucleated from one small region of the **1**-Au NP seed. According to the HRTEM images of the Ag domains in the Au-Ag heterodimers, we can conclude that the selected areas should be single crystalline.

174
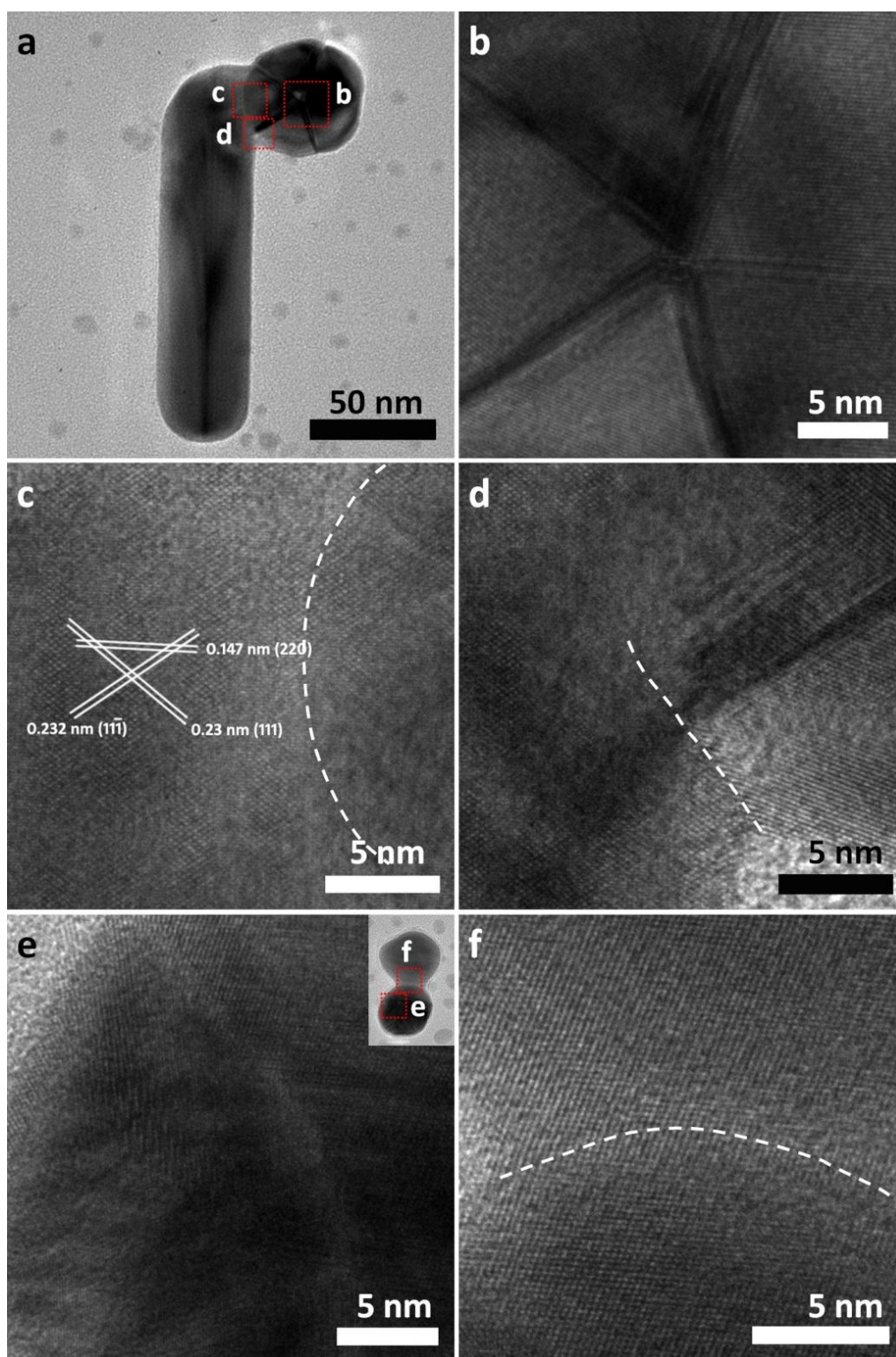
Figure 5-8 HRTEM analyses of two typical Au-Ag heterodimers synthesized by incubating the **1**-NPs, AgNO₃, as well as ascorbic acid in the presence of PVP. (a) low magnification TEM image of the heterodimer; HRTEM image of the Au seed (b), Au-Ag connection region with the same lattice orientation (c), and Au-Ag connection region with the different lattice orientation (d), corresponding to the square regions of b, c, and d in a. (e and f) HRTEM

images of another heterodimer (shown in the inset). (e) HRTEM image of Au seed reflected the polycrystalline structure. (f) HRTEM image of the Au-Ag connection region exhibited the same lattice orientation.
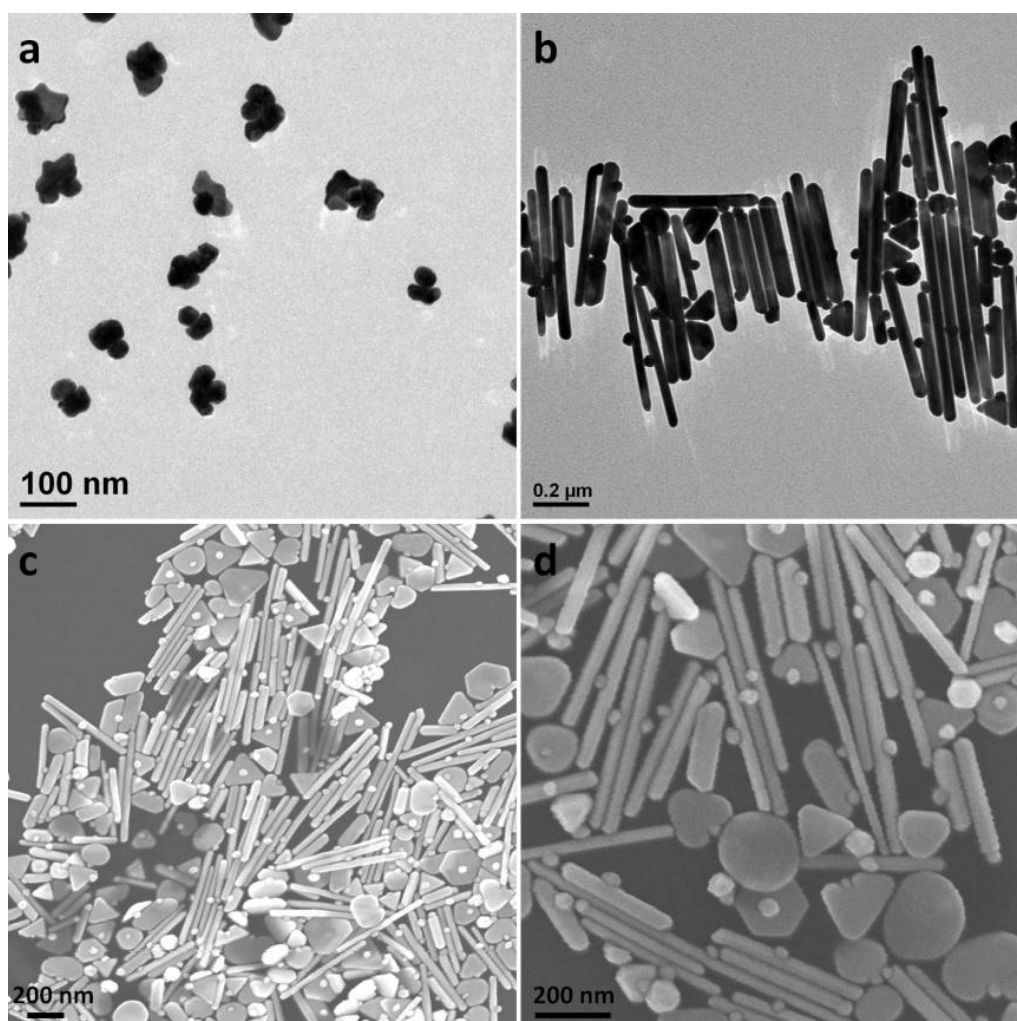
Figure 5-9 TEM images of the AuNPs growth based on the 1-AuNPs (70 μL of 0.1 mM **1** was added into 1500 μL as-synthesized AuNPs solution. The mixture was incubated for 20 min): (a) PVP; (b) CTAB was used as stabilizer. (c, d) SEM images of the AuNPs growth with different magnification: corresponding to the products in b.

Au-Au heterodimers. This typical **1**-AuNP seeds also can be used for the Au-Au heterodimers formation. As shown in Figure 5-9a, Au-Au heterodimers were obtained by using ascorbic acid reducing $HAuCl_4$ in PVP solution. Due to the fast reaction, the shape of the grown Au cannot be easy to control. CTAB

was one important surfactant in the AuNPs growth, which can slow down the reduction reaction of $HAuCl_4$. The growth solution was prepared as we discussed in the last section. Then **1**-AuNP seeds were added gently. The solution color changed to purple in several hours, indicating the formation of Au-Au heterodimers. Figure 5-9b showed the TEM image of the products, in which AuNRs and Au nanoplates coexisted. In each grown NP, one spherical NP with the size about 36 nm can be found. This was consistent with the seeds we added. So we concluded that the AuNRs and Au nanoplates were formed from the **1**-AuNP seed mediated growth. The SEM characterization clearly demonstrated that the seeds were usually loaded in the centre of the NRs (Figure 5-9c and d). These results reflected that **1** functionalized polycrystalline AuNPs can serve as one-site nucleation seed for the hetero-NPs growth. This may expand the species of seeds to synthesize multi-component nanostructures.

5.3.3 Spectra Characterization of the Heterodimer Nanocomposites

As we discussed in Chapter 1, SPR of metallic NPs highly associates with the shapes and size of NPs. In this section, the SPR of the Pt-M and Au-M (M = Au or Ag) heterodimers were examined and discussed. As shown in Figure 5-10A, PtNPs showed one absorption peak at about 313 nm, which was consistent with the literature report.[30] When 10 μL of $AgNO_3$ was reduced in the presence of PtNP seeds, there was only one absorption peak (about 430 nm), indicating the formation of AgNPs.[47] When 20 μL of $AgNO_3$ was used, besides

one new peak at about 350 nm, a shoulder band appeared in the region of 500~700 nm. The UV-vis spectrum exhibited remarkable change when the AgNO$_3$ amount increased to 200 μL. In addition to these peaks, one new absorption band peaked at about 700 nm, which indicated the formation of Ag triangles.[48] Interestingly, when the PVP concentration decreased from 770 mM to 77 mM, the absorption band peak red-shifted to 800 nm and the intensity of peak at 450 nm increased, which reflected the morphology change (thickness increased and edge length decreased). 7.7 mM PVP and 77 mM PVP exhibited similar results (Figure 5-10B). So the thin Ag nanotriangles were highly determined by the high concentration of PVP. It was found that in these cases, there was no notable plasma coupling between Pt and Ag. Figure 5-10C showed the UV-vis spectra of Pt-Au hetero-structures. Besides the typical peak at about 560 nm, which reflected the formation of AuNPs, one broad absorption band coexisted at 300~500 nm region. This assignment may be due to the superimposition of the absorption bands of PtNPs as well as AuNPs.

Figure 5-11 showed the UV-Vis spectra of AuNPs as well the Au-M (M = Au and Ag) heterodimers based on these AuNP seeds. It was found that all these Au-Ag heterodimer samples exhibited three absorption peaks (bands): 420 nm, 530 nm, 650~750 nm, which were assigned to the Ag transverse plasmon absorption, Au transverse plasmon absorption (it was enshrouded by the strong Ag plasmon absorption), and Au-Ag longitudinal plasmon coupling absorption, respectively.[49] Due to the different amount of **1** addition, the peaks at around

420 nm showed very little shift. However, the peak owing to the Au-Ag

plasmon coupling showed large change decided by the varying morphologies of

Ag domains.
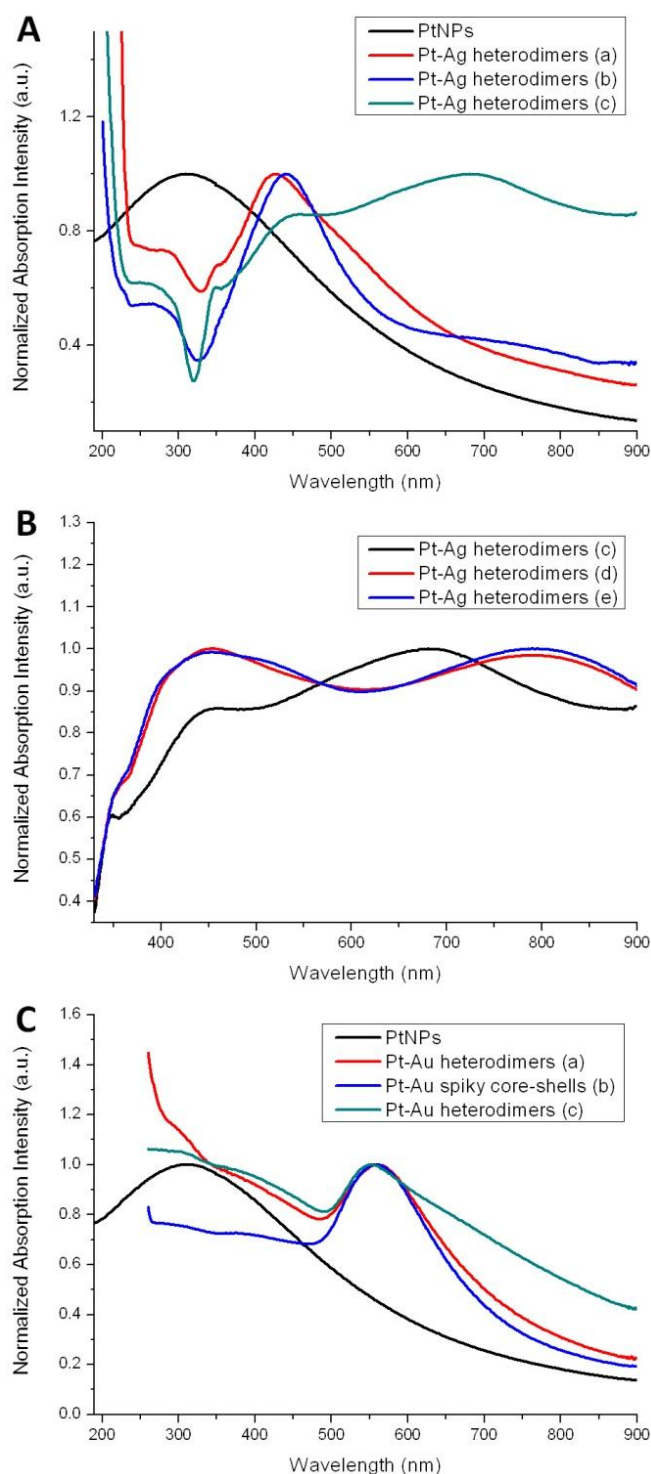
Figure 5-10 UV-Vis spectra of PtNPs, Pt-Ag hetero-composites, and Pt-Au
hetero-composites. In A, Pt-Ag heterodimers were synthesized with different

amount of AgNO₃ (50 mM): (a) 10 µL; (b) 30 µL; (c) 200 µL. In B, Pt-Ag heterodimers were synthesized with different PVP concentration: (c) 770 mM; (d) 77 mM; (e) 7 mM. In C, Pt-Au heterodimers were synthesized under different conditions: (a) PVP as stabilizer, sodium citrate as reducing agent; (b) PVP as stabilizer, ascorbic acid as reducing agent; (c) CTAB as stabilizer, sodium citrate as reducing agent.
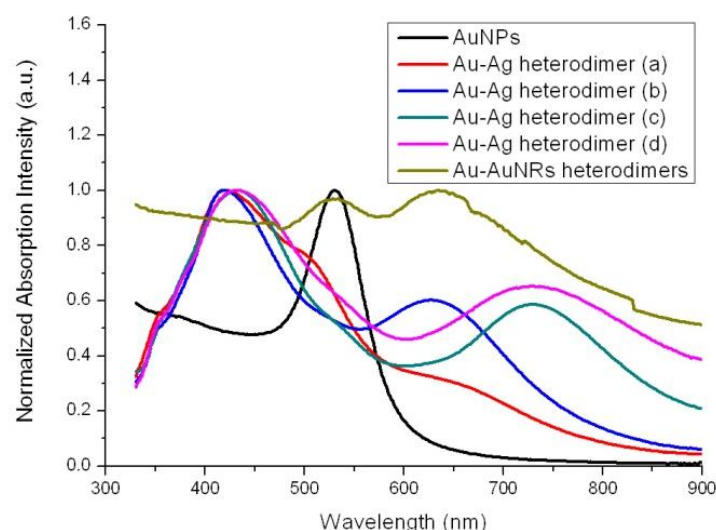
Figure 5-11 UV-Vis spectra of Au-Ag and Au-AuNRs heterodimers. Au-Ag heterodimers were synthesized by incubating Au NPs with (a) 5 µL; (b) 10 µL; (c) 40 µL; and (d) 100 µL of 0.1 mM **1** at room temperature for 15 min, and then reducing Ag.

5.3.4 Mechanism Analysis

Lattice (mis)matching and surface energies are usually applied to explain the seed-mediated growth phenomena.[15, 50-57] The growth modes are mainly determined by these factors of the growth matter and substrate (seeds). When the two matters have good lattice matching and a lower surface energy, the growth matter can progress layer-by-layer mode to completely cover the surface of substrate (Frank-van der Merwe, *abbr*. FM growth mode). When the two matters have a high surface energy, and w/o large lattice mismatching, the growth matter can just grow on the substrate separately to form the island-like

180

structure to reduce the interface energy (Volmer-Weber, *abbr*. VW growth mode). When the conditions are in between, the growth matter firstly performs lay-by-layer growth. Meanwhile the interfacial strain will increase. When this strain cannot be overcome, the growth matter turns to the island-like deposition. (Stranski–Krastanov mode, *abbr*. SK growth mode).[52]

So in the Pt-M (M = Ag or Au) hetero-composites system, the growth can be explained by the VW growth mode, in which the Pt-Ag or Pt-Au mismatch is too large (3.8%). This means when the Ag/Au atoms firstly nucleate on the PtNP seed and the rest of the atoms will deposit on the nucleus of each PtNP seed to reduce the possible interface between Ag/Au and Pt. For the Pt@Au spiked nanostructure case, As the Au deposition rate is too high, this energy selectivity is depressed, and thus the multi-nucleation sites will appear on each PtNP seed. Then the Au atoms deposit on these sites to form the spiked core-shell structure. When the reduction speed decreases, heterodimer structure will replace the core-shell structure. This demonstrates that the Au reduction kinetics also can play an important role in tuning the growth mode.[57]

In the Au-M (M = Ag or Au) case, the results reflect the SK growth mode, even the VW growth mode take action by tuning the concentration of ligand **1**, which can coat on the AuNPs surface with different density. This surface functionalization will change the surface property (*e.g.* interfacial energy). From low to high density of surface coating (*via* tuning the **1** amount), the thickness of the Ag shell on the AuNP seed decrease. Finally this shell cannot

be observed from the TEM image. This is perhaps because the surface energy is too large to allow the atoms deposition, thus the VW growth mode is adopted.

In the two kinds of seed cases, the growth materials are deposited on the seeds *via* the VW growth mode, that is the formation NPs are formed based on one nucleation site of each seed. Thus we demonstrate that the hetero-dimeric nanostructures can be obtained by polycrystalline seeds by choosing the large lattice mismatching seeds or tuning the surface energy via surface functionalization.

5.4 Conclusion

In summary, we reported the syntheses of hetero-composites through the seed-mediated growth method. Two different polycrystalline NP (spiky PtNSs and AuNSs) were used as seeds. Lattice mismatching as well as the increased surface energy played an important role in controlling the formation of hetero-nanostructures. The increased surface energy was induced by small molecules coating. Since the NPs nucleated from one small nucleation site and followed the epitaxial growth mode, this may offer one opportunity to prepare single crystalline NPs through the polycrystalline NP seeds. It can be predicted that the surface energy-controlled seeds can be expanded to many species. Consequently, abundant hetero-nanocomposites can be synthesized (such as, Ag-Au, Ag-Ag heterodimers, *etc.*).

5.5 Bibliography

[1] Kelly, K. L., Coronado, E., Zhao, L. L., and Schatz, G. C., The Optical Properties of Metal Nanoparticles: The Influence of Size, Shape, and Dielectric Environment. *J. Phys. Chem. B*, **107**, 668 (2002).

[2] Van de Hulst, H. C., *Light Scattering by Small Particles*. 1981, New York: Dover.

[3] Jin, R. C., Cao, Y. W., Mirkin, C. A., Kelly, K. L., Schatz, G. C., and Zheng, J. G., Photoinduced Conversion of Silver Nanospheres to Nanoprisms. *Science*, **294**, 1901 (2001).

[4] Sonnichsen, C., Franzl, T., Wilk, T., von Plessen, G., Feldmann, J., Wilson, O., and Mulvaney, P., Drastic Reduction of Plasmon Damping in Gold Nanorods. *Phys. Rev. Lett.*, **88**,   (2002).

[5] Sosa, I. O., Noguez, C., and Barrera, R. G., Optical Properties of Metal Nanoparticles with Arbitrary Shapes. *J. Phys. Chem. B*, **107**, 6269 (2003).

[6] Orendorff, C. J., Sau, T. K., and Murphy, C. J., Shape-Dependent Plasmon-Resonant Gold Nanoparticles. *Small*, **2**, 636 (2006).

[7] Eustis, S. and El-Sayed, M. A., Why Gold Nanoparticles Are More Precious Than Pretty Gold: Noble Metal Surface Plasmon Resonance and Its Enhancement of the Radiative and Nonradiative Properties of Nanocrystals of Different Shapes. *Chem. Soc. Rev.*, **35**, 209 (2006).

[8] Murphy, C. J., Sau, T. K., Gole, A. M., Orendorff, C. J., Gao, J., Gou, L., Hunyadi, S. E., and Li, T., Anisotropic Metal Nanoparticles: Synthesis, Assembly, and Optical Applications. *J. Phys. Chem. B*, **109**, 13857 (2005).

[9] Tian, N., Zhou, Z.-Y., and Sun, S.-G., Platinum Metal Catalysts of High-Index Surfaces: From Single-Crystal Planes to Electrochemically Shape-Controlled Nanoparticles. *J. Phys. Chem. C*, **112**, 19801 (2008).

[10] Tian, N., Zhou, Z.-Y., Sun, S.-G., Ding, Y., and Wang, Z. L., Synthesis of Tetrahexahedral Platinum Nanocrystals with High-Index Facets and High Electro-Oxidation Activity. *Science*, **316**, 732 (2007).

[11] Wang, F., Li, C., Sun, L.-D., Wu, H., Ming, T., Wang, J., Yu, J. C., and Yan, C.-H., Heteroepitaxial Growth of High-Index-Faceted Palladium Nanoshells and Their Catalytic Performance. *J. Am. Chem. Soc.*, **133**, 1106 (2010).

[12] Zhou, Z.-Y., Huang, Z.-Z., Chen, D.-J., Wang, Q., Tian, N., and Sun, S.-G.,

High-Index Faceted Platinum Nanocrystals Supported on Carbon Black as Highly Efficient Catalysts for Ethanol Electrooxidation. *Angew, Chem., Int. Ed.*, **49**, 411 (2010).

[13] Habas, S. E., Lee, H., Radmilovic, V., Somorjai, G. A., and Yang, P., Shaping Binary Metal Nanocrystals through Epitaxial Seeded Growth. *Nat. Mater.*, **6**, 692 (2007).

[14] Xing, S. X., Feng, Y. H., Tay, Y. Y., Chen, T., Xu, J., Pan, M., He, J. T., Hng, H. H., Yan, Q. Y., and Chen, H. Y., Reducing the Symmetry of Bimetallic Au@Ag Nanoparticles by Exploiting Eccentric Polymer Shells. *J. Am. Chem. Soc.*, **132**, 9537 (2010).

[15] Fan, F. R., Liu, D. Y., Wu, Y. F., Duan, S., Xie, Z. X., Jiang, Z. Y., and Tian, Z. Q., Epitaxial Growth of Heterogeneous Metal Nanocrystals: From Gold Nano-Octahedra to Palladium and Silver Nanocubes. *J. Am. Chem. Soc.*, **130**, 6949 (2008).

[16] Lim, B., Kobayashi, H., Yu, T., Wang, J., Kim, M. J., Li, Z.-Y., Rycenga, M., and Xia, Y., Synthesis of Pd−Au Bimetallic Nanocrystals Via Controlled Overgrowth. *J. Am. Chem. Soc.*, **132**, 2506 (2010).

[17] Cho, E. C., Camargo, P. H. C., and Xia, Y., Synthesis and Characterization of Noble-Metal Nanostructures Containing Gold Nanorods in the Center. *Adv. Mater.*, **22**, 744 (2010).

[18] Seo, D. and Song, H., Asymmetric Hollow Nanorod Formation through a Partial Galvanic Replacement Reaction. *J. Am. Chem. Soc.*, **131**, 18210 (2009).

[19] Seo, D., Yoo, C. I., Jung, J., and Song, H., Ag−Au−Ag Heterometallic Nanorods Formed through Directed Anisotropic Growth. *J. Am. Chem. Soc.*, **130**, 2940 (2008).

[20] Gole, A. and Murphy, C. J., Seed-Mediated Synthesis of Gold Nanorods: Role of the Size and Nature of the Seed. *Chem. Mater.*, **16**, 3633 (2004).

[21] Frens, G., Controlled Nucleation for Regulation of Particle-Size in Monodisperse Gold Suspensions. *Nature Phys. Sci.*, **241**, 20 (1973).

[22] Cui, Z. M., Jiang, S. P., and Li, C. M., Highly Dispersed Moox on Carbon Nanotube as Support for High Performance Pt Catalyst Towards Methanol Oxidation. *Chem. Commun.*, **47**, 8418 (2011).

[23] Gu, H., Yang, Z., Gao, J., Chang, C. K., and Xu, B., Heterodimers of Nanoparticles: Formation at a Liquid−Liquid Interface and Particle-Specific Surface Modification by Functional Molecules. *J. Am. Chem. Soc.*, **127**, 34 (2004).

[24] Chen, T., Chen, G., Xing, S. X., Wu, T., and Chen, H. Y., Scalable Routes to Janus Au-Sio2 and Ternary Ag-Au-Sio2 Nanoparticles. *Chem. Mater.*, **22**, 3826 (2010).

[25] Hurst, S. J., Payne, E. K., Qin, L., and Mirkin, C. A., Multisegmented One-Dimensional Nanorods Prepared by Hard-Template Synthetic Methods. *Angew, Chem., Int. Ed.*, **45**, 2672 (2006).

[26] Mokari, T., Rothenberg, E., Popov, I., Costi, R., and Banin, U., Selective Growth of Metal Tips onto Semiconductor Quantum Rods and Tetrapods. *Science*, **304**, 1787 (2004).

[27] Li, X., Lian, J., Lin, M., and Chan, Y., Light-Induced Selective Deposition of Metals on Gold-Tipped Cdse-Seeded Cds Nanorods. *J. Am. Chem. Soc.*, **133**, 672 (2010).

[28] Lee, H. J., Habas, S. E., Somorjai, G. A., and Yang, P. D., Localized Pd Overgrowth on Cubic Pt Nanocrystals for Enhanced Electrocatalytic Oxidation of Formic Acid. *J. Am. Chem. Soc.*, **130**, 5406 (2008).

[29] Yu, T. Y., Zeng, J., Lim, B., and Xia, Y. N., Aqueous-Phase Synthesis of Pt/Ceo2 Hybrid Nanostructures and Their Catalytic Properties. *Adv. Mater.*, **22**, 5188 (2010).

[30] Bigall, N. C., Hartling, T., Klose, M., Simon, P., Eng, L. M., and Eychmuller, A., Monodisperse Platinum Nanospheres with Adjustable Diameters from 10 to 100 Nm: Synthesis and Distinct Optical Properties. *Nano Lett.*, **8**, 4588 (2008).

[31] Brown, K. R., Walter, D. G., and Natan, M. J., Seeding of Colloidal Au Nanoparticle Solutions. 2. Improved Control of Particle Size and Shape. *Chem. Mater.*, **12**, 306 (2000).

[32] Gole, A. and Murphy, C. J., Azide-Derivatized Gold Nanorods: Functional Materials for "Click" Chemistry. *Langmuir*, **24**, 266 (2008).

[33] Zeng, J., Xia, X., Rycenga, M., Henneghan, P., Li, Q., and Xia, Y., Successive Deposition of Silver on Silver Nanoplates: Lateral Versus Vertical Growth. *Angew, Chem., Int. Ed.*, **50**, 244 (2011).

[34] Wiley, B., Sun, Y., Mayers, B., and Xia, Y., Shape-Controlled Synthesis of Metal Nanostructures: The Case of Silver. *Chemistry – A European Journal*, **11**, 454 (2005).

[35] Jin, R. C., Cao, Y. C., Hao, E. C., Metraux, G. S., Schatz, G. C., and Mirkin, C. A., Controlling Anisotropic Nanoparticle Growth through Plasmon Excitation. *Nature*, **425**, 487 (2003).

[36] Germain, V., Li, J., Ingert, D., Wang, Z. L., and Pileni, M. P., Stacking

Faults in Formation of Silver Nanodisks. *J. Phys. Chem. B*, **107**, 8717 (2003).

[37] Maillard, M., Giorgio, S., and Pileni, M. P., Silver Nanodisks. *Adv. Mater.*, **14**, 1084 (2002).

[38] Burda, C., Chen, X., Narayanan, R., and El-Sayed, M. A., Chemistry and Properties of Nanocrystals of Different Shapes. *Chem. Rev.*, **105**, 1025 (2005).

[39] Rodríguez-Lorenzo, L., Álvarez-Puebla, R. n. A., Pastoriza-Santos, I., Mazzucco, S., Stéphan, O., Kociak, M., Liz-Marzán, L. M., and García de Abajo, F. J., Zeptomol Detection through Controlled Ultrasensitive Surface-Enhanced Raman Scattering. *J. Am. Chem. Soc.*, **131**, 4616 (2009).

[40] Sanchez-Gaytan, B. L. and Park, S.-J., Spiky Gold Nanoshells. *Langmuir*, **26**, 19170 (2010).

[41] Murphy, C. J. and Jana, N. R., Controlling the Aspect Ratio of Inorganic Nanorods and Nanowires. *Adv. Mater.*, **14**, 80 (2002).

[42] Ming, T., Feng, W., Tang, Q., Wang, F., Sun, L., Wang, J., and Yan, C., Growth of Tetrahexahedral Gold Nanocrystals with High-Index Facets. *J. Am. Chem. Soc.*, **131**, 16350 (2009).

[43] Chen, G., Wang, Y., Yang, M. X., Xu, J., Goh, S. J., Pan, M., and Chen, H. Y., Measuring Ensemble-Averaged Surface-Enhanced Raman Scattering in the Hotspots of Colloidal Nanoparticle Dimers and Trimers. *J. Am. Chem. Soc.*, **132**, 3644 (2010).

[44] Wang, Y., Chen, G., Yang, M., Silber, G., Xing, S., Tan, L. H., Wang, F., Feng, Y., Liu, X., Li, S., and Chen, H., A Systems Approach Towards the Stoichiometry-Controlled Hetero-Assembly of Nanoparticles. *Nature Communications*, **1**, 87 (2010).

[45] Gao, C., Zhang, Q., Lu, Z., and Yin, Y., Templated Synthesis of Metal Nanorods in Silica Nanotubes. *J. Am. Chem. Soc.*, **133**, 19706 (2011).

[46] Borsook, H. and Keighley, G., Oxidation Reduction Potential of Ascorbic Acid (Vitamin C). *Proc. Natl. Acad. Sci. U. S. A.*, **19**, 875 (1933).

[47] Huang, H. H., Ni, X. P., Loy, G. L., Chew, C. H., Tan, K. L., Loh, F. C., Deng, J. F., and Xu, G. Q., Photochemical Formation of Silver Nanoparticles in Poly(N-Vinylpyrrolidone). *Langmuir*, **12**, 909 (1996).

[48] Jin, R., Cao, Y., Mirkin, C. A., Kelly, K. L., Schatz, G. C., and Zheng, J. G., Photoinduced Conversion of Silver Nanospheres to Nanoprisms. *Science*, **294**, 1901 (2001).

[49] Brown, L. V., Sobhani, H., Lassiter, J. B., Nordlander, P., and Halas, N. J.,

Heterodimers: Plasmonic Properties of Mismatched Nanoparticle Pairs. *ACS Nano*, **4**, 819 (2010).

[50] Bauer, E. and van der Merwe, J. H., Structure and Growth of Crystalline Superlattices: From Monolayer to Superlattice. *Physical Review B*, **33**, 3657 (1986).

[51] Buck, M. R., Bondi, J. F., and Schaak, R. E., A Total-Synthesis Framework for the Construction of High-Order Colloidal Hybrid Nanoparticles. *Nat Chem*, **4**, 37 (2012).

[52] Casavola, M., Buonsanti, R., Caputo, G., and Cozzoli, P. D., Colloidal Strategies for Preparing Oxide-Based Hybrid Nanocrystals. *Eur. J. Inorg. Chem.*, **2008**, 837 (2008).

[53] Casavola, M., Falqui, A., García, M. A., García-Hernández, M., Giannini, C., Cingolani, R., and Cozzoli, P. D., Exchange-Coupled Bimagnetic Cobalt/Iron Oxide Branched Nanocrystal Heterostructures. *Nano Lett.*, **9**, 366 (2008).

[54] Lim, S. I., Varon, M., Ojea-Jimenez, I., Arbiol, J., and Puntes, V., Pt Nanocrystal Evolution in the Presence of Au(Iii)-Salts at Room Temperature: Spontaneous Formation of Aupt Heterodimers. *J. Mater. Chem.*, **21**, 11518 (2011).

[55] Peng, Z. M. and Yang, H., Designer Platinum Nanoparticles: Control of Shape, Composition in Alloy, Nanostructure and Electrocatalytic Property. *Nano Today*, **4**, 143 (2009).

[56] Wang, C., Tian, W., Ding, Y., Ma, Y.-q., Wang, Z. L., Markovic, N. M., Stamenkovic, V. R., Daimon, H., and Sun, S., Rational Synthesis of Heterostructured Nanoparticles with Morphology Control. *J. Am. Chem. Soc.*, **132**, 6524 (2010).

[57] Zeng, J., Zhu, C., Tao, J., Jin, M., Zhang, H., Li, Z.-Y., Zhu, Y., and Xia, Y., Controlling the Nucleation and Growth of Silver on Palladium Nanocubes by Manipulating the Reaction Kinetics. *Angew, Chem., Int. Ed.*, DOI: 10.1002/anie.201107061 (2011).

Chapter 6 Thiol-ended Phospholipid Directed Silver Cluster Superlattices by Colloidal Self-Assembly

6.1 Introduction

"Bottom-up" technique is an efficient method for the architecture of materials in micro- or nano-scale with excellent properties and functions.[1-3] In the past several decades, many works have documented the nano-objects assemblies for fabricating various dimensional regular arrays with optical and electronic properties.[4-11] It has been witnessed that the hexagonal arrays formed by the assembly of block copolymers promise wonderful significances of lithography application.[12-14] Well-ordered block copolymer patterning can also be used as the template to manipulate metallic materials with anticipant arrays.[15-18] Under the assistant of polymer templates, metal atoms were well aligned, thus the ordered metal NPs could be further formed on the selective domains.[16, 18] The length scale of the patterning feature based on this method is often larger than 20 nm due to the formation of polymer micelles. Furthermore, the block copolymer spherical domains are formed by the random curliness of

polymer chains, thus the morphology often lacks precise control and shows random distribution.

Small molecules, on the other hand, are easier to be synthesized with special functional group and controlling molecule interaction, thus they are widely used in self-assembly or direction of NP assembly. The structures of self-assembled monolayers (SAMs) of small molecules on Au substrate were widely explored. They often showed well-aligned and close packing superlattice structures, thereby promising potential applications in chemical sensors, molecular electronics, and nanoscale lithography.[19-22] Recently, Xu and co-workers used small molecules to direct NP assemblies, of which showed stimuli-responsive properties.[23] Previously, some superlattice structures of lipids molecules assemblies were represented through the theoretical predications or spectra study.[24, 25] However, these methods are usually with the aid of silicon substrates, and therefore cannot be facilitated to prepare materials in large scale. Hence, it is critical to explore the methodologies to fabricate superlattice structure products with dispersible trait in colloidal solution system. More recently, Li and Cao groups used monodisperse nano-crystals as building blocks to synthesize supercrystalline colloidal spheres with 3D superlattice structure.[8-11]

Up to now, the assembly of small clusters in nanoscale is still a major challenge because the assembly is mainly based on the substrate with the aid of polymer patterning. Therefore, the assembly technique is still a far cry from the

rationally controlled structure of small clusters in large scale. In this chapter, we report a facile method utilizing thiol-ended phospholipid ligand, 2-dipalmitoyl-*sn*-glycero-3-phosphothioethanol (sodium salt; *abbr.* DPPTE) for the assembly of silver cluster superlattices by colloidal self-assembly approach.

6.2 Materials and Methods

6.2.1 Materials

All chemical reagents were obtained from commercial suppliers and used without further purification. Hydrogen tetrachloroaurate(III) hydrate ($HAuCl_4$ H_2O), 99.9% (metals basis Au 49%), silver nitrate (99+%) was purchased from Alfa Aesar; amphiphilic diblock copolymer polystyrene-block-poly(acrylic acid) (PS_{154}-b-PAA_{49}, M_n = 16000 for the polystyrene block and M_n = 4300 for the poly(acrylic acid) block, M_w/M_n=1.15) was obtained from Polymer Source, Inc.; DMF, 99.8% was purchased from Tedia Company, Inc.; 1,2-dipalmitoyl-*sn*-glycero-3-phosphothioethanol (Sodium Salt, *abbr.* DPPTE), was purchased from Avanti Polar Lipids. Deionized water (resistance > 18 MΩ cm^{-1}) was used in all of our reactions. All other chemicals were purchased from Aldrich. Copper specimen grids (200 mesh) with formvar/carbon support film (referred to as TEM grids in the text) were purchased from Electron Microscopy Sciences.

6.2.2 Methods

Preparation of silver clusters superlattice. In a typical reaction, 180 μL of H_2O was added to 900 μL of DMF solution, DPPTE (40 μL, 2mg/mL in EtOH),

and $AgNO_3$ (20 μL, 1 mg/mL in H_2O) were then added to the reaction mixture in sequence. The total volume of the final mixture was 1140 μL, where V_{DMF}/V_{H2O} = 4.5, $[AgNO_3]$ = 0.103 mM, [DPPTE] = 0.096 mM. The mixture was heated at 90 ℃ for 1.5 h and then allowed to cool down gradually until room temperature.

Preparation of polymer encapsulated silver clusters superlattices. In a typical reaction, 180 μL of H_2O was added to 600 μL of dioxane solution, which was prepared by mixing PS_{154}-*b*-PAA_{49} (40 μL, 4 mg/mL in dioxane), and dioxane (560 μL). DPPTE (40 μL, 2mg/mL in EtOH), and $AgNO_3$ (20 μL, 1 mg/mL in H_2O) were then added to the reaction mixture in sequence. The total volume of the final mixture was 840 μL, where $V_{dioxane}/V_{H2O}$ = 3, $[AgNO_3]$ = 0.140 mM, [DPPTE] = 0.130 mM. The mixture was heated at 75 ℃ for 1.5 h and then allowed to cool down gradually until room temperature.

UV irradiation operation of the polymer encapsulated silver cluster superlattice. 840 μL of as-synthesized polymer encapsulated silver cluster superlattice sample was transferred into a dialysis tube, which was placed in a beaker containing 1000 mL of H_2O with stirring for 24 hrs to remove the organic solvents and remainder ions. During the dialysis, the water was changed two times. Then the solution was transferred into a quartz cuvette. Finally, the cuvette was put under the UV lamp for 25 hrs to induce the silver reduction and aggregation.

Preparation of polymer encapsulated silver clusters superlattice loaded AgNPs. In a typical reaction, AgNPs were synthesized according to our previous method,[26] and then transferred to 180 μL of H_2O. This solution was added to 900 μL of DMF solution, which was prepared by mixing PS_{154}-*b*-PAA_{49} (40 μL, 4 mg/mL in DMF), and DMF (860 μL). DPPTE (40 μL, 2mg/mL in EtOH), and $AgNO_3$ (20 μL, 1 mg/mL in H_2O) were then added to the reaction mixture in sequence. The total volume of the final mixture was 1140 μL, where $V_{DMF}/V_{H2O} = 4.5$, $[AgNO_3] = 0.103$ mM, $[DPPTE] = 0.096$ mM. The mixture was heated at 100 ℃ for 2 h and then allowed to cool down gradually until room temperature.

6.3   Results and Discussions

A one-pot, "heating and cooling" method is utilized for the assembly of metallic nanoclusters, which is similar to our previous method for the encapsulation of various nano-objects.[27-29] Briefly, DPPTE and $AgNO_3$, were mixed in DMF/H_2O (v/v = 4.5:1) mixture, followed by heating at 90 ℃ for 1.5 hrs, and then slowly cooled down to induce the self-assembly. To isolate the superlattices, the resulting products were purified by using centrifugation to remove the organic solvent, and re-dispersed into water.

Figure 6-1a showed the scheme of the silver cluster superlattice formation. When the mixture solution containing metallic ions and DPPTE was heated, the metal ions would firmly anchor on DPPTE by the coordination and electrostatic attraction. Meanwhile, phospholipid ligand may form vesicles spontaneously

when exposed to water.[30] So the metallic ions bonded phospholipid ligand would be gathered, and assembled together to form ions enriched phospholipid vesicles in order to reduce the surface energy. Synchronously, the vesicles are further assembled, hemi-fused[31] and stuck together to form superlattices based on the hydrophobic van der Waals interaction of the alkyl chain during the cooling down process. At this process, Ag^+ ions may be reduced to Ag^0 owing to the heating treatment in organic solvent, which will be discussed later. This arrangement of the alkyl chain can reduce the total energy as much as possible.

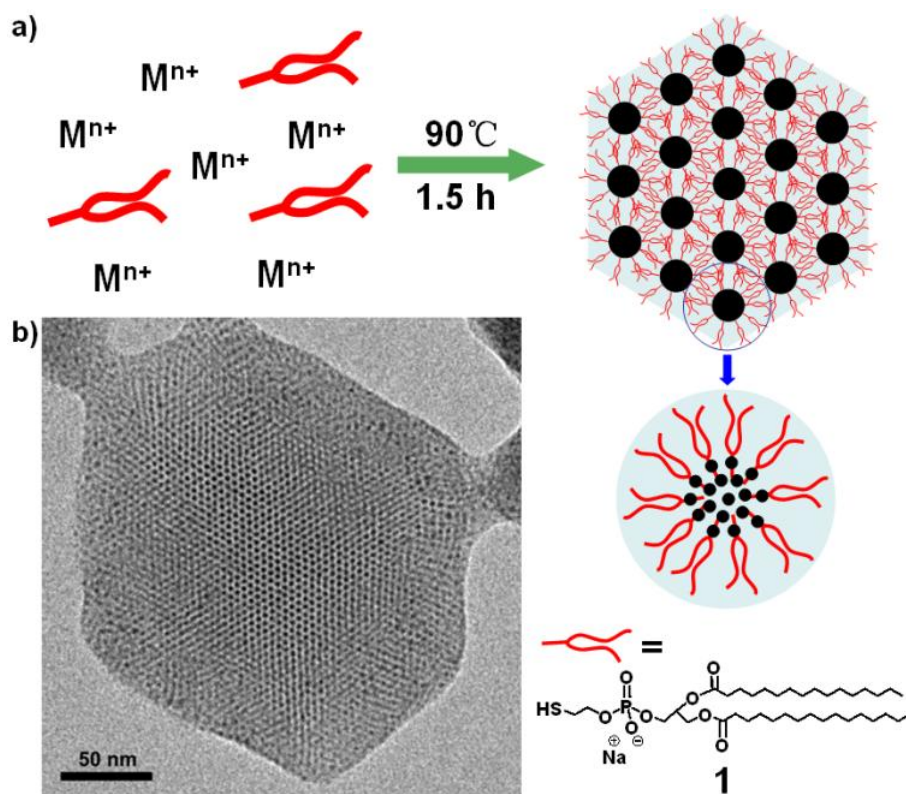**Figure 6-1** (a) Schematic representation of the proposed formation of Ag cluster superlattice in aid of phospholipid ligand, DPPTE under heating circumstance in DMF/H_2O mixture. (b) TEM image of Ag cluster superlattice after purification by H_2O.

Figure 6-1b showed a typical transmission electron microscopy (TEM) image of the resulting superlattices which were self-assembled from the silver

194

clusters in the presence of thiol-ended phospholip ligand in DMF/H_2O mixture. The products were purified by using H_2O and prepared for TEM sample without stain. It was found that numerous mono-dispersed black dots with the diameter of about 2.6 nm were arranged regularly and uniformly to form hexagonal arrays, which was similar to the block copolymer assembled lithography.[12, 13] The average distance between the centers of two neighboring black dots approximately equaled to 1.6 nm. This distance was shorter than the fully dehydrated lipid tail length in bilayer (sum of the both alkyl chains; around 2.5 nm).[32] This may be because the chains between two adjacent black dots interlaced during the vesicles shrinking together process. From the contrast of TEM image, we argued that this kind of superlattices were three-dimensional structures.

Other metallic ions were investigated to study the superlattice formation. Some ions, such as Zn^{2+}, Cd^{2+}, which could coordinate with the thiol group well, could direct the regular lattice structures, in despite of the structures being not very good (Figure 6-2a and b). However, for the case of $HAuCl_4$ salt, there were some irregular packing structures and some large Au nanoparticles (AuNPs) in the system, which were due to the further reduction of $HAuCl_4$ in DMF solution (Figure 6-2c). Figure 6-2d showed the TEM image of superlattices when $AgNO_3$ amount was increased to five times. Some large AgNPs coexisted in the product indicated that the formed Ag clusters could be

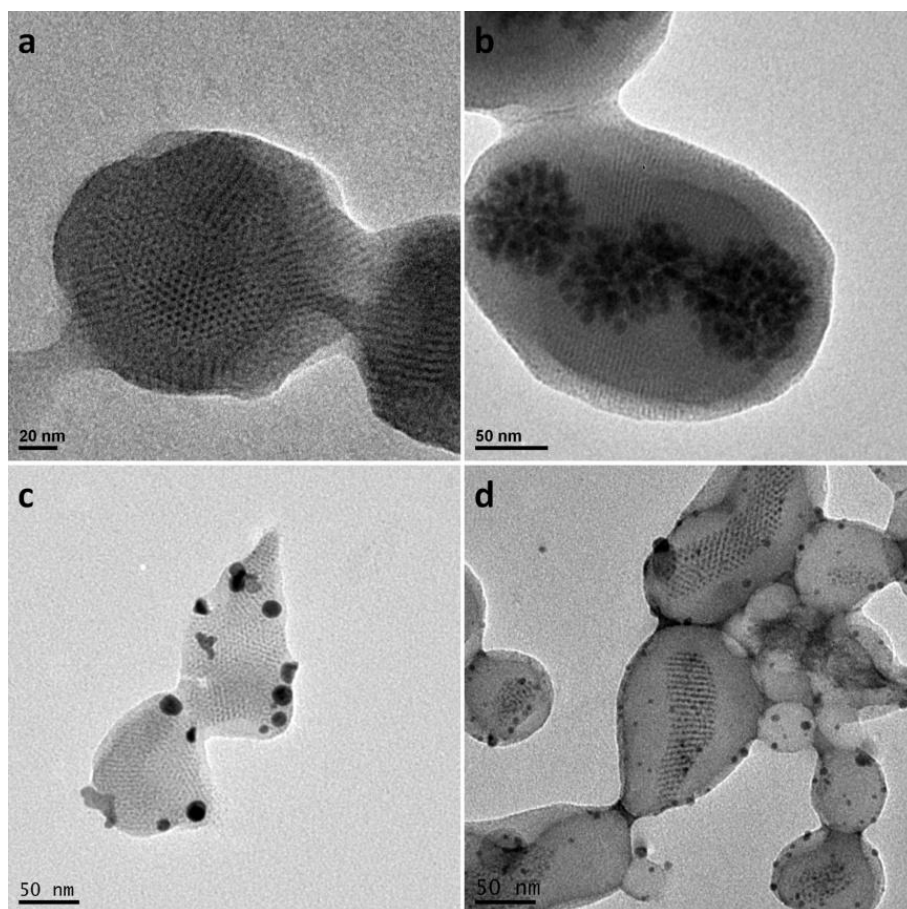further aggregated due to the high concentration, also proving that the perhaps reduction of Ag^+ to Ag^0.

Figure 6-2 TEM images of different metal ions induced superlatticle structures. (a) $Zn(CH_3COO)_2$; (b) $CdCl_2$; (c) $HAuCl_4$; (d) 5 times amount of $AgNO_3$ was used in the presence of polymer, which can encapsulate the superlattice structure by self-assembly. The polymer coating will be discussed in the following part.

It is also found that other thiol-ended ligand cannot be used to produce the superlattice well, which may be due to the different hydrophobic properties of these ligands. In some cases, large AgNPs were the main products, which demonstrated that DPPTE also played an important role in stabilizing and protecting the small clusters during the heating procedure (Figure 6-3a-c). However, 1,2-dimyristoyl-*sn*-glycero-3-phosphocholine (*abbr*. DMPC), which

has the same hydrophobic alkyl chains, also did not work well for the silver cluster superlattice formation (Figure 6-3d). This unexpected result proved that the thiol group in the phospholipids was very important for the superlattice formation. If $HAuCl_4$ was treated with the DMPC, the result solution represented some cyan color. The TEM survey showed that there was no superlattice assembly but some large AuNPs. Combining with the previous results, we may argue that the thiol-ended ligand with long alkyl chain is crucial for the superlattice assembly.
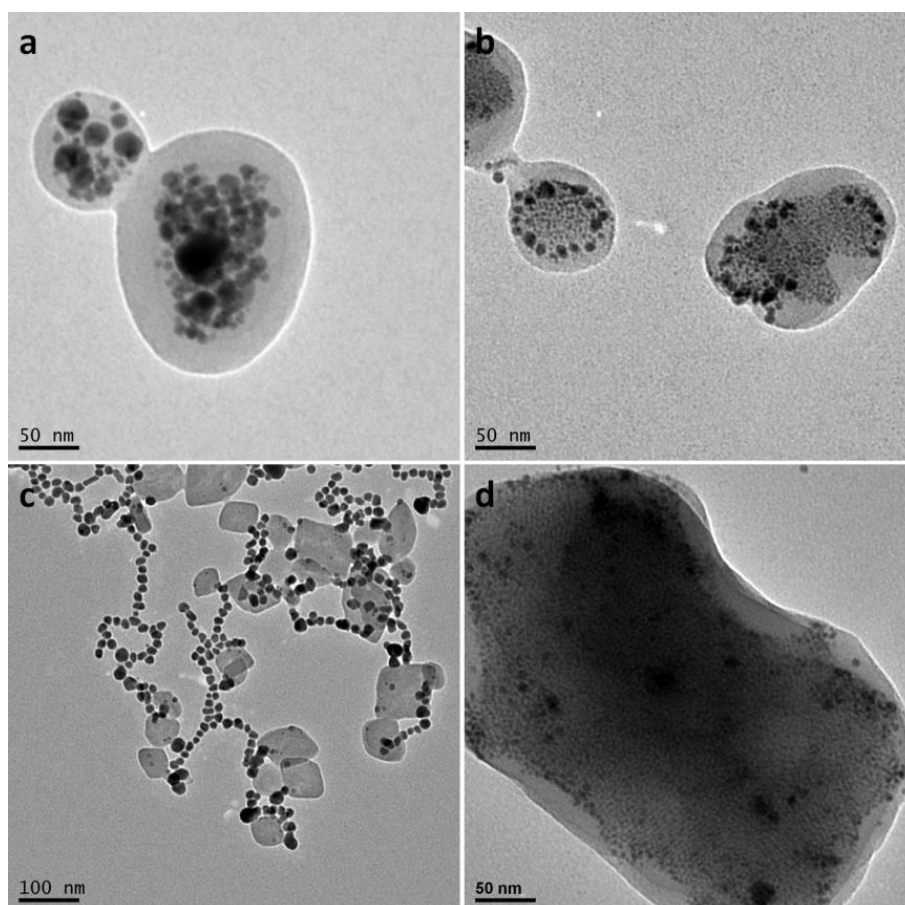

Figure 6-3 TEM images of different ligands induced silver nanostructures in the presence of polymer: (a) Naphthalene-thiol; (b) 1-Hexadecanethiol; (c) 4-Mercaptobenzoic acid; (d) DMPC.

In order to test the stability of these silver cluster superlattices, the product was treated by $NH_3 H_2O$. From the TEM characterization, we could find the well-ordered superlattice structures were destroyed, which demonstrated that the hydrophobic packing of phospholipid chains was not close enough to prevent the entrance of $NH_3 H_2O$ into the vesicle.

In the past several years, our group has been successful in encapsulation of various nano-objects by coating copolymers on the surface of hydrophobic ligand functionalized NPs, in which the polymer shells on the surface not only can stabilize the nano-objects, but also can be further functionalized to improve the properties of the core materials.[27-29] Therefore, the superlattice structures were encapsulated by using diblock copolymer. Owing to the factor that polymer shell can protect the superlattice from the damage of measurements and solvents, more information of the superlattice can be obtained by surveying the stabilized assembly, which also finally helps us to study the superlattice formation mechanism.

In a typical superlattices encapsulation approach, diblock copolymer PS_{1250}-b-PEO_{409}, was added directly into the dioxane/H_2O (v/v = 3:1) mixture containing DPPTE and $AgNO_3$. The mixture was heated at 75 ℃ for 2 hrs and then slowly cooled down to induce the polymer self-assembly. The resulting products were purified by using centrifugation, and re-dispersed into water.
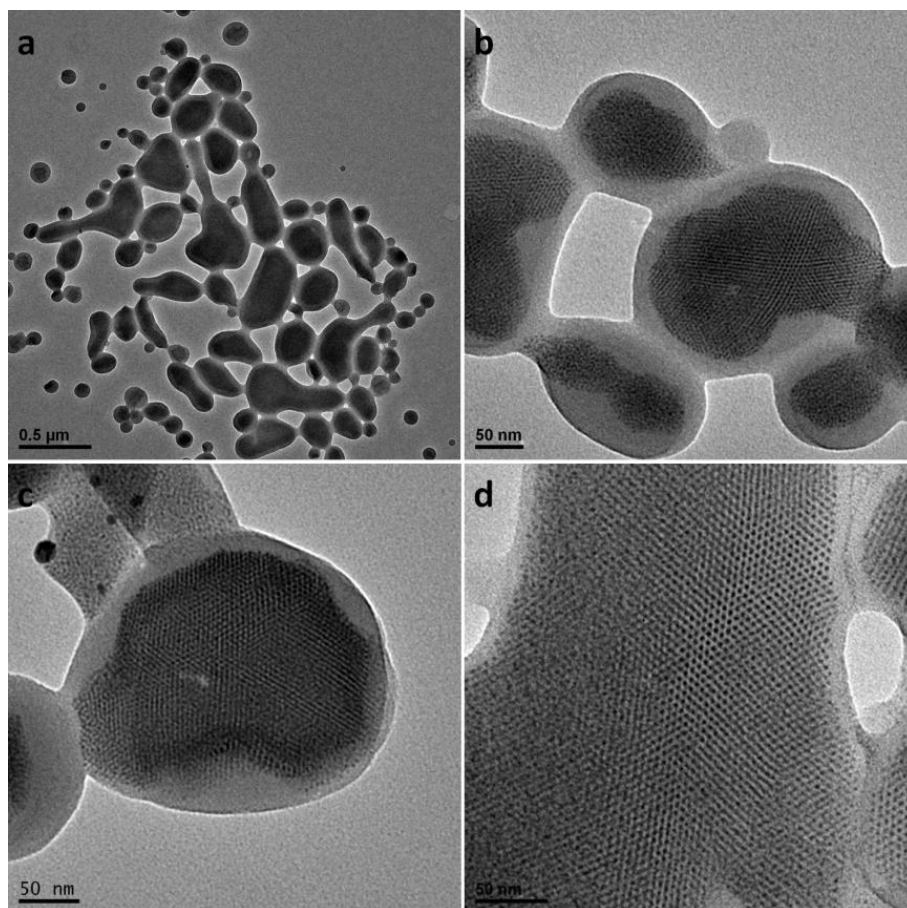
Figure 6-4 (a and b) low and high magnified TEM images of the superlattice assemblies, which were encapsulated by PS_{1250}-b-PEO_{409}; (c) TEM images of the superlattice assemblies, which were encapsulated by PS_{1442}-b-PEO_{795}; (d) TEM images of the superlattice assemblies, which were encapsulated by PS_{154}-b-PAA_{49}. These samples were prepared in dioxane/H_2O (a, b, d) and DMF/H_2O (c) mixture solution.

Figure 6-4 showed the superlattice assemblies of silver clusters, which were encapsulated in the PS-b-PEO or PS-b-PAA micelles. From Figure 6-4a, we observed that the size distribution of superlattices were very large (the diameters range from 100 nm to 500 nm), and various shapes were obtained. It was very interesting that though the lengths of the hydrophobic or hydrophilic chains in the copolymers were highly different for these four samples, the distances of two black dots approximately equaled to 2.6 nm, which were

consistent with the lattice space of pure DPPTE superlattice assembled in DMF/H$_2$O mixture. This phenomenon proved that the copolymer chain could not influence the superlattice structure, and also demonstrated that the superlattice structures were just dependent on the thiol-ended phospholipid ligand (Figure 6-5a and b). However, these superlattice assemblies were not as regular as the pure DPPTE assemblies with AgNO$_3$. This may be due to the polymer shrinkage, which could inflect the DPPTE induced well-ordered superlattices. These core-shell structures could maintain the superlattice arrangements well after the NH$_3$ H$_2$O etching treatment, demonstrated that the polymer shells covered the superlattice very closely and thus prevented the silver cluster from etching (Figure 6-5c).

Control experiments were performed to confirm the polymer encapsulated superlattices assemblies were not the self-assembly of diblock copolymer. When DPPTE was removed from the synthesis solution, only the polymer and AgNO$_3$ were heated in the dioxane/H$_2$O mixture. TEM images reflected that the products were similar to Eisenberg's results, in which the addition of AgNO$_3$ in the polymer system can help the formation of various strange micelles (Figure 6-5d).[33] These phenomena demonstrated that the formation of superlattice structures were under the cooperation of phospholipid ligand, and AgNO$_3$, but not relied on the copolymer.
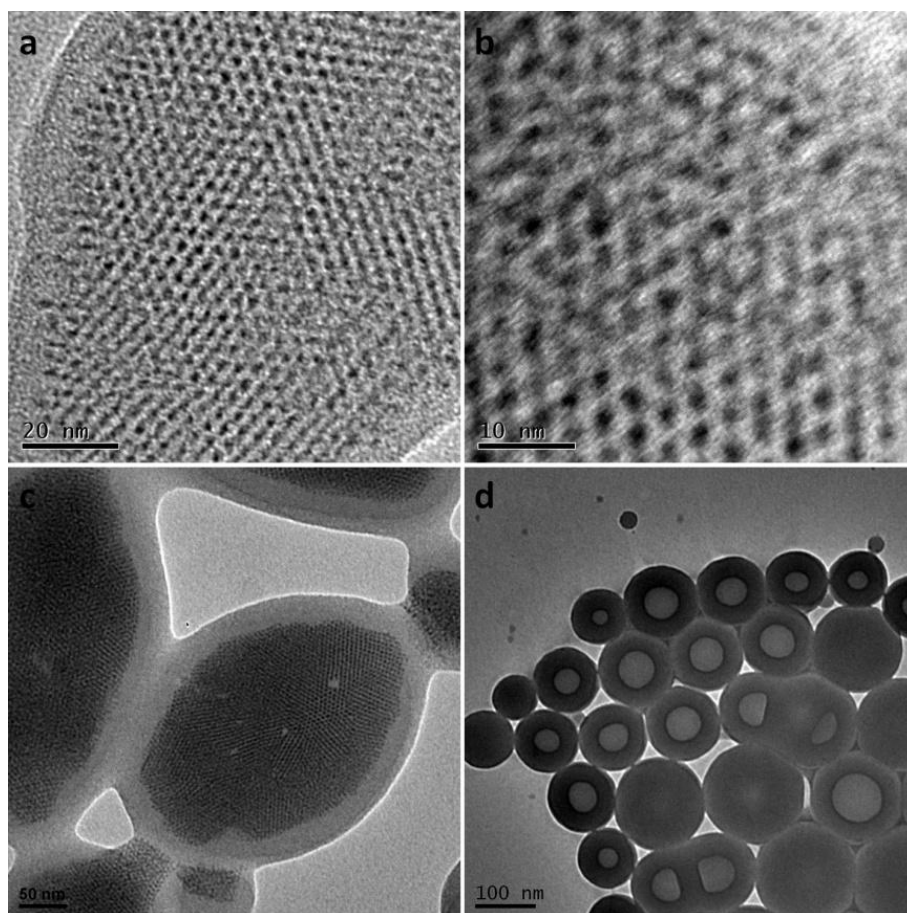
Figure 6-5 (a and b) High resolution TEM images of the superlattice structures encapsulated in the PS$_{1250}$-*b*-PEO$_{409}$ polymer shell, which demonstrated that the superlattice arrangement were not influenced by the polymer coating. (c) TEM image of the PS$_{1250}$-*b*-PEO$_{409}$ coated superlattice structures after the NH$_3$ H$_2$O etching treatment. (d) TEM images of the vesicle structures formed by incubating AgNO$_3$, PS$_{1250}$-*b*-PEO$_{409}$ in dioxane/H$_2$O mixture at 75 ℃ for 2 hrs.

When the solvent was changed to DMF/H$_2$O (v:v = 4.5:1) mixture, the encapsulation morphologies showed some change. From the TEM images, it was found that PS$_{1250}$-*b*-PEO$_{409}$ didn't encapsulate all the superlattice assemblies, in which there was no polymer corona around some superlattice assemblies, although the superlattice structures were perfectly regular (Figure 6-6a and b). For the PS$_{154}$-*b*-PAA$_{49}$ encapsulation, the silver clusters could not be assembled to form regular lattice as well as in dioxane/H$_2$O system, and in

some cases, even large AgNPs existed (Figure 6-6c and d). However, in PS$_{1442}$-b-PEO$_{795}$, the regular lattice packing as well as the fully polymer coating could be obtained in DMF/H$_2$O mixture (Figure 6-4c).This may be due to the varying solubility of the polymers, which influences the polymer self-assembly.
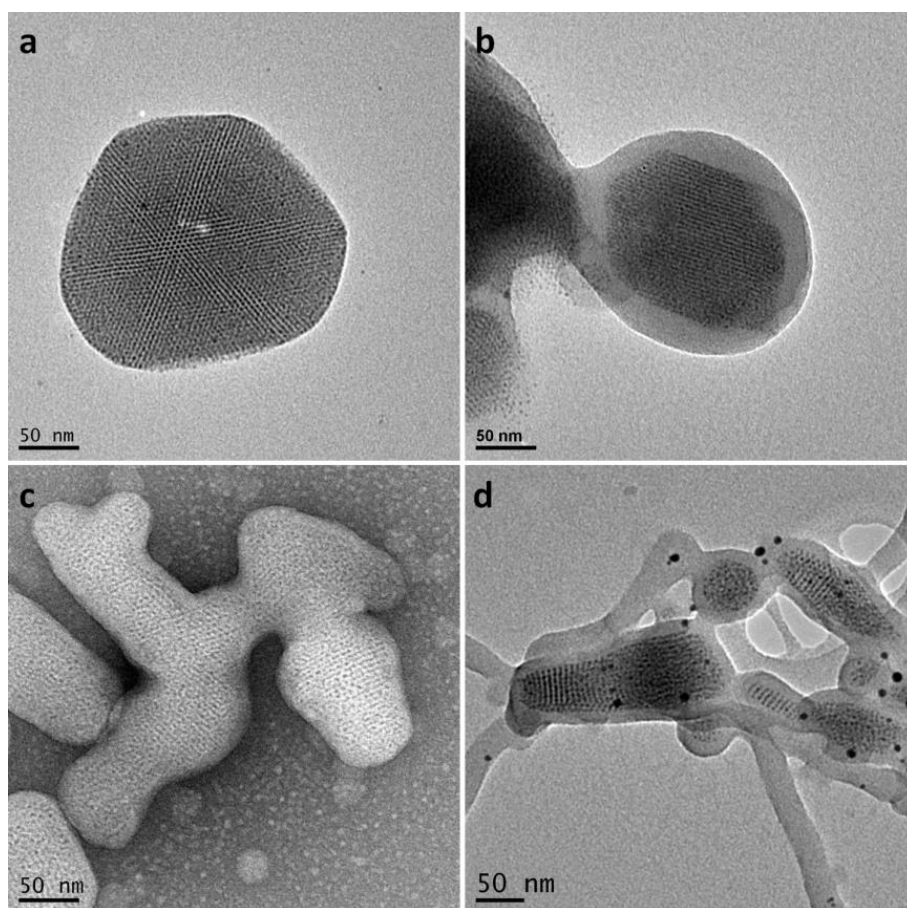

Figure 6-6 TEM images of superlattice formed in DMF/H$_2$O mixture solution in the presence of PS$_{1250}$-b-PEO$_{409}$ (a and b), or PS$_{154}$-b-PAA$_{49}$ (c and d).

The PS$_{1250}$-b-PEO$_{409}$ encapsulated superlattice sample was dialyzed overnight in H$_2$O to remove the organic solvent and any residue AgNO$_3$. TEM images of the dialyzed sample demonstrated the superlattices have not been destroyed during the dialysis progress (Figure 6-8a). UV lamp was used to irradiate the dialyzed sample for 25 hrs. The superlattice arrangements were destroyed gradually with increasing irradiation time. Figure 6-8b showed the

TEM image of the encapsulated superlattice sample treated by UV irradiation for 13 hrs. It was found that some small size AgNPs generated and the lattice arrangement was partially reorganized to irregular packing. When the irradiation time reached 25 hrs, in some cases, large AgNPs appeared and located in the cavities of the micelles (Figure 6-8d). Figure 6-8c showed the intermediate state of the large AgNPs formation, in which small AgNPs moved to one side of the cavity and aggregated to form large NPs. This morphology changing process could further prove that the superlattice structure was silver clusters superlattice, and not the self-assembly of polymer or ligand. Therefore, it seemed that the core-shell superlattice structures formation contained two steps: superlattice structures formation and polymer encapsulation process.

These AgNPs located in the polymer cavities were created by the UV irradiation. This energy caused silver clusters aggregation and further reorganization. Previous literatures[34-36] have represented that UV light could produce electron-hole pairs by exciting the PS domains of the copolymers, in which electrons could reduce the Ag^+ to Ag^0 by the strong reducing ability. In our case, the high energy of the UV light could heat the small clusters to fuse them together and then further restructure the shapes. We tried to use selected area electron diffraction (SAED) to check the superlattice domains. Unfortunately, we cannot obtain any diffraction pattern. When we performed the SAED testing for the AgNPs in the UV irradiated superlattice, the diffraction pattern of polycrystalline Ag was obtained (Figure 6-7).
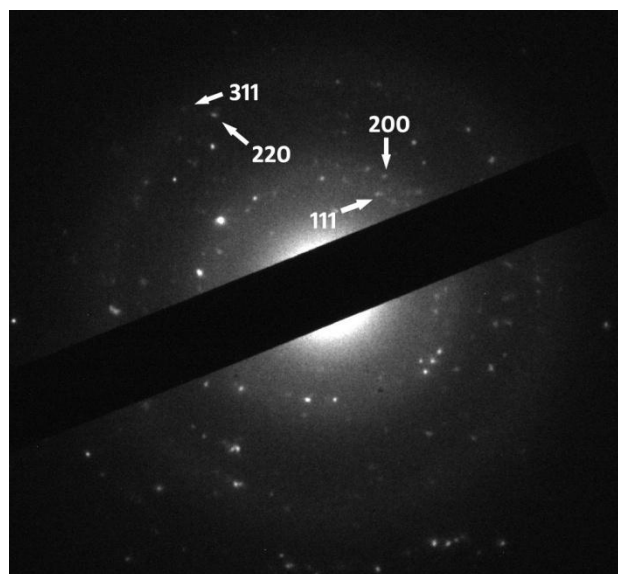
Figure 6-7 Selected area electron diffraction (SAED) patterns of the AgNPs formed by the UV irradiation on the superlattices.
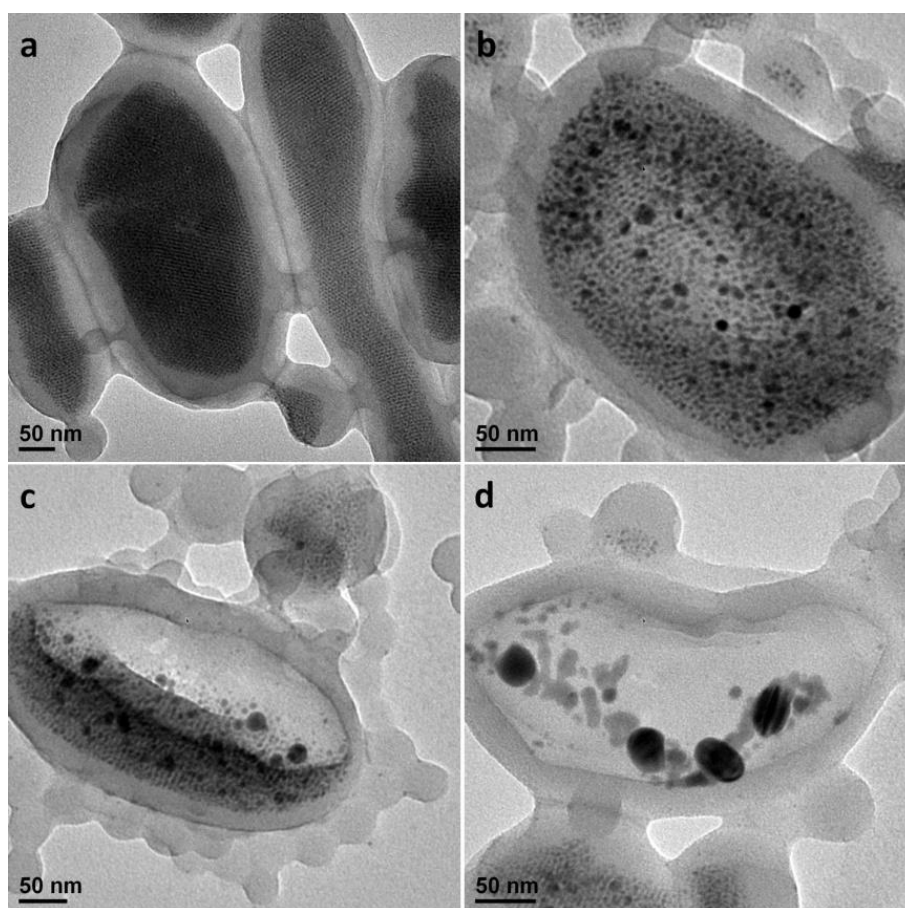

Figure 6-8 TEM images of the polymer encapsulated silver clusters superlattice structures treated by UV irradiation for different time: (a) after dialysis and before irradiation; (b) irradiate for 13 hrs; (c and d) irradiate for 25 hrs.
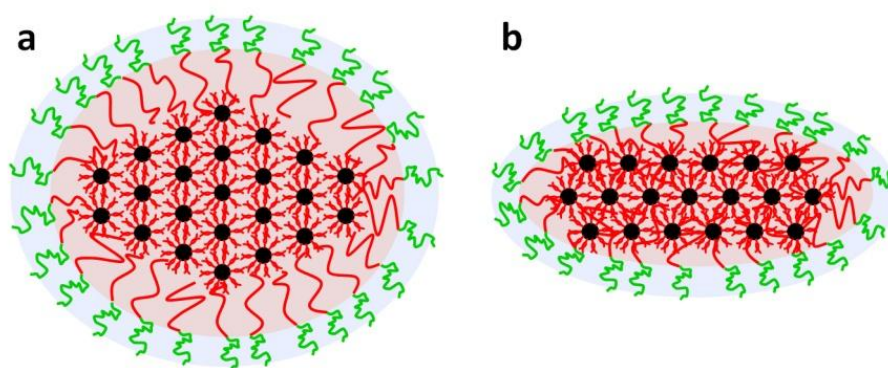
Figure 6-9 Schematic illustrations of the polymer encapsulated superlattice structures: top view (a) and side view (b).

The mechanism of the superlattice formation could be proposed according to the results. Figure 6-9a and b illustrated the structure of superlattice coated by a vesicle micelle. When AgNO$_3$ was introduced into the heating DPPTE solution, Ag$^+$ ions coordinated to the thiol group of the DPPTE, as well as some Ag$^+$ ions could be enriched in the lipid head area through the charge attraction. These Ag$^+$ ions may be reduced owing to the high temperature treatment in organic solvent. These Ag clusters were coated with DPPTE, which could prevent the Ag clusters from further growth. During cooling down process, these Ag clusters bound phospholipid ligands would gather, and assemble together to form silver enriched phospholipid vesicles in order to reduce the surface energy. Meanwhile, the vesicles were further hemi-fused and gathered together to form the superlattice structures due to the hydrophobic van der Waals interaction of the alkyl chain. This resulted in the formation of 3D silver cluster superlattices. The polymers also assembled owing to the low solubility of PS in the cooling solvent. The PS segments were allowed to dig into the micelles, which could encapsulate the hydrophobic silver clusters superlattice.

Consequently, we observed the large vesicle structure of polymer after the UV irradiation. Since the superlattice formation is related to the silver enriched phospholipid vesicles fusion process, I believe the large size distribution of the superlattice domains is related to this random lipid fusing process. The simultaneous polymer assembly also may influence this fusion procedure.
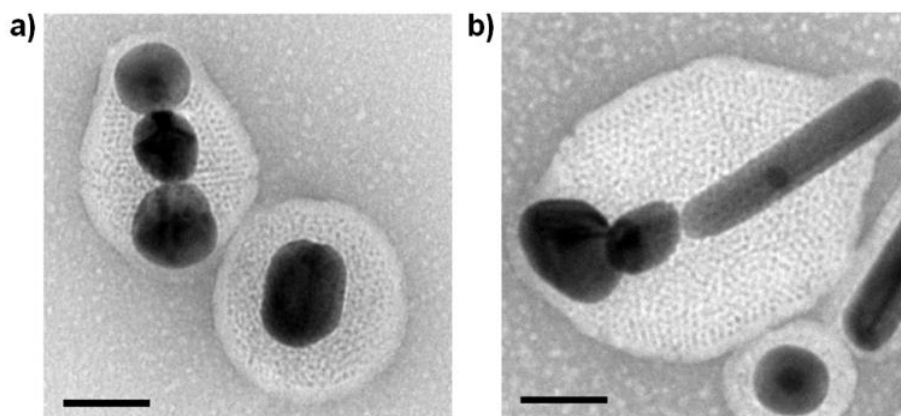

Figure 6-10 (a) and (b) TEM images of the copolymer (PS_{144}-*b*-PAA_{28}, and PS_{154}-*b*-PAA_{49}, respectively) encapsulated AgNPs, in which silver clusters superlattice are assembled in the swelling polymer micelles. Scale bars: 50 nm.

It is also found that the superlattices could be decorated on the surface of other NPs by introducing the NPs into the copolymer encapsulation system. Figure 6-10 showed the typical TEM images of the copolymer encapsulated AgNPs, in which silver clusters superlattice was assembled in the swelling polymer micelles. Because of the high contrast of the NPs, superlattice structures could not be observed clearly. Moreover, there were still some NPs without any superlattices, but encapsulated by copolymer with normal polymer shell thickness. This may be due to the random loading of the superlattices. During the cooling down process, some polymers did not contain the

superlattice, and thus encapsulate the NPs as usual.[27-29] It can be predicted that this kind of superlattice structures can be docked onto various nanomaterials.

We believe that the superlattices should be 3D. The most convincing method is checking the shape of these superlattices. However, due to the polymer coating, we cannot determine it by SEM characterization. Theoretically, the superlattice formation is due to the phospholipid fusion, in which the total surface energy is minimized. Therefore, they prefer to form 3D packing. Moreover, in the TEM images of nanocomposites containing nanoparticles and superlattices (Figure 6-10), superlattices still can be observed for all the samples. If they are 2D, it is impossible to find this phenomenon.

6.4   Conclusions

In summary, a facile method was developed to synthesize silver cluster superlattices by utilizing thiol-ended phospholipid ligand. The detailed investigation showed that these superlattices were due to the assembly of the silver enriched phospholipid vesicles. The superlattice could be further encapsulated into diblock copolymer shells without the morphology change. This procedure could increase the stability of the superlattice, and offer an insulating coating on the surface. After UV irradiation on the polymer encapsulated superlattice, large AgNPs could be formed in the vesicle cavity. The superlattices could also be decorated on the surface of NPs by the polymer encapsulation. Thus, this total synthesis method contained the assembly,

encapsulation, decoration of the silver superlattices, in which new properties and potential application may create.

6.5 Bibliography

[1] Velev, O. D. and Gupta, S., Materials Fabricated by Micro- and Nanoparticle Assembly-the Challenging Path from Science to Engineering. *Adv. Mater.*, **21**, 1897 (2009).

[2] Cheng, J. Y., Ross, C. A., Smith, H. I., and Thomas, E. L., Templated Self-Assembly of Block Copolymers: Top-Down Helps Bottom-Up. *Adv. Mater.*, **18**, 2505 (2006).

[3] Nie, Z. and Kumacheva, E., Patterning Surfaces with Functional Polymers. *Nat. Mater.*, **7**, 277 (2008).

[4] Mirkin, C. A., Letsinger, R. L., Mucic, R. C., and Storhoff, J. J., A DNA-Based Method for Rationally Assembling Nanoparticles into Macroscopic Materials. *Nature*, **382**, 607 (1996).

[5] Collier, C. P., Vossmeyer, T., and Heath, J. R., Nanocrystal Superlattices. *Annu. Rev. Phys. Chem.*, **49**, 371 (1998).

[6] Tang, Z., Zhang, Z., Wang, Y., Glotzer, S. C., and Kotov, N. A., Self-Assembly of Cdte Nanocrystals into Free-Floating Sheets. *Science*, **314**, 274 (2006).

[7] Kim, S. H., Lee, S. Y., Yi, G. R., Pine, D. J., and Yang, S. M., Microwave-Assisted Self-Organization of Colloidal Particles in Confining Aqueous Droplets. *J. Am. Chem. Soc.*, **128**, 10897 (2006).

[8] Bai, F., Wang, D. S., Huo, Z. Y., Chen, W., Liu, L. P., Liang, X., Chen, C., Wang, X., Peng, Q., and Li, Y. D., A Versatile Bottom-up Assembly Approach to Colloidal Spheres from Nanocrystals. *Angew. Chem., Int. Ed.*, **46**, 6650 (2007).

[9] Zhuang, J. Q., Wu, H. M., Yang, Y. A., and Cao, Y. C., Supercrystalline Colloidal Particles from Artificial Atoms. *J. Am. Chem. Soc.*, **129**, 14166 (2007).

[10] Zhuang, Z., Peng, Q., Zhang, B., and Li, Y., Controllable Synthesis of Cu2s Nanocrystals and Their Assembly into a Superlattice. *J. Am. Chem. Soc.*, **130**, 10482 (2008).

[11] Zhuang, J. Q., Wu, H. M., Yang, Y. G., and Cao, Y. C., Controlling Colloidal Superparticle Growth through Solvophobic Interactions. *Angew. Chem., Int. Ed.*, **47**, 2208 (2008).

[12] Ruiz, R., Kang, H., Detcheverry, F. A., Dobisz, E., Kercher, D. S., Albrecht, T. R., de Pablo, J. J., and Nealey, P. F., Density Multiplication and Improved Lithography by Directed Block Copolymer Assembly. *Science*, **321**, 936 (2008).

[13] Bita, I., Yang, J. K. W., Jung, Y. S., Ross, C. A., Thomas, E. L., and Berggren, K. K., Graphoepitaxy of Self-Assembled Block Copolymers on Two-Dimensional Periodic Patterned Templates. *Science*, **321**, 939 (2008).

[14] Tang, C., Lennon, E. M., Fredrickson, G. H., Kramer, E. J., and Hawker, C. J., Evolution of Block Copolymer Lithography to Highly Ordered Square Arrays. *Science*, **322**, 429 (2008).

[15] Darling, S. B., Directing the Self-Assembly of Block Copolymers. *Prog. Polym. Sci.*, **32**, 1152 (2007).

[16] Lopes, W. A. and Jaeger, H. M., Hierarchical Self-Assembly of Metal Nanostructures on Diblock Copolymer Scaffolds. *Nature*, **414**, 735 (2001).

[17] Watanabe, S., Fujiwara, R., Hada, M., Okazaki, Y., and Iyoda, T., Site-Specific Recognition of Nanophase-Separated Surfaces of Amphiphilic Block Copolymers by Hydrophilic and Hydrophobic Gold Nanoparticles. *Angew. Chem., Int. Ed.*, **46**, 1120 (2007).

[18] Spatz, J. P., Chan, V. Z. H., Mossmer, S., Kamm, F. M., Plettl, A., Ziemann, P., and Moller, M., A Combined Top-Down/Bottom-up Approach to the Microscopic Localization of Metallic Nanodots. *Adv. Mater.*, **14**, 1827 (2002).

[19] Crooks, R. M. and Ricco, A. J., New Organic Materials Suitable for Use in Chemical Sensor Arrays. *Acc. Chem. Res.*, **31**, 219 (1998).

[20] Willner, I. and Katz, E., Integration of Layered Redox Proteins and Conductive Supports for Bioelectronic Applications. *Angew. Chem., Int. Ed.*, **39**, 1180 (2000).

[21] Joachim, C., Gimzewski, J. K., and Aviram, A., Electronics Using Hybrid-Molecular and Mono-Molecular Devices. *Nature*, **408**, 541 (2000).

[22] Tinazli, A., Piehler, J., Beuttler, M., Guckenberger, R., and Tampe, R., Native Protein Nanolithography That Can Write, Read and Erase. *Nat. Nanotechnol.*, **2**, 220 (2007).

[23] Zhao, Y., Thorkelsson, K., Mastroianni, A. J., Schilling, T., Luther, J. M., Rancatore, B. J., Matsunaga, K., Jinnai, H., Wu, Y., Poulsen, D., Frechet, J. M. J., Alivisatos, A. P., and Xu, T., Small-Molecule-Directed Nanoparticle Assembly Towards Stimuli-Responsive Nanocomposites. *Nat. Mater.*, **8**, 979 (2009).

[24] Virtanen, J. A., Somerharju, P., and Kinnunen, P. K. J., Prediction of Patterns for the Regular Distribution of Soluted Guest Molecules in Liquid-Crystalline Phospholipid-Membranes. *Journal of Molecular Electronics*, **4**, 233 (1988).

[25] Tang, D. and Chong, P. L. G., E/M Dips - Evidence for Lipids Regularly Distributed into Hexagonal Super-Lattices in Pyrene-Pc/Dmpc Binary-Mixtures at Specific Concentrations. *Biophys. J.*, **63**, 903 (1992).

[26] Chen, G., Wang, Y., Yang, M. X., Xu, J., Goh, S. J., Pan, M., and Chen, H. Y., Measuring Ensemble-Averaged Surface-Enhanced Raman Scattering in the Hotspots of Colloidal Nanoparticle Dimers and Trimers. *J. Am. Chem. Soc.*, **132**, 3644 (2010).

[27] Chen, H. Y., Abraham, S., Mendenhall, J., Delamarre, S. C., Smith, K., Kim, I., and Batt, C. A., Encapsulation of Single Small Gold Nanoparticles by Diblock Copolymers. *ChemPhysChem*, **9**, 388 (2008).

[28] Wang, X. J., Li, G. P., Chen, T., Yang, M. X., Zhang, Z., Wu, T., and Chen, H. Y., Polymer-Encapsulated Gold-Nanoparticle Dimers: Facile Preparation and Catalytical Application in Guided Growth of Dimeric Zno-Nanowires. *Nano Lett.*, **8**, 2643 (2008).

[29] Yang, M. X., Chen, T., Lau, W. S., Wang, Y., Tang, Q. H., Yang, Y. H., and Chen, H. Y., Development of Polymer-Encapsulated Metal Nanopartictes as Surface-Enhanced Raman Scattering Probes. *Small*, **5**, 198 (2009).

[30] Bangham, A. D. and Horne, R. W., Negative Staining of Phospholipids + Their Structural Modification by-Surface Active Agents as Observed in Electron Microscope. *J. Mol. Biol.*, **8**, 660 (1964).

[31] Chen, Y. A. and Scheller, R. H., Snare-Mediated Membrane Fusion. *Nat. Rev. Mol. Cell Biol.*, **2**, 98 (2001).

[32] Lewis, B. A. and Engelman, D. M., Lipid Bilayer Thickness Varies Linearly with Acyl Chain-Length in Fluid Phosphatidylcholine Vesicles. *J. Mol. Biol.*, **166**, 211 (1983).

[33] Zhang, L. F., Yu, K., and Eisenberg, A., Ion-Induced Morphological Changes in "Crew-Cut" Aggregates of Amphiphilic Block Copolymers. *Science*, **272**, 1777 (1996).

[34] Yong, Z., Shu, H. Y., Cui, Y. W., Xiao, G. L., Yu, R. Z., and Zu, Y. C., A Novel Ultraviolet Irradiation Photoreduction Technique for the Preparation of Single-Crystal Ag Nanorods and Ag Dendrites. *Adv. Mater.*, **11**, 850 (1999).

[35] Dmitry, G. S., Igor, L. R., and Gleb, B. S., Photoinduced Reduction of Silver inside Microscale Polyelectrolyte Capsules. *ChemPhysChem*, **4**, 1101 (2003).

[36] Zhang, J., Xu, S., and Kumacheva, E., Photogeneration of Fluorescent Silver Nanoclusters in Polymer Microgels. *Adv. Mater.*, **17**, 2336 (2005).

Chapter 7 Summary and Future Work

7.1 Summary

Multi-component nanostructures usually have abundant structural variety. They can provide not only the properties of each individual, but also the new feature owing to the interaction of them. Therefore, insight into the multi-component system may explore new synthetic strategies and novel architectures, satisfying the requirement of future nanodevices.

In this thesis, two strategies were used for the manufacture of multi-component nanomaterials: rational assembly and direct growth based on wet chemistry. Based on these methods, stoichiometry controlled hetero-assembly of NPs were obtained. Then we accomplished the ultrathin NW shape transformation by the metal layer overgrowth: from single NW to double helix. Helical gold NWs also were prepared via one pot synthesis in the colloidal solution. Heterodimeric nanostructures were achieved by choosing specific seeds or fine-tuning the surface properties of seeds. Finally, one type of Ag superlattice structures was prepared by the self-assembly of Ag ions and thiol-ended ligands in colloidal solution.

First, we developed a complete nanoreaction system whereby colloidal nanoparticles are rationally assembled and purified. Generally, sodium citrate

stabilized AuNPs (called as B-NPs) was functionalized with one kind of multi-thiol ended ligand. Then these NPs were purified, and could re-disperse well in DMF (called as A-NPs). When these two types of gold nanoparticles (A and B) were mixed together, they were bonded to give specific products AB, AB_2, AB_3 and AB_4 in different solution by carefully varying the ionic strength. The stoichiometry control is realized by fine-tuning the charge repulsion among the B-NPs. The products are protected by polymer, which allowed their isolation in high purity. With the concrete integration of hetero-assembly, stoichiometry control, protection scheme, and separation method, we attempt to create a scalable means to fabricate sophisticated nanostructures. By using this strategy, many nanostructures, which cannot be obtained through the routine method, also have been fabricated.

Then, we develop one new strategy to synthesize ultrathin Au-Ag NWs in polar solvent. This kind of NWs exhibited unprecedented behavior in the colloidal solution: the NW winds around itself to form a metallic double helix when a thin layer of metal (Pd, Pt, or Au) was grown on its surface. The uniformity of these winding could be controlled by choosing different metal deposition speed. The mechanism of the NWs winding was also studied based on the high resolution TEM characterization of the as-synthesized NWs. These Au-Ag alloy NWs likely had the Boerdijk-Coxeter-Bernal type twisted lattice. The winding was originated from the instinct chirality within the NW. When the metal deposited, the expansion of the NW lateral dimension increases the

strain therein. To minimize the overall lattice energy, the NWs were forced to untwist (twisting in the opposite direction of the BCB lattice). Besides the potential catalysis applications of the formed Au-Ag@M (Pd or Pt) core-shell nanostructures, this environment-responded shape transformation system (chemical stimuli) may offer the opportunity for smart nanodevices application.

Helical gold nanowires have been synthesized via one pot synthesis strategy without any hard template. Different from the previous methods, in which hard template were used, our system is easy to accomplish the large-scale synthesis because of the colloidal procedure: gold precursor, reducing agent, seeds as well as the capping agents were incubated in the mixture of ethanol and H_2O for several hrs. This was the first case of metallic nanosprings synthesized in colloidal solution. By analyzing the reaction conditions, we found that the growth solution consists of several small organic molecules derived from 4-mercaptobenzonic acid. However, the yield was still very low, which prevented insight into the growth mechanism. The HRTEM analysis reflected that these helical NWs were perfect single crystalline structures with little lattice aberrance.

It has been witnessed that wet chemistry synthesis strategy was one powerful weapon to create multi-component nanostructures, especially since the seed-mediated growth procedure was used. Two kinds of polycrystalline NPs were used as seeds to synthesize heterodimers. Pt-M, (M = Au, or Ag) heterodimers were obtained owing to the large lattice mismatching of Pt-Au

and Pt-Ag, in which Volmer-Weber growth mode was adopted. Au-M (M = Au, or Ag) heterodimers were obtained by tuning the surface molecules coating. When the molecules coated on the Au seeds surfaces, the interface energy would increase, thus the Stranski-Krastanov growth mode, even the Volmer-Weber growth mode would perform. It was also found that these formed Ag domains were with the same lattice orientation as the nucleation sites on the seeds. This may offer one opportunity to prepare single crystalline NPs through the polycrystalline NP seeds.

Finally, we reported one kind of Ag cluster superlattices, which were synthesized in colloidal solution in the presence of a thiol-ended ligand with long hydrophobic alkyl chain. These superlattices structures could be encapsulated into the copolymer cavity and docked onto other nanostructures by the polymer coating procedure. This kind of superlattices could be destroyed by the long time UV irradiation. The superlattice structures collapsed, and large AgNPs were generated simultaneously. We proposed that the superlattices were formed by the close packing of Ag domains, which were fully coated by thiol-ended hydrophobic molecules. This assembly mode can decrease the surface energy of each hydrophobic Ag domain as much as possible. This kind superlattice structures may potentially be used in the optical field.

7.2 Future Work

Based on the understanding of the multi-component system and the strategies developed previously, several topics of work in the future are

proposed:

(1) Synthesis of multi-component nanostructures based on the nanoreaction system. Dumbbell-like Fe_3O_4-Au heterodimers, which were well studied by Prof. Sun's group[1], could be selective functionalized by **1** on the Au surface. Thus these functionalized dimers could be used to react with Ag or Au NPs to form hetero-trimeric aggregates (Figure 7-1a). Although this kind of hetero-structures have been reported very recently,[2] our method can be performed more easier. The products could combine the magnetism properties of Fe_3O_4 and the SPR coupling of Au-Ag or Au-Au heterodimers. Therefore, this kind of nanomaterials can be potentially used in the bio-sensing and bio-images system. Furthermore, Pt or Pd NPs can be chosen as the B-NPs to perform the rational assembly. The formed Fe_3O_4-Au-Pt/Pd multi-component nanomaterials can be used in the catalysis reaction, in which the catalysts are easily separated with one magnet.

As we know, different size of AgNPs can be synthesized with very small size distribution.[3] Trimeric Ag-Ag-Ag nanoclusters can be produced with high yield by using the similar method for the creation of Au-Au-Au trimeric nanoclusters. Under the same concept, different kind of hetero-trimeric nanoclusters of Au or Ag could be produced. These structures will be perfect models for the study of optical property, such as SPR, SERS, and so on by ensemble measuring due to the high yield and purity (Figure 7-1b). The primary testing of the UV-Vis spectra of these nanoclusters reflected the varying SPR

phenomena (Figure 7-2). These nanomaterials also are prospectively used in many fields owing to the easy tuning of SPR.
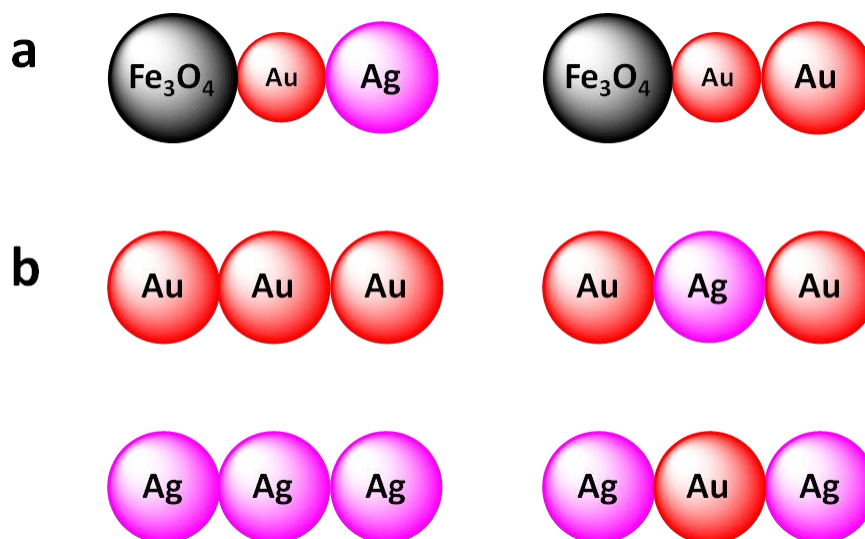

Figure 7-1 Schematic diagram of complex nano-composites that can be synthesized by using our nanoreaction strategy.
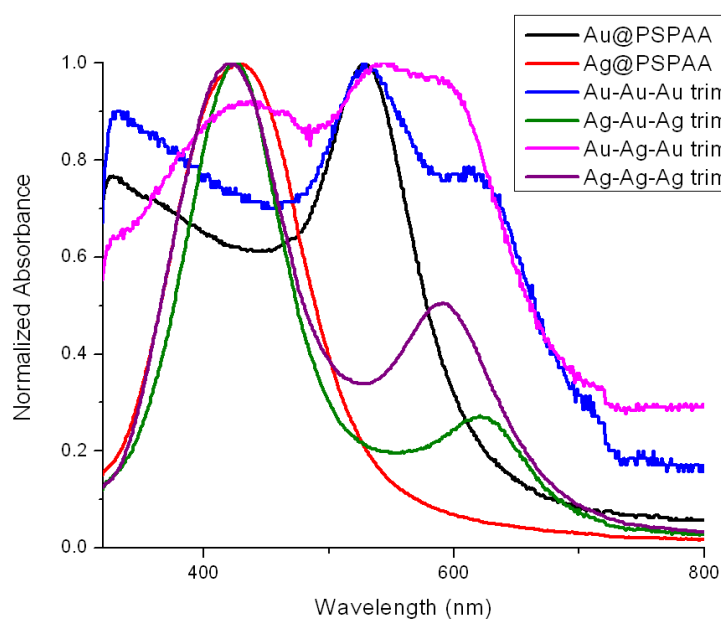

Figure 7-2 UV-Vis spectra of the AuNPs, AgNPs, as well as the trimeric nanocomposites.

Previous work of our group has demonstrated that the controlled nanoclusters can be used as the catalyst for ZnO NWs growth[4]. So the high purified multi-component nanoclusters may be used for the controlled nanowire

growth. Considering the fusion possibility of the nanoclusters, high melting-point NPs, such as PtNPs, SiO_2 NPs (or magnetic NP embedded SiO_2 NPs) can be used as the A-NPs (Figure 7-3). Controlled-NW clusters can be achieved finally. Because the grown NWs can be changed to many species, this kind of multi-component nanomaterials can be used in many fields.
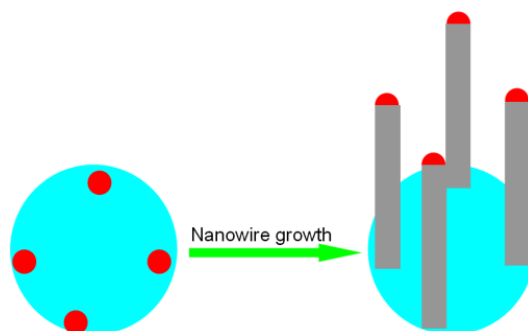

Figure 7-3 Schematic diagram of the controlled NW arrays grown on the nanoclusters.

The primary works on the conductive polymer encapsulation of these nanoclusters demonstrated that uniform polymer shells could coat the nanoclusters completely (Figure 7-4a and c).[5-7] These encapsulated nanoclusters could be etched selectively because the **1** coated NPs would not be injured. Thus the NPs with cavities structures were obtained (Figure 7-4b and d). These structures can be used as templates for the multi-component nanostructures synthesis.[8]
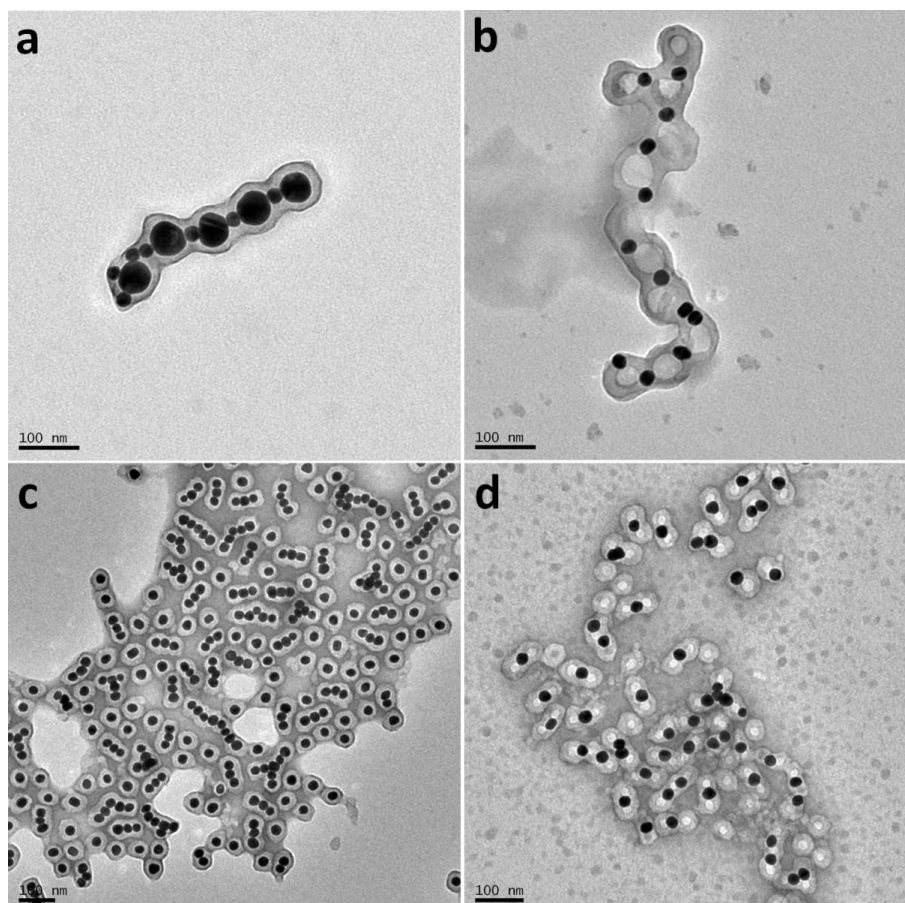
Figure 7-4 TEM images of the BAB type linear assemblies as well as the nano-cavities formed by etching the B-NPs.

(2) Formation mechanism study of the Au-Ag alloy NWs. Although the twisting behaviour of the new kind of Au-Ag alloy NWs has been studied in detail, the study of the synthesized Au-Ag alloy NWs is still limited. Why do these NWs contain the instinct chirality? What's the formation mechanism of the NWs? In despite of many strains in these NWs, why can they form and be stable for several months? The insight understanding of these questions may help us to produce more species of NWs with instinct chirality.

(3) Electrocatalytic properties of the core-shell NWs. It is well known that Pd or Pt are good catalysts, and have been widely used in fuel cell. Our Au-Ag@M (M = Pd or Pt) multi-component nanostructures have extreme large

specific surface area owing to the ultrathin Au-Ag NW cores. Very recently, one group published that Ag@Pd core-shell structures can be used for the hydrogen producing from the decomposition of formic acid at room temperature. Therefore, it is essential to study the electrocatalytic properties of our ultrathin core-shell nanostructures. For this study the PVP coating may be one huge challenge because it has been demonstrated that residue PVP may influence the real catalytic property.[9, 10]

(4) Improve the yield of helical gold NWs. In chapter 4, we demonstrated the synthesis of helical gold NWs in colloidal solution without hard template. However, the nice products were produced by using the aged 4-MBA as capping agent. Although the helical NWs can be synthesized by tuning the amount of 4-MBA deviates, the yield is still very low. Consequently, I have to continue studying the synthesis control to improve the yield. High yield of the helical gold NWs may be widely used in the future smart nanodevices. After systemic understanding of the formation mechanism, it may be expanded to other metallic helical NWs growth.

7.3 Bibliography

[1] Yu, H., Chen, M., Rice, P. M., Wang, S. X., White, R. L., and Sun, S. H., Dumbbell-Like Bifunctional Au-Fe3o4 Nanoparticles. *Nano Lett.*, **5**, 379 (2005).

[2] Buck, M. R., Bondi, J. F., and Schaak, R. E., A Total-Synthesis Framework for the Construction of High-Order Colloidal Hybrid Nanoparticles. *Nat*

Chem, **4**, 37 (2012).

[3] Chen, G., Wang, Y., Yang, M. X., Xu, J., Goh, S. J., Pan, M., and Chen, H. Y., Measuring Ensemble-Averaged Surface-Enhanced Raman Scattering in the Hotspots of Colloidal Nanoparticle Dimers and Trimers. *J. Am. Chem. Soc.*, **132**, 3644 (2010).

[4] Wang, X. J., Li, G. P., Chen, T., Yang, M. X., Zhang, Z., Wu, T., and Chen, H. Y., Polymer-Encapsulated Gold-Nanoparticle Dimers: Facile Preparation and Catalytical Application in Guided Growth of Dimeric Zno-Nanowires. *Nano Lett.*, **8**, 2643 (2008).

[5] Sindoro, M., Feng, Y. H., Xing, S. X., Li, H., Xu, J., Hu, H. L., Liu, C. C., Wang, Y. W., Zhang, H., Shen, Z. X., and Chen, H. Y., Triple-Layer (Au@Perylene)@Polyaniline Nanocomposite: Unconventional Growth of Faceted Organic Nanocrystal on Polycrystalline Au. *Angew. Chem., Int. Ed.*, accepted (2011).

[6] Xing, S. X., Tan, L. H., Chen, T., Yang, Y. H., and Chen, H. Y., Facile Fabrication of Triple-Layer (Au@Ag)@Polypyrrole Core-Shell and (Au@H2o)@Polypyrrole Yolk-Shell Nanostructures. *Chem. Commun.*, 1653 (2009).

[7] Xing, S. X., Tan, L. H., Yang, M. X., Pan, M., Lv, Y. B., Tang, Q. H., Yang, Y. H., and Chen, H. Y., Highly Controlled Core/Shell Structures: Tunable Conductive Polymer Shells on Gold Nanoparticles and Nanochains. *J. Mater. Chem.*, **19**, 3286 (2009).

[8] Gao, C., Zhang, Q., Lu, Z., and Yin, Y., Templated Synthesis of Metal Nanorods in Silica Nanotubes. *J. Am. Chem. Soc.*, **133**, 19706 (2011).

[9] Crespo-Quesada, M., Andanson, J.-M., Yarulin, A., Lim, B., Xia, Y., and Kiwi-Minsker, L., Uv–Ozone Cleaning of Supported Poly(Vinylpyrrolidone)-Stabilized Palladium Nanocubes: Effect of Stabilizer Removal on Morphology and Catalytic Behavior. *Langmuir*, **27**, 7909 (2011).

[10] Narayanan, R. and El-Sayed, M. A., Effect of Catalysis on the Stability of Metallic Nanoparticles: Suzuki Reaction Catalyzed by Pvp-Palladium Nanoparticles. *J. Am. Chem. Soc.*, **125**, 8340 (2003).

List of Publications

1. **Wang, Y.**, Chen, G., Yang, M. X., Silber, G., Xing, S. X., Tan, L. H., Wang, F., Feng, Y. H., Liu, X. G., Li, S. Z., and Chen, H. Y., A Systems Approach Towards the Stoichiometry-Controlled Hetero-Assembly of Nanoparticles. *Nature Communications*, **1**, 87 (2010).

2. **Wang, Y.**, Wang, Q., Sun, H., Zhang, W., Chen, G., Wang, Y., Shen, X., Han, Y., Lu, X., and Chen, H., Chiral Transformation: From Single Nanowire to Double Helix. *J. Am. Chem. Soc.*, **133**, 20060 (2011).

3. Chen, G., **Wang, Y.**, Tan, L. H., Yang, M. X., Tan, L. S., Chen, Y., and Chen, H. Y., High-Purity Separation of Gold Nanoparticle Dimers and Trimers. *J. Am. Chem. Soc.*, **131**, 4218 (2009).

4. Chen, G., **Wang, Y.**, Yang, M. X., Xu, J., Goh, S. J., Pan, M., and Chen, H. Y., Measuring Ensemble-Averaged Surface-Enhanced Raman Scattering in the Hotspots of Colloidal Nanoparticle Dimers and Trimers. *J. Am. Chem. Soc.*, **132**, 3644 (2010).

5. Feng, Y. H., **Wang, Y.**, Wang, H., Chen, T., Tay, Y. Y., Yao, L., Yan, Q. Y., Li, S. Z., Chen, H. Y., Engineering "Hot" Nanoparticles for Surface-Enhanced Raman Scattering by Embedding Reporter Molecules in Metal Layers. *Small*, **8**, 1613 (2011).

6. Chen, T., Wang, H., Chen, G., **Wang, Y.**, Feng, Y. H., Teo, W. S., Wu, T., and Chen, H. Y., Hotspot-Induced Transformation of Surface-Enhanced Raman Scattering Fingerprints. *ACS Nano*, **4**, 3087 (2010).

7. Wang, H., Xu, J., Wang, J. H., Chen, T., **Wang, Y.**, Tan, Y. W., Su, H. B., Chan, K. L., and Chen, H. Y., Probing the Kinetics of Short-Distance Drug Release from Nanocarriers to Nanoacceptors. *Angew. Chem., Int. Ed.*, **49**, 8426 (2010).

8. Yang, M. X., Chen, T., Lau, W. S., **Wang, Y.**, Tang, Q. H., Yang, Y. H., and

Chen, H. Y., Development of Polymer-Encapsulated Metal Nanopartictes as Surface-Enhanced Raman Scattering Probes. *Small*, **5**, 198 (2009).

9. Shen, X. S., Chen, L. Y., Li, D. H., Zhu, L. F., Wang, H., Liu, C. C., **<u>Wang, Y.</u>**, Xiong, Q. H., and Chen, H. Y., Assembly of Colloidal Nanoparticles Directed by the Microstructures of Polycrystalline Ice. *ACS Nano*, **5**, 8426 (2011).

10. Yang, M. X., Chen, G., Zhao, Y. F., Silber, G., **<u>Wang, Y.</u>**, Xing, S. X., Han, Y., and Chen, H. Y., Mechanistic Investigation into the Spontaneous Linear Assembly of Gold Nanospheres. *Phys. Chem. Chem. Phys.*, **12**, 11850 (2010).

11. Wang, J. A., Wang, F., Xu, J., **<u>Wang, Y.</u>**, Liu, Y. S., Chen, X. Y., Chen, H. Y., and Liu, X. G., Lanthanide-Doped LiYF$_4$ Nanoparticles: Synthesis and Multicolor Upconversion Tuning. *C. R. Chim.*, **13**, 731 (2010).